Magnetic and Transport Properties of Some Manganites with Colossal Magnetoresistance

By

Junhui Zhao

A Thesis Submitted to the Faculty of Graduate Studies
in Partial Fulfillment of the Requirements for the degree of

DOCTOR OF PHILOSOPHY

Department of Physics
University of Manitoba
Winnipeg, Manitoba

THE UNIVERSITY OF MANITOBA

FACULTY OF GRADUATE STUDIES

*****

COPYRIGHT PERMISSION PAGE

MAGNETIC AND TRANSPORT PROPERTIES OF SOME MANGANITES WITH COLOSSAL MAGNETORESISTANCE

BY

Junhui Zhao

A Thesis/Practicum submitted to the Faculty of Graduate Studies of The University of Manitoba in partial fulfillment of the requirements of the degree of

DOCTOR OF PHILOSOPHY

Abstract

The magnetic and electrical transport properties of the manganese perovskites are investigated through measurements of the field and temperature dependent ac susceptibility and resistivity respectively. Magnetic critical behaviour and the underlying physics are studied in detail using an approach based on scaling theory. The resistivity data are analyzed in terms of the double exchange and (bi)polaron theories. Also, measurements of the spontaneous resistive anisotropy (SRA) are presented and discussed based on the localized and itinerant models.

The experimental data on $La_{1-x}Ca_xMnO_3$ (x = 0.33) indicate that the critical phase transition (from a paramagnetic to ferromagnetic state) is of the second order/continuous type, critical exponent values found are consistent with those predicted by the near-neighbor 3-dimensional Heisenberg model despite uncertainties introduced at both lower and higher field which arise from the effect of both a mixed inhomogeneous state and possible single ion anisotropy. In contrast with this double exchange system, the pyrochlore, $Tl_2Mn_2O_7$, is studied using detailed measurements of field and temperature dependent ac susceptibility. Results demonstrate that the critical phase transition is of the second order type and the critical exponent values are in good agreement with the predictions of the Heisenberg model in spite of a marked regular (non-critical) component in the response near T_c, unexpected in view of the absence of Mn^{3+} ions. The comparison of these two systems reflects the same universality class despite the different exchange interaction mechanisms.

Measurements of temperature and field-dependent resistivity on sample $La_{0.67}Ca_{0.33}MnO_3$ indicate that the transport behaviour can be generally cate-

gorized into three regimes: a ferromagnetic metal dominated by double exchange at temperatures lower than T_c; a metal insulator transition near T_c with the coexistence of double exchange and polaron formation; and a paramagnetic insulator characterized by small polaronic hopping at high temperature. SRA measurements yield a typical value of about -1.1% below T_c, which is in good agreement with recent itinerant model calculations but does not follow well a linear decrease as the critical point is approached from below, as expected in a localized model.

The magnetic and transport behaviour of Ar-annealed $La_{0.67}Ca_{0.33}MnO_3$ is investigated and compared with that of untreated $La_{0.67}Ca_{0.33}MnO_3$. In particular, the transport data for both paramagnetic and ferromagnetic phases are analyzed in terms of the small polaron model; the results are consistent with predictions based on polaronic hopping, but inconsistent with recent quantitative predictions for magnetic small polaron mediated conduction in a phase separated picture.

Systematic measurements on the series $La_{1-x}Mg_xMnO_3$ ($0.05 \leq x \leq 0.6$) are presented with emphasis on the effect of the small average A-site radius on magnetic and transport properties. The experimental data show all samples undergo a paramagnetic to ferromagnetic transition with decreasing temperature. The Curie temperature, T_c, decreases with increasing doping level, x, beyond the 0.1 level. Data analyses of various low temperature features observed basically preclude the occurrence of a reentrant transition in favour of a phenomenon of technical origin. The resistivity always remains insulating over the entire temperature range studied, and the metal-insulator transition is completely suppressed due to the extremely small average A-site ion size. Based on these results, a phase

diagram for the $La_{1-x}Mg_xMnO_3$ ($0.05 \leq x \leq 0.6$) system is constructed.

The study of the series $(La_{1-x}Nd_x)_{0.67}Pb_{0.33}MnO_3$ ($0 \leq x \leq 1$) shows the influence of the substitution of Nd^{3+} ions at the A-site on the magnetic and transport properties under the condition of a fixed ratio of Mn^{3+}/Mn^{4+}. With increases in x, the transition temperature T_c decreases; whereas resistivity and magnetoresistance increase. All of the compounds display a phase transition from a paramagnetic insulator to ferromagnetic metal, a typical characteristic of double-exchange systems.

Acknowledgements

I would like to thank my supervisor, Professor Gwyn Williams for his support and guidance throughout this research project. I have benefited greatly in many ways by working with him.

I am also grateful to Dr. X. Z. Zhou and Dr. H. P. Kunkel for their invaluable help.

I wish to thank Dr. A. H. Morrish for allowing me use some equipment in his laboratory. Special thanks go to Dr. R. Roshko and Mr. T. Song for their Preisach model simulations on part of the experimental data.

Finally I wish to express my gratitude to my wife for her patience and encouragement during the completion of this research project.

Contents

Abstract i

Acknowledgements iv

1 Introduction **1**

2 Overview of the Properties of Manganites **7**

2.1 Basic Background 7

2.2 Properties of Manganites 12

2.2.1 Crystal and Electronic Structure 12

2.2.2 Double-Exchange and the Polaron Mechanism 15

2.2.3 The Phase Diagrams 23

3 The Magnetic Phase Transition **28**

3.1 Introduction 28

3.2 Critical Point Exponents 30

3.3 The Scaling Approach 32

4 Experimental Apparatus and Methods **43**

4.1 Sample Preparation 43

4.2 Susceptibility Measurement 44
4.2.1 Susceptometer and Cryostat 44
4.2.2 Signal Calibration and Background Correction 46
4.3 Resistivity and Magnetoresistance Measurements 49
4.4 The Quantum Design PPMS 6000 System 53
4.4.1 Description of the Equipment 53
4.4.2 Measurement Methods 57

5 Results and Discussion **58**

5.1 Critical Behaviour of $La_{0.67}Ca_{0.33}MnO_3$ 58
5.2 Critical Behaviour of the Pyrochlore $Tl_2Mn_2O_7$ 74
5.3 Magnetotransport and Spontaneous Resistive Anisotropy for the Ca-doped Perovskite 88
5.3.1 Magnetotransport Properties 93
5.3.2 Spontaneous Resistive Anisotropy (SRA) 98
5.4 Transport and Magnetic Properties of Ar-annealed $La_{0.67}Ca_{0.33}MnO_3$ 106
5.4.1 Experimental Procedure 107
5.4.2 Magnetic Properties 108
5.4.3 Transport Behaviour 114
5.5 The Magnetic and Electrical Transport Properties of the $La_{1-x}Mg_xMnO_3$ System 132
5.5.1 Hole-doped $La_{1-x}Mg_xMnO_3$ for $x \leq 0.4$ 136

5.5.2 Electron-doped $La_{1-x}Mg_xMnO_3$ for $0.45 \leq x \leq 0.6$ 171

5.5.3 Transport Properties 199

5.6 Preliminary Study of $(La_{1-x}Nd_x)_{0.67}Pb_{0.33}MnO_3$ 215

5.6.1 $Nd_{0.67}Pb_{0.33}MnO_3$ 217

5.6.2 $(La_{1-x}Nd_x)_{0.67}Pb_{0.33}MnO_3$ 227

6 Conclusions **239**

Bibliography **244**

Chapter 1

Introduction

In recent years, the properties of manganese pervoskites have received intense study following the discovery of the colossal magnetoresistance (CMR) displayed by many of these compounds. The term colossal magnetoresistance refers to a very large change in electrical resistance which occurs when a magnetic field is applied. This phenomenon has potential application in the magnetic data storage industry and further investigation could also lead to a new generation of electronic devices based on electron spin rather than charge transport (for examples, spin valves, spin transistors etc [1]). In addition to possible applications, the manganese perovskites provide an ideal natural platform for studying the physics of strongly correlated electronic systems. A detailed study could therefore lead to a deeper fundamental understanding of such systems as well as provide new possibilities for technological applications[2, 3].

The manganites most frequently studied have the general chemical formula $A_{1-x}B_xMnO_3$ where A is a trivalent lanthanide cation (e.g. La, Nd, Pr) and B is a divalent cation (e.g. the alkaline-earth elements Ca, Sr, Ba, Pb). The ground

state of the parent compound, $LaMnO_3$, is a layered antiferromagnet which is also an electrical insulator. The substitution at the A site by B divalent cations, typically to levels around $x = 0.2 - 0.4$, produces a modified ground state - specifically a ferromagnetic/metallic state appears below the Curie temperature, T_c. This modified compound not only displays a paramagnetic to ferromagnetic transition but also an insulator to metal transition when the temperature decreases. The metal-insulator transition is also sensitive to an applied magnetic field. This phenomenon was first observed and studied by Jonker and Van Saten in the 1950's [4], with the first clear explanation provided by Zener [5] using the so-called Double Exchange theory, a concept that was further developed by Anderson, Hasegawa and de Gennes [6]. However, more recently Millis, Littlewood, and Shraiman [7] have pointed out that Double Exchange alone cannot fully explain the transport behaviour of these perovskites. They suggested that some form of lattice-polaronic effects resulting from a strong electron-phonon coupling (possibly arising from a strong Jahn-Teller distortion) could explain the large resistivity within the paramagnetic phase. By contrast, Alexandrov et al [8, 9] have suggested that polaronic transport is operative in the ferromagnetic phase as well, and have proposed a theory of colossal magnetoresistance based on the idea of a current-carrier-density collapse (CCDC) due to an interplay of the electron-phonon and exchange interactions in doped manganites. Thus the present understanding of the physics of manganites is far from complete, and more theoretical and experimental studies are clearly necessary.

In the approach proposed by Millis et al, the metal-insulator transition

and the observed CMR in manganites are caused by a combination of the double-exchange interaction between ferromagnetically coupled Mn^{3+} and Mn^{4+} ions and electron-lattice coupling. To better understand how the metal-insulator transition and CMR is associated with the paramagnetic to ferromagnetic transition, it is important to fully investigate the nature of the magnetic phase transition, especially in light of the fact that the proposed Double-Exchange interaction between ferromagnetically coupled Mn^{3+} and Mn^{4+} ions is quite different from the conventional direct-exchange interaction (Heisenberg exchange interaction model) and the indirect-exchange interaction (superexchange interaction or RKKY models). For instance, the double-exchange coupling between the spins S_i and S_j is proportional to $\cos(\theta_{ij}/2)$, while for the direct Heisenberg interaction, the exchange coupling between the spins S_i and S_j is proportional to $\cos(\theta_{ij})$. On the other hand, the relationship between the polaronic conduction mechanism and the magnetic state and the role played by them in CMR materials is still not clear. Therefore, further investigation of the nature of the magnetic phase transition in these perovskites as well as the related conduction process is necessary as this information may assist in distinguishing between the rival theories mentioned above.

This thesis, at first, mainly focuses on the investigation of the nature of the magnetic phase transition since it has variously been described as first order, second order but crossing over to weakly first order near T_c or second order, but with a variety of critical exponents. The approach used here is based on the scaling theory predictions for analyzing critical exponents. Critical exponents

describe the behaviour near the critical point of various physical quantities which then can be related to the nature of the interactions. The scaling approach, often called the static scaling law or homogeneous function approach, because of the simple assumption it makes concerning the basic form of a thermodynamic potential, can yield functional relationships among the critical-point exponents and makes specific predictions concerning the form of the equation of state. These theoretical predictions will be compared with experimental results to further the understanding of the magnetic behaviour of the manganites.

Second main point in this thesis is concerned with the nature of electrical conduction process and charge carrier. The resistivity, magnetoresistance and spontaneous resistive anisotropy are investigated in perovskite systems, in particular, the polaronic transport behaviour in both the high temperature paramagnetic state and the low temperature ferromagnetic state is studied. The electrical transport properties in magnetic systems are different from non-magnetic systems, especially when passing through the critical point. Thus the investigation of the behaviour of resistivity in double-exchange systems can lead to a deeper understanding of the electronic and magnetic structure. Historically, the conduction mechanisms in ferromagnetic materials were discussed on the basis of two models, a localized model or an itinerant model. Recently, polaron models have suggested the electrical conduction has a polaronic characteristic in the perovskite systems both above T_c and, more recently, below T_c. Experimental data will be analyzed and compared with these theoretical model predictions.

In chapter two, an overview of previous studies of manganite systems is

presented. First, basic magnetic and electrical properties of ferromagnets are briefly reviewed, then crystal structure as well as general magnetic and electronic behaviour of the manganites are described; following this, the magnetoresistance and the nature of the metal-insulator transition are discussed in both the double-exchange and (bi)polaron model. Finally some important experimental results on these systems are reviewed briefly.

In chapter three, basic concepts concerning magnetic phase transitions are presented first, and then the definition of relevant critical exponents and the scaling approach are discussed; finally, three types of possible magnetic ground states and a theoretical model developed by Sherrington-Kirkpatrick for magnetic disorder are briefly presented.

The experimental apparatus and methods are briefly described in chapter four. Magnetic properties, such as ac susceptibility, are measured using either a home-built susceptometer or a Quantum Design PPMS 6000 system; resistivity, magnetoresistance and spontaneous resistive anisotropy are measured using conventional four probe methods.

In chapter five, experimental results and data analysis are presented. First, the magnetic phase transition of $La_{0.67}Ca_{0.33}MnO_3$ is investigated. Second, in comparison with the perovskite system, the critical behaviour of the pyrochlore, $Tl_2Mn_2O_7$, is examined. Then the general characteristics of the electrical transport displayed by the Ca-doped system and the spontaneous resistive anisotropy are studied. As a special case, an Ar-annealed $La_{0.67}Ca_{0.33}MnO_3$ sample is investigated and interesting features in the magnetism and electrical conduction are

discussed in detail; in particular the transport behaviour is found to have polaronic characteristics both above and below the Curie temperature. The series $La_{1-x}Mg_xMnO_3$, which involves a variation in Mg doping level, is investigated for the first time and the dependence of the magnetic and transport properties on doping level is examined. Finally, a preliminary study of $(La_{1-x}Nd_x)_{0.67}Pb_{0.33}MnO_3$ is presented, showing the effect of rare-earth Nd ion substitution at the A sites on the magnetic and transport properties.

The conclusions of the present work are summarized in the final chapter.

Chapter 2

Overview of the Properties of Manganites

2.1 Basic Background

Prior to a discussion on manganite systems, it is useful to review some basic principles of ferromagnetism. It was first established experimentally that the temperature dependence of the susceptibility, χ, for many ferromagnetic substances, at high temperature ($T > T_c$) can be expressed in the form [10]

$$\chi = \frac{C}{T - \theta} \tag{2.1}$$

where χ is the paramagnetic susceptibility, $\chi = \frac{M}{H}$, the ratio of the magnetization to the applied magnetic field, C is the Curie constant, θ is the paramagnetic Curie temperature, and T is the absolute temperature. This expression is called the Curie-Weiss law and can be theoretically deduced following Weiss's molecular exchange field assumption.

For a ferromagnetic system, Heisenberg proposed the following localized

exchange Hamiltonian for the interaction of spins

$$\vec{H} = -\sum_{i,j} J_{i,j} \vec{S}_i \cdot \vec{S}_j \tag{2.2}$$

Here $\vec{S}_i$ and $\vec{S}_j$ denote spins at lattice sites i and j, and J_{ij} is the exchange coupling constant which, when J_{ij} is positive, favours parallel spin alignment resulting in ferromagnetic ordering; when J_{ij} is negative, it favours antiparallel spin alignment leading to antiferromagnetic ordering. The variation of the sign and magnitude of the coupling constant, J_{ij}, can result in other more complex magnetic spin arrangements.

According to the Heisenberg exchange model, the so-called molecular field is the average effect of electron spin interactions between all atoms in the system and the mean field model actually arises from a first order approximation of the Heisenberg exchange interaction Hamiltonian.

In real materials, the exchange interaction varies with the distance between atoms as well as with the configuration of atoms. If the details of the interaction between atoms are considered, the behaviour at low temperature and near the critical point can be explained by including the interaction between nearest-neighbour spins in the Hamiltonian.

The exchange interaction normally is a short-range interaction arising from the direct overlap of electron wave functions. On the other hand, to explain the origin of magnetism in insulating magnetic compounds where the magnetic ions are separated by non-magnetic ions and there are few free electrons, Kramers [11]

proposed the so-called superexchange interaction based on the Heisenberg model, and later developed by Anderson [12]. No direct interaction between magnetic ions exists; instead, they interact indirectly with each other through non-magnetic ions lying between them.

In rare earth metals and alloys, the magnetic 4f electrons are buried in the inner core of the atom, and their wave functions are well localized. Neighbouring 4f ions do not thus interact strongly via direct exchange. Here magnetic interactions are transmitted indirectly by conduction electrons. This is the so-called RKKY exchange interaction, which successfully explained the magnetism of rare earth metals and their dilute alloys.

In addition to the localized models mentioned above, one other important approach was developed to account for experimental results on transition metals such as Fe, Ni, and Co that cannot be explained completely by localized models. This is called the itinerant electron model, which assumes that the 3d electrons are neither localized like 4f electrons nor essentially free like the 3s electrons. These 3d electrons are itinerant within a narrow energy band. Thus, the itinerant electron model is often used to deal with transition metals. Within this approach, the density of states N(E) is divided into two parts: $N(E) = N_+(E) + N_-(E)$, where $N_+(E)$ and $N_-(E)$ represent the density of spin-up and spin-down electrons with energy E, respectively. If the external magnetic field is zero and the exchange interaction is not considered, $N_+(E)$ and $N_-(E)$ are equal and there is no net spin moment. The presence of an exchange interaction splits the spin-up and spin-down bands, as is schematically illustrated in figure (2.1). A positive

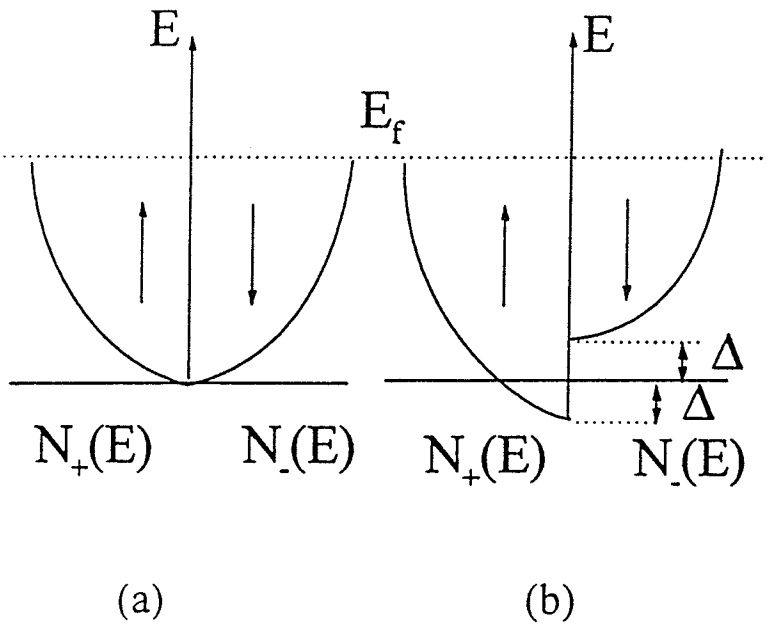

Figure 2.1: The schematic density of states: (a) without an exchange interaction, (b) with an exchange interaction.

exchange interaction between electrons (equivalent to a positive internal magnetic field) lowers the energy of the $N_+(E)$ sub-band relative to the $N_-(E)$ sub-band. The number of spin-up and spin-down electrons occupying the $N_+(E)$ and $N_-(E)$ states become unequal, resulting in a net magnetic moment that is manifested as a spontaneous magnetization. Because the 3d and 4s electrons may form a hybridized band, the band structure of transition elements can be quite complicated.

The magnetic state of a system also influences its transport behaviour. In non-magnetic metals, the electrical resistivity is often assumed to follow Matthiessen's rule [13], i.e.

$$\rho_T(T) = \rho_0 + \rho_P(T) \tag{2.3}$$

Here ρ_0 is the residual resistivity arising from scattering by impurities and defects while $\rho_P(T)$ is the pure metal resistivity produced by lattice (phonon) scattering of charge carriers. At low temperature, pure metals often display the temperature dependence $\rho_P(T) \propto T^5$ [14], while at high temperature a linear relationship on temperature, $\rho_P(T) \propto T$, occurs.

The electrical transport in a ferromagnet metal is, however, more complicated, frequently displaying an abrupt change in slope at the Curie point. This behaviour is attributed to the exchange coupling between local spins and conduction electron spins which gives rise to a change in spin disorder scattering. Well above the ordering temperature, in the paramagnetic regime, this contribution can be written as [15]:

$$\rho_m = \frac{K_F(mJ)^2}{4\pi l^2 z\hbar^3} S(S+1) \tag{2.4}$$

where K_F is the Fermi wave vector, z is the number of conduction electrons per atom, S is the local spin moment, J is the interaction strength between the conduction electrons and the local moments. This contribution to the resistivity is temperature independent above T_c. Near T_c, the resistivity depends on spin-spin correlations which also dominates $d\rho/dT$ and the specific heat of the magnetic system; both are predicted to display the same critical behaviour when T approaches T_c. At low temperature, magnetic scattering arising from electron-magnon (spin wave) scattering produces a contribution proportional to T^2 or $T^{3/2}$ depending on the specific magnetic state[16].

2.2 Properties of Manganites

2.2.1 Crystal and Electronic Structure

The manganese oxides that display colossal magnetoresistance possess the simple perovskite crystal structure shown in figure (2.2). The most widely studied family of the Ruddlesden-Popper compounds has the chemical formula $A_{1-x}B_xMnO_3$ (where A is a rare earth such as La or Nd, and B is a divalent alkali earth such as Sr or Ca). The parent compound is $LaMnO_3$ in which both lanthanum and manganese are trivalent ions, $La^{3+}$and Mn^{3+}, with the combined charge entirely balanced by the three oxygen O^{-2} ions. The ground state of $LaMnO_3$ is insulating and a layered antiferromagnet (i.e. ferromagnetic coupling in a plane perpendicular to the long axis of the crystal, while antiferromagnetic coupling between neighbouring ferromagnetic layers).

The electronic configuration of the Mn^{3+} ion is $1s^2 2s^2 2p^6 3s^2 3p^6 3d^4 4s^0$; the corresponding ground state of this 3d-configuration in free space is schematically shown in figure (2.3) where there are four electrons in its outermost 3d energy level. Hund's rule requires that the four electron spins align parallel to minimize the electrostatic repulsion energy; thus the four electrons occupy spin-up states, and this lowest energy state in free space corresponds to the angular momentum being L = 2. Because the Mn^{3+} ion lies at the center of an octahedron formed by the six neighbouring oxygen ions, the electric crystal field produced by the oxygen ions has cubic symmetry. The 3d levels of the Mn^{3+} ion are thus split into doubly degenerate $e_g(\Gamma_3)$ and triply degenerate $t_{2g}(\Gamma_5)$ orbital states by the crystal field, as is illustrated in figure (2.3) [17]. Three of the electrons occupy the

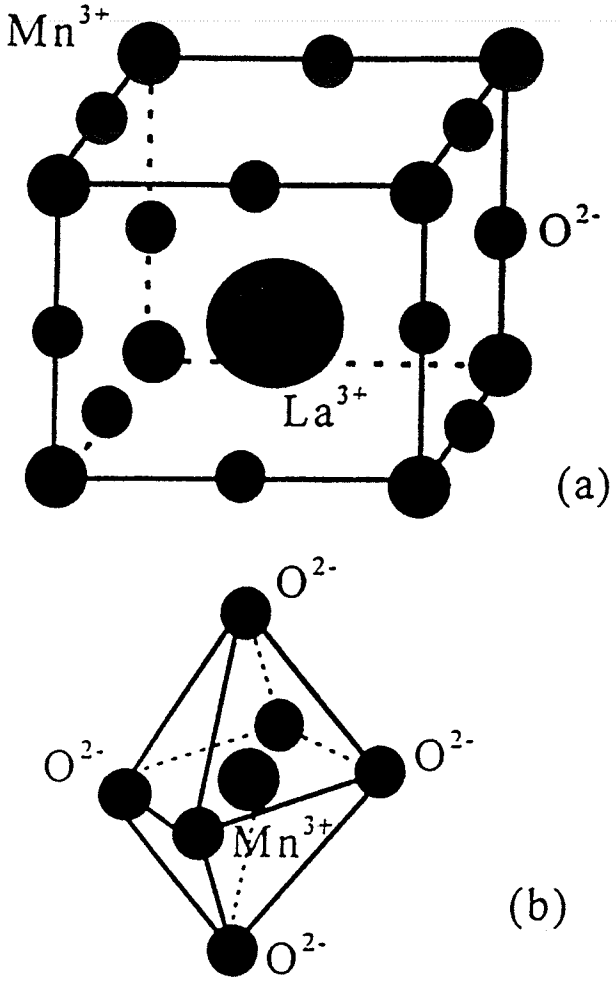

Figure 2.2: The crystal structure of the perovskite manganites: (a) $LaMnO_3$ consists of a large lanthanum ion at the center surrounded by manganese and oxygen ions; (b) a manganese and six neighbouring oxygen ions form a series of regular octahedra.

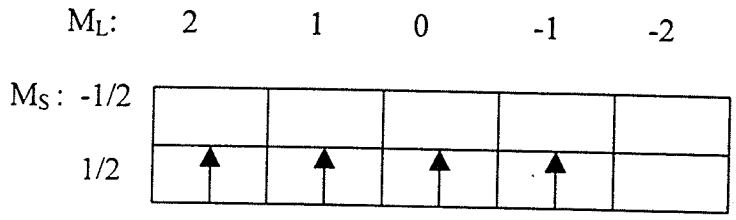

(a)

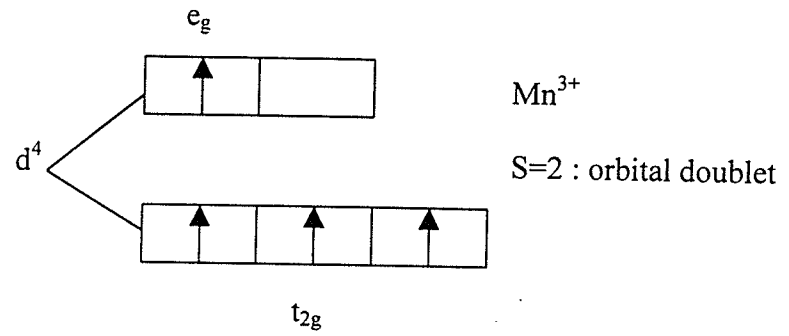

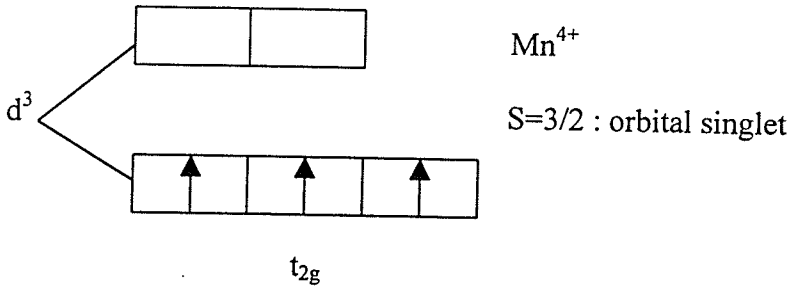

(b)

Figure 2.3: (a) Construction of the ground state of the d^4 configuration in free space; (b) Construction of the ground state of the d^4 and d^3 configuration in an octahedral field within the strong crystal field approach, but assuming the spin coupling to be stronger than the crystal field energy [17].

lower energy triplet state and the remaining single electron occupies the doublet state at a higher energy. In $LaMnO_3$, the e_g electrons are immobile due to the strong electrostatic force. The material is an antiferromagnetic insulator due to the antiferromagnetic superexchange interaction between t_{2g} core spins.

2.2.2 Double-Exchange and the Polaron Mechanism

The magnetic and electrical properties of the parent compound, $LaMnO_3$, however, can be modified by substituting divalent alkaline earth elements (such as calcium or strontium) into some of the lanthanum sites. This substitution converts some of the Mn^{3+} into Mn^{4+} ions, and creates holes in the e_g state. The remaining e_g electrons can become mobile by hopping via the oxygen 2p orbital to a neighbouring Mn^{4+} ion (i.e. producing an O(2p)-Mn(e_g) band). Coincidentally, neighbouring t_{2g} core spins experience a ferromagnetic interaction as these mobile carriers - the e_g electrons - hop between the Mn^{3+} and Mn^{4+} ions, a direct consequence of the requirements of the Hund's rules coupling. As a result, the antiferromagnetic insulating phase in the parent compound evolves into a ferromagnetic metallic phase in the doped manganites.

This process is schematically illustrated in figure (2.4). The so-called Double-exchange theory based on the mechanism described above was first proposed by Zener [5]; it is expressed mathematically by the following Hamiltonian:

$$H = -\sum_{i,j,\sigma} t_{ij}(c^{+}_{i\sigma}c_{j\sigma} + h.c.) - J_H \sum_{i} \vec{\sigma_i} \cdot \vec{S_i} \tag{2.5}$$

where σ_i and S_i denote the spins of itinerant e_g electrons and localized t_{2g} elec-

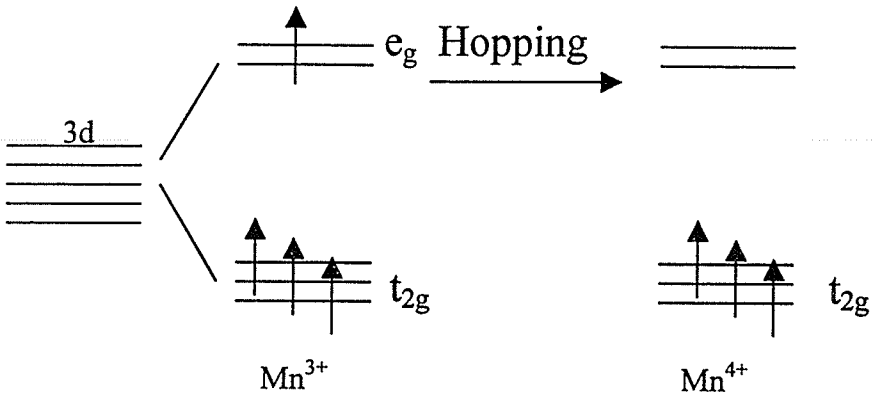

(a)

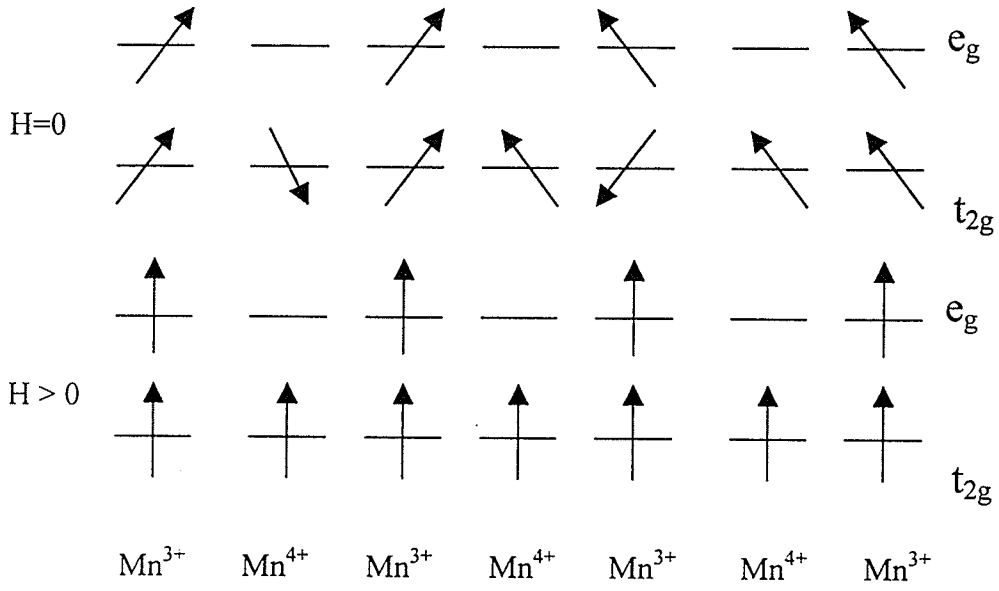

(b)

Figure 2.4: (a) Intra-site Hund's rule coupling requires that the t_{2g} spins are parallel when e_g electrons hop from Mn^{3+} to Mn^{4+}. (b) In zero field, disordered t_{2g} spin alignment does not favour e_g electron hopping, field induced alignment of t_{2g} spins enhances the hopping process.

trons respectively. J_H is the Hund's coupling constant between the e_g and t_{2g} electrons and t_{ij} is the hopping matrix element between nearest neighbour sites. An effective Hamiltonian for the limit $J_H S \to \infty$ was introduced by Anderson and Hasegawa [6] in the following form

$$H_{eff} = -\sum_{i,j} t(\vec{S}_i, \vec{S}_j)(c_i^+ c_j + h.c.) \tag{2.6}$$

$$t(\vec{S}_i, \vec{S}_j) = tcos(\theta_{ij}/2) \tag{2.7}$$

where θ_{ij} is the angle between the i-and j-th t_{2g} core spins. It can be seen that electron hopping between neighbouring sites becomes a maximum when the corresponding core spins are parallel and vanishes when they are anti-parallel, as results, on average, in the disordered phase. When a magnetic field is applied, spin disorder is suppressed and the alignment of electron spins reduces the scattering, leading to a reduction in resistivity, i.e. magnetoresistance. The manganese perovskites display magnetoresistance much larger than that occurring in normal ferromagnetic materials and often larger than in magnetic multilayers; thus the term colossal magnetoresistance (CMR) was coined to describe the drop in resistance in an applied magnetic field that is observed near the Curie temperature. The above picture derived from the double-exchange model gives a clear explanation (though qualitatively) of how ferromagnetism and metallic conduction are correlated.

From the band theory point of view, the mobile e_g electrons move in a conduction band throughout the solid. The motion of charge carriers is greatly

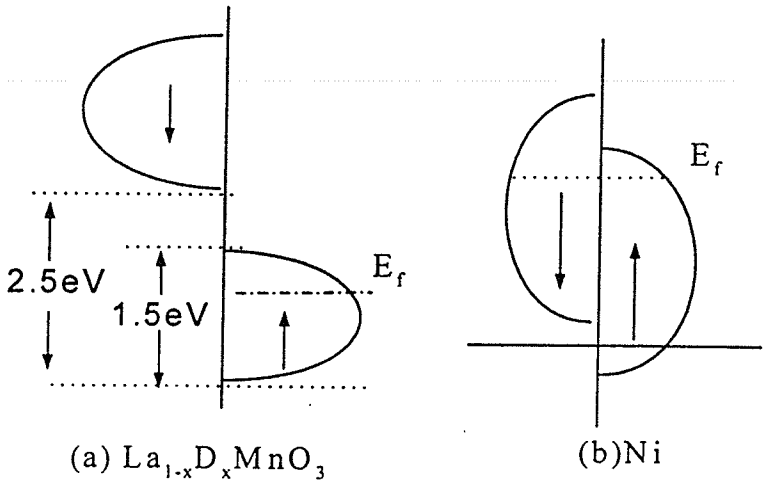

Figure 2.5: (a)Schematic density of states for $La_{2/3}D_{1/3}MnO_3$ at T = 0 in comparison with Ni metal in (b) [21].

influenced by the width of the conduction band, which is determined by the overlap of the manganese and oxygen orbitals which, in turn, depends on the geometric arrangement of the ions. Figure (2.5)(a) schematically shows the density of states for $La_{2/3}D_{1/3}MnO_3$; here the spin-up and spin-down bands are well separated, so that only spin-up electrons occupy the conduction band, leading to the coexistence of ferromagnetism and metallic conduction. Figure (2.5)(b) shows the density of states for a ferromagnetic metal such as Ni; in contrast with the polarization of 11% in Ni, the $La_{2/3}D_{1/3}MnO_3$ has a spin polarization of 100% [19, 20, 21]. The real situation, however, is more complicated than that illustrated in figure (2.5)(a). as is discussed below.

As previously described, the Mn^{3+} ions are located within oxygen octahedra

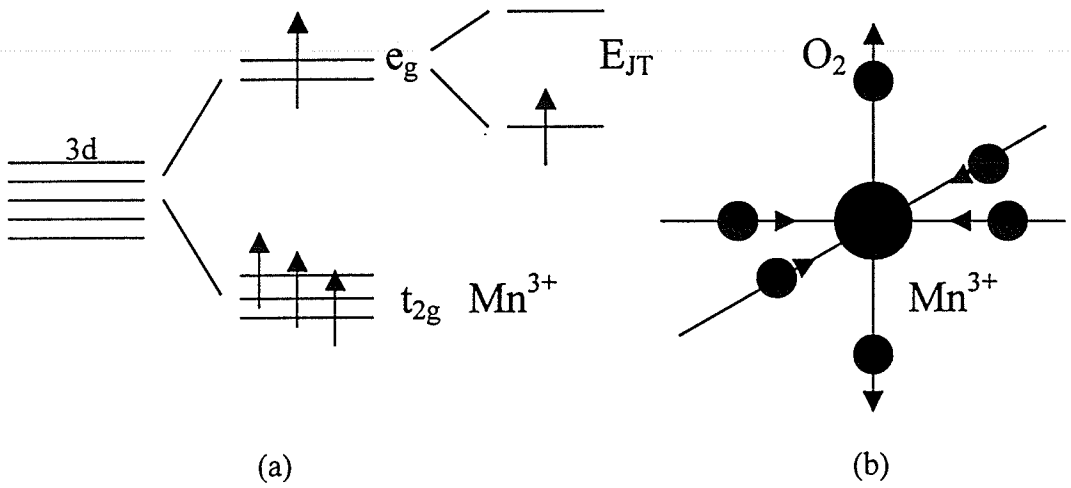

Figure 2.6: (a) Schematic representation of Jahn-Teller splitting. (b) The Mn^{3+} ion is at the center of a MnO_6 octahedra, the arrows represent the movement of O^{2-} ions [7].

where the e_g electrons occupy a high energy doublet state, which is unstable and can be further split into two energy levels as a result of electron lattice coupling as illustrated in figure (2.6)(a). Basically two types of electron-lattice coupling are involved. First is the distortion of the crystal lattice due to the atomic size difference of the dopant atom at the A sites, which can affect the Mn-O-Mn bond length as well as the bond angle resulting in a modification of the exchange interaction. The static Jahn-Teller effect [18] is another example of such a lattice distortion, which occurs here when the oxygen octahedra around the Mn^{3+} ion buckle to lift the e_g orbital degeneracy and lower the electronic energy. The second is the conventional dynamic electron-phonon coupling that arises from the instantaneous deviations of atom from their ideal crystallographic positions,

as illustrated in figure (2.6)(b). The interactions between charge carriers and the lattice vibrations play a fundamental role in determining the resistance of any system. Here the vibration of the lighter oxygen ions has the potential to affect the electron states on the manganese ion, thus enhancing the Jahn-Teller effect which already induces a local distortion of the lattice. The local lattice distortion can produce a lower energy state by incorporating an electron and trapping it, forming a so-called self-trapped state. The electron, together with the lattice distortion, is called a lattice polaron, i.e. it is not a simple electron charge carrier, rather the carrier is dressed with the lattice distortion. Jahn-Teller polarons tend to form when the Jahn-Teller stabilization energy becomes large compared to the incipient conduction electron bandwidth. Self-trapping competes with the mobility of charge carriers; this process can be represented by the parameter: $\lambda = E_{latt}/t_{eff}$, where E_{latt} is the energy gained from electron-phonon coupling and t_{eff} reflects the hopping ability of electrons [7]. In the high temperature paramagnetic phase, the electron-phonon coupling constant λ is thought to be so large that the charge carriers are indeed polarons. When the temperature decreases through the Curie temperature, the growing ferromagnetic order increases t_{eff} and thus decreases λ sufficiently so that metallic behaviour occurs. The Jahn-Teller polaron mechanism thus provides an explanation for the large resistance in the paramagnetic phase and the associated magntoresistance. Experimentally much evidence [22] exists and indirectly confirms the existence of the Jahn-Teller polaron, and thus that the electron-phonon coupling plays an essential role in the transport behaviour.

Other arguments, nevertheless, have been proposed concerning the specific nature of the polaronic mechanism [8, 9]. Alexandrov and Bratkovsky have suggested that the current carriers have oxygen p hole character rather than Mn 3d (e_g) character [23]. The coupling of itinerant p holes with the $3d^4$ local moment on the Mn^{3+} ions aligns the moments ferromagnetically [24]. The bipolaron model takes into account a tendency of polarons to form bound pairs because the attractive interaction between them can be larger than the Coulomb repulsion. There are two types of bipolarons: the first is called the onsite bipolaron and consists of two polarons occupying the same unit cell (on the same oxygen) which tends to form a singlet state; the other is the intersite bipolaron consisting of two polarons occupying different unit cells which can also form a triplet state. The onsite bipolaron has a large effective mass and a small disorder will make the bipolaron immobile; on the other hand, the effective mass of intersite bipolarons is much less and thus it is relatively mobile.

The bipolaron theory of CMR in ferromagnets was established by incorporating the presence of both electron-phonon and exchange interactions in the doped manganites. Owing to the strong electron-phonon interaction, polaronic carriers are bound into almost immobile singlet bipolarons in the paramagnetic phase of CMR materials. The non-degenerate polarons (singlet) induce a polarization of the localized Mn d electrons. As a result, the exchange interaction dissociates the bipolarons below T_c if the p-d exchange interaction energy $J_{pd}S$ of the polaronic carriers with the localized Mn d electrons is larger than the bipolaron binding energy Δ. Hence, the density of current carriers (free polarons)

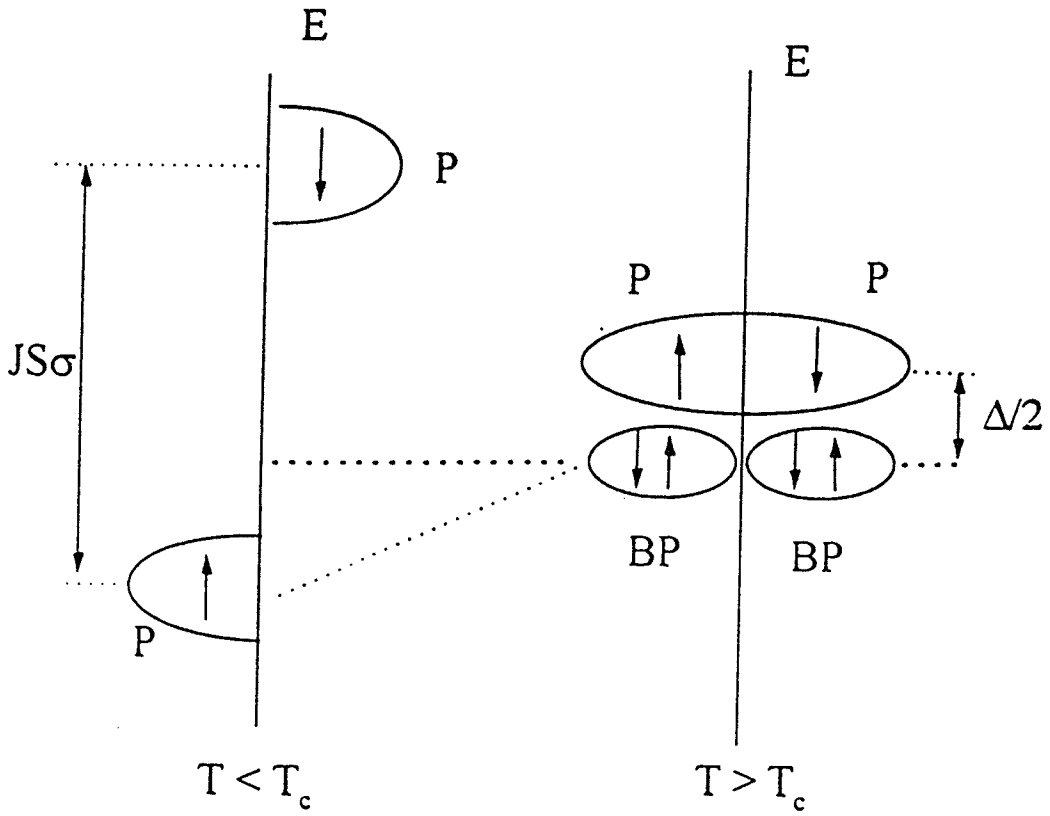

Figure 2.7: Schematic diagram of the free polaron (P) and the bound bipolaron (BP) density of states at temperatures below and above T_c for spin up ($\uparrow$) and spin down ($\downarrow$) moments. The polaron pairs (BP) break up below T_c if the exchange energy $J_{pd}S\sigma$ exceeds the pair binding energy Δ [8]

suddenly increases below T_c. The above process leads to the resistivity peak and the CMR observed in many ferromagnetic oxides, the mechanism is illustrated in figure (2.7) [8]. If the ferromagnetic exchange however becomes weak compared to the bipolaron binding energy, the charge carriers may retain their polaronic behaviour well below T_c. Thus, there would exist a non-metallic conduction behaviour in the ferromagnetic phase.

2.2.3 The Phase Diagrams

The magnetoresistance associated with a ferromagnetic metal/paramagnetic insulator transition arises from the existence of a Mn^{3+} and Mn^{4+} mixed valence state. A variety of phases, characterized by their magnetic and transport properties, can be produced by changing the ratio of Mn^{3+} to Mn^{4+} (i.e. changing the doping level or carrier concentration). For example, figure (2.8) shows the phase diagram for $La_{1-x}Ca_xMnO_3$ in the doping level (x) and temperature plane [25]: for x = 0, the undoped compound (parent compound) is insulating at all temperatures and a layered antiferromagnet below 140 K. Within a given plane perpendicular to the long (c) axis of the crystal, the Mn magnetic moments align ferromagnetically but alternate layers couple antiferromagnetically. The insulating ground state persists until x is greater than about 0.2 while the magnetic order changes in a complicated way. Above $x \approx 0.2$, the material becomes a ferromagnetic metal below the Curie temperature and a paramagnetic insulator at higher temperature. The ferromagnetic coupling becomes strongest around x = 0.3-0.4 for which the Curie temperature reaches its maximum value. The colossal magnetoresistance is observed near the Curie temperature. For $x \geq 0.5$

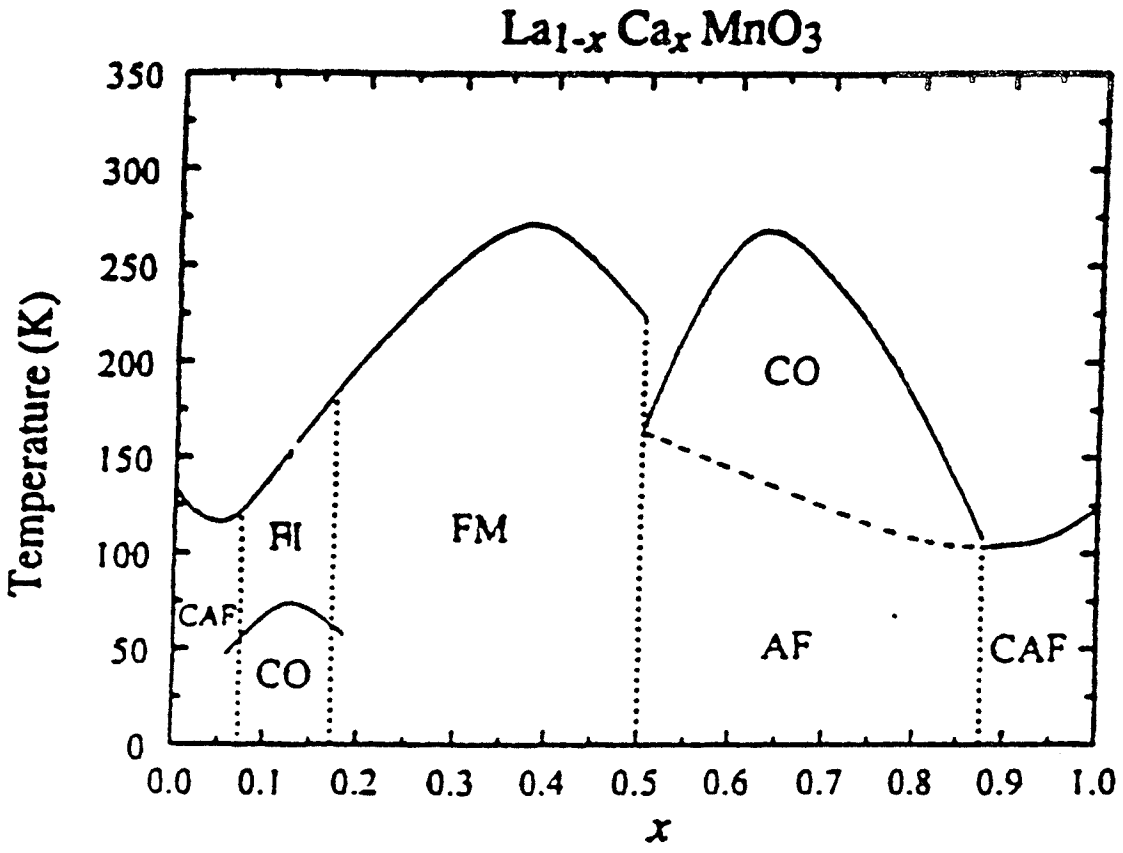

Figure 2.8: Magnetic and electronic phase diagram of $La_{1-x}Ca_xMnO_3$. The various states are: canted antiferromagnetic (CAF), ferromagnetic insulating (FI), ferromagnetic metal (FM) antiferromagnetic (AF), charge ordered (CO). Data from Cheong et al [25]

the system is paramagnetic at high temperature and undergoes a transition to an insulating charge ordered state as the temperature is reduced. Further lowering of the temperature causes the localized magnetic moments to become ordered and the material becomes antiferromagnetic.

From the above example, it is clear that the ferromagnetic ordering temperature T_c varies with the doping level, x; in addition, many experimental results have demonstrated that the structural distortions induced by changing the average A-site ionic radius $< r_A >$ [26, 27, 28] and applied pressure [29, 30, 31] also can affect the ferromagnetic ordering. These effects are attributed to changes of the conduction bandwidth W, which reflects the probability of electron hopping between Mn sites. The magnetic and transport properties vary considerably with the average atomic size of the A site atoms which can affect the crystal structure; the tolerance factor $t = (r_B + r_o)/\sqrt{2}(r_A + r_o)$ [4] is often used to measure deviations from perfect cubic structure ($t = 1$), here r_B, r_A and r_o are the radii of the divalent, trivalent and oxygen ions, respectively. Selection of appropriate mixtures of A (La, Pr, Nd) and B (Ca, Sr, Ba, Pb) elements allows t to be varied. Figure (2.9) shows a phase diagram of transition temperature versus tolerance factor [26].

By changing the Mn^{3+}/Mn^{4+} concentration ratio and the average ionic radius of the ions on the A site, the magnetic and transport properties of these perovskites can be tuned. The Mn^{3+}/Mn^{4+} concentration controls the kinetic energy of the charge carriers; the average ionic size affects the Mn-O-Mn bond angle which in turn determines the one-electron bandwidth of the e_g electrons.

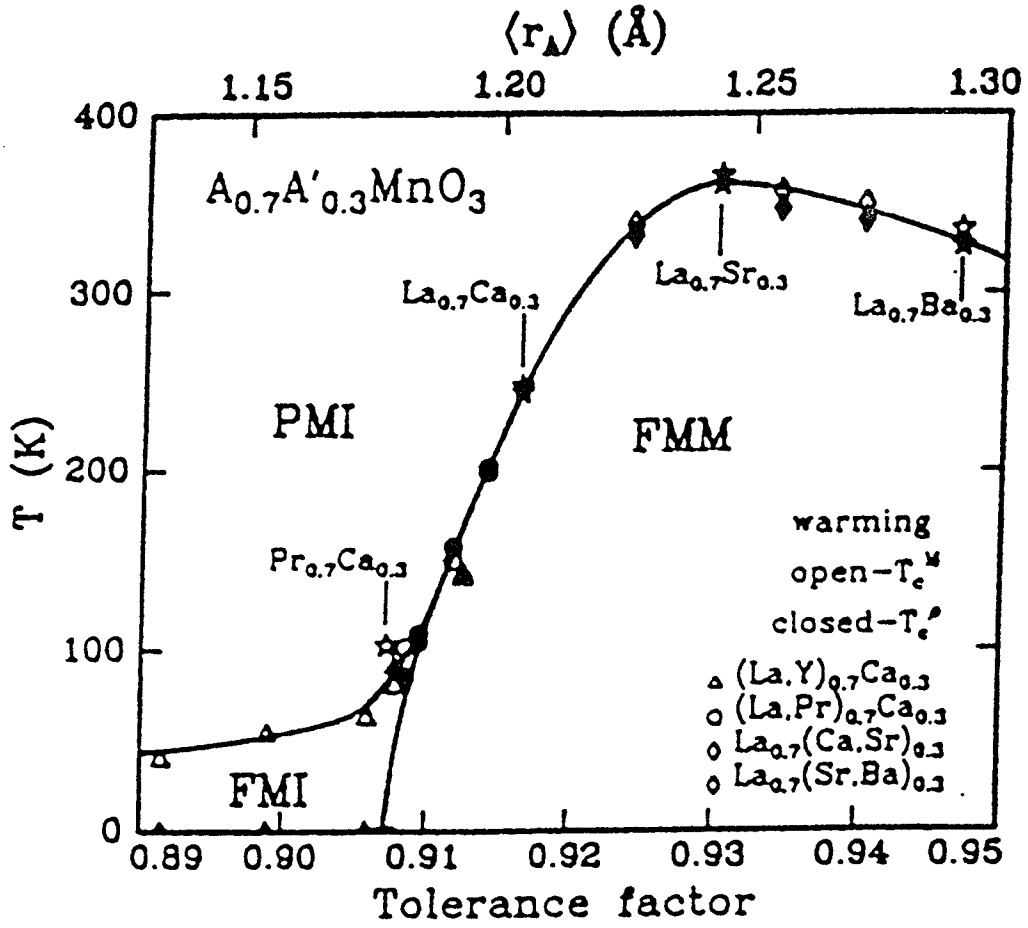

Figure 2.9: Phase diagram of transition temperature versus tolerance factor for $A_{0.7}A'_{0.3}MnO_3$ from reference [26]

For the ideal perovskite structure, the Mn-O-Mn bond angle is 180^o, and the overlapping of the manganese and oxygen orbitals is largest. The replacement of lanthanum by smaller ions causes the octahedra to buckle, resulting in a smaller bond angle. This decreases the overlap between the orbitals and narrows the energy band. Materials with a narrow energy band show poor conductivity and weaker ferromagnetic coupling which leads to a lower Curie temperature.

It is apparent that the physics of the manganites is very complex because of the interplay of the many interactions, such as antiferromagnetic superexchange in the $Mn^{3+(4+)}$-O^{2-}-$Mn^{3+(4+)}$ bonds, double-exchange in the Mn^{3+}-O^{2-}-Mn^{4+} pairs, electron-electron and electron-phonon interactions, and the Jahn-Teller effect. All of these result in a variety of magnetic and magnetotransport properties which in turn can be modified through the appropriate selection of doping ions and the adjustment of the charge carrier density.

Chapter 3

The Magnetic Phase Transition

3.1 Introduction

Phase transitions passing through a critical point are known as critical phase transitions. There are two kinds of critical phase transitions, which can be classified in terms of the behaviour of the Gibbs free energy G. If there is a discontinuity in the first derivative of G, such a transition is called a first order phase transition. First order phase transitions involve a latent heat and are generally difficult to understand on a microscopic scale because the physical properties of the two phases can be radically different. A second order or continuous phase transition is characterised by a discontinuity in the second or higher derivative of G and does not involve a latent heat. In magnetic systems, a continuous phase transition often occurs from an ordered ferromagnetic state to a disordered paramagnetic state; the critical point is at a temperature known as the Curie temperature, T_c, in zero applied magnetic field.

Three properties characterize all critical phase transitions. First is the order parameter that displays a broken symmetry at the critical point. The order

parameter is a continuous function of temperature, which is zero for temperatures above T_c and non zero below T_c. For ferromagnetism, the conventional order parameter is the magnetization. The order parameter may be a scalar or a vector quantity of a given dimensionality (number of degrees of freedom). The dimensionality of the order parameter has a strong influence on the properties of the phase transition. The second fundamental property is the correlation length, ξ, which reflects the spatial extent of the fluctuations in the order parameter. The third is the response time of the system. The latter two diverge as the critical point is approached from any direction.

In magnetic systems, the eigenstates of the Hamiltonian for the exchange interaction are generally too complicated to be solved. Several simplified models have however been developed with different values for the dimensionality of the order parameter; they are generally not applicable to real systems although some models have analytical solutions [32]. The three dimensional Heisenberg model uses the following Hamiltonian expression

$$\vec{H} = -\sum_n \sum_i J_i \vec{S_n} \cdot \vec{S_{n+i}} \tag{3.1}$$

as an approximation for isotropic magnetic materials. It is, in fact, not solvable; even for the simplified three dimensional Ising model there is no exact solution available. One solvable model is based on the Ginzberg-Landau theory, and involves a mean field assumption (long range interactions) for a continuous phase transition. In this approach the thermodynamic energy function is expanded as a Taylor series in the order parameters near the critical point although this is

technically inappropriate due to the non-analytical nature of properties at the critical point.

As a consequence, much effort has been directed towards the investigation of critical point exponents rather than finding a comprehensive theory that fits the experimental data over the entire temperature range.

3.2 Critical Point Exponents

Critical point exponents describe the behaviour of various physical quantities near the critical point [32, 33, 34]. Phenomenologically the experimental data are often appropriately rationalized before a complete theory can be developed to describe a system. In the magnetic case, for instance, physical measurements that are generally available near the critical point include the susceptibility, the specific heat, the correlation length, and the magnetization. The first three of these all become very large as the critical point is approached. Many careful measurements have been made of the divergence in these quantities as the critical point is approached, and almost all of them seem to obey a simple power law. For example, measurements of the isothermal susceptibility, χ, in small fields at temperatures close to and just above T_c, indicate that the experimental data can be fitted to the power law, $\chi_T = ct^{-\gamma}$ $(T > T_c)$ where c and γ are constants, and t is the reduced temperature, $t = (T - T_c)/T_c$; γ is called a critical exponent.

Critical exponents are generally defined in the following way. A function f(x) has a critical exponent λ close to the critical point x = 0 as the critical point

Table 3.1: Critical exponent values predicted for various models [32].

Critical Exponents	γ	γ'	β	δ
Definition	$\chi \propto t^{-\gamma}$	$\chi \propto (-t)^{-\gamma}$	$M \propto (-t)^{-\beta}$	$M \propto H^{1/\delta}$
Condition	$H=0,\ T>T_c$	$H=0,\ T<T_c$	$H=0,\ T<T_c$	$H=0,\ T=T_c$
2d Ising model	1.75	1.75	0.125	15
3d Ising model	1.238	1.25	0.326	4.78
3d Spherical	2	–	0.5	5
3d Heisenberg	1.388	–	0.367	4.78
Mean Field Theory	1	1	0.5	3.0
Experimental result	1.2 ~ 1.4	–	0.2 ~ 0.4	3 ~ 6

is approached from positive x if

$$f(x) \propto x^{\lambda} \qquad when\ x \to 0^{+} \tag{3.2}$$

where λ is defined by the following expression

$$\lambda = \lim_{x \to 0^{+}} \frac{lnf(x)}{ln(x)} \tag{3.3}$$

The expression exhibits an asymptotic behaviour close to the critical point. If the critical point is approached from negative x, then a critical point λ' can be defined for $x \to 0^{-}$.

Critical exponents are measurable while the complete functional behaviour may not be. Critical exponents are frequently determined from the slope of log-log plots of experimental data obtained near the critical point. There are a large number of relationships between the various exponents that result from fundamental thermodynamic and statistical mechanical considerations. Table (3.1) gives the critical exponents values generally used to describe magnetic systems.

3.3 The Scaling Approach

The scaling approach was originally proposed by Kadanoff [33, 34, 35] to deal with critical phase transitions; it was intended as an alternative to the direct approach of solving the standard models because of the technical difficulties presented by the latter. The basic assumption of scaling theory is that any correlated region can be divided into cells containing L lattice sites in each direction, with $1 < L < \xi/a$ where a is the lattice parameter and ξ is the correlation length. In a d-dimensional lattice, this gives L^d sites per cell. Each cell can be described by a Hamiltonian which includes interactions with neighboring cells. It is assumed that the form of the Hamiltonian does not change as the cell size is varied; only the parameters in the Hamiltonian vary. By defining the dimensionless variables $t = (T - T_c)/T_c$ and $h = g\mu_B H_e/k_B T$, where H_e is the effective field between cells, the Gibbs free energy of a cell can be written as $G(t, h)$. Scaling theory further assumes that the functional form of the free energy does not change with L, only with the parameters t and h. When the cell size is varied from La to λLa, the parameters defining G change from t and h to $\tilde{t}$ and $\tilde{h}$, and the free energy

changes to G ($\tilde{t}$,$\tilde{h}$). Scaling theory asserts that

$$\lambda G(h,t) = G(\tilde{h},\tilde{t}) \tag{3.4}$$

Cooper [36] showed that t and h have a linear relationship with $\tilde{t}$ and $\tilde{h}$

$$\tilde{t} = \lambda^p t \tag{3.5}$$

$$\tilde{h} = \lambda^q h \tag{3.6}$$

and thus

$$\lambda G(h,t) = G(\lambda^p t, \lambda^q h) \tag{3.7}$$

This relation essentially states that G is a generalized homogeneous function of this argument. In magnetic systems, the order parameter M can be found from the Gibbs function using

$$M(t,h) = -\frac{\partial G(t,h)}{\partial h} \tag{3.8}$$

From the definition of a homogeneous function given in equation (3.7), we have

$$\lambda \frac{\partial G(t,h)}{\partial h} = -\frac{\partial G(\lambda^p t, \lambda^q h)}{\partial h} \tag{3.9}$$

that is

$$M(t,h) = \lambda^{q-1} M(\lambda^p t, \lambda^q h) \tag{3.10}$$

There are two independent critical point exponents associated with the behaviour of the magnetization near the critical point. The exponent β describes the behaviour when $h = 0$ and $t \to 0$; while the exponent δ refers to the behaviour when $t = 0$ and $h \to 0$. For $h = 0$, and letting $\lambda = (-t)^{-1/p}$, then

$$M(t, 0) = \lambda^{q-1} M(\lambda^p t, 0) = (-t)^{(1-q)/p} M(1, 0) \tag{3.11}$$

Comparing the above equation with the power-law relation $M(t, 0) \propto (-t)^{\beta}$, we have

$$\beta = \frac{1 - q}{p} \tag{3.12}$$

The above equation expresses the critical point exponent β in terms of the two unknown scaling parameters p and q. Similarly, the exponent δ can also be expressed in terms of the scaling parameters by letting $\lambda = h^{-1/q}$ when $t = 0$, $h \to 0$

$$M(0, h) = \lambda^{(1-q)/q} M(0, 1) \tag{3.13}$$

Comparing this with the relation $M(0, h) \propto h^{1/\delta}$, yields

$$\delta = q/(1 - q) \tag{3.14}$$

By differentiating equation (3.10), the isothermal susceptibility can be obtained from $\chi = \partial M / \partial h$, i.e.

$$\lambda^{2q} \chi(\lambda^q h, \lambda^p t) = \lambda \chi(h, t) \tag{3.15}$$

Letting $h = 0$, $\lambda = (-t)^{-1/p}$, yields

$$\chi(0,t) = (-t)^{-(2q-1)/p}\chi(0,1) \tag{3.16}$$

Comparing (3.16) with the expected power law behaviour $\chi \propto (-t)^{-\gamma'}$, yields

$$\gamma' = \frac{2q-1}{p} \tag{3.17}$$

If $t \to 0^+$, then $\chi(0,t) \propto (t)^{-\gamma}$ and we have $\gamma = \gamma'$. This, in the scaling approach, indicates that all of the primed exponents (when $T < T_c$) are identical to their unprimed equivalents (when $T > T_c$).

Since there are only two unknown, independent static scaling parameters, it is expected that the value of the exponent γ is not independent of the values of β and δ. In fact, they are related through the expression

$$\gamma = \beta(\delta - 1) \tag{3.18}$$

which is called the Widom equality.

Scaling theory expresses all the static critical exponents in terms of just two parameters, p and q. The relationships between critical exponents are known as scaling laws.

Using this approach, it is possible to derive the following general expression for the magnetic equation of state

$$M(t,h) = t^{\beta}F(H/t^{\gamma+\beta}) \tag{3.19}$$

which leads to the following asymptotic power laws

$$M(0,t) \propto t^{\beta} \qquad T < T_c \tag{3.20}$$

$$\chi(0,t) \propto t^{\gamma} \qquad T > T_c \tag{3.21}$$

$$M(h,0) \propto h^{1/\delta} \qquad T = T_c \tag{3.22}$$

$$\gamma = \beta(\delta - 1) \qquad (Widom\ equality) \tag{3.23}$$

These relationships have been widely used to experimentally determine the critical exponents γ, β and δ.

From the above discussion it can be seen that the static scaling law or homogeneous function approach does not directly produce specific numerical values for any critical point exponents, rather the scaling hypothesis predicts functional relationships between the critical point exponents. In addition, the general form of the thermodynamic equation of state is predicted, which takes the form of a homogeneous function of field and temperature and has been used to derive a very useful expression for the susceptibility [37].

$$\chi = \partial M/\partial h = t^{\beta}(t^{-(\gamma+\beta)})\dot{F}(h/t^{\gamma+\beta}) \tag{3.24}$$

where $\dot{F}$ is the derivative of $F(h/t^{\gamma+\beta})$ with respect to its argument $h/t^{\gamma+\beta}$. This

result can be rewritten as

$$\chi = h^{-\gamma/(\gamma+\beta)}(h/t^{\gamma+\beta})^{\gamma/(\gamma+\beta)}\dot{F}(h/t^{\gamma+\beta}) = h^{-\gamma/(\gamma+\beta)}H(h/t^{\gamma+\beta}) \tag{3.25}$$

where $H(x) = x^{\gamma/(\gamma+\beta)}\dot{F}(x)$.

From equation (3.25) the susceptibility is predicted to have a peak at a reduced temperature, t_m, which is given by

$$(\partial\chi/\partial t)_{t=t_m} = 0 \quad i.e.\ \dot{H}(h/t_m^{\gamma+\beta}) = 0 \tag{3.26}$$

The above equation is satisfied when the argument of the function H is a constant, thus we have

$$t_m \propto h^{1/(\gamma+\beta)} \tag{3.27}$$

and using the Widom equality, the susceptibility at this peak temperature becomes

$$\chi(h, t_m) \propto h^{(1-\delta)/\delta} \tag{3.28}$$

In equation (3.27), $(\gamma + \beta)$ is called the cross-over exponent and the equation itself demonstrates that the peak in the ac susceptibility occurs at a reduced temperature, t_m, which shifts up with increasing magnetic field. Equation (3.28) indicates that the amplitude of the susceptibility peak decreases with increasing field (provided $\delta > 1$) along the cross-over line (defined as a locus of maxima in *chi*) in the (h,t) plane. The measurement of δ along the cross-over line is clearly independent of the choice of T_c, a particular advantage over the original

scaling approach in which not only is T_c required to be well defined, but also the measuring temperature must have sufficient stability.

The physical origin of these susceptibility peaks can be understood as follows; the cross-over line separates two regimes, one is a temperature dominated region where $(\partial\chi/\partial t)_h < 0$ and the other is field dominated in which $(\partial\chi/\partial t)_h > 0$. According to the fluctuation-dissipation theorem [32], the susceptibility obeys the expression

$$\chi(H,T) \sim \frac{1}{T}(< S_z^2 > - < S_z >^2) \tag{3.29}$$

In the high temperature regime, $\chi(H,T)$, measured in any fixed field H, varies as T^{-1} since $< S_z^2 > \rightarrow S(S+1)/3$ and $< S_z > \rightarrow 0$ when $T >> T_c$; thus $(\partial\chi/\partial t)_h < 0$, and thermal fluctuations are dominant. On the other hand, when the temperature is below the critical temperature, T_c, any non-zero field drives the magnetization towards saturation, causing a decrease in magnetic fluctuations, this process becomes more marked with increasing field; thus $\chi(H,T)$ decreases as T decreases away from T_c and $(\partial\chi/\partial t)_h > 0$. The above behaviour of the susceptibility as a function of temperature and field has been confirmed experimentally in many systems [38]. Theoretical model calculations of the temperature dependence of the susceptibility in a Sherrington-Kirkpatrick (SK) like model [39] qualitatively agree with the behaviour predicted by the above equations deduced from the scaling approach, as is shown in figure (3.1).

In addition to the existence of paramagnetic and ferromagnetic phases, magnetic systems may exhibit other possible forms of magnetic ordering due to the complications of the magnetic interactions, such as the so-called spin-glass state,

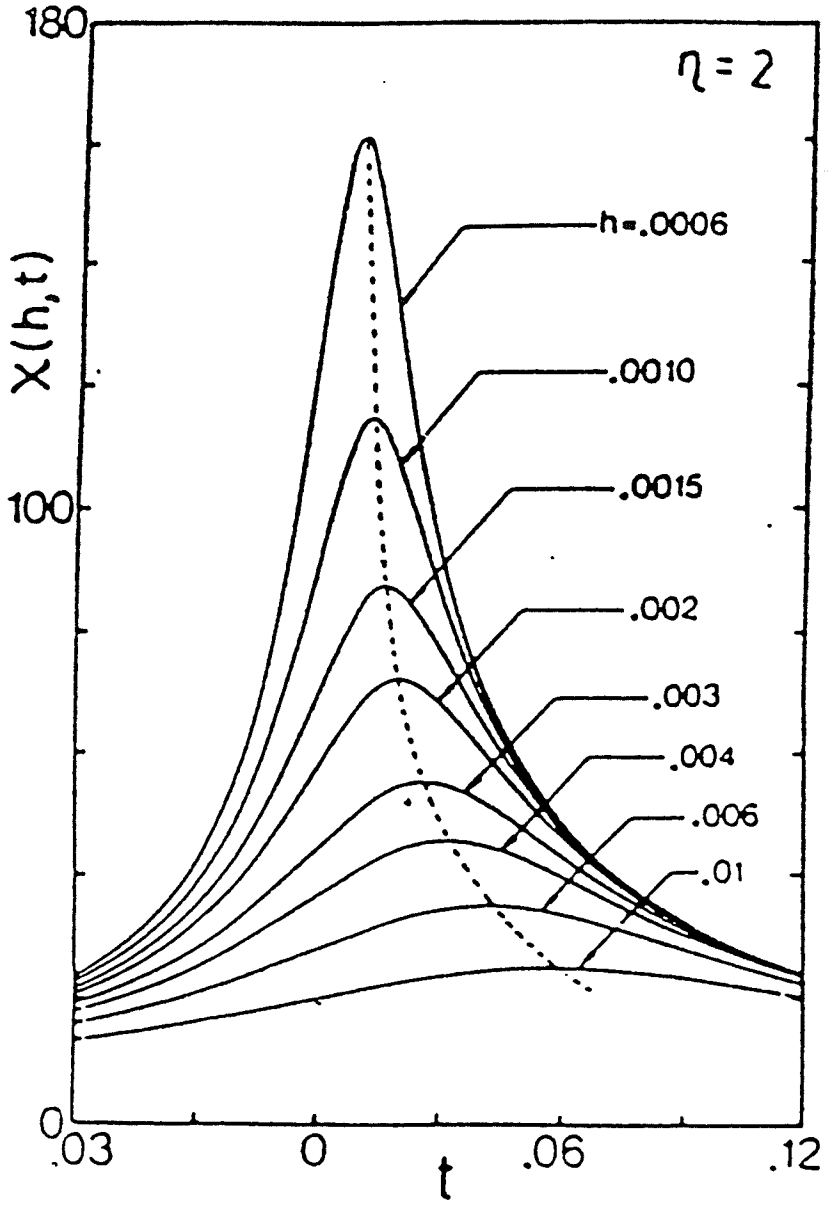

Figure 3.1: The field and temperature dependence of susceptibility plotted as the function of the reduced temperature at various applied fields as predicted by the model calculation. The dashed line defines the cross-over line. [39]

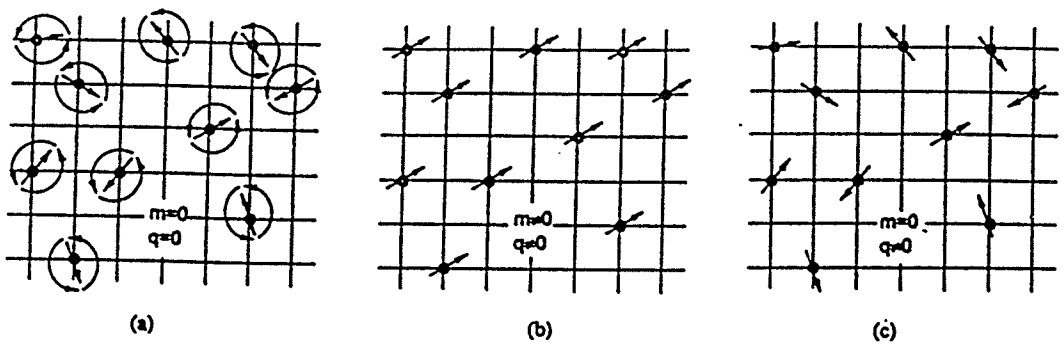

Figure 3.2: Schematic spin arrangements. (a) paramagnet; (b) ferromagnet below T_c; (c) spin-glass below T_{sg} [37].

a state often referred to as a randomly frozen spin arrangement. Since some spin-glass-like features have also been reported in the perovskites [40, 41, 42], the general features associated with three possible magnetic states are briefly outlined below.

Figure (3.2) shows a schematic diagram of the spin arrangement for paramagnetic, ferromagnetic and spin-glass systems [37]. The phase transitions between these three magnetic states are commonly discussed in terms of the behaviour of the order parameters m and q, which are defined as

$$m = << S_i >_T >_J \tag{3.30}$$

$$q = << S_i^2 >_T >_J \tag{3.31}$$

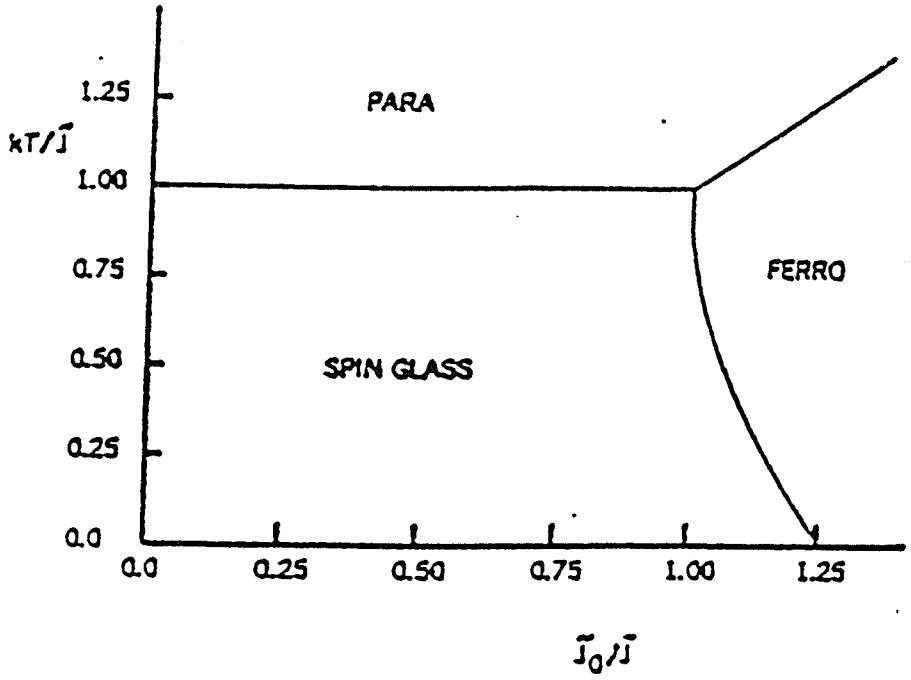

Figure 3.3: Sherrington-Kirkpatrick model phase diagram [43]

where the symbol $<>_T$ denotes an average over thermal fluctuations and $<>_J$ is an average over the exchange distribution; m is an order parameter for ferromagnetism and q is believed to be the order parameter for a spin-glass. Figure (3.3) shows the phase diagram predicted by the Sherrington-Kirkpatrick model [43] in which the exchange bond distribution in a magnetically disordered system is assumed to be Gaussian and J_0 represents the mean value (first moment) and J represents width of the distribution (second moment). This approach yields a set of coupled equations for m and q [44].

$$m = \frac{1}{\sqrt{2\pi}} \int_{-\infty}^{\infty} sB_s[\frac{s}{k_B T}(J_0 m + Jq^{1/2}\alpha + h_a)]e^{-\alpha^2/2} d\alpha \qquad (3.32)$$

$$q = \frac{1}{\sqrt{2\pi}} \int_{-\infty}^{\infty} s^2 B_s^2[\frac{s}{k_B T}(J_0 m + Jq^{1/2}\alpha + h_a)]e^{-\alpha^2/2} d\alpha \qquad (3.33)$$

The quantity $\eta = J_0/J$ is used to describe the degree of exchange bond disorder within a system. Briefly, $\eta >> 1$ indicates an essentially positive exchange coupling distribution, which leads to a ferromagnetic ground state; $\eta < 1$ corresponds to a high degree of bond disorder which induces a spin-glass state [45]; and for $1 < \eta < 1.25$, such models predict the existence of three states: namely paramagnetic, ferromagnetic and spin-glass states respectively as the temperature is lowered. If the magnetic system first undergoes the transition from paramagnetic to ferromagnetic, and then enters the spin-glass state, the second transition is often referred to as a reentrant process [46, 47].

Chapter 4

Experimental Apparatus and Methods

4.1 Sample Preparation

The bulk polycrystalline samples used in this study were prepared using standard solid state reaction methods. Appropriate metal oxides or metal carbonates were weighed in calculated proportions and nominal stoichiometric mixtures of these compounds were ball-milled in acetone for 24 hours to ensure that they were mixed thoroughly. Following this, the dried powder was pressed into pellet form and preheated in air at $800°C$ for 24 hours. The products were then hand-ground into a fine powder using a mortar and pestle, and the powder were then mixed with a binder (polyvinyl alcohol solution), granulated and pressed into a disk shape. Such samples were sintered for typically 24 hours at around $1200°C$ in air or flowing oxygen. Because both the sintering temperature and sintering atmosphere will affect the properties of samples, the specific preparation conditions used for different samples may vary.

Crystal structures were generally examined using x-ray diffraction to con-

firm that the prepared samples are single phase. The effect of the preparation conditions on the grain size of the samples was determined using Scanning Electron Microscopy in particular for the samples of $La_{0.67}Ca_{0.33}MnO_3$.

4.2 Susceptibility Measurement

Susceptibility measurements were performed initially using a home-made phase-locked susceptometer, and later a commercial Quantum Design (PPMS) was employed. The former is described first.

4.2.1 Susceptometer and Cryostat

The real (in-phase) component of ac susceptibility, $\chi = dM/dH$, was measured using a home-built susceptometer and cryostat which were previously described in detail [48, 49]. Here the operating principle of the susceptometer is briefly discussed. As is shown in figure (4.1), an AC signal is applied to the two matched LC oscillators, typically with an amplitude of 30 mOe and a frequency of 2.4 kHz. The sample is placed in one of the coils and the differential signal from the two oscillators, which is produced due to the inductance change of the coil caused by the sample, is generated by a phase detector; thus an output voltage proportional to the relative shift in the signal's phase is produced. This signal is amplified and then fed back to the sample coil through a voltage controlled reactance which controls the frequency of the oscillator. In this way a correction signal, which is proportional to the sample susceptibility, is generated as the output of the susceptometer.

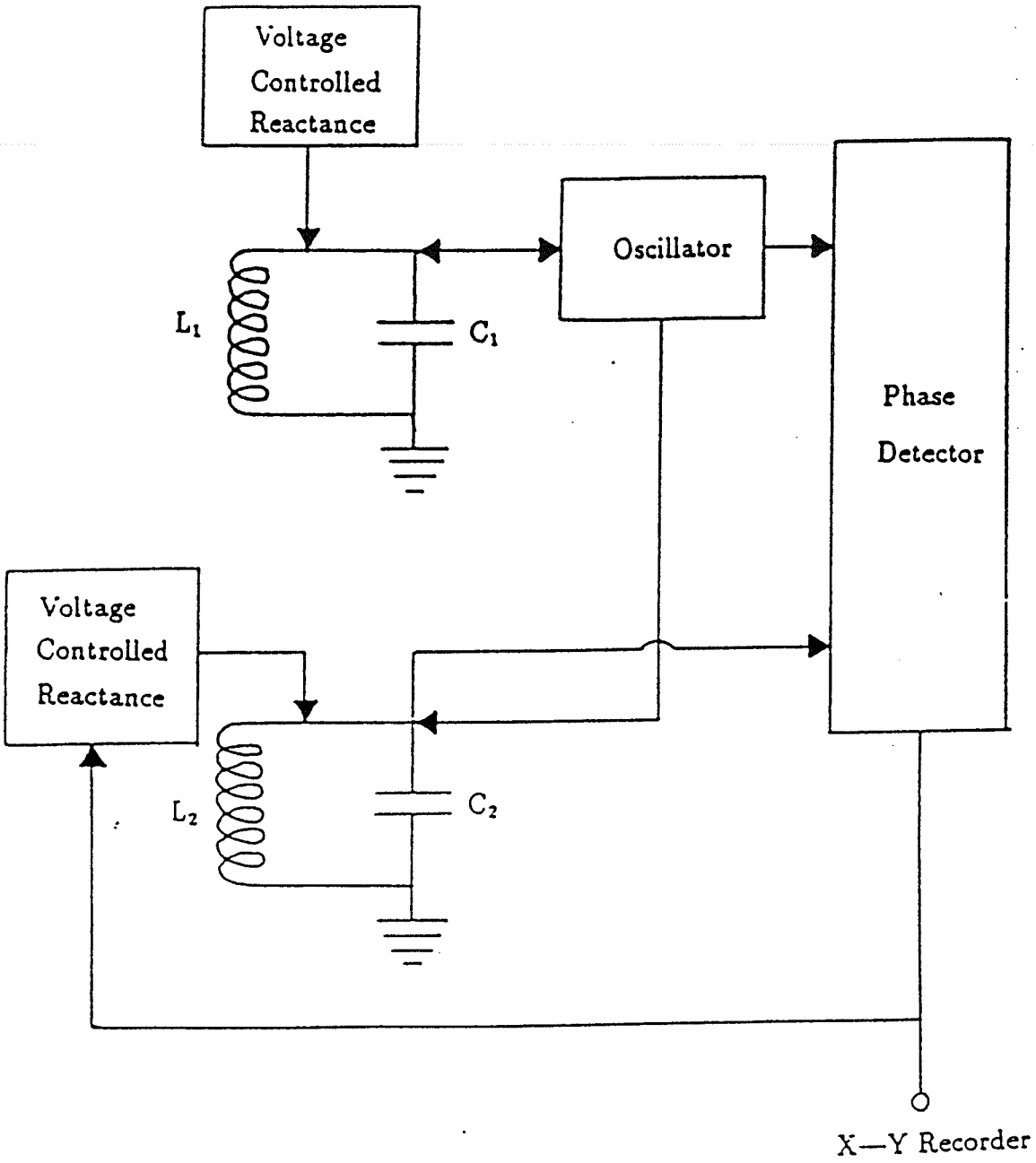

Figure 4.1: Block diagram of the ac susceptometer [48].

To perform low temperature measurements, a cryostat was built as shown in figure (4.2). The sample probe is inserted into the tail of a liquid helium dewar. The sample is placed in a bundle of copper wires attached to the sample probe into which a germanium resistor and an Au+0.03% Fe-Chromel thermocouple are also seated just above the sample position. A Nichrome wire, which is wound around the copper block of the sample holder, provides temperature control. The copper braid provides a good thermal contact to the sample and also allows the ac driving field to penetrate into the sample volume. Around the sample probe/copper wire bundle are mounted the detecting coils as well as two solenoids which are used to provide a dc biasing field which has a maximum amplitude of 1000 Oe. The coils are immersed in liquid nitrogen. The temperature range covered by this cryostat is from 1.7 K to room temperature and a typically warming rate of 0.01-0.3 K/min is used in most experiments.

4.2.2 Signal Calibration and Background Correction

The measured signal does not directly give the absolute susceptibility value. Small background contributions from the copper braid, the temperature sensor and the sample block need to be subtracted from the total signal. This is done by the zero reading method, i.e., by withdrawing the sample from the pickup coil and performing a separate zero measurement. A further background measurement is then performed by removing the sample and taking a series of background readings that provides an appropriate correction curve.

To obtain the true susceptibility, the susceptometer was calibrated using 99.999%

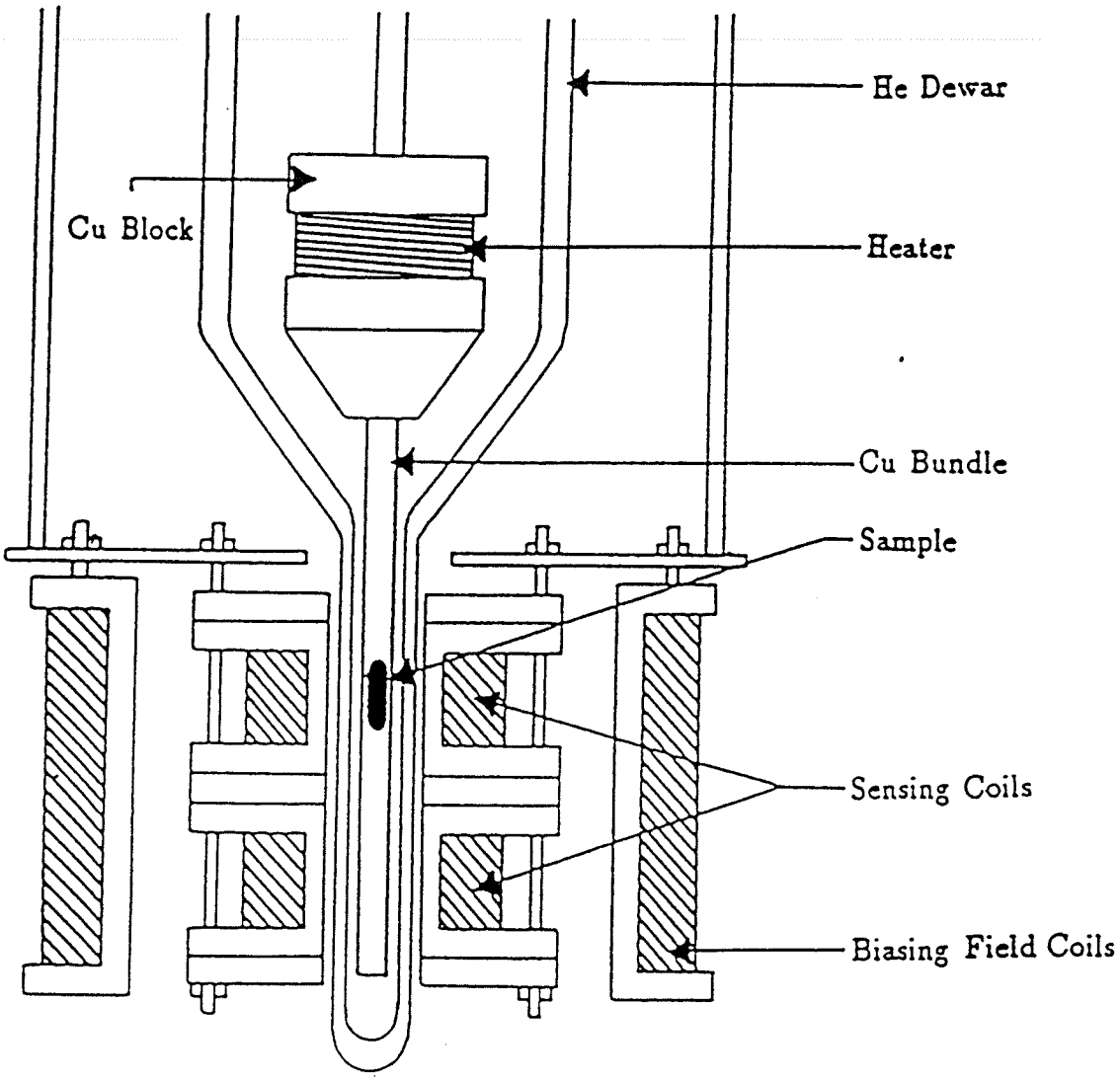

Figure 4.2: The cryostat and the arrangement of the ac susceptometer components [48].

pure Gd_2O_3 powder; the latter obeys the Curie-Weiss law

$$\chi = \frac{N\mu_{eff}^2}{3k_B(T-\theta)} \tag{4.1}$$

where N is the number of Gd atoms per gram, $\mu_{eff} = (7.70 \pm 0.04)\mu_B$, and θ = -13 K for antiferromagnetic Gd_2O_3 [50]. The measured signal also depends on the mass of the specimen, so that

$$\chi = cV/m \tag{4.2}$$

where V is the susceptometer output in volts and c is the appropriate calibration factor (determined using equation (4.1)) and m is the mass.

Another important consideration is the demagnetization correction. The internal magnetic field is given by $H_i = H_a - NM$, where H_a is the external applied field and N is the demagnetization factor. If $\chi_m = dM/dH_a$ denotes the measured susceptibility and $\chi_t = dM/dH_i$ represents the true susceptibility, then the following equation relates the true and measured susceptibilities

$$\chi_t = \frac{\chi_m}{1 - N\chi_m} \tag{4.3}$$

Two types of measurements are generally performed using this home-made susceptometer, the first is the temperature dependence of the susceptibility in a fixed applied biasing field, while the second is the field dependence of the susceptibility at a fixed temperature.

4.3 Resistivity and Magnetoresistance Measurements

The resistivity measurements were usually performed using a conventional four-probe technique. The current and the potential drop across the sample are measured and the resistance is obtained directly following Ohm's law.

Both a DC and an AC technique are available. The DC method is more accurate in terms of finding absolute resistivity values, but tends to be sensitive to thermal emf's, which can be compensated for using a current reversing switch. When very small changes in resistance are measured, the AC technique is more appropriate due to its much greater sensitivity. A detailed circuit diagram for the AC technique is shown in figure (4.3). The basic operation principle is now briefly described. A signal generator (General Radio 1311A Audio Oscillator) applies an AC current of 37 Hz to the sample, and also simultaneously sends a reference signal to a lock-in amplifier (Princeton Applied Research HR8) and to an AC back-off circuit. The relatively large sample voltage, V_0, can then be backed off so that small voltage changes induced by an applied field or temperature change can be amplified and measured accurately. A variometer is incorporated into the back-off circuit to eliminate the (quadrature) effects of capacitances and inductances in the measuring circuit, and the lock-in amplifier is adjusted to detect the "in phase" (with respect to the reference) signal, so that any quadrature components will not affect the output signal.

Figure (4.4) shows the cryostat and sample holder previously described in detail [49]. For temperature control and measurement, a Lakeshore Cryogenics

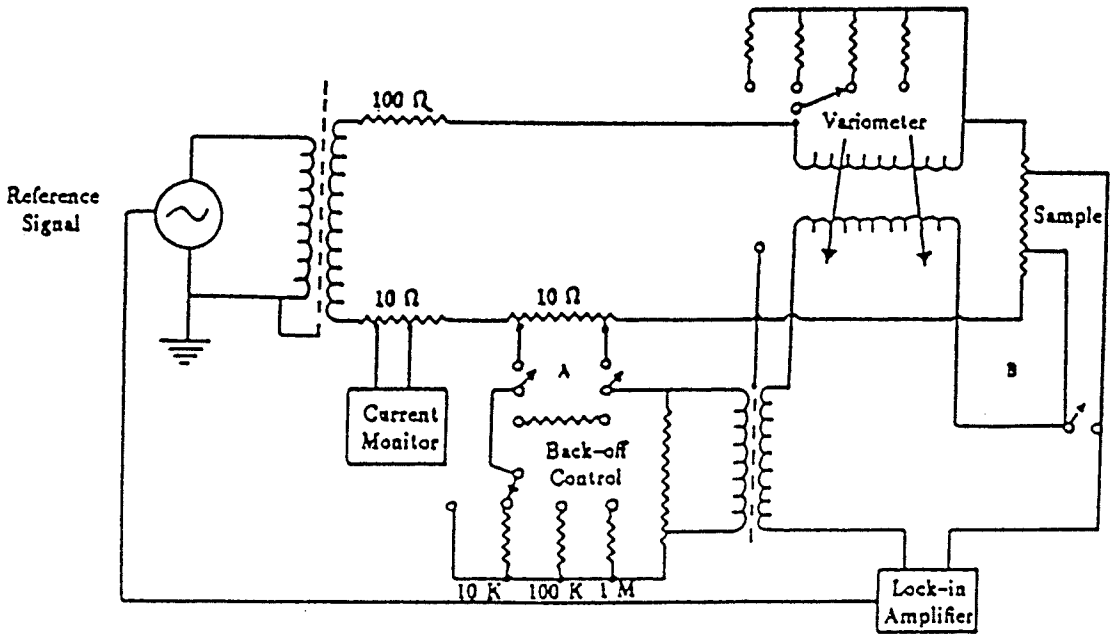

Figure 4.3: Circuit diagram of the ac resistivity measurement system [49].

CG2000 calibrated carbon-glass resistor was used in conjunction with a Lakeshore model 520 temperature controller. A heater on the sample block was made using Cupron wire with a nominal resistance of 25 Ω at 77 K. Temperatures ranging from 1.7 K to 300 K can be achieved; the resistivity in zero field can be measured up to room temperature, but a maximum temperature of 80 K is possible when a liquid helium cooled superconducting magnet is operative. The superconducting solenoid manufactured by American Magnets with a length of 25 cm and a bore of 6.55 cm and capable of providing an axial field up to 3 tesla was used. The apparatus also can measure the spontaneous resistive anisotropy (SRA) (discussed in more detail later) as the sample holder can be rotated by 90 degrees with respect to the field direction.

A relatively small apparatus for measuring the DC resistivity was also utilized and is now briefly described. The sample holder was made by attaching a printed circuit board onto a copper block using GE varnish. Four separate circuit leads on the circuit board were coated with Indium to achieve good electrical contact with the sample which was then pressed onto the four indium contacts with a screw and yoke system. A copper-constantan thermocouple was attached under the circuit board, and insulated heater wires were wound around the copper support rod above the sample holder to provide heating power. Temperatures from 77 K to 350 K can be attained with this system by inserting the sample probe into a small dewar which can be filled with liquid nitrogen. The tail of the dewar was positioned between the two poles of an electromagnet, which can produce a field of approximate 1.6 tesla with a working gap of 1.6 cm. The magnetic field

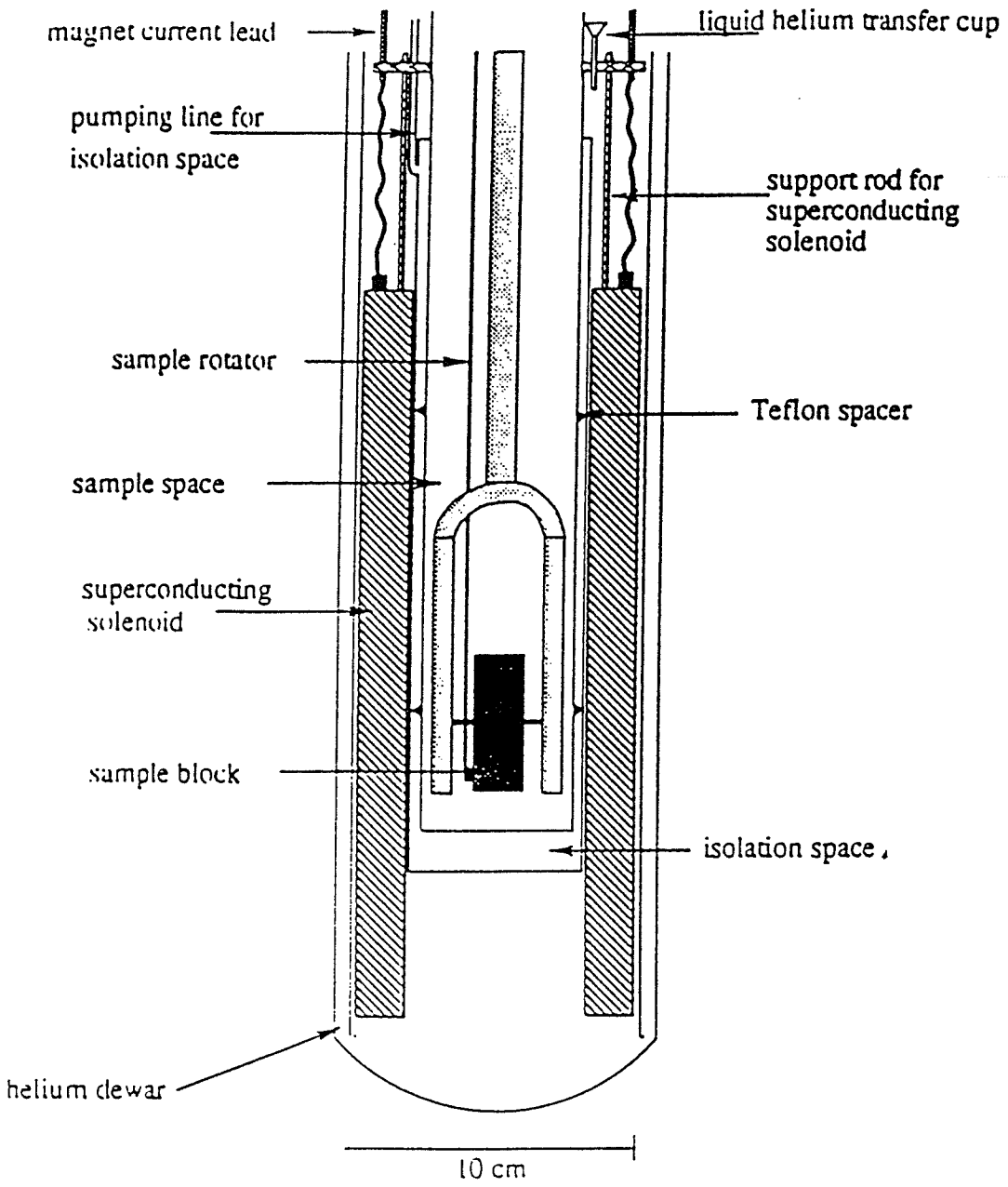

Figure 4.4: The resistivity cryostat and the arrangement of the major components including the SRA sample block [49].

was measured using a Hall probe. The magnet power supply for this system was operated either manually for a fixed field or driven by a Synthesized Function Generator (Stanford Research System Model DS335) for field sweeps. The constant sample current was provided by a homemade current source (46.44 mA) or by a Keithley 224 programmable current source (current limit from 0.1 nA to 0.1 A); and the voltage output across the sample was measured using a HP 34401A multimeter. Data were collected using a computer with a GPIB interface card and homemade data acquisition software.

4.4 The Quantum Design PPMS 6000 System

4.4.1 Description of the Equipment

Measurements were also carried out in a commercially produced system, a Quantum Design PPMS magnetometer. The cryostat of the PPMS system is an aluminum dewar that contains the liquid helium bath that is used to cool the superconducting magnet and to provide temperature control. The probe shown in figure (4.5) is a central element of the PPMS. It incorporates all of the basic temperature control hardware, superconducting magnet, the helium level meter, a variety of electrical connections, and gas pumping lines. Its main function is to provide a space where specific measurement components can be fitted. Temperature and field control can be realized by another important component – the Model 6000 Controller, which houses all of the gas control valves and system electronics. The major components of the Model 6000 includes: the CPU board (Processor), the motherboard (system integration), the system bridge board (tem-

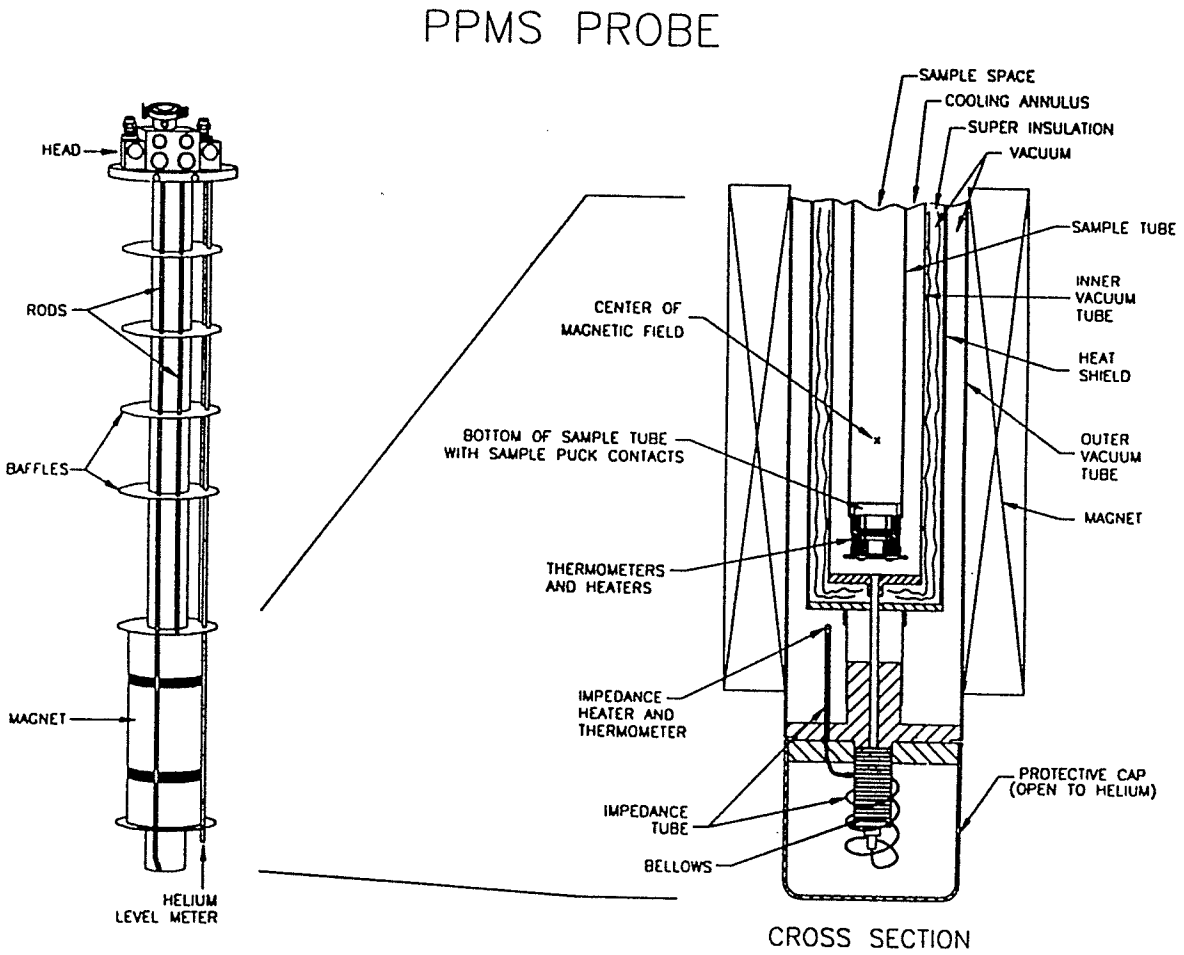

Figure 4.5: The diagram of the PPMS probe

perature readings), the gas valves and gas lines (temperature control), the front panel (user interface) and the rear panel (connections). The Model 6000 can provide a temperature range from 1.8 K to 400 K by controlling the helium gas cooling system and heater; magnetic fields up to 9 tesla can be produced by a superconducting solenoid.

The AC measurement system (ACMS) insert (shown in figure (4.6)) is designed for AC susceptibility and DC magnetization measurements, and can be installed into the PPMS sample chamber. The ACMS contains the system's drive and detection coils, thermometer and electrical connections. The sample space lies within the uniform field region of the PPMS magnet. The sample is mounted on the end of a thin, rigid sample rod that fits into the ACMS insert. The sample rod is translated longitudinally by a DC servo motor in the sample transport assembly mounted on the top of the PPMS probe. An AC driving coil provides an alternating excitation field and a pickup coil detects the induced signals from the sample movement and excitation field. The driving coil can generate alternating fields of up to 16 Oe rms in a frequency range from 10 Hz to 10 KHz. The DC measurement system detects the signal that is induced by rapidly extracting the sample from the detecting coil in an applied field. The AC system measures the signals that are produced by applying an alternating field to the sample. A personal computer can communicate with the Model 6000 through a GPIB interface which sends instructions and retrieves the data from the Model 6000 automatically.

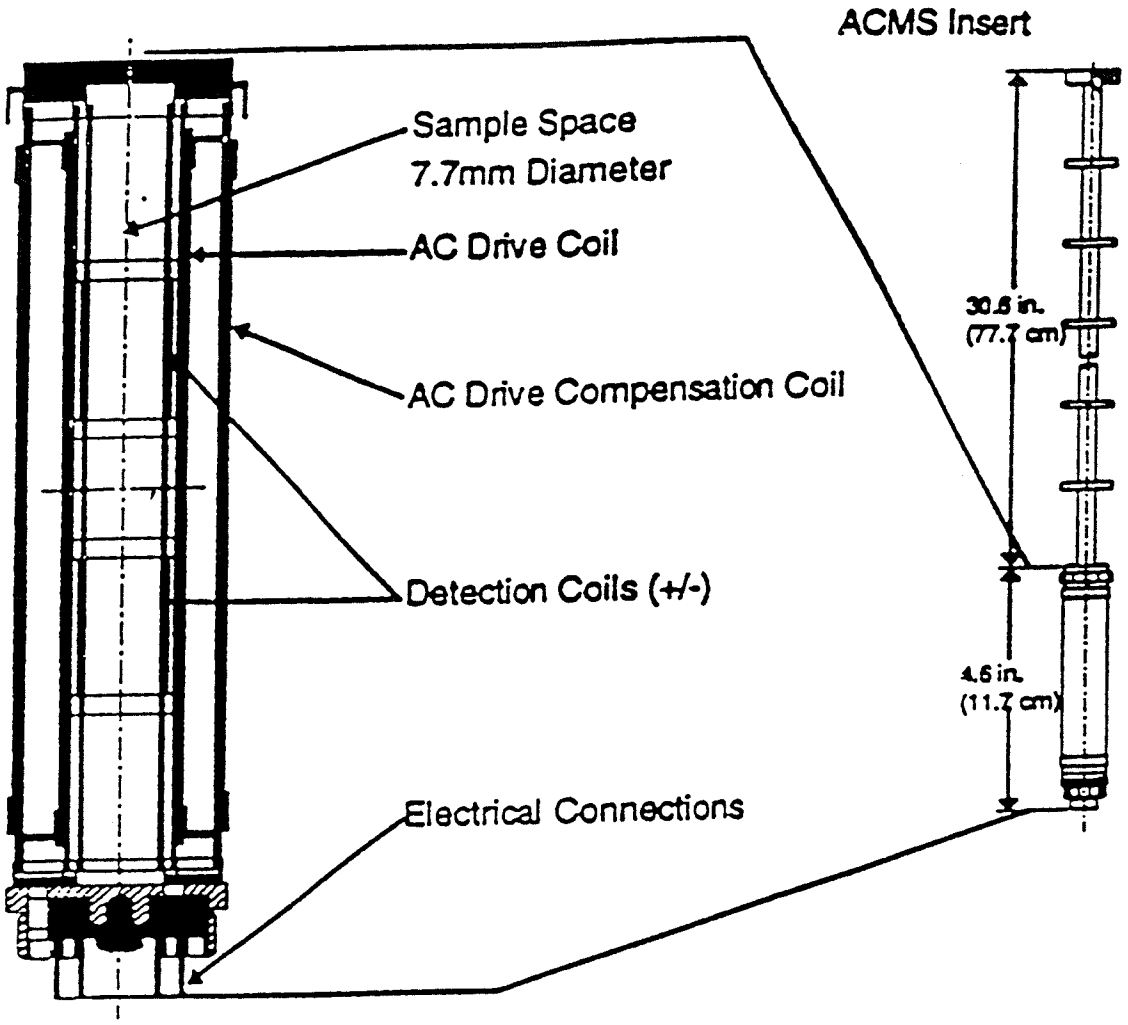

Figure 4.6: The ACMS insert and coils

4.4.2 Measurement Methods

The ACMS option is both a DC magnetometer and AC susceptometer. The DC magnetometer measures a sample's magnetic moment, M, in a given applied magnetic field, H, at a specific temperature. The ACMS moves the sample through a set of copper coils (the extraction method) and analyzes the induced signal with a digital signal processor to determine the sample's magnetic moment. The sensitivity of the DC measurement is about 2.5×10^{-5} emu.

The AC susceptibility measurement is made by applying a small alternating field (in addition to possibly a large applied field from the PPMS superconducting magnet) and measures the sample's magnetic response. Both the amplitude and phase, or the in-phase and quadrature components of the sample's response, can be measured. The amplitude is the change in the magnetic moment (not the absolute magnetic moment or the susceptibility); susceptibility can be obtained by dividing the amplitude of this change, Δm, in moment by the amplitude of the driving field, Δh, this gives $\chi = \Delta m/\Delta h$. The sensitivity of the measurement is 1×10^{-8} emu.

Chapter 5

Results and Discussion

5.1 Critical Behaviour of $La_{0.67}Ca_{0.33}MnO_3$

The magnetic and electrical phase diagram of $La_{1-x}Ca_xMnO_3$ has been explored in considerable detail and representative data has been shown in figure (2.8) of chapter two. When the Ca^{2+}substitution level, x, is about 0.33, the Curie temperature reaches its maximum value, thus suggesting the strongest ferromagnetic coupling. The colossal magnetoresistance (CMR) is also typically observed close to the Curie temperature [51]. Therefore, the sample with doping level of x = 0.33 was chosen to study its magnetic and transport properties as well as the related CMR, especially the nature of the phase transition and the spontaneous resistive anisotropy.

The polycrystalline samples of $La_{0.67}Ca_{0.33}MnO_3$ were prepared using the standard ceramic method described previously. General magnetic and transport properties of four specimens prepared using various fabrication procedures will be discussed in detail in section 5.3, here we first focus on the investigation of the nature of the magnetic critical phase transition displayed by one of the samples

identified as (B).

Figure (5.1) shows the zero field ac susceptibility and the field-dependent ac susceptibility of the sample B as a function of temperature (measured in a 2.4 kHz, 30 mOe rms driving field using a phase-locked susceptometer). The zero field susceptibility displays behaviour typical of a paramagnetic to ferromagnetic phase transition. The maximum in the zero field susceptibility, referred to as the Hopkinson or principal maximum, is generally considered to arise from contributions from domain wall motion and coherent rotation (i.e. technical processes). When an external static biasing field, H_a, is applied, the Hopkinson maximum is suppressed; increasing fields result in the progressive suppression of the Hopkinson maximum in both temperature and amplitude, permitting secondary, critical susceptibility peaks to be resolved as shown in the inset of figure (5.1). These critical maxima decrease in amplitude and move upward in temperature as the static biasing field, H_a, increases. This behaviour clearly demonstrates the presence of critical fluctuations accompanying a continuous magnetic transition; the characteristics are consistent with the static scaling law description of a second order paramagnetic to ferromagnetic transition [32]. As is described in chapter 3, the appearance of such peaks in finite field can be explained qualitatively by the fluctuation-dissipation theorem [39]. It is also a quantitative prediction of numerical solutions of the ferromagnetic phase of Sherrington-Kirkpatrick-like models [43]. The locus of these critical maxima defines the crossover line above which the magnetic response is thermally dominated and below which the response is field dominated. Based on the static scaling law described earlier, the critical

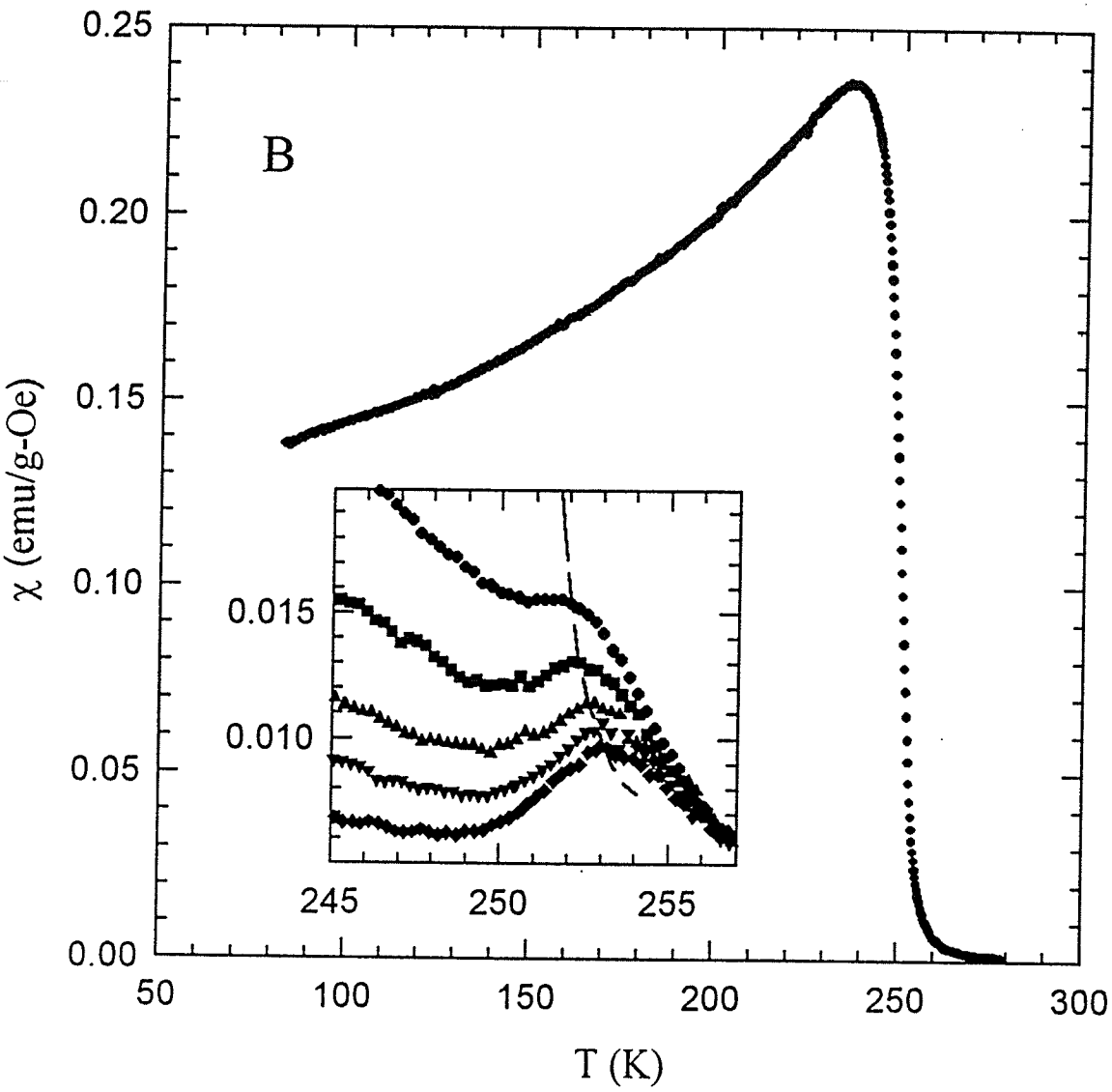

Figure 5.1: The zero field susceptibility vs temperature for sample B. The inset shows the susceptibility in dc biasing fields of 600, 700, 800, 900 and 1000 Oe, top to bottom. The dashed line represents the crossover line.

exponents can be extracted from various log-log plots of the experimental data. First, a value for δ can be easily found using equation (3.28), $\chi(h, t_m) \propto h^{(1-\delta)/\delta}$, because a plot of the susceptibility data against the applied fields does not depend on the choice of the critical temperature, T_c. The peak susceptibility was plotted versus internal field on a log-log scale as shown in figure (5.2). It is clear that the data do not fall on a straight line. If the four data points at higher fields are fitted to a straight line (solid line), δ is found to be 4.76 which is very close to the Heisenberg value. The relatively high susceptibilities in low fields are generally attributed to the contribution of a large background susceptibility below T_c which is evidenced in the inset of figure (5.1); more discussion on this point will be given later. For the other critical exponents, using equation (3.27), $t_m \propto h^{1/(\gamma+\beta)}$, the crossover exponent $(\gamma + \beta)$ can be estimated. By extracting peak temperatures, T_m, amplitudes, χ_m, and internal fields, H_i, from the data, the values for the critical exponents $(\gamma + \beta)$ and γ are determined from the log-log plots. An initial estimate for T_c can be obtained by plotting the peak temperature as a function of $H_i^{0.571}$, where the value of 0.571 is the 3D Heisenberg model prediction for $1/(\gamma+\beta)$. A linear fit to these data gives an estimate for T_c of 248.8 K - from the temperature intercept as shown in figure (5.3). Using this estimate the reduced temperatures $t_m = (T_m - T_c)/T_c$ were calculated and plotted as a function of internal field on a log-log scale in figure (5.4). The asymptotic value for the so-called cross-over exponent, $(\gamma+\beta)^{-1} = 0.569$, was obtained in this case by fitting the points to a straight line. The crossover line represents the line at which the system passes from a field dominated to a temperature dominated regime. An

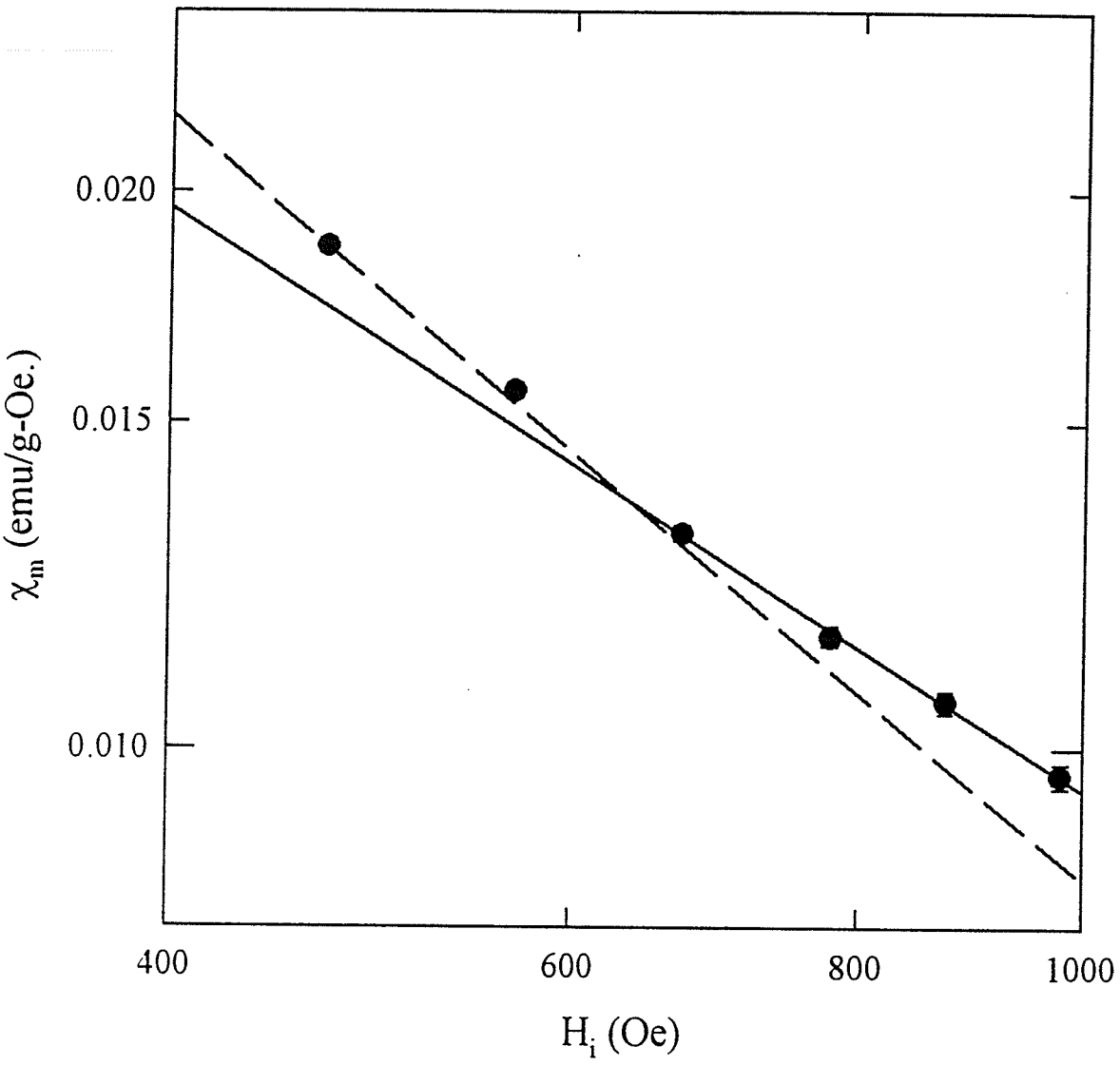

Figure 5.2: The peak susceptibility plotted as a function of internal field on a log-log plot, the fit of the four high field data points yields a value $\delta = 4.76$.

independent value for γ was found using equation (3.11), $\chi_m \propto t_m^{-\gamma}$; the log-log plot of χ_m vs t_m also depends on the estimated value of T_c. The value of γ, found by fitting the four points at high fields, is 1.39 as shown in figure (5.5). The best value for $\gamma + \beta$ and γ can be obtained through iteration with small adjustments of T_c.

The Kouvel-Fisher effective exponent γ^* [52] was found from the zero field susceptibility data using the relation, $\gamma^* = d\ln\chi/d\ln t$, and is plotted in figure (5.6) as a function of reduced temperature. The effective γ^* at low reduced temperature rises to a peak value at $t \approx 0.065$ before dropping at higher temperature towards the mean field value of 1. This behaviour is typical of systems with large amounts of magnetic disorder.

The above data analysis qualitatively demonstrates that the behaviour of the AC susceptibility in applied magnetic fields is typical of that observed in the vicinity of a second order (continuous) phase transition. However, a quantitative analysis to yield critical exponent values has proven to be more difficult because of the presence of a large regular (non-critical) background component to the susceptibility, although attempts to extract critical exponents by fitting the high field points where the large (non - critical) regular component is suppressed do yield values that are consistent with the predictions of the Heisenberg model. A further discussion regarding the origin of such difficulties in the critical exponent analysis is now presented.

The theoretical predictions of equation (3.27) and (3.28) rely on the assumption that the magnetic response measured in the vicinity of the critical point

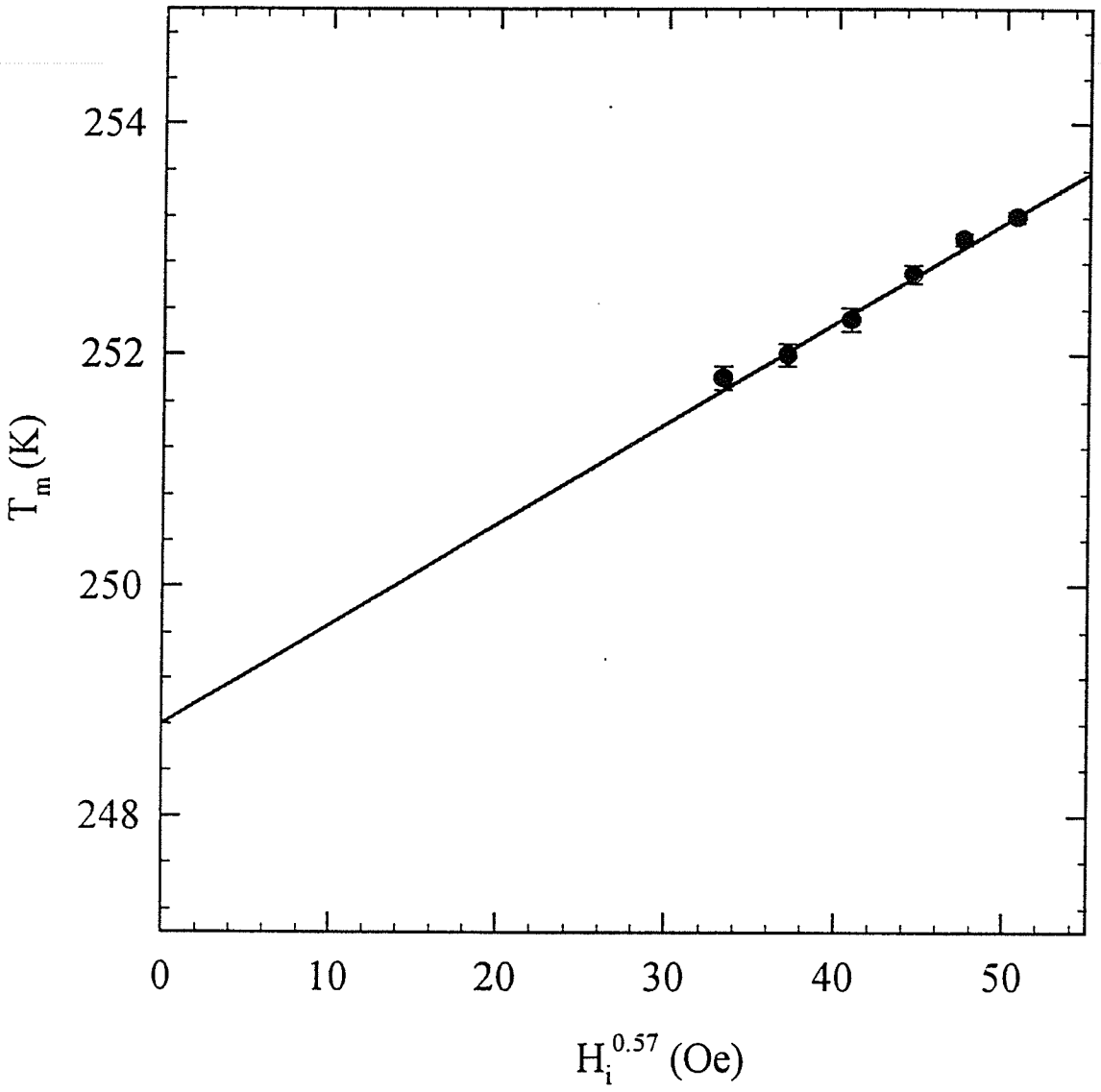

Figure 5.3: Estimation of T_c from the critical peak temperatures in various internal fields in a form of t_m vs $H_i^{0.57}$.

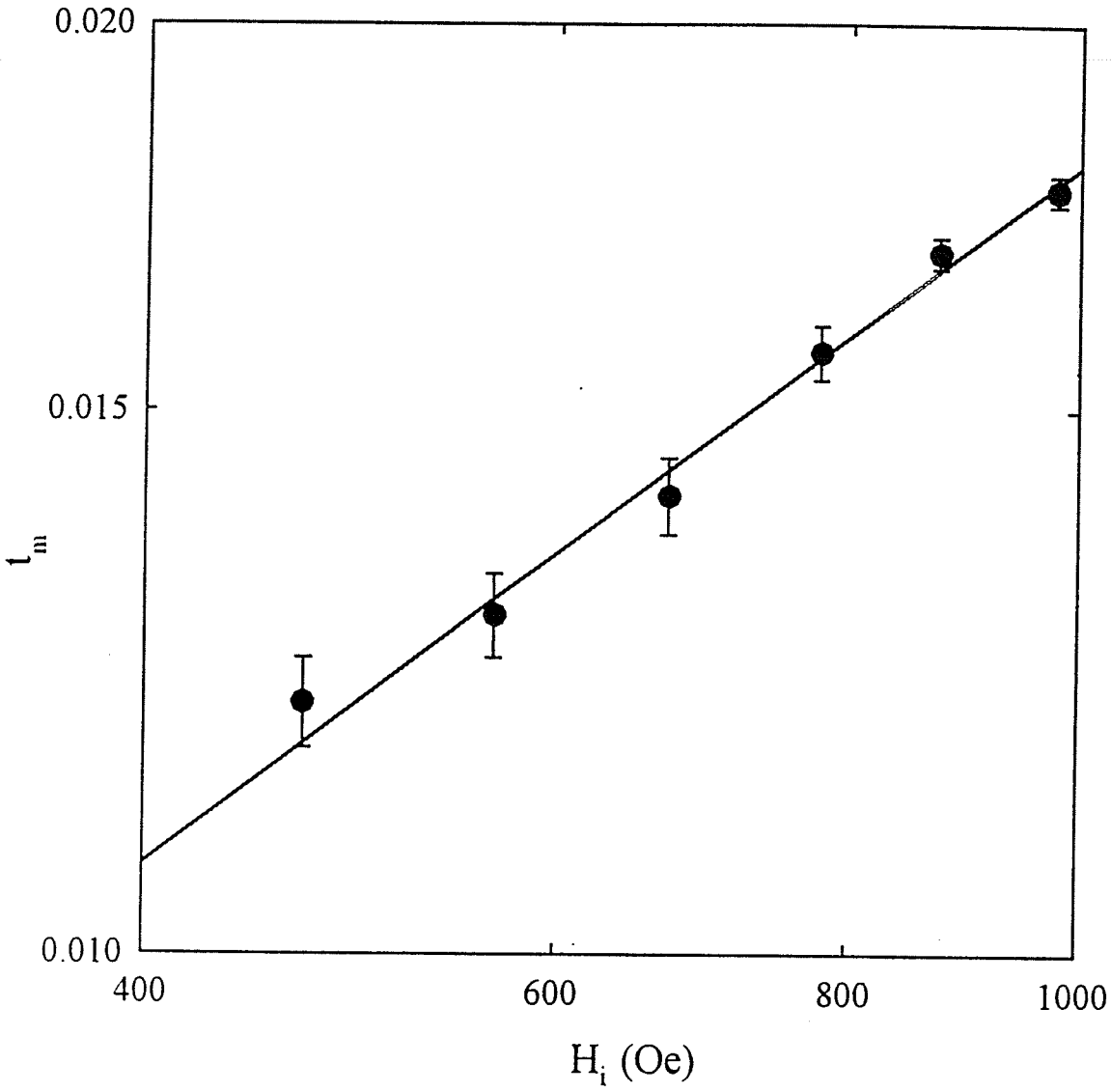

Figure 5.4: Cross-over exponent plot of reduced peak temperatures vs internal field.

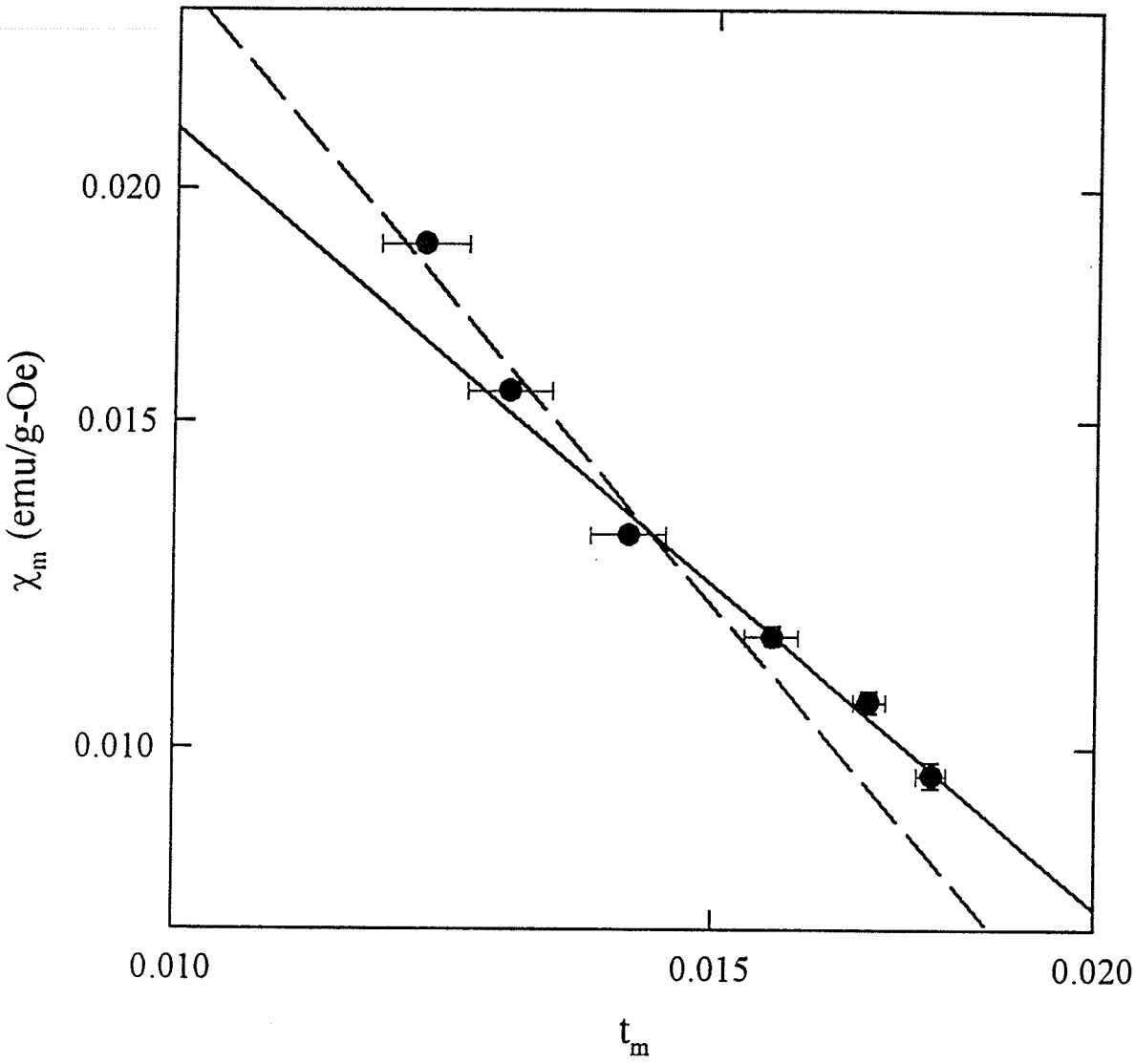

Figure 5.5: The peak susceptibility plotted versus the reduced peak temperatures, the fit for the four high field data points yields a value $\gamma = 1.39$.

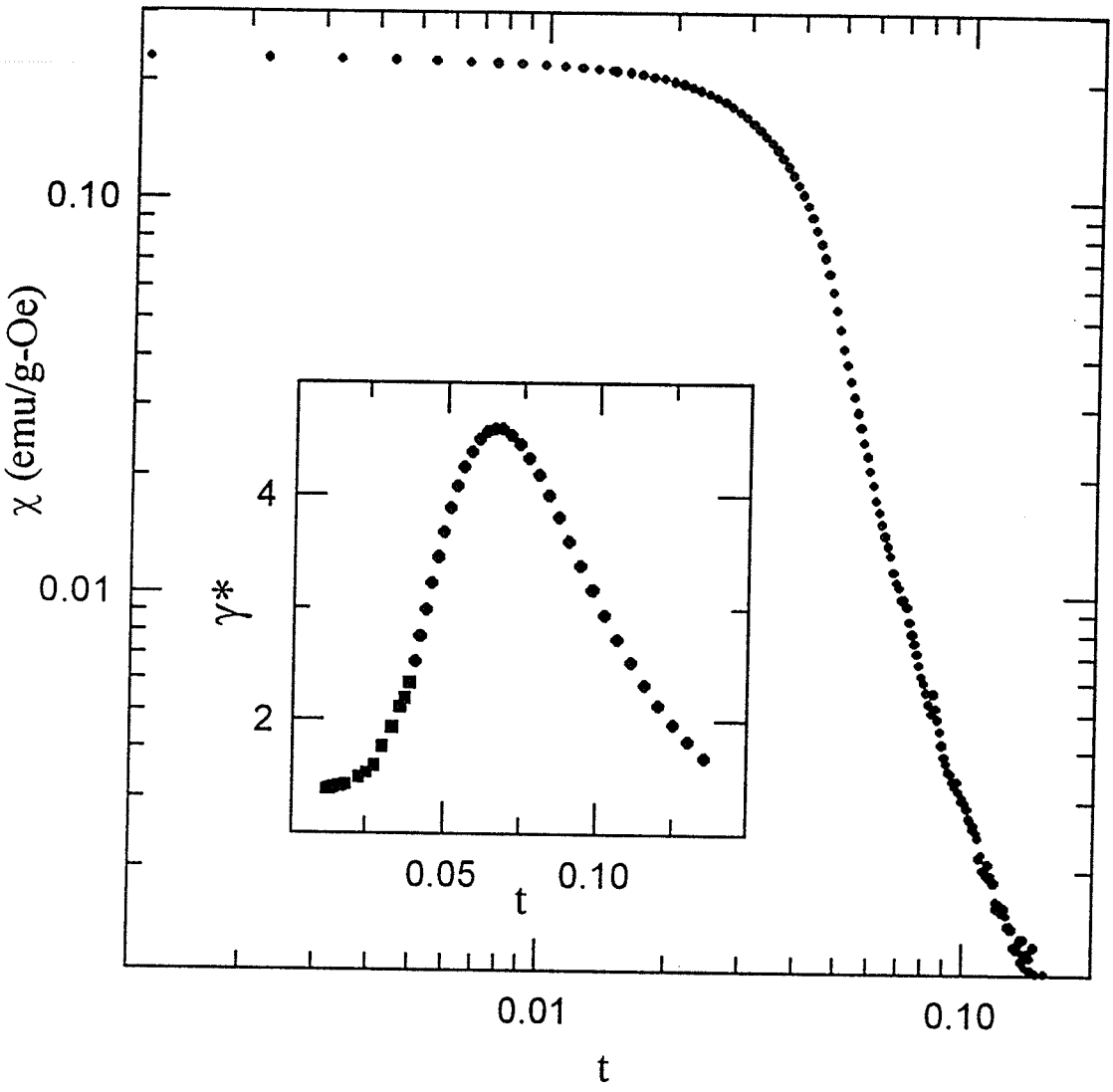

Figure 5.6: Zero field susceptibility plotted as a function of reduced temperature on a log-log scale. The inset shows the effective exponent $\gamma^*(t)$ plotted as a function of reduced temperature.

(more correctly, along the crossover line defined by equation (3.27)) is dominated principally by the critical fluctuations (i.e. the so-called singular contribution). Thus, the contribution to the measured response arising from the regular contributions to the susceptibility, i.e. from technical sources such as domain wall motion and coherent rotation etc., must be small or easily suppressed to saturation by a low applied magnetic field. Magnetically harder systems, in contrast to technically soft materials, are more difficult to saturate and thus the emergence of critical peaks is obscured in them [37, 53], resulting in complication of subsequent exponent value estimates. Furthermore, even if the critical peak structure can be resolved, this regular contribution to the peak amplitude can not be considered small. In most of the systems studied to date, technical hardness appeared to originate from single ion anisotropy associated with spin-orbit coupling [53]. Here Mn^{3+}, being a Jahn-Teller ion, could play an important role in providing such anisotropy. As a corollary, it is worthwhile to investigate the behaviour of the spontaneous resistive anisotropy in these doped perovskites, as this would reflect the presence of spin-orbit coupling on Mn^{3+} ions, which will be discussed later.

Generally the coercive field, H_c, provides a measure of the technical hardness and thus of the applied field necessary to suppress the regular response. In particular, prior experience has indicated that an applied field of roughly 2-3 times larger than H_c, measured just below T_c, is usually sufficient to achieve the technical saturation necessary to resolve the critical peak structure. Figure (5.8) reproduces the temperature dependence of the coercivity H_c, which was estimated

from butterfly loop measurements - $\chi(H_a, T)$ vs H_a - at various fixed temperatures as shown in the inset. Contrary to expectation, here applied fields of 20 to 30 times the H_c value are necessary to first observe such structure, more than an order of magnitude larger than the corresponding fields required in conventional systems. This leads to difficulties in fitting the critical data to model predictions at low fields, as mentioned above.

In figure (5.7) each constant field curve or isokap shown in figure (5.1) is normalized to its peak value and plotted against the inverse of the argument $(t/h^{1/(\gamma+\beta)})$ of the scaling function $(\chi(h,t)/\chi(h,t_m) = H(X)/H$, since $X = C$ (from equation (3.25)). This procedure should produce a universal curve, i.e., all data should collapse onto a single curve. The inset shows that this procedure works well for the conventional, soft ferromagnet [54] PdFe; however, for all the perovskite samples reported here the data above the maximum, the thermally dominated regime, scale onto a single curve, but those below this maximum, in the field dominated regime, do not.

Thus, both the scaling behaviour and the applied field necessary to resolve such behaviour (specifically the H_a/H_c ratio) display some unusual features. It was initially suggested that this might originate from the same source as a comparable unusual feature in neutron scattering data from the same systems [55]. In the latter, the appearance of a quasielastic (i.e. non-critical) component dominates the critical contribution close to T_c; moreover, the correlation length remains finite at T_c. Such behaviour has been attributed the presence of spin diffusion modes [55]. If such modes retain spectral weight in the frequency range appropriate to the

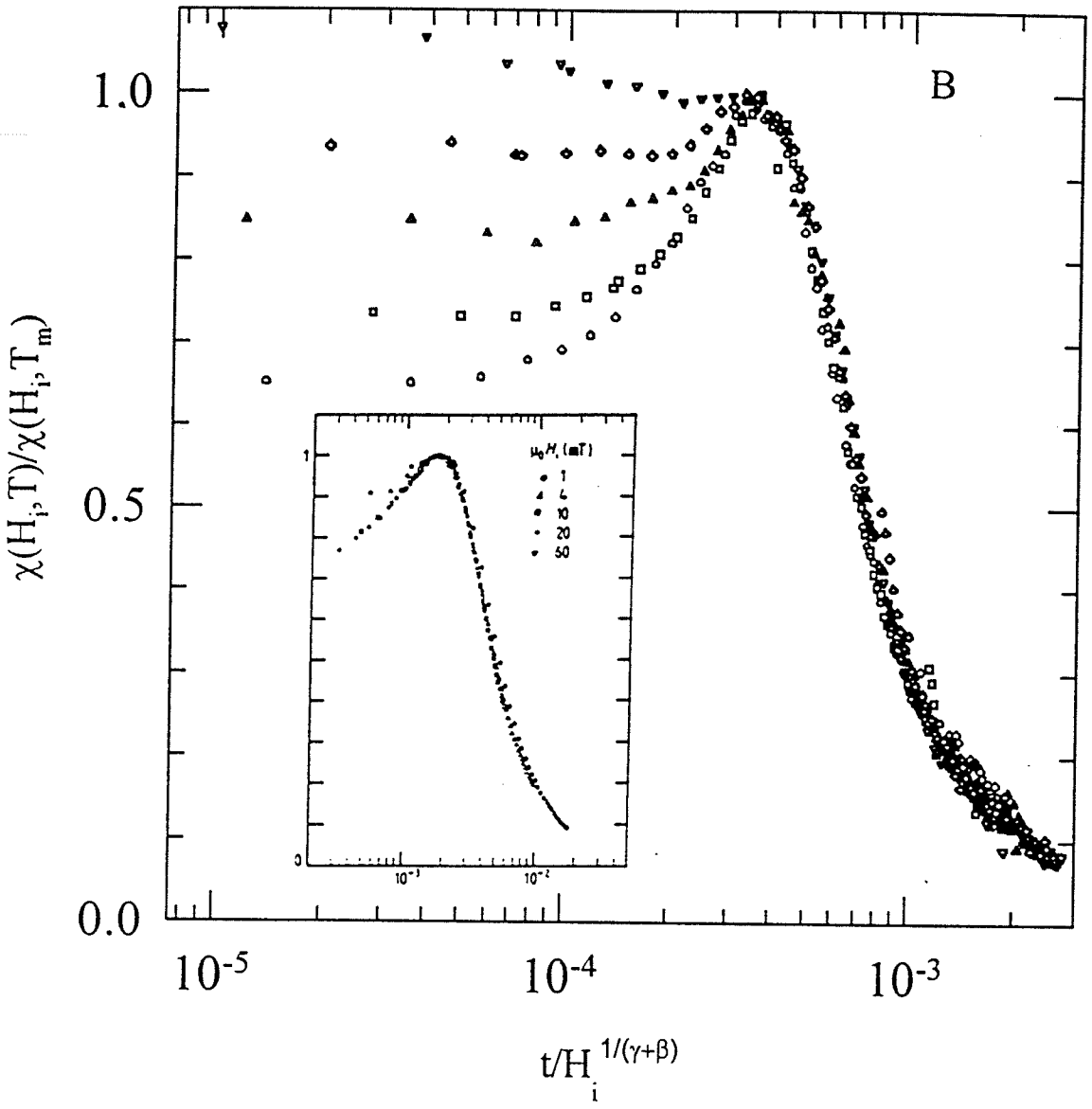

Figure 5.7: The scaling plot for sample B. The data are the isokaps shown in figure (5.1) with the susceptibility normalized to the respective peak values plotted against the inverse argument $(t/h^{1/(\gamma+\beta)})$ of the scaling function. The inset shows the scaling plot for a conventional soft ferromagnetic (PdFe), where the data were taken in applied fields of 10, 40, 100, 200, and 600 Oe.

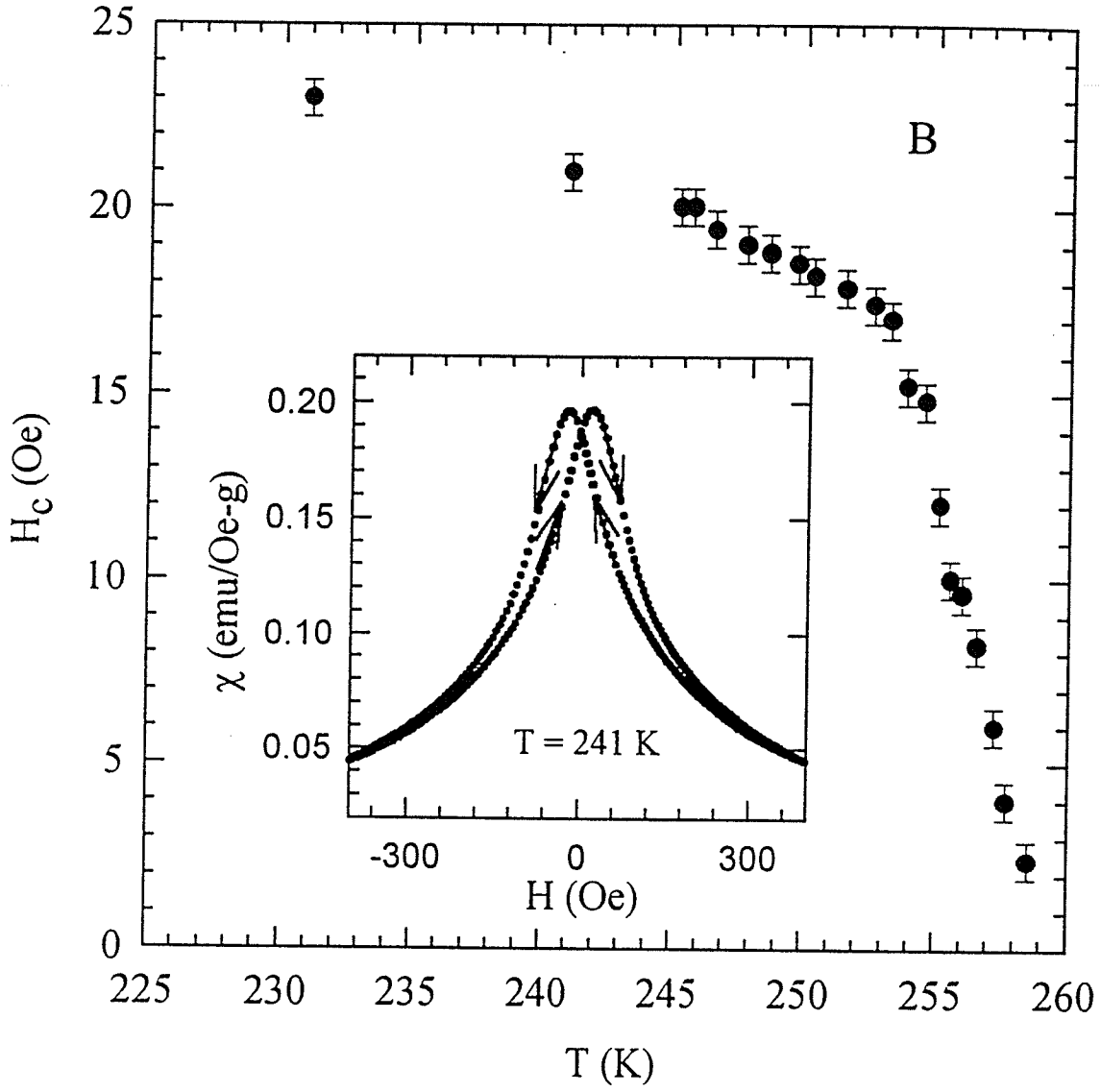

Figure 5.8: The coercivity H_c plotted as a function of temperature, the inset shows the susceptibility measured as a function of field (i.e. the butterfly loop) from which H_c can be obtained.

present experiment, then they might be a source for the regular, i.e. non-critical, component which complicates the ac susceptibility analysis. From a physical picture, such modes could originate from regions within which the spin correlations are predominantly antiferromagnetic due to the presence of the inhomogeneous mixed valent (Mn^{3+}-Mn^{4+}) state in these doped perovskites. Within regions that are statistically rich in Mn^{4+} ions, double exchange and consequently ferromagnetic correlations would predominate. By contrast, in environments where Mn^{4+} is statistically deficient, Mn^{3+}-Mn^{3+} antiferromagnetic interactions (the so-called t_{2g}-$O(2p_\pi)$-t_{2g} superexchange) would be more prevalent. Furthermore, comparison with the undoped host would indicate that a high field might be required to suppress any such antiferromagnetic fluctuations, which would be necessary before critical peaks associated with the onset of long range ferromagnetic ordering could be observed. This is in qualitative agreement with the present observations. The situation described above bears considerable similarity to the inhomogeneous two-phase structure envisioned by Lynn [55]. In addition, experiments on the compound $(La,Sr)_{n+1}Mn_nO_{3n+1}$ [56, 57] show coexisting ferromagnetic and antiferromagnetic critical peaks in neutron scattering data in qualitative agreement with the above picture, but the precise nature of the magnetic fluctuations here remains somewhat unresolved. Further, since this central quasielastic peak in the neutron scattering data is not seen by all investigators, such a discussion remains tentative.

It is apparent that more measurements on these and related systems are necessary to clarify the above issues, in particular AC susceptibility studies on substi-

tuted manganites and pyrochlores. Since pyrochlores do not display a quasielastic scattering component and the spin stiffness falls to zero at T_c [58], the experimental data for such a compound will be discussed in the following section for subsequent comparison with the manganite compounds .

5.2 Critical Behaviour of the Pyrochlore $Tl_2Mn_2O_7$

CMR has also been observed in the compound $Tl_2Mn_2O_7$ which has a pyrochlore structure [59, 60, 61]. In this cubic structure MnO_6 octahedra are corner sharing, forming a sparse network intersecting with a network of Tl-O chains. Neutron and single-crystal x-ray diffraction [62] studies have concluded that the CMR is intrinsic to the stoichiometric compound and that the CMR mechanism in this pyrochlore is different from that of the perovskites. The latter are antiferromagnetic when not intentionally doped and only exhibit metallic behaviour and ferromagnetism at a certain level of admixture of Mn^{4+} into the $LaMnO_3$ parent compound. Another important difference between the two materials is that $Tl_2Mn_2O_7$ is metallic above T_c whereas the perovskites are insulating. Specifically the pyrochlore has no mixed valence and contains only Mn^{4+} ions; therefore, both Jahn-Teller effects and the double-exchange interaction are not present, and the metal-anion-metal bond angle displays a large deviation from 180^o (actually equal to 134^o). The studies suggest that the ferromagnetic ordering results from a superexchange interaction rather than from the double exchange associated with an electronic kinetic energy gain in the insulator/metal transition. CMR in this compound is related to spin-fluctuation scattering between localized Mn^{4+} moments and the conduction band formed by the 6s electrons on the Tl-O sublattice [63].

While the current explanations of the CMR in these two types of systems are different, the attendant spin dynamics also show dissimilarity. The magnetic cor-

relation length diverges while the spin stiffness collapses as T_c is approached from above and below respectively in this pyrochlore in marked contrast to the doped manganites, particularly for Ca doping [55, 58]. In the latter as described previously, a quasielastic spin diffusion component, possibly associated with polaronic behaviour, dominates the critical fluctuation spectrum. Therefore, it is interesting to investigate the quasistatic magnetic response in the critical regime and to probe the basic interactions responsible for the magnetic order in the pyrochlore as well as the doped perovskites.

Measurements of the ac susceptibility (at 2.4 kHz in a 30 mOe rms driving field) and the dc magnetization were carried out simultaneously in a Quantum Design Model PPMS 6000 magnetometer on a polycrystalline sample weighing 257 mg with approximate dimensions $(5 \times 3 \times 3)$ mm^3 (sample was provided by M. A. Subramanian of Dupont Central Research and Development). At each temperature selected, an appropriate time interval was allowed to elapse prior to commencing measurements.

Figure (5.9) shows the ac susceptibility measured in various static biasing fields. As shown in the main body of this figure, the application of such fields of increasing strength progressively suppresses the principal (Hopkinson) maximum evident in the zero-field response shown in the inset, thus allowing the secondary critical peaks to be resolved. The temperatures, T_m, of these critical maxima shift upward while their amplitudes decrease as H_a increases. As discussed in detail previously for the $La_{0.67}Ca_{0.33}MnO_3$ sample, such peaks are a characteristic signature of critical fluctuations accompanying a continuous magnetic phase tran-

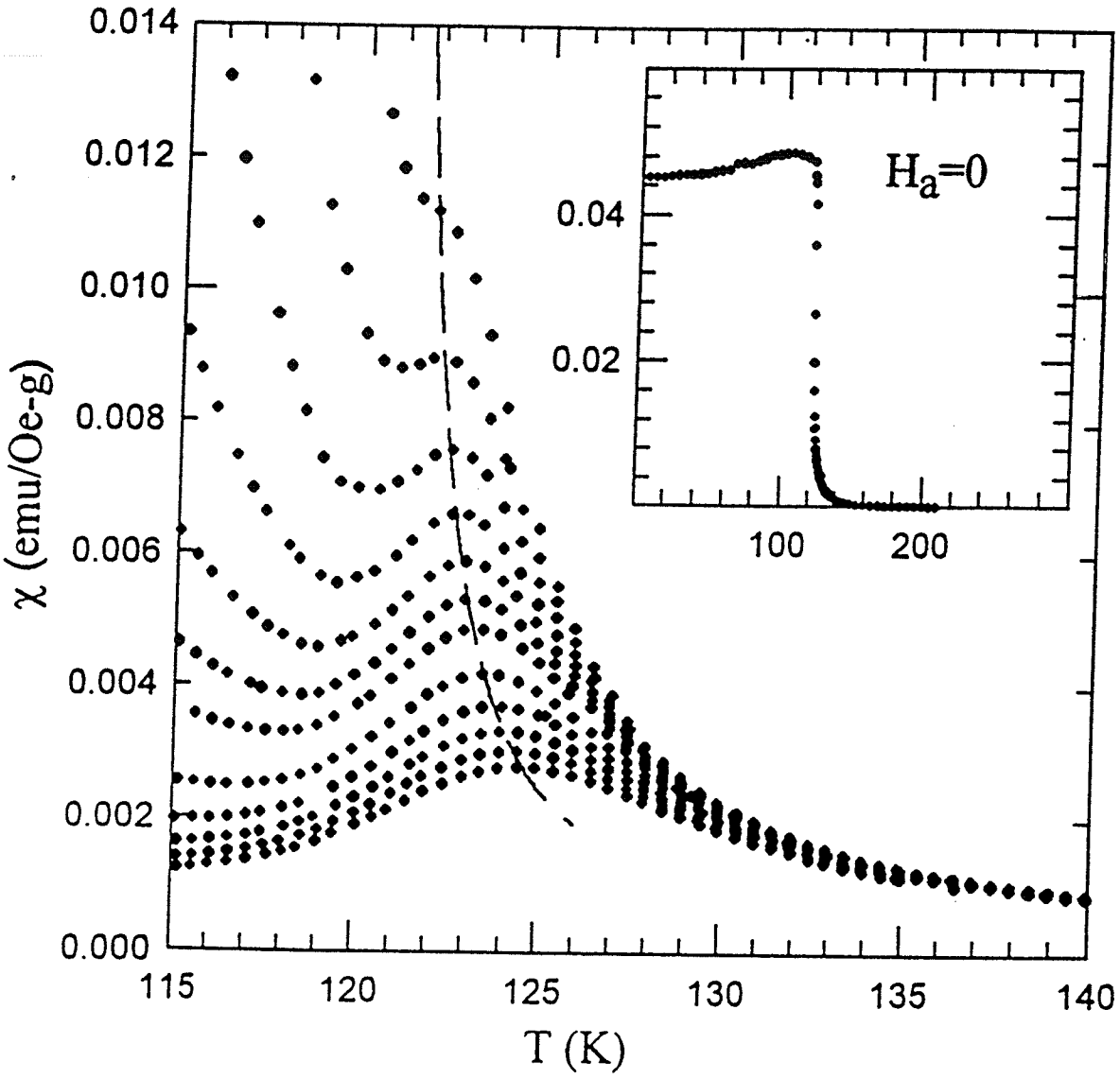

Figure 5.9: The ac susceptibility versus temperature measured in static biasing fields increasing from 400 Oe (top) to 2000 Oe (bottom), clearly showing the emergence of the critical maxima. The dashed line denotes the crossover line. The inset shows the temperature dependence of the zero field ac susceptibility.

sition. The temperature and field dependence of the peaks are consistent with the static scaling law description of such a transition while the emergence of such peaks in finite field can be explained qualitatively on the basis of the fluctuation-dissipation theorem. Furthermore, the field/temperature dependence agrees with numerical solutions for the ferromagnetic phase of a Sherrington-Kirkpatrick like model (mean field approach). The locus of the critical maxima shown in figure (5.9) delineates the crossover line, above which the response is thermally dominated while below which the response is field dominated. Therefore, according to the scaling law equation of state discussed previously, the various critical exponents can be deduced directly from the critical peak structure evident in figure (5.9). From equation (3.27), the plot of the critical peak temperatures T_m against $H_i^{1/(\gamma+\beta)}$ should be linear, and its intercept gives the critical temperature T_c as shown in figure (5.11). Figure (5.10) shows the so-called shearing curve, which is the magnetization measured in low field near T_c, from which the slope N^{-1}, the demagnetization factor, can be found and hence the internal field ($H_i = H_a - NM$) can be deduced. By choosing the isotropic, near-neighbour Heisenberg model values for $\gamma + \beta = 1.75$, $T_c = 120.65(\pm 0.15)$ was obtained. Figure (5.12) confirms both these exponents and T_c estimates; here the reduced peak temperatures, t_m, are plotted against the internal field, H_i, on a double logarithmic scale with Heisenberg model exponents, viz. $(\gamma + \beta)^{-1} = 0.57(\pm 0.01)$, the straight line drawn confirms the power law prediction (equation (3.27)). The exponent δ is found directly from the field dependence of the magnetization measured along the critical isotherm at T_c as shown in figure (5.13). These data yield

$\delta = 4.65(\pm 0.15)$, which is in agreement with the Heisenberg model value of 4.80 within experimental uncertainty. The exponent γ is found from the data summarized in figure (5.14) where the amplitude of the susceptibility maxima are plotted against the reduced peak temperature on a double logarithmic scale. These data confirm the power-law prediction of equation (3.24); here $\gamma = 1.31(\pm 0.05)$, which is marginally lower than the Heisenberg model value of 1.386.

Further investigation of the applicability of Heisenberg model exponents to this system is provided in figure (5.15); here each constant field scan or isokap shown in figure (5.9) was corrected for background and demagnetizing effects and normalized to its peak value following the scaling function $\chi(h,t)/\chi(h,t_m) = H(X)/H(X = C)$. The isokaps scale onto a single curve when plotted against the inverse of the argument X of the scaling function.

Despite the validity of Heisenberg model exponents as demonstrated above, the magnetic response of this pyrochlore displays some unusual characteristics, specifically in the low field region near T_c. This can be seen directly from figure (5.9), in which fields in excess of 400 Oe are necessary to first resolve critical peak structure. Such a situation reflects the presence of a substantial regular component in this response. This regular component is clearly not driven to saturation in low fields ($\leq 400Oe$) near T_c; thus this pyrochlore system displays features normally associated with technical hardness. This result is difficult to understand as previous detailed analysis has convincingly demonstrated that this pyrochlore is devoid of Mn^{3+} ions so that $Tl_2Mn_2O_7$ displays neither a double-exchange interaction mediated by a mixed valence (Mn^{3+}/Mn^{4+}) nor an associ-

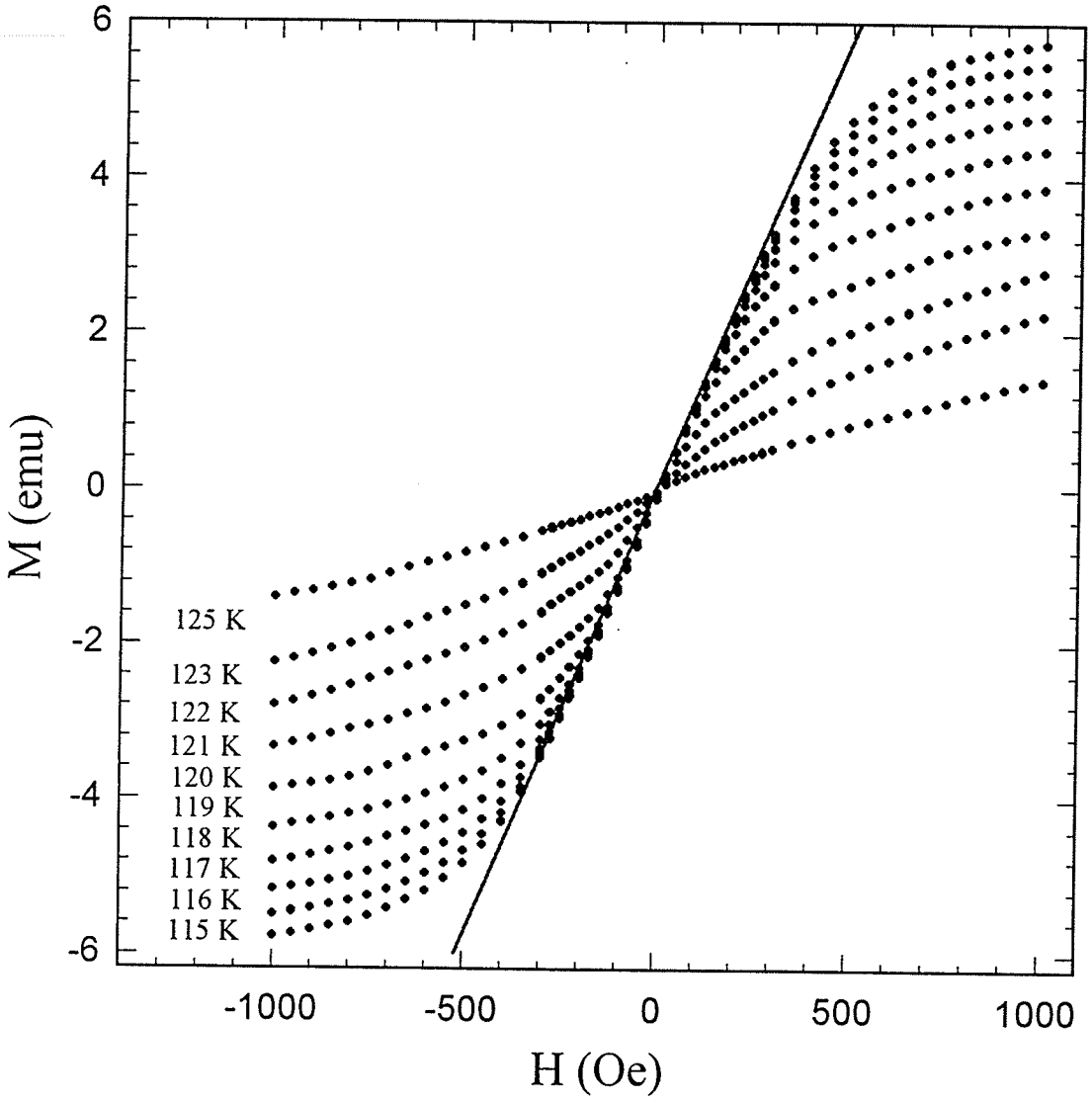

Figure 5.10: The shearing curve measured in low fields around the transition temperature. The demagnetization factor can be obtained by measuring the slope represented by the solid line.

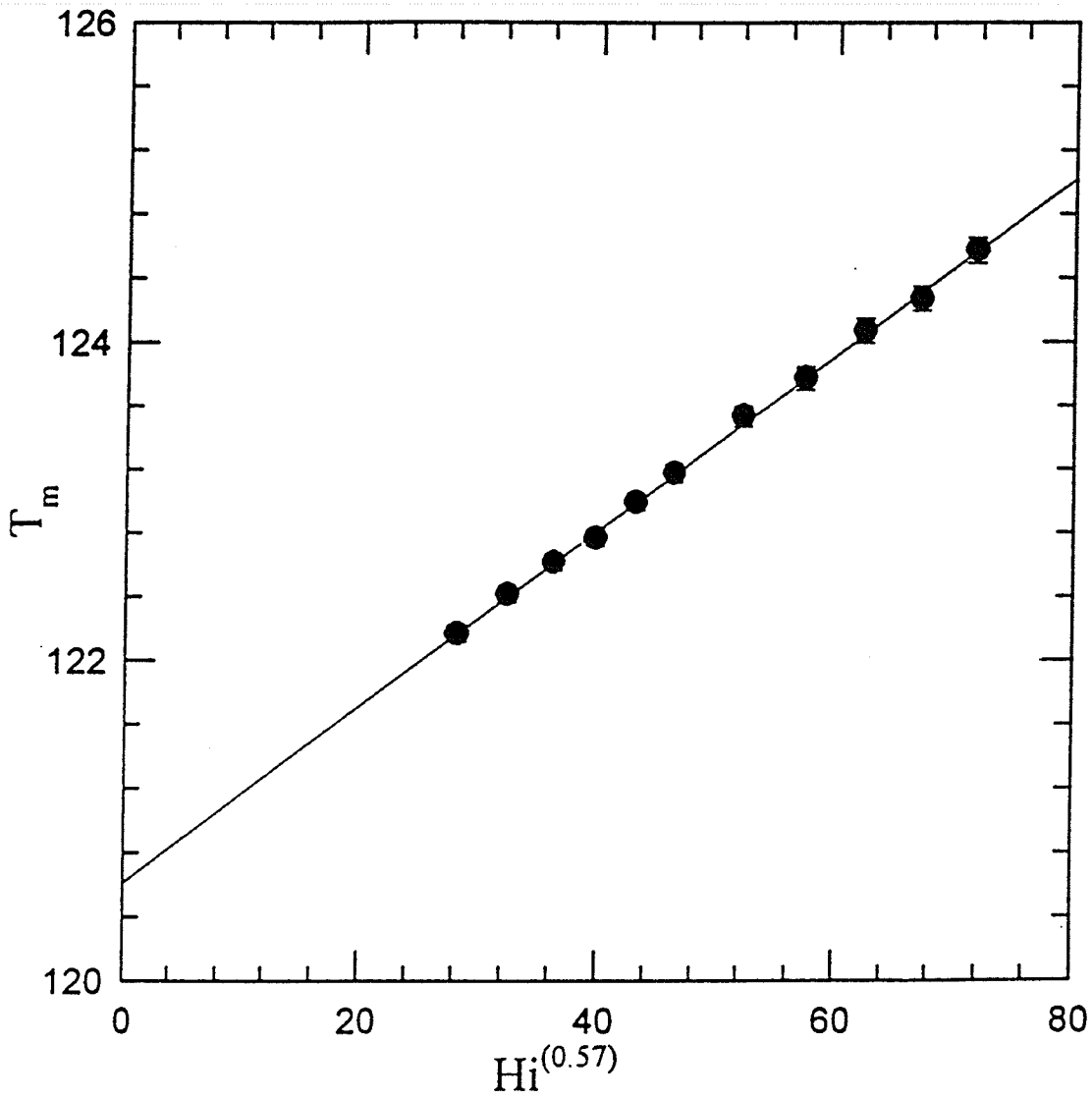

Figure 5.11: The peak temperature versus internal field to the power of 0.57. The intercept of line yields the critical temperature $T_c = 120.65(\pm 0.15)K$.

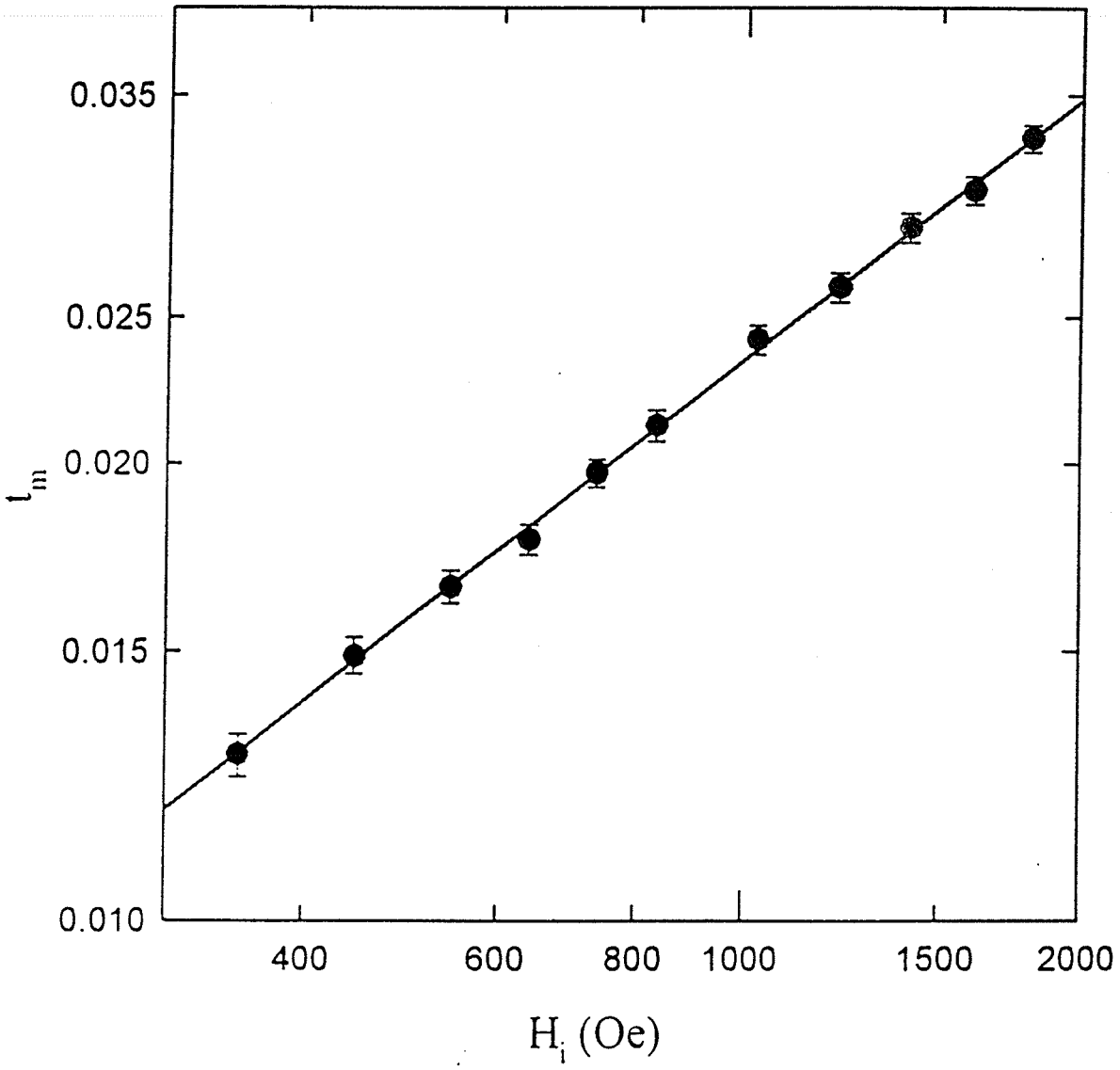

Figure 5.12: Reduced peak temperature as a function of internal field, the solid line fit gives the crossover exponent $(\gamma + \beta)^{-1} = 0.57(\pm 0.01)$.

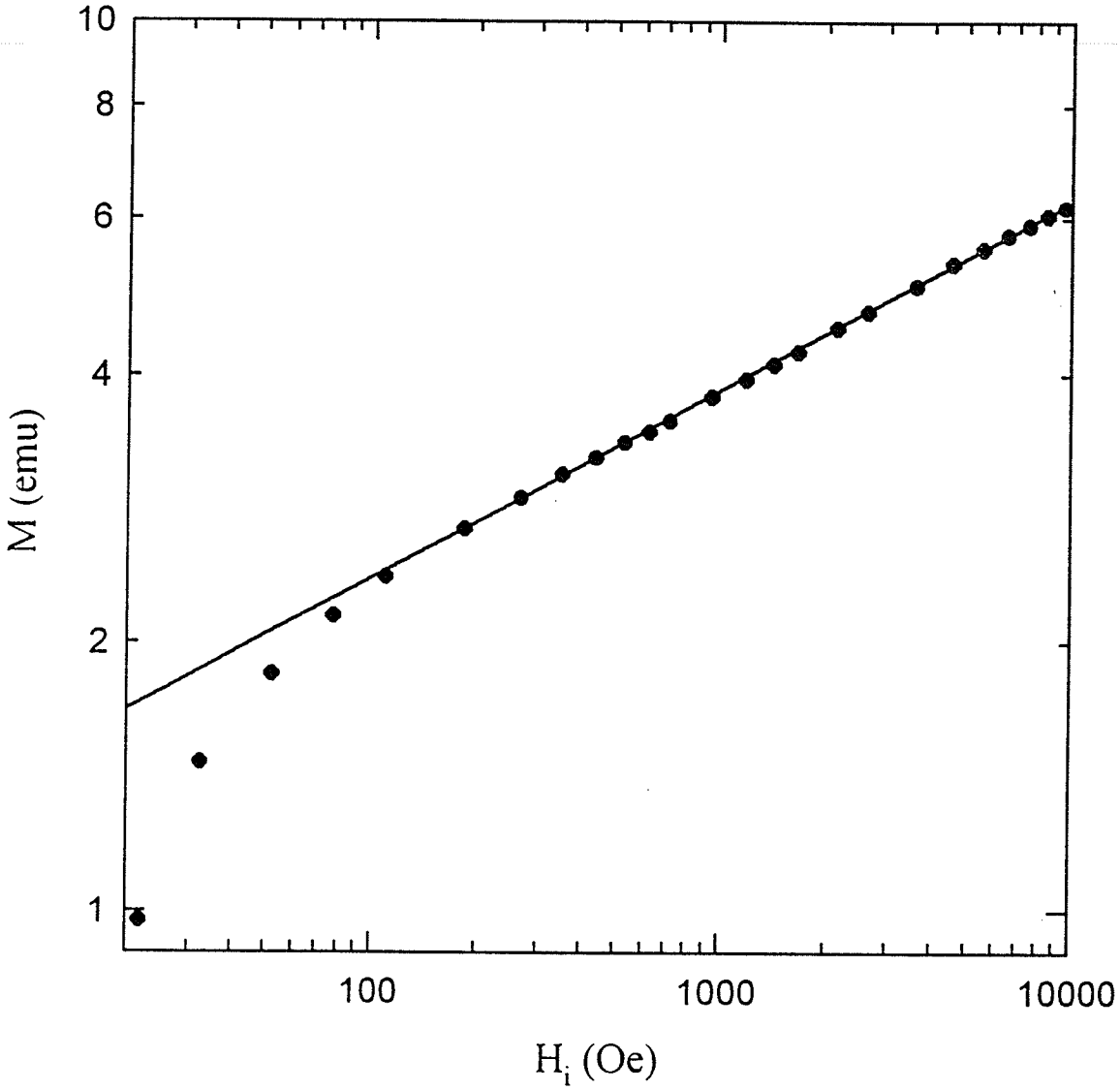

Figure 5.13: The field dependence of the magnetization measured along the critical isotherm, the fit yields $\delta = 4.65(\pm 0.15)$.

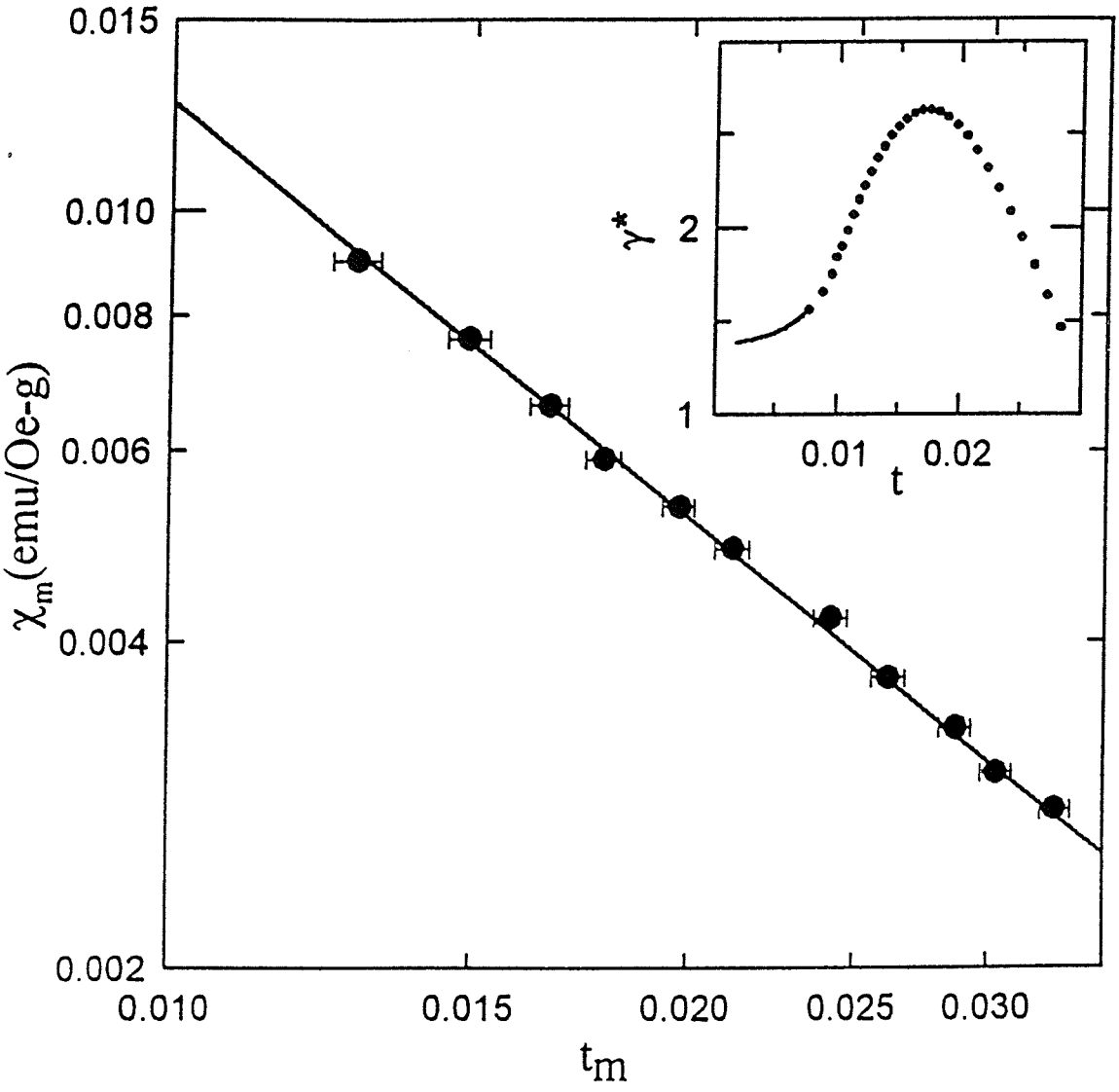

Figure 5.14: The amplitude of the susceptibility maxima plotted against the reduced peak temperature, the fit to the data yields $\gamma = 1.31(\pm 0.05)$. The inset shows the effective exponent $\gamma^*(t)$deduced from the zero field susceptibility.

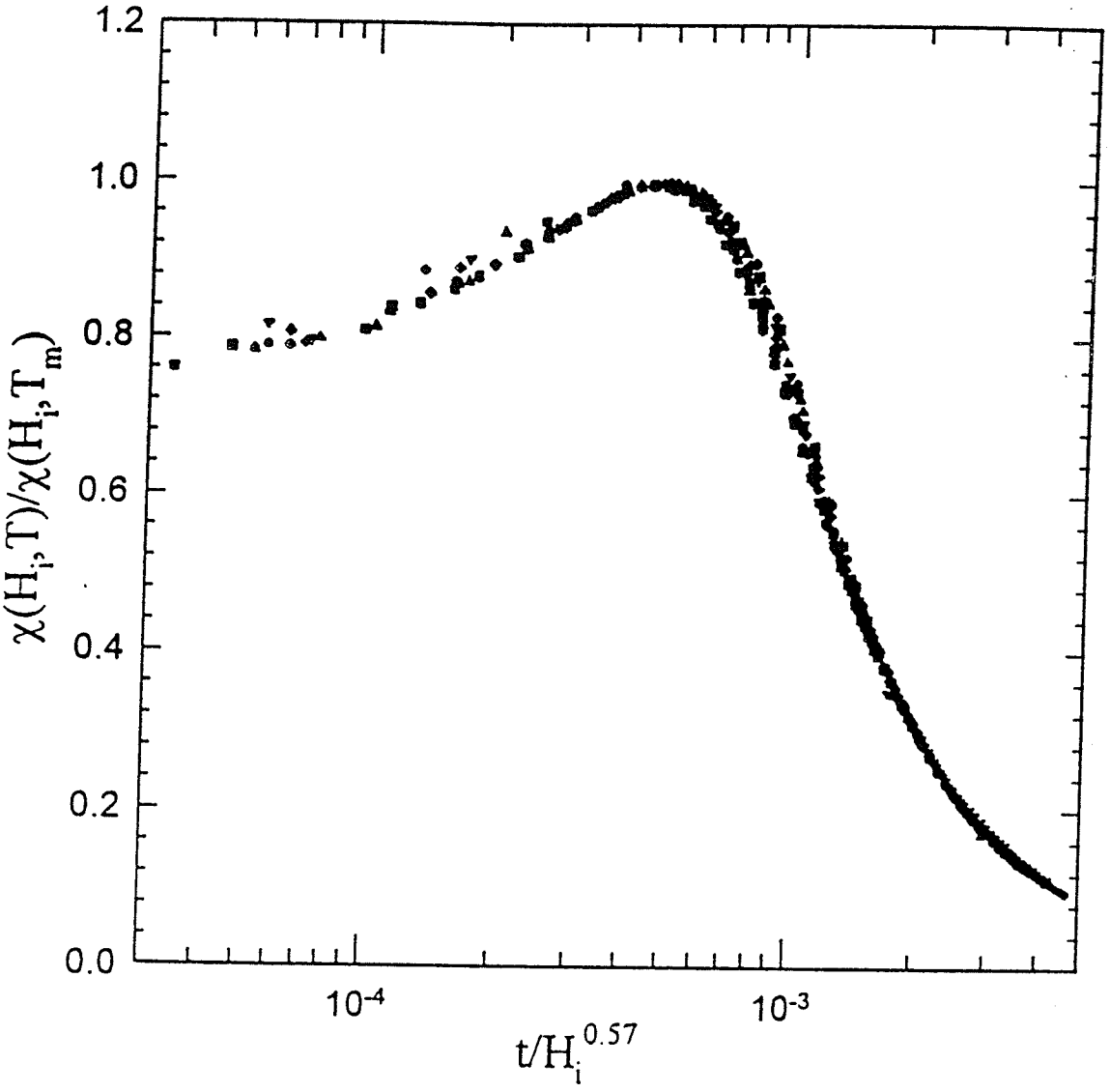

Figure 5.15: The "scaling plot" for the isokaps shown in figure (5.9). The susceptibility normalized to the respective peak amplitudes is plotted against the (inverse) argument $(t/h^{1/(\gamma+\beta)})$ of the scaling function.

ated Jahn-Teller effect. The Jahn-Teller effect is particularly important in the present context since the observation of technical hardness in a variety of other systems has been attributed to the presence of single ion anisotropy resulting from spin-orbit coupling. The absence of a Jahn-Teller ion, such as Mn^{3+}, precludes such a coupling in the present system, so that the origin of this apparent hardness remains unclear. The presence of a regular component in the low field response is also confirmed indirectly by the behaviour of the effective Kouvel-Fisher susceptibility exponent deduced from the zero field susceptibility shown in the inset in figure (5.9) and reproduced in the inset in figure (5.14). While the asymptotic ($t \rightarrow 0$) behaviour is consistent with the Heisenberg model value of $\gamma = 1.386$, the temperature variation of the effective exponent is often ascribed to magnetic disorder resulting in a distribution of magnetic interactions [37, 67]. In the doped manganese perovskites such disorder could result from the inhomogeneous mixed valent state which leads to spatially inhomogeneous magnetic interactions, i.e. ferromagnetic double-exchange is predominate in regions statistically rich in the dopant ions while competing with the antiferromagnetic superexchange characteristic of the host $LaMnO_3$. For the pyrochlore, however, this explanation is not appropriate, and we contend that the temperature dependence of $\gamma^*(t)$ results from an anomalous regular component in the low field response evident in figure (5.9). Figure (5.16) illustrates the measurement of the coercive field H_c at 4.2 K; it is estimated to be only about 2 Oe from this butterfly loop. In general, H_c is considered to be a measure of technical hardness, and generally fields of magnitude 2-3 times H_c ($T \leq T_c$) are sufficient to saturate the regular compo-

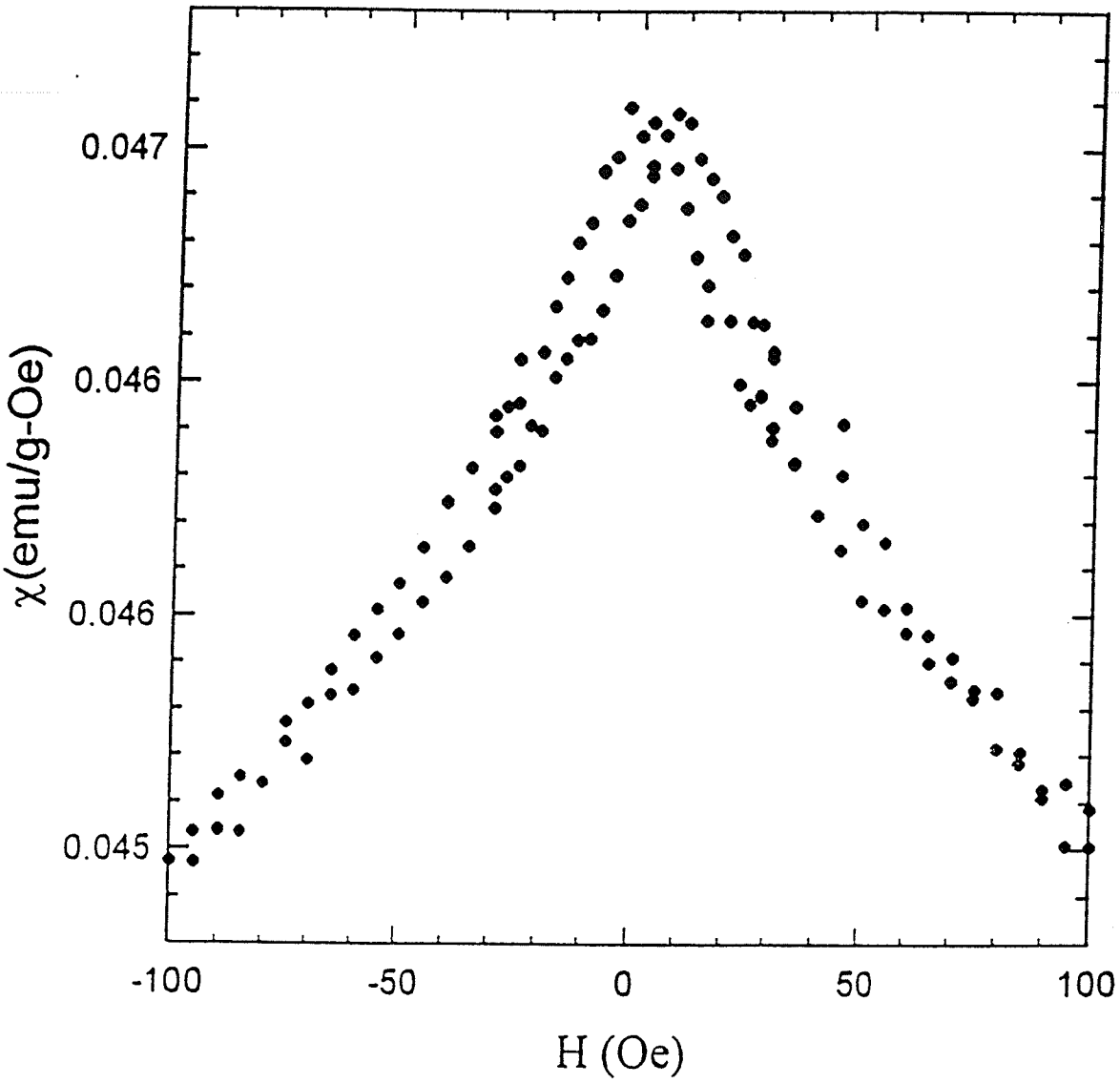

Figure 5.16: The butterfly loop from which the coercive field at 4.2 K can be estimated, here H_c is 2 Oe.

nent arising from technical sources. This low value for H_c is clearly qualitatively consistent with the absence of an orbital component in the total moment at Mn sites in this pyrochlore.

In summary, from the above data analysis it is concluded that the pyrochlore, $Tl_2Mn_2O_7$, exhibits static magnetic critical exponents consistent with those predicted by the isotropic, near neighbour three dimensional Heisenberg model. This contrasts with our results for Ca-doped manganese perovskites and the conclusions reached from recent detailed measurements on Sr-doped manganese perovskites [64, 66]. The former are subject to considerable difficulty to yield critical exponent values; the latter, for polycrystalline ceramic $La_{0.8}Sr_{0.2}MnO_3$, gives $\gamma = 1.10$, $\beta = 0.496$, and $\delta = 3.13$, and for single crystal $La_{0.8}Sr_{0.2}MnO_3$, $\gamma = 1.22$, $\beta = 0.37$, and $\delta = 4.20$. Despite these differences, these two types of systems, in which ferromagnetic order results from superexchange and double exchange respectively, show some similarities in the universality classes.

5.3 Magnetotransport and Spontaneous Resistive Anisotropy for the Ca-doped Perovskite

In this section the general magnetic properties, electrical transport and the associated magnetoresistance are first reported for $La_{0.67}Ca_{0.33}MnO_3$, then the spontaneous resistive anisotropy (SRA) is discussed theoretically and the experimental data are subsequently presented.

Four samples were prepared using conventional ceramic techniques from stoichiometric quantities of La_2O_3 (ultrapure), $CaCO_3$ and MnO_2 as described previously. Here different heat treatment procedures were carried out in order to improve the resistivity behaviour. The specific fabrication conditions are described in Table (5.1), in which several magnetic and transport properties of four such specimens are also summarized. Room temperature x-ray measurements demonstrated a single-phase orthorhombic structure for these samples (a quantitative result is given in the next section).

Figure (5.17) shows the temperature dependence of the zero-field resistivity $\rho(T)$ and the AC susceptibility in zero biasing (magnetic) field. The susceptibility data display features typical of a paramagnetic/ferromagnetic phase transition and it is accompanied by metal/insulator transition, this is indicated by the dashed line in this figure despite a pseudoinflection point for specimen A. While the main body of this figure shows that the principal (Hopkinson) maximum in the zero field ac susceptibility varies considerably, the field-dependent susceptibilities display similar critical behaviour, as discussed previously for sample B; a detailed analysis yields the magnetic ordering temperature, T_c, shown in Ta-

Table 5.1: A summary of magnetic and transport properties along with the preparation procedures for the four samples.

Sample	T_c (K)	ρ_o (Ω-cm) (at 295 K)	MR($\Delta\rho/\rho_0 \times 100\%$) (Near T_c, 1.5 T)	Grain size (μm)	H_c (Oe) (230 K)
A	242	580	16	1-2	32
B	248.8	0.056	25	3-5	23
C	242	1.22	23	20-40	15
D	243.5	0.028	41	20-40	13

A: 800 °C (12hrs) in air, 1200 °C (24hrs) in air (using CaO).
B: 800 °C (24hrs) in air, 1200 °C (48hrs) in oxygen.
C: 800 °C (24hrs) in air, 1200 °C (48hrs) in oxygen, 1440 °C (24hrs) in air.
D: 800 °C (24hrs) in air, 1200 °C (48hrs) in oxygen, 1440 °C (24hrs) in air, 1200 °C (24hrs) in oxygen.

ble (5.1), indicating minimal changes in T_c for these samples. Figure (5.18) shows the magnetization curves measured in magnetic fields up to 6 Tesla at temperatures of 2 K, 200 K, 240 K, 300 K respectively. The data show that all four samples have almost same magnetization behaviour both below and above the Curie temperature, and the magnitude of the saturation magnetization at 4.2 K is in good agreement with a calculation based on the assumption that all spins are coupled ferromagnetically with a mixed valence state of spins S = 3/2 or 2. The calculated magnetization has a value of 97.6 emu/g.

While the magnetic data show relative insensitivity to the preparation methods, resistivity displays a large variation in magnitude by a factor of 10^3. This behaviour is discussed below. All samples show metallic behaviour ($d\rho/dT > 0$) at low temperature; sample D exhibits characteristics comparable with the best

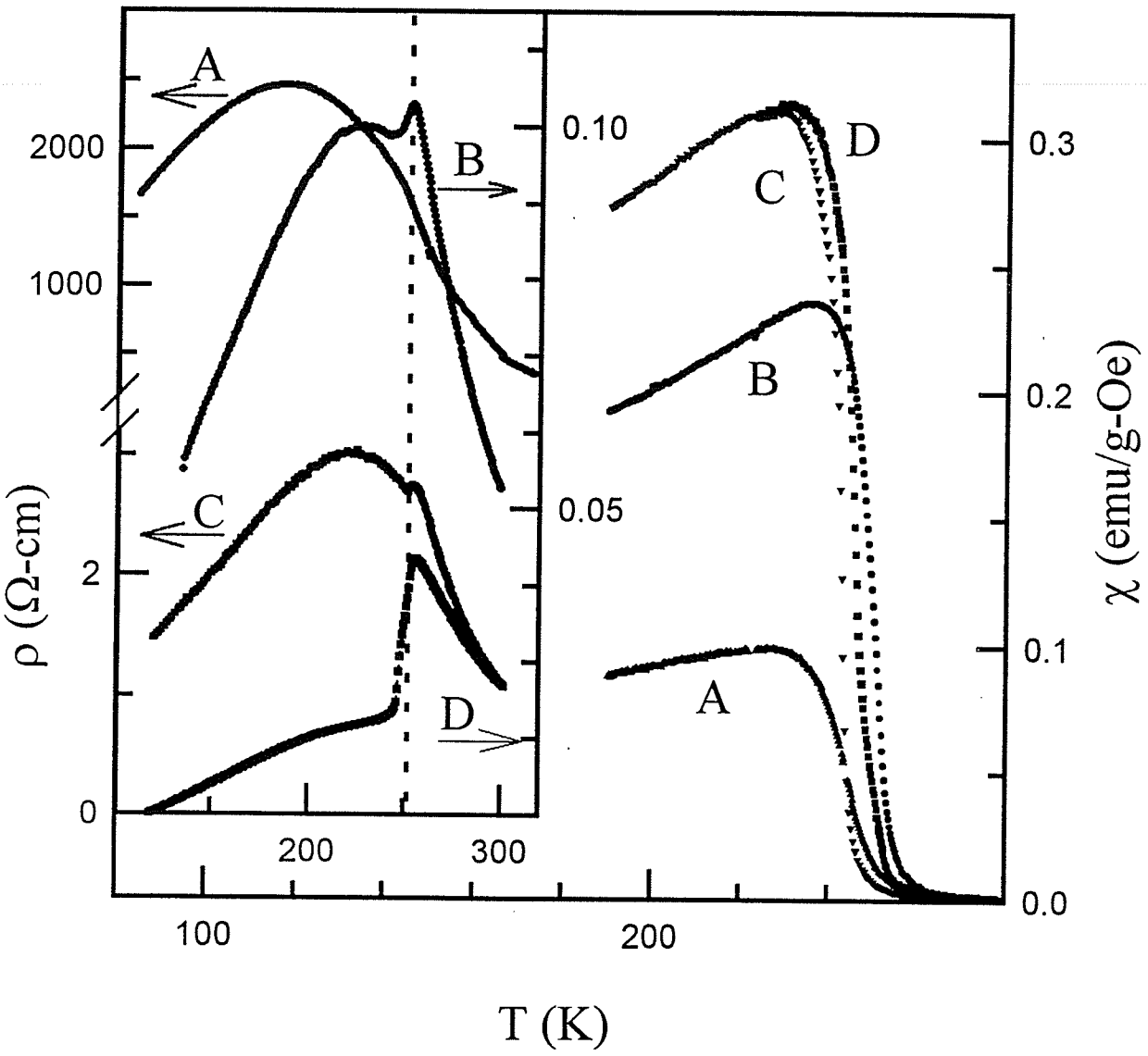

Figure 5.17: The zero field ac susceptibility and the resistivity as a function of temperature for four samples prepared under different fabrication procedures detailed in table (5.1)

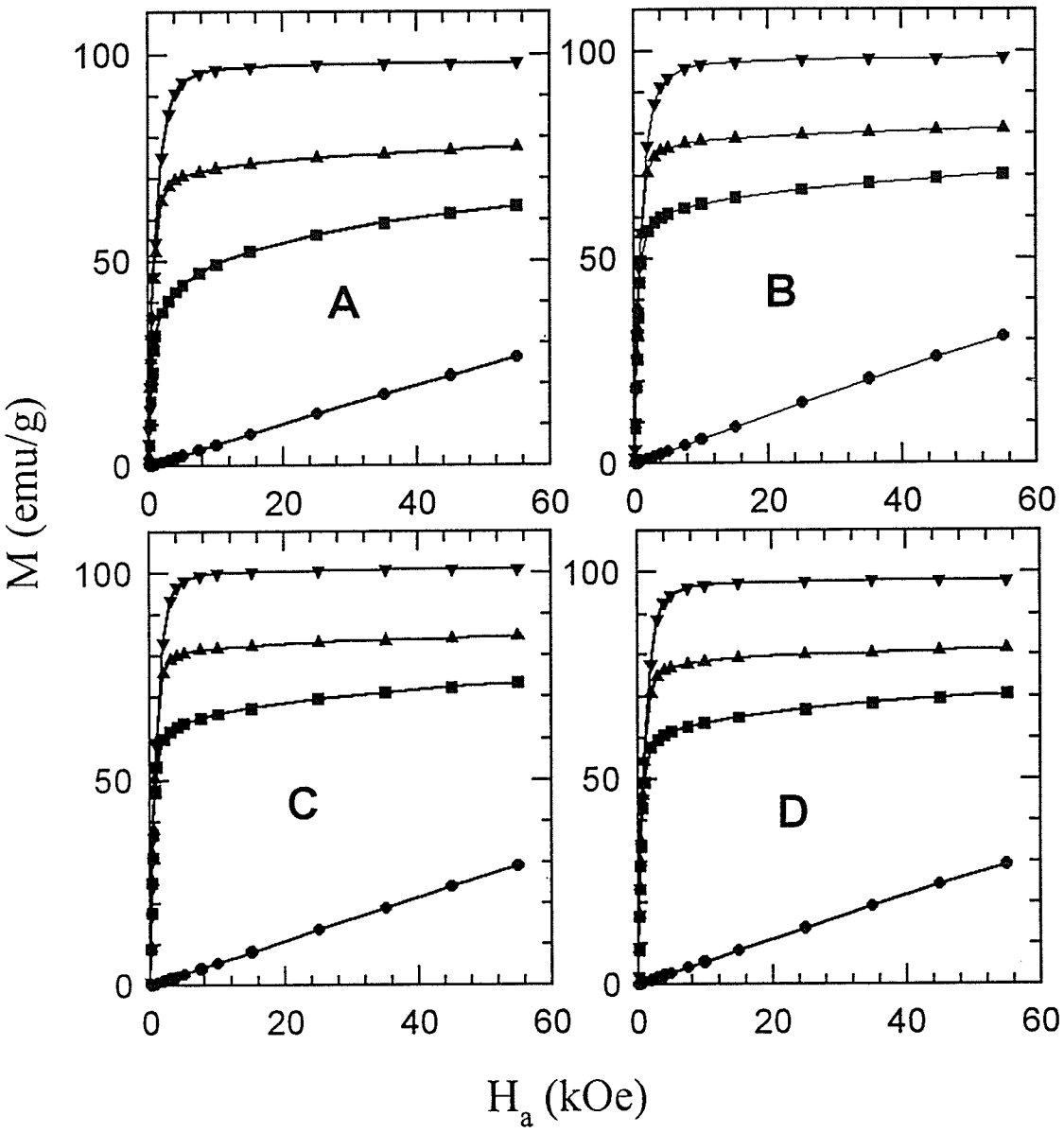

Figure 5.18: Magnetization versus applied field at temperatures of 4.2 K, 200 K, 240 K, 300 K (top to bottom) for the four samples (A, B, C and D).

polycrystalline specimens reported to date [25, 31]. The broad metal-insulator transition in sample A and the obvious second broad peak in the resistivity in sample B and C have been reported and intentionally investigated. They are generally considered to be caused by grain size effects [68, 69, 70] or oxygen deficiency [71]. The average grain size at the surface of the above samples was estimated from the SEM photographs and is summarized in Table (5.1). The samples C and D have a bigger grain size than A and B, and this is a direct result of sintering at higher temperature, which produces high density and less porosity of the sample. On the other hand, it is obvious that samples C and D display a large difference in resistivity although they show similar grain size due to having the same sintering temperature; however, sample D was annealed in oxygen atmosphere at lower temperature. This demonstrates that, apart from the grain size effect, oxygen content plays an important role in interpreting the occurrence of the second broad peak in the resistivity as is evident in sample C. Of course, the behaviour of samples A and B could also involve contributions both from grain boundaries and oxygen content. Based on our experimental data, since grain boundary contributions and oxygen content effects on resistivity both exist, the specific roles played by each still remain to be clarified. Because this is not our main concern in this study, we do not investigate it any further at this time. As a special case and an important example, however, the specific effect of oxygen deficiency on the magnetic and transport properties of the manganites (Ar-annealed $La_{0.67}Ca_{0.33}MnO_3$) will be studied in detail later. Here the best sample D, showing the sharpest metal-insulator transition, was used to exam-

ine the detailed magnetic and transport behaviour, magnetoresistance and the spontaneous resistive anisotropy.

5.3.1 Magnetotransport Properties

In order to produce the sharpest metal-insulator transition and lower resistivity value, sample D was further annealed at 950°C for 24 hours in flowing oxygen. The temperature dependence of the zero field resistivity is shown in figure (5.19). This specimen displays an insulating behaviour ($d\rho/dT < 0$) above the peak temperature (~273 K) below which a sharp transition into metallic-like transport ($d\rho/dT > 0$) occurs. This is the typical characteristic of double-exchange systems in which the magnetic phase transition is accompanied by the change in transport behaviour. Tt is convincingly demonstrated by the magnetization variation with temperature measured in a field of 1000 Oe between temperature 4.2 K to 300 K on warming, as is shown in the inset of figure (5.19). Also the temperature dependence of the zero field ac susceptibility and inverse susceptibility, shown in figure (5.20), indicate that the magnetism and transport are well correlated. Despite this improved resistivity behaviour, the field-dependent susceptibility exhibits the critical behaviour similar to that for sample B, thus there is no need to repeat critical data analysis. Here we discuss the temperature dependence of the zero-field resistivity. Because it is obvious that the resistivity displays a weak, broad shoulder between 120 K and 250 K, which is usually attributed to grain boundary scattering [69, 70], the behaviour is only qualitatively described below.

The transport behaviour can be subdivided into three different tempera-

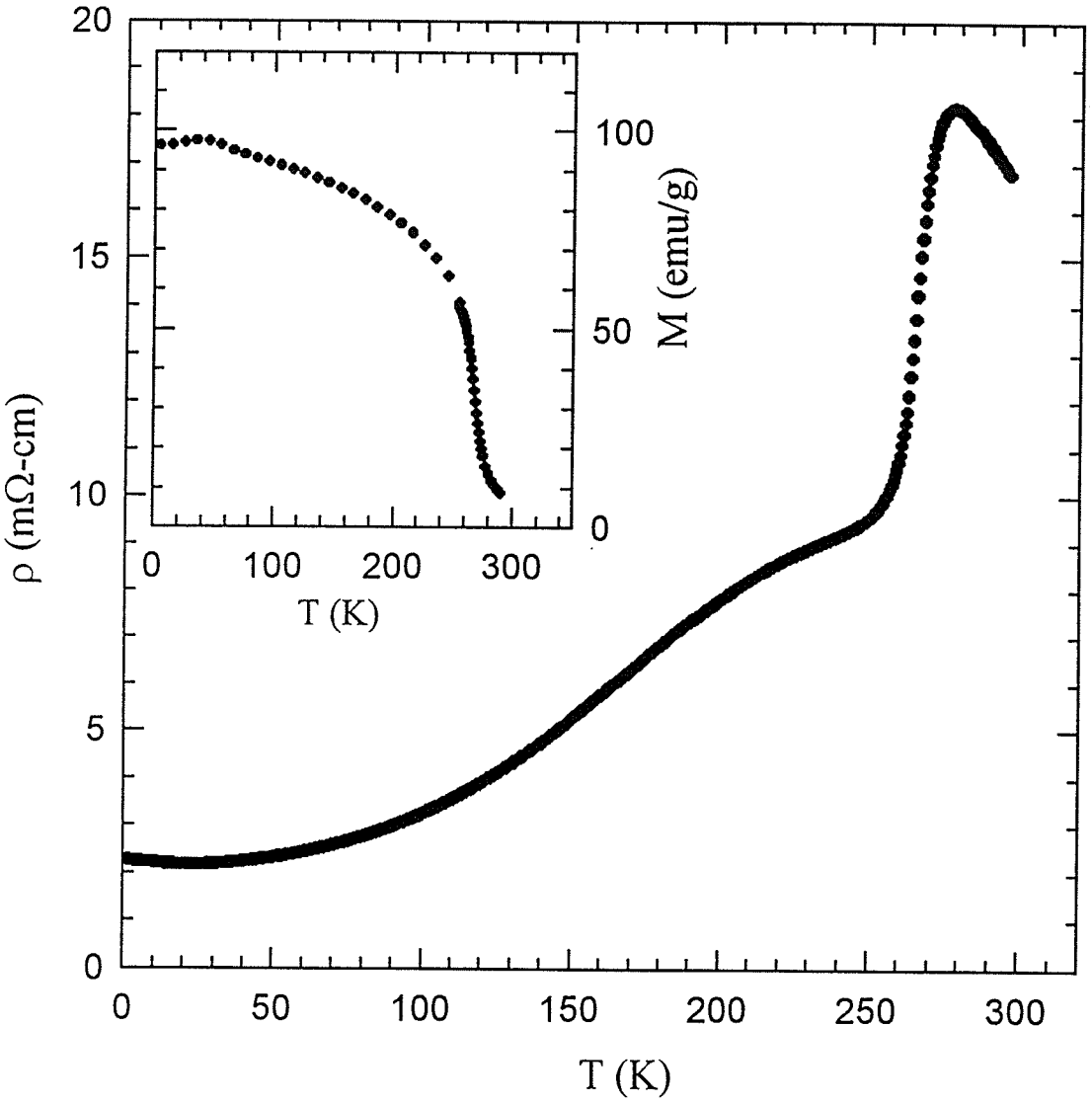

Figure 5.19: The temperature dependence of the zero field resistivity. The inset shows the magnetization variation with temperature measured in a field of 1000 Oe.

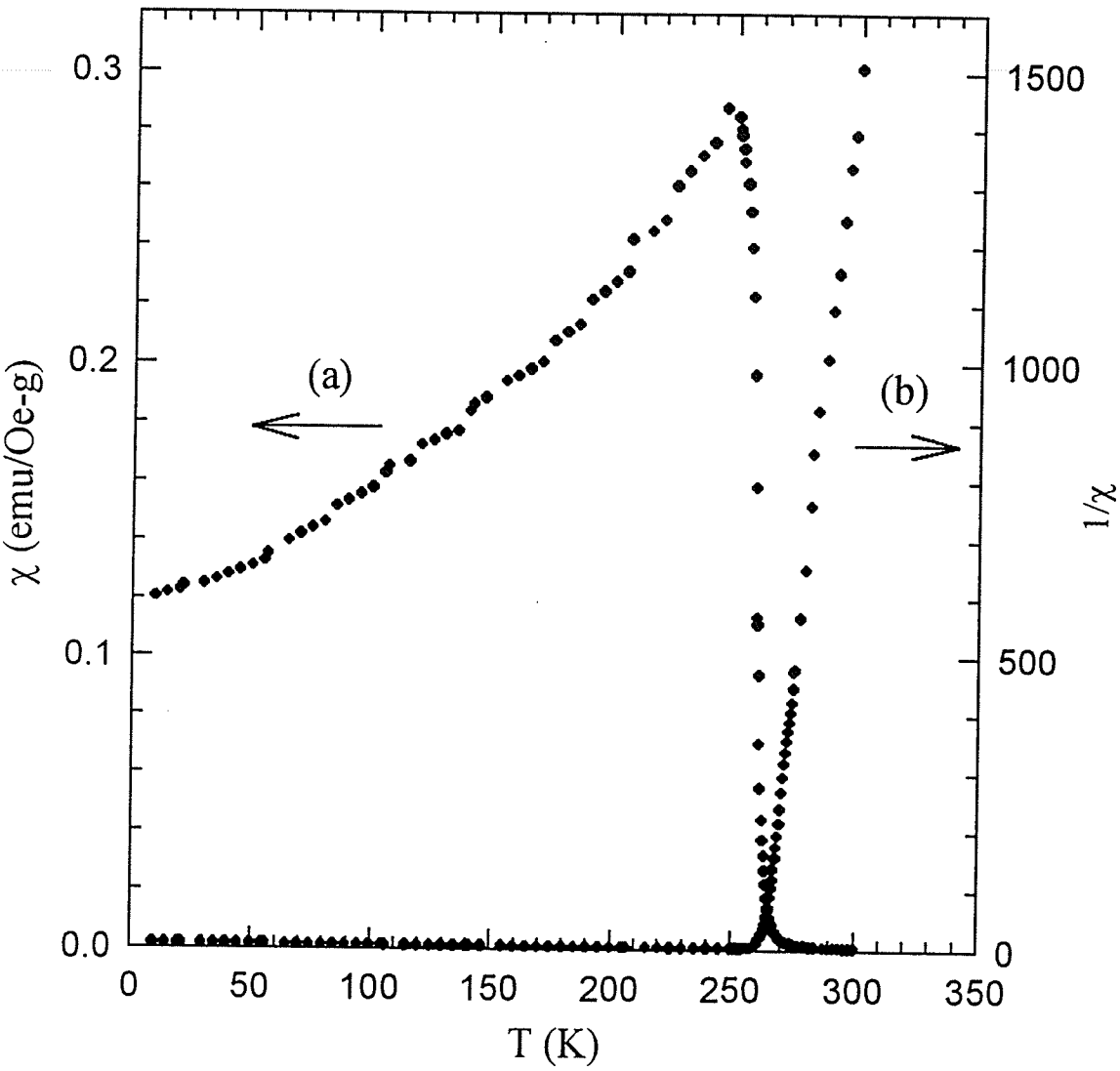

Figure 5.20: The zero-field susceptibility (a) and inverse susceptibility (b) versus temperature.

ture regimes: well below T_c, much higher than T_c and in the vicinity of T_c. The high temperature transport displays semiconducting behaviour and is believed to be characteristic of small lattice polarons. This will be discussed in detail in the next section. The external magnetic field has little effect on the transport properties, and the magnetoresistance essentially disappears in this regime because the mean free path for charge carriers is much smaller than the grain size. The low-temperature resistivity usually incorporates two parts: one is identified as the grain boundary scattering contribution while the other is ascribed to intrinsic scattering such as electron-magnon, electron-electron and electron-phonon scattering. Here the double exchange mechanism is believed to dominate spin hopping within narrow and fully spin-polarized bands. In the region around T_c, the Jahn-Teller effect on the Mn^{3+} ions and double exchange coexist. On the one hand, the strong Jahn-Teller effect leads to polaron formation and possible self-trapping; on the other hand, the onset of ferromagnetism increases the effective bandwidth, resulting in polarons dissolving into band electrons. Polaronic distortions in the paramagnetic state may persist over some temperature range into the ferromagnetic phase [72].

The magnetoresistance behaviour is shown in figure (5.21); in the inset resistivity is measured against temperature in magnetic fields of zero, 0.8 T and 1.5 T respectively. It is apparent that the metal/insulator transition shifts to higher temperature with increasing field, and the magnetoresistance $\frac{\rho(0)-\rho(H)}{\rho(0)}$ has a peak value of about 50 percent around T_c. The large residual magnetoresistance of 10 - 20 percent at low temperature has been identified as spin-polarized tunnel-

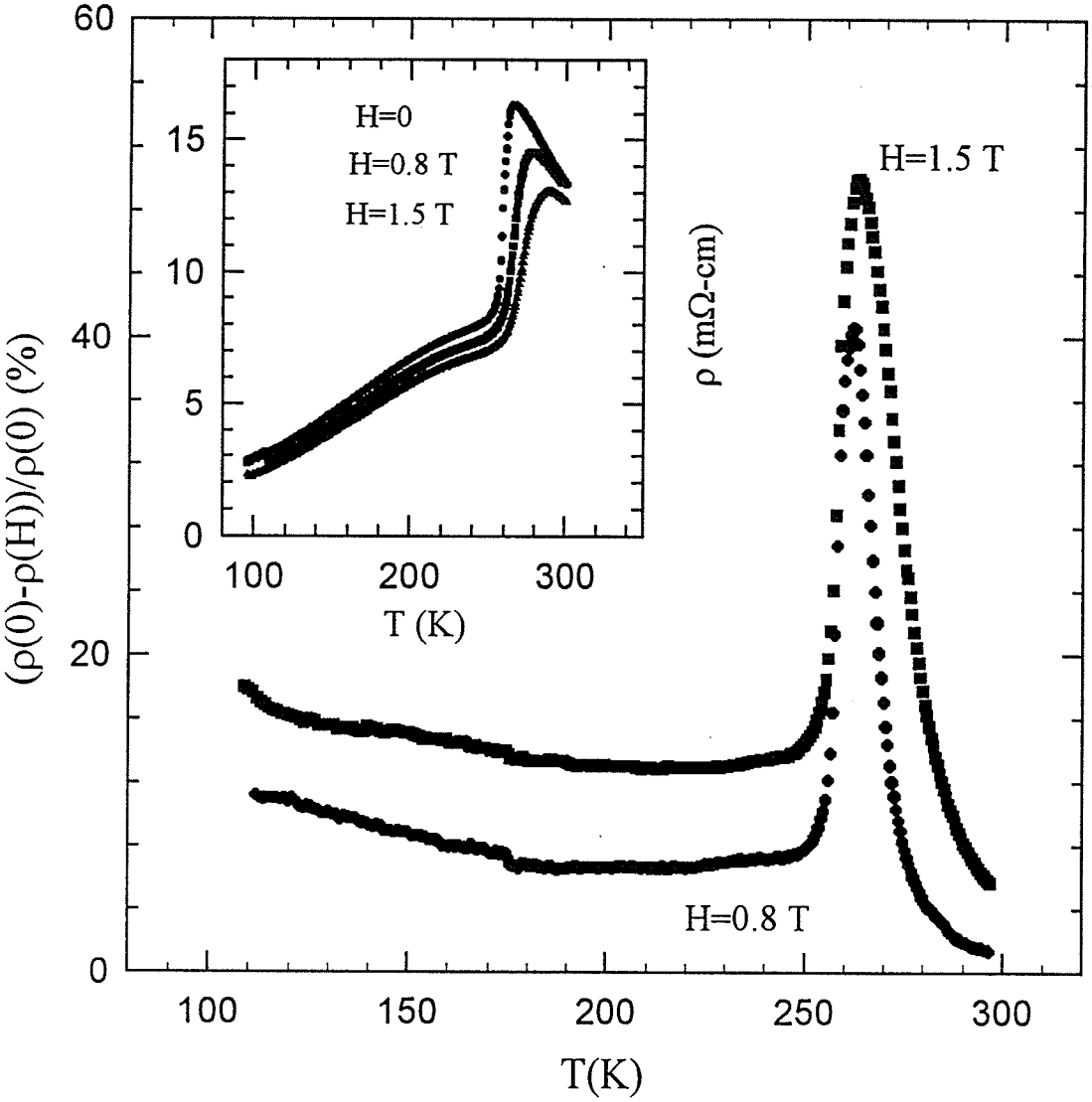

Figure 5.21: The magnetoresistance versus temperature in fields of 0.8 T and 1.5 T. The inset shows the resistivity variation with temperature in the fields of zero, 0.8 T and 1.5 T, respectively.

ing through intergrain barriers [70]. The extrinsic transport properties of CMR manganites, resulting from such mechanisms as grain boundary scattering, mechanical strain, and deviations from nominal stoichiometry etc, are clearly quite important; studies on these extrinsic CMR may lead to practical technological applications for these materials.

5.3.2 Spontaneous Resistive Anisotropy (SRA)

The spontaneous anisotropy in the resistivity (SRA) is interesting because of its underlying physics as well as for its practical application to magnetic sensors. Before the SRA in $La_{0.67}Ca_{0.33}MnO_3$ is discussed, a brief review of the SRA in polycrystalline ferromagnets is necessary. The resistivity in a magnetized isotropic material has the following form [16]

$$\rho_{B=0} = \frac{\rho_{\parallel} + 2\rho_{\perp}}{3} + (\cos^2\theta - \frac{1}{3})(\rho_{\parallel} - \rho_{\perp}) \tag{5.1}$$

where $\rho_{B=0}$ is the resistivity extrapolated to zero induction B, $\rho_{\parallel}$ and $\rho_{\perp}$ are the resistivity for current $\vec{J}$ parallel and perpendicular to the magnetization $\vec{M}$ at B = 0, respectively, and θ is the angle between $\vec{J}$ and $\vec{M}$. The relative spontaneous anisotropy in the resistivity is defined as follows

$$\frac{\triangle\rho}{\rho} = \frac{\rho_{\parallel} - \rho_{\perp}}{\frac{1}{3}\rho_{\parallel} + \frac{2}{3}\rho_{\perp}} \tag{5.2}$$

Two principal models are widely used to deal with this effect: one is localized in nature, the other itinerant, but both rely on the existence of spin-orbit coupling

and a polarizing field at the scattering sites. The localized model has been mainly used to interpret the SRA induced by an externally applied polarizing field in paramagnetic systems such as AuHo [73]. The second, the two-current model, is based on the itinerant picture and has often been utilized to describe extensive sets of measurements on dilute ferromagnetic alloys consisting of transition metal hosts [16, 74, 76]. Both approaches are briefly described below.

Localized Model

The localized model is mainly applicable to 4f rare-earth metals and alloys, where, due to the compact nature of the unfilled 4f shell, it is regarded as ion-like with a nonspherical charge distribution caused by unquenched angular momentum. As a result of this non- spherical charge distribution, a conduction electron encounters a slightly different (charge) scattering cross section, depending on the relative orientation between the magnetic moment and the current direction. Even in polycrystalline samples, a multipole moment analysis of this distribution indicates that the anisotropy of resistivity is proportional to first order to the electronic quadruple moment of the particular rare earth ion, thus displaying the expected $(3\cos^2\theta - 1)$ angular dependence from the field direction (i.e. axial symmetry). The interaction between the conduction electron and the impurity site can be described by the following scattering Hamiltonian [75]:

$$H = [V + J(\vec{\sigma}\cdot\vec{S}) - \frac{D}{K_F^2}((\vec{S}\cdot\vec{K})(\vec{S}\cdot\vec{K}') - \frac{S(S+1)}{3}\vec{K}\cdot\vec{K}') + \cdots]\vec{\alpha}^{+}_{\vec{K}'}\vec{\alpha}_{\vec{K}} \quad (5.3)$$

in which the first term represents the Coulomb interaction of the conduction electrons with the shielded ion cores. The second term is the exchange interaction between a localized spin(s) and a conduction electron(s) and in the third term, D is the quadrupole moment. The first two terms, while being anisotropic in single crystals, are isotropic in a polycrystalline material, so that the third term dominates the resistive anisotropy. The latter is given as follows [75]

$$\frac{\Delta\rho}{\rho_0} = \frac{D}{V}(< S_z^2 > - \frac{S(S+1)}{3}) \tag{5.4}$$

For $T >> \mu_B H_E/k_B$ (where H_E is the exchange field), $< S_z^2 >= \frac{S(S+1)}{3}$, thus predicting that the SRA will disappear in the paramagnetic state because of the complete spin disorder.

Two Current Model

In transition metals, both 4s electrons and 3d electrons are involved in electrical conduction. Within a band picture, spin-up and spin-down electrons have a different density of states at the Fermi level, i.e. they form spin-up and spin-down sub-bands, giving rise to different spin-up and spin-down electrical currents. Two current channels are formed corresponding to two well-defined spin directions if magnon scattering and spin-orbit effects are ignored. Conduction is thus composed of two parallel independent currents. If the corresponding resistivities are represented by $\rho\uparrow$ and $\rho\downarrow$, respectively, the total resistivity is [16]

$$\rho = \frac{\rho\uparrow\rho\downarrow}{\rho\uparrow + \rho\downarrow} \tag{5.5}$$

In fact, spin-mixing will occur due to electron-magnon and spin-orbit coupling, and a more general expression is

$$\rho = \frac{\rho\uparrow\rho\downarrow + \rho\uparrow\downarrow(\rho\uparrow + \rho\downarrow)}{\rho\uparrow + \rho\downarrow + 4\rho\uparrow\downarrow} \tag{5.6}$$

where $\rho\uparrow\downarrow$ is the resistivity associated with the transfer of electrons between sub-bands induced by spin-flip scattering processes [16]. Spin-mixing in transition metal systems is generally composed of two parts; one comes from s-s electron scattering that yields $\rho_{ss}\uparrow = \rho_{ss}\downarrow$ as this term is usually isotropic; the other comes from s-d scattering for which $\rho_{sd}\uparrow \neq \rho_{sd}\downarrow$ since s-d scattering is anisotropic, a result of the spin-orbit coupling $\lambda\vec{L}\cdot\vec{S} = \lambda L_z S_z + \lambda/2(L^+S^- + L^-S^+)$. From the often used relationship: $\rho\downarrow = \rho_{ss}\downarrow + \rho_{sd}\downarrow$, and $\rho\uparrow = \rho_{ss}\uparrow + \rho_{sd}\uparrow$, the anisotropy of resistivity is obtained following a second order perturbation approach [76, 77]:

$$\frac{\Delta\rho}{\rho_0} = \frac{\gamma[\rho_{sd}\downarrow - \rho_{sd}\uparrow]^2}{\rho\uparrow\rho\downarrow + \rho\uparrow\downarrow(\rho\uparrow + \rho\downarrow)} \tag{5.7}$$

where $\gamma \propto \lambda^2/(K^2 \pm H_{ex}^2)$, K is the crystalline field anisotropy, H_{ex} is the exchange field, and γ is the spin-orbit coupling coefficient. When the temperature approaches the Curie point from below (i.e. within the ferromagnetic state), H_{ex} will approach zero; and the numbers of spin-up and spin-down electrons becomes equal. The anisotropy of the resistivity will thus disappear when $T \geq T_c$. Near T_c, $\rho_{sd}\uparrow$ and $\rho_{sd}\downarrow$ can be approximated as $\rho_{sd} \pm sH_{ex}$ to leading order, where s is the first derivative of ρ_{sd} with respect to field; with $H_{ex} \propto (< M >) \propto (1 - T/T_c)^{1/2}$ in mean field, the SRA becomes proportional to $(1 - T/T_c)$, which approaches

zero linearly near T_c.

Results and Discussion on the SRA of $La_{0.67}Ca_{0.33}MnO_3$

For the best sample of $La_{0.67}Ca_{0.33}MnO_3$ described above figure (5.22) displays the longitudinal $\rho_{||}$ (H_a parallel to the measuring current) and the transverse, $\rho_{\perp}$, magnetoresistivity at 79 K in fields up to 1.5 T. In both orientations the low field magnetoresistance ($H_a < 0.5$ T) falls sharply, as shown in the inset, an effect often attributed to technical magnetization processes [70]. The large difference evident between the two orientations originates principally from demagnetizing field effects (estimated to be about 0.2 T). At higher fields ($\geq$ 1 T) there is a much slower, essentially linear decrease in $\rho(H_a)$ with increasing applied field H_a.

The SRA is generally acquired by extrapolating to zero induction. The extrapolation is usually performed from a field region sufficiently high to (technically) saturate the sample; by contrast, the low field region of the curves shown in the inset of figure (5.22) depends on the prevailing domain structure which is history dependent and hence not well defined [16]. The extrapolations, shown by the dashed lines in this figure, are fitted to the (technically saturated) data beyond $\mu_0 H_a \approx 1$ T where a simple linear, essentially parallel, fit reproduces the data for both orientations very well. These extrapolations are extended to B = 0, where $B = \mu_0 H_a + M(\mu_0 - N)$ in the usual notation and demagnetizing factors are found from the corresponding shearing curves (N=165 Oe/emu for the parallel and N=1460 Oe/emu for the perpendicular orientation). The value estimated for the SRA at 79 K using this approach is about -1.1%. Since a non-vanishing SRA requires both a polarizing field and spin-orbit coupling at

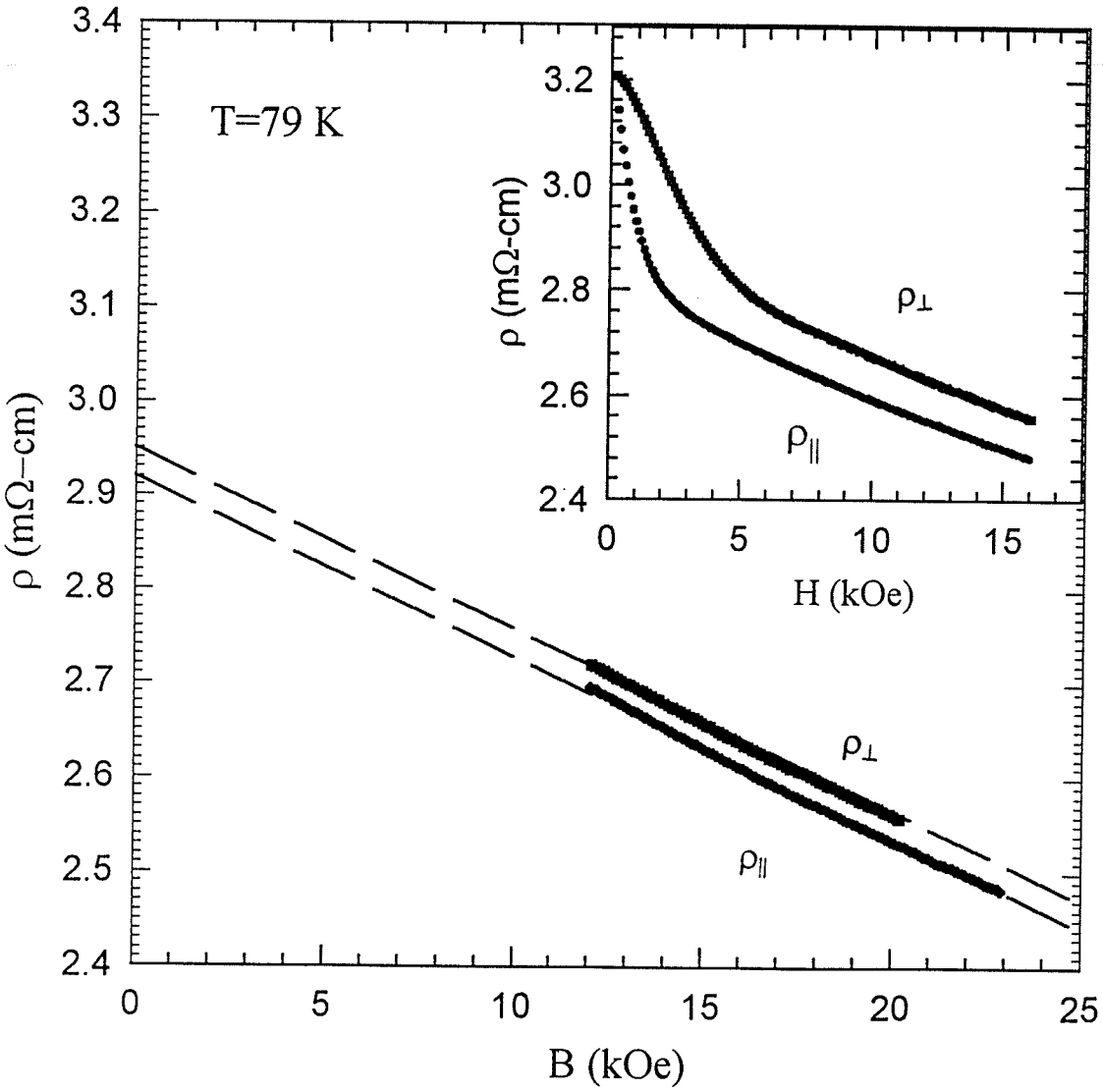

Figure 5.22: Resistivity extrapolation following the demagnetization correction to find the SRA. The inset shows the resistivity as a function of external field in the parallel and perpendicular configurations.

scattering sites in either an itinerant or localized model approach, this result is qualitatively consistent with the presence of Mn^{3+} ions mentioned above. Both the sign and magnitude of this effect in the Ca substituted system is similar to that reported for epitaxial films of $La_{0.67}Sr_{0.33}MnO_3$ at the same temperature [78] and for post annealed films of $La_{0.67}Ca_{0.33}MnO_3$ on $SrTiO_3$ at higher temperature [79]. A recent calculation of the SRA in an itinerant model approach within a single spin-polarizing $e_g^{\uparrow}$ sub-band, generally believed to apply to the manganese perovskites, yields [79]

$$\frac{\Delta\rho}{\rho_0} = \frac{3}{2}[\frac{\lambda^2}{(H_{ex} - \Delta_{CF})^2} - \frac{\lambda^2}{\Delta_{CF}^2}] \tag{5.8}$$

where λ is the spin-orbit coupling constant, H_{ex} the exchange field and Δ_{CF} the crystal field splitting; with the latter estimated at 2 and 1.5 eV respectively, and the predicted value for the SRA is $\sim 0.85\%$ [79]. The data obtained here is in general agreement with this estimate in both sign and magnitude. The temperature dependence of the SRA was also measured, as is shown in figure (5.23). The behaviour below 50 K, where the SRA value decreases with decreasing temperature, can not be explained according to the theoretical prediction described above; from 50 K to the Curie temperature, the SRA does not show the clear linear relationship with temperature as expected, it declines very slowly until the Curie temperature is approached. This is quite different from a similar measurement performed for a $La_{0.67}Pb_{0.33}MnO_3$ sample [80] in our laboratory, where the temperature dependence of the SRA above 50 K displays a near linear approach to zero close to T_c, which is in good agreement with the model prediction.

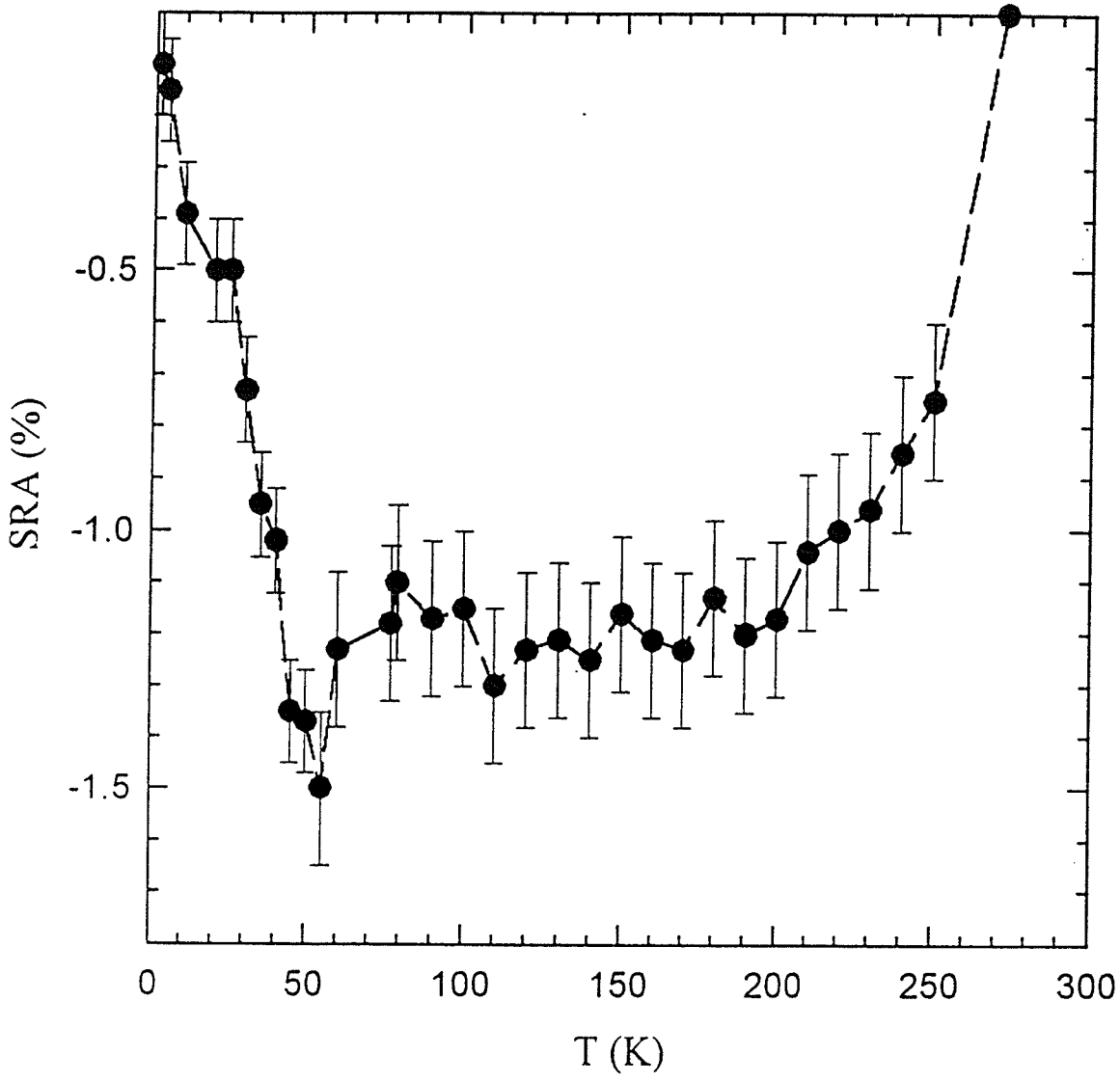

Figure 5.23: The temperature dependence of the SRA of $La_{0.67}Ca_{0.33}MnO_3$.

5.4 Transport and Magnetic Properties of Ar-annealed $La_{0.67}Ca_{0.33}MnO_3$

This section presents experimental data on Ar-annealed $La_{0.67}Ca_{0.33}MnO_3$, in particular the transport behaviour both in the high temperature paramagnetic phase and the low temperature ferromagnetic phase. It has been reported that the strong electron-phonon coupling and/or Jahn-Teller distortions need to be incorporated to account for the relatively large resistivity associated with the insulating response in the high temperature paramagnetic phase [7, 8, 9]. The polaron concept has been introduced to identify the transport behaviour in this magnetically disordered regime. Several recent experiments have been carried out to support the prediction of such polaron models (i.e. the strong electron-phonon coupling), including very large oxygen isotope effects reported for $La_{1-x}Ca_xMnO_3$ at $x \leq 0.2$ [81]. Furthermore, some experimental data [82, 83] have suggested that the polaronic behaviour could even exist in the low temperature magnetically ordered regime in such systems.

Here further experiments have been done to provide supportive evidence for polaronic transport through investigating the effect of Ar-annealing on polycrystalline ceramic samples of $La_{0.67}Ca_{0.33}MnO_3$. For this specimen the electrical response is semiconducting both above and below T_c, displaying a marked change compared with that prior to Ar-annealing. The resistivity can be best described by a form predicted for charge transport by polarons over the entire temperature range from 77 K to 320 K. The results, in general agreement with recent conclusions drawn for the $La_{0.67}Mn_{1-x}Al_xO_3$ system [83], are presented below.

5.4.1 Experimental Procedure

Samples were prepared using conventional techniques from stoichiometric quantities of La_2O_3 (ultrapure), $CaCO_3$ and MnO_2 as described in chapter 4. After these samples were sintered at 1200^oC in flowing oxygen, they were annealed at 950^oC and 650^oC in oxygen for periods of 24 hours and 48 hours respectively. Then they were heated at 950^oC for 72 hours in Ar gas in a deliberate attempt to modify the oxygen content. The samples treated in Ar display very different magnetic and transport behaviour compared with the untreated samples. However by simply re-annealing the samples in oxygen, specifically at 1200^oC for 48 hours followed by 950^oC for 24 hours, the magnetic and transport properties of the Ar-treated samples can be changed back to those typical of the system prior to Ar annealing. This indicates the reversibility of this heat treatment process, specifically relating to the oxygen content. Room temperature X-ray measurements revealed a single-phase orthorhombic structure in both the untreated and the Ar-annealed specimens with lattice parameters: a = 5.4585 $\AA$, b = 5.4586 $\AA$ and c = 7.7026 $\AA$, and a = 5.5071 $\AA$, b = 5.5100 $\AA$ and c = 7.6991 $\AA$, respectively. An examination of the linewidths of the prominent lines in the XRD pattern, specifically the (020) reflection near $\theta = 32.9^o$, shows an increase in the FWHD from 0.17^o in the untreated specimen to 0.35^o in the O-depleted state. For the latter the broadening is considered to be mainly caused by strain associated with an inhomogeneous distribution of O-vacancies produced by Ar-annealing, rather than changes in the average grain size which was found to be unaffected by the annealing process. This grain size was estimated to be approximately 4

μm by averaging roughly 100 grains from SEM photographs for both cases, with an uncertainty of typically ± 0.5 μm arising principally from the non-uniformity in the shape of individual grains. These average sizes are comparable to those reported in other bulk specimens[71] although they are typically fifty times larger than those in thin-film specimens[84]. Susceptibility and magnetization measurements on a sample of approximate dimensions $(1 \times 1.5 \times 6)$ mm^3 were carried out in a Quantum Design PPMS model 6000 system; transport measurements on the same specimen were performed utilizing a conventional 4-probe technique, both of which have been discussed previously.

5.4.2 Magnetic Properties

The zero-field ac susceptibility was measured on warming (in a driving field with an amplitude of 30 mOe rms and frequency 2.4 kHz) for both Ar-annealed and untreated samples as shown in figure (5.24). It can be seen that the critical temperature, T_c, of the Ar-annealed sample is significantly depressed relative to that of the untreated sample. The difference between the two critical temperatures is estimated to be about 90 K, so $\Delta T_c/T_c \sim 30\%$. This depression in T_c is accompanied by a substantial decrease in the zero-field susceptibility; the principal/Hopkinson maximum falls by more than a factor of six. Since the magnetic response of ferromagnets at or below the Hopkinson maximum is governed by technical process [85], this likely reflects the increase in coercivity reported below. For the untreated sample, the detailed critical behaviour and transport properties have been investigated and reported previously in this thesis. For the Ar-annealed sample not only is there a remarkable change in the

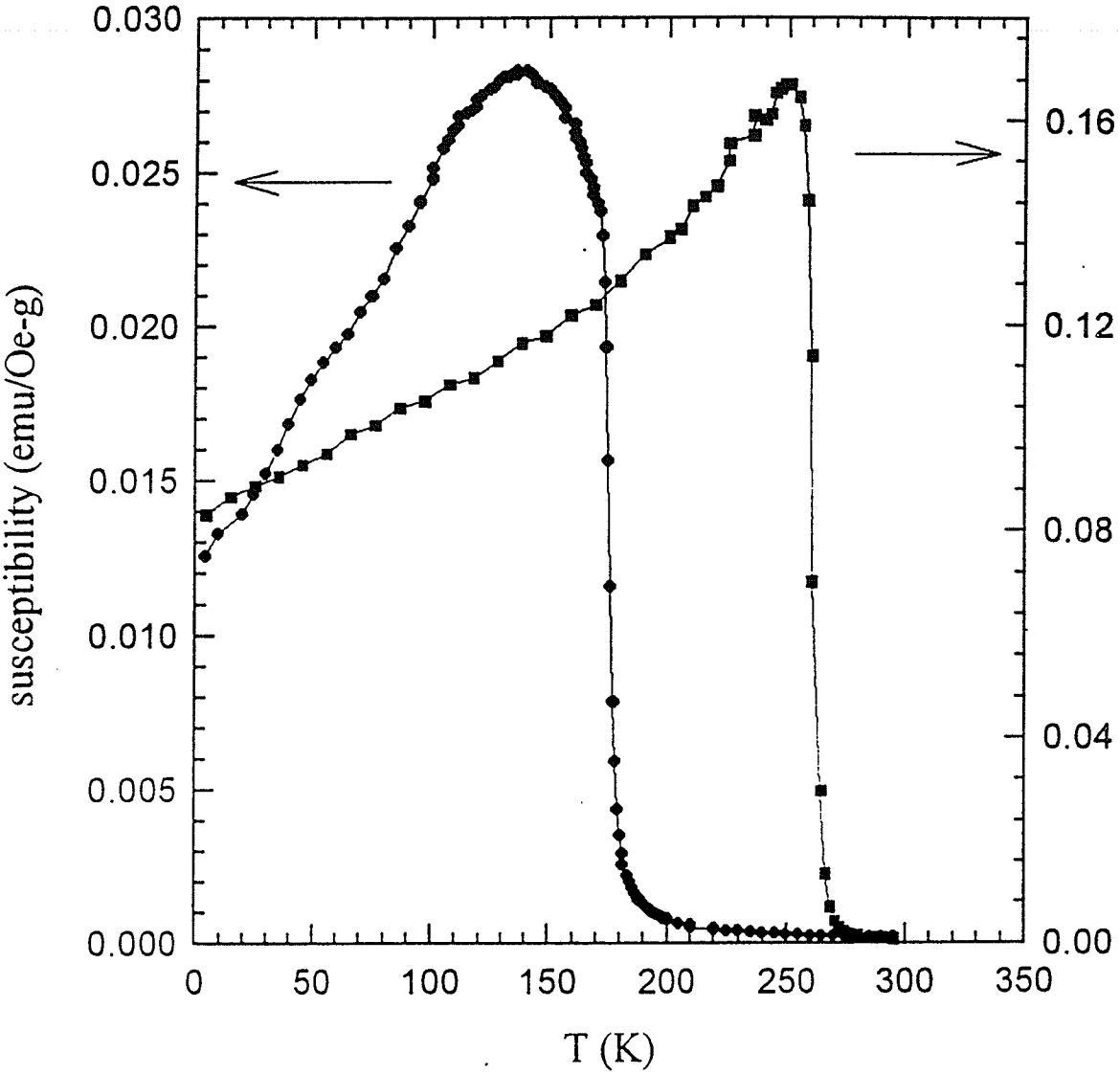

Figure 5.24: Susceptibility plotted against temperature for the Ar-annealed samples (left) and the untreated samples (right) of $La_{0.67}Ca_{0.33}MnO_3$.

magnetic properties described above but also the electrical transport displays insulating/semiconducting behaviour over the entire temperature range from 77 K to 300 K. In particular no metal-insulator transition occurs near the critical point, T_c, or indeed at any other temperature accessed by the present experiment. Detailed analysis of these data, therefore, is necessary for further understanding of these marked changes. The magnetic behaviour is first presented.

In figure (5.25), a plot of the susceptibilities versus temperature measured in applied fields exhibits the same features as those in the untreated sample presented earlier. When the superimposed static biasing fields, H_a, up to 3.5 kOe were applied along the largest specimen dimension, the Hopkinson/principal maximum was continuously suppressed in both amplitude and temperature, allowing critical peaks to be resolved, as is shown in this figure. These critical peaks decrease in amplitude but shift towards higher temperatures from T_c as H_a increases; this confirms the presence of a continuous magnetic phase transition, as these data are consistent with the predictions by the static scaling law and the mean-field model calculations discussed earlier. The solid line in figure (5.25) represents the crossover line which separates the thermally dominated regime at higher temperature from the field-dominated region at lower temperature. The crossover exponent $\gamma + \beta$ can be obtained from the locus defined by the critical maxima and the value here was found to be 1.75, with T_c of approximate 170 K. This exponent $(\gamma + \beta)$ value is basically consistent with Heisenberg model prediction. Nevertheless, in contrast to untreated $La_{0.67}Ca_{0.33}MnO_3$, applied fields in excess of 1000 Oe are required to first resolve such critical peak structure in the

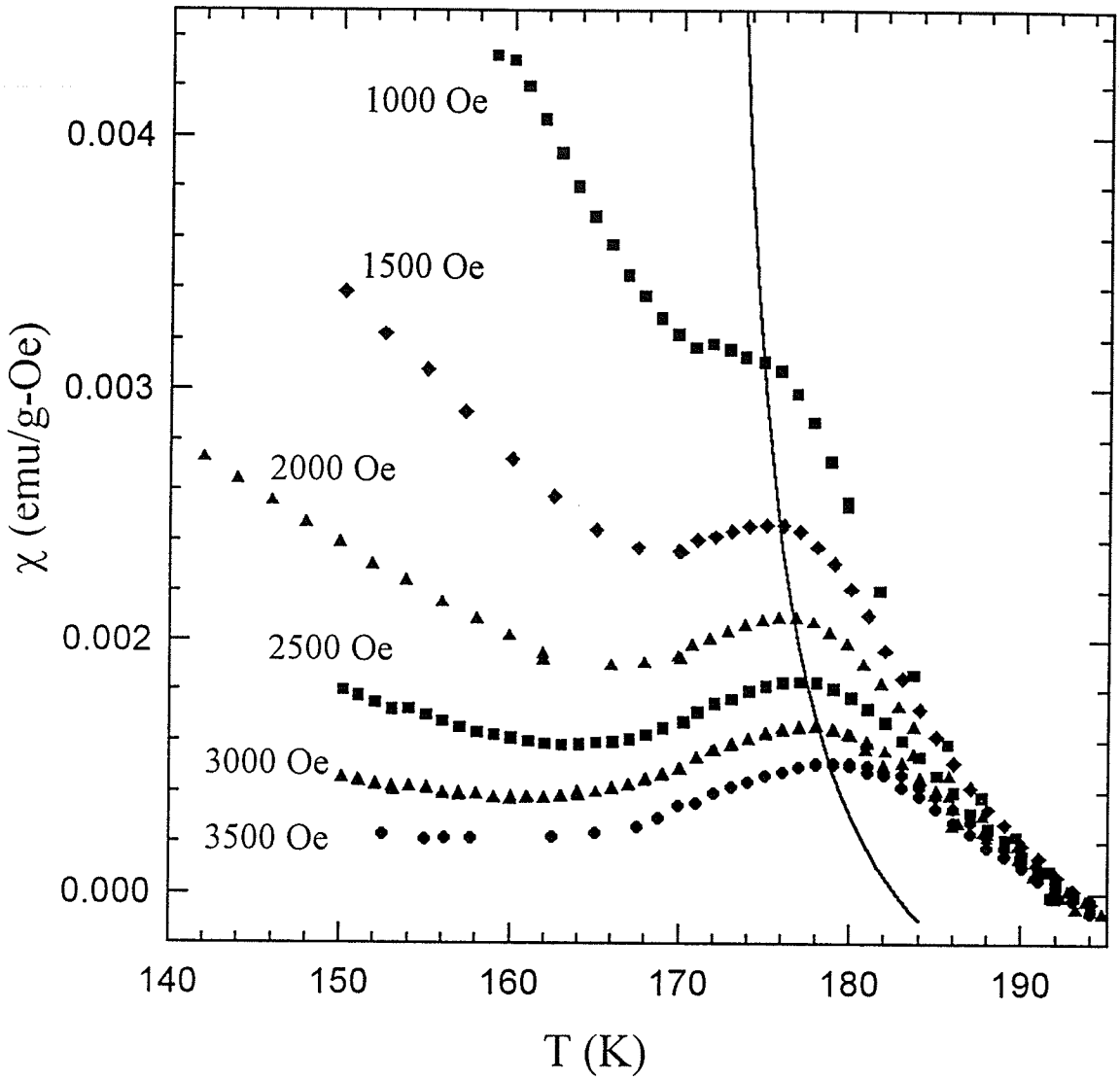

Figure 5.25: Susceptibility versus temperature measured in applied fields from 1000 Oe to 3500 Oe in 500 Oe steps. The solid line depicts the crossover line.

Ar annealed sample. Such fields are more than a factor of 10^3 larger than those necessary ($\sim$0.4 Oe) to resolve such structure in the most favorable case (PdFe), and a factor of 2-3 higher than in the untreated sample. This is likely related to the substantially higher coercive field and the large reversible magnetization in this Ar-treated specimen, as seen in figure (5.26) and its inset. The latter shows the coercive field to be close to 550 Oe, more than an order of magnitude larger than the estimates at the same temperature for the untreated sample (50 Oe at 4.2 K). As a consequence, further analysis of the present data to determine true, asymptotic critical exponents is precluded.

As far as annealing in Ar is concerned, the heat treatment was carried out under reduced O_2 partial pressure, this results in oxygen deficiency in the sample [71, 88]. With increasing oxygen deficiency the average manganese oxidation state decreases and thus the average manganese ionic size increases, resulting in an increase in the lattice parameter for the manganese oxide. Because there is no direct means of evaluating the oxygen content currently available to us, the change in the manganese oxidation state is estimated indirectly. Charge balance requires that the state $La^{3+}_{1-x}Ca^{2+}_{x}Mn^{3+}_{1-x+2\delta}Mn^{4+}_{x-2\delta}O^{2-}_{3-\delta}$ be established if the compound is oxygen deficient. If the modified Mn^{4+} concentration, $x - 2\delta$, is equated to that Mn^{4+}composition in the untreated system for which the T_c is at 170 K (a correspondent Mn^{4+} is of 15 percent), for x = 0.33 δ is found to be 0.09. This approximate estimate is consistent with that made by Dörr et al for a thin film sample of comparable T_c [84].

In the Double Exchange model, the presence of both Mn^{3+} and Mn^{4+} is

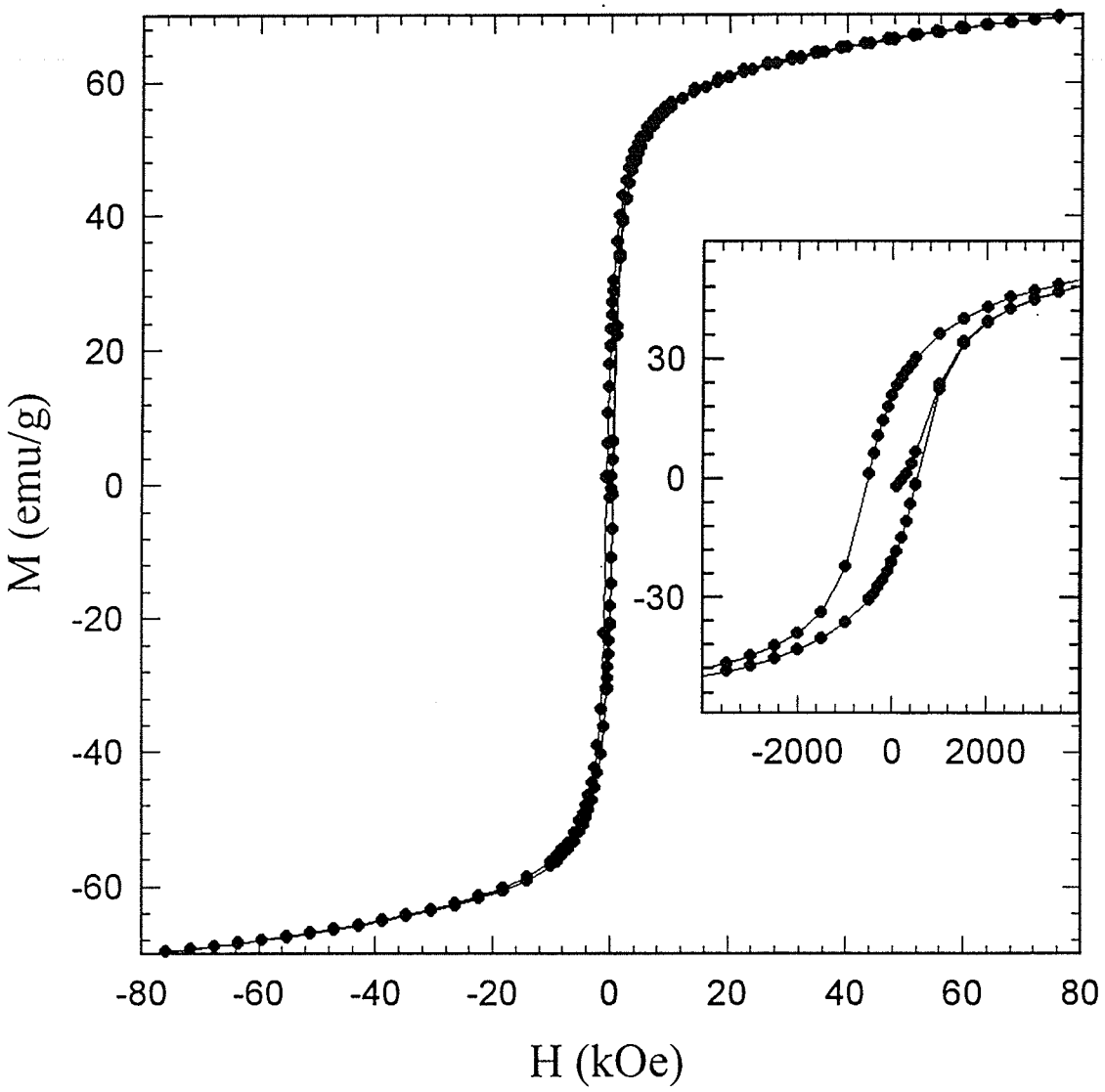

Figure 5.26: Hysteresis loop measured at 4.2 K for the Ar-annealed sample. The inset shows the relatively large coercive field of 500 Oe.

essential for the occurrence of ferromagnetism. The reduction in the number of Mn^{3+}/Mn^{4+} pairs thus weakens the ferromagnetic interaction and results in a lower Curie temperature as well as a lower magnetization, as indicated in figure (5.24) and (5.26).

5.4.3 Transport Behaviour

The above analysis of the magnetic data also provides a qualitative understanding of the dramatic change in the resistivity. Figure (5.27)a reproduces the temperature dependence of the zero-field and in-field resistivity for the untreated sample, which was already reported in detail previously in this chapter, while Figure (5.27)b presents the temperature dependence of the zero field resistivity for the Ar-annealed sample; the latter clearly displays insulating behaviour over the entire temperature range from 77 K to 300 K without any obvious anomaly near T_c. More details regarding the underlying conduction mechanisms both above T_c and below T_c are discussed below.

Magnetically disorderd regime ($T > T_C$)

The transport behaviour in the paramagnetic phase above T_c for $La_{1-x}Ca_xMnO_3$ ($x \sim 0.33 - 0.35$) has been studied previously [22, 26, 81, 87]. The resistivity data have been widely discussed in terms of a small polaron model, and such data have been shown to be well-fitted by the predictions of polaronic transport, viz. [89]

$$\rho(T) = \rho_0 T^n e^{E_a/k_B T} \tag{5.9}$$

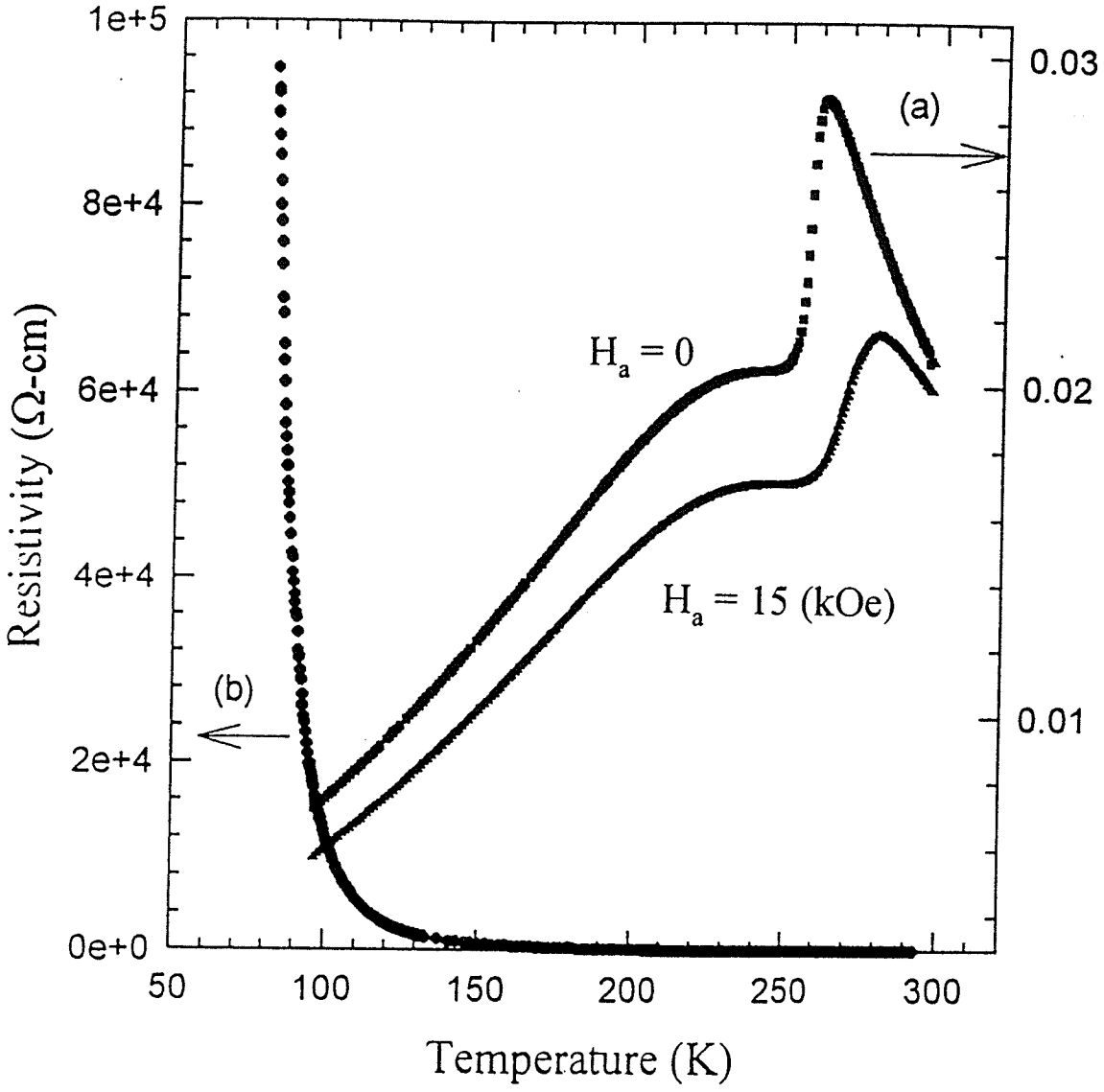

Figure 5.27: Resistivity plotted as a function of temperature for the Ar-annealed $La_{0.67}Ca_{0.33}MnO_3$ sample (b) and the untreated sample (a).

Table 5.2: Parameters characterizing small polaron fits in the paramagnetic regime.

$T > T_c$	Ar-treated sample			untreated sample		
	E_a(meV)	ρ_0 (Ω–cm)	Std Err	E_a (meV)	ρ_0 (Ω–cm)	Std Err*
$\rho = \rho_0 T \exp(E_a/k_B T)$	178.8	1.60×10^{-5}	0.028	89.0	2.15×10^{-6}	0.00028
$\rho = \rho_0 T^{3/2} \exp(E_a/k_B T)$	189.4	6.22×10^{-7}	0.030	105.0	6.76×10^{-8}	0.00025

* The low standard error reflects the small fitting range.

where E_a is the activation energy which is related to the polaron formation energy. In equation (5.9) n = 1 or 3/2 corresponds to the adiabatic and non-adiabatic situation respectively. The adiabatic limit means that the electronic motion is assumed to be much faster than the ionic motion of the lattice and in the non-adiabatic limit the electron does not move faster than the relevant optical-mode lattice fluctuation. Many investigations [22, 81] have been unable to conclusively differentiate the appropriateness of fits provided by these two choices for the index n, as in the situation here.

For the untreated specimen, comparable fits for n = 1 and for n = 3/2 are obtained by a least-squares fit of equation (5.9) to the present data. Based on the adiabatic assumption, Figure (5.28) reproduces the data contained in figure (5.27) in the form of $\ln(\rho/T)$ vs 1/T. The line - least squares fit - drawn in figure (5.28)

yields

$E_a = 89.0$ meV; $\rho_0 = 2.15\times10^{-6}\Omega$-cm/K; for $T > T_c$

These parameters, along with those characterizing the non-adiabatic fit and corresponding standard errors, are summarized in Table (5.2). Both sets of parameters are in good agreement with previously reported values, particularly thin film data [22]. This result is important in the present context since it demonstrates that the presence of grain boundaries in these bulk ceramic samples does not influence significantly the transport behaviour in this insulating regime. Hence the polaronic conduction reported here is considered to be intrinsic.

Recently the equation (5.9) with n = 1 has also been proposed as a form representing the resistivity of non-metallic phase-separated manganites [90], in which small ferromagnetic metallic droplets, or magnetic polarons, are considered to be embedded into the insulating antiferromagnetic matrix. Charge transport is assumed to be accomplished by electron transitions between droplets because the droplets (magnetic polarons) themselves are easily pinned by crystal lattice defects. The phase-separated state has been explored for the perovskite manganites with CMR experimentally and theoretically, here attempts are made to fit our experimental data to this model to verify its applicability, as discussed later.

For the Ar-annealed specimen, the experimental data is displayed in figure (5.29), where the upper insert shows these data over the entire temperature range in a form appropriate for non-adiabatic small polaron transport, i.e. $\ln(\rho/T^{3/2})$ vs T^{-1}. These data are markedly different from those in figure (5.28), especially at low temperatures below T_c. This figure demonstrates that the pre-

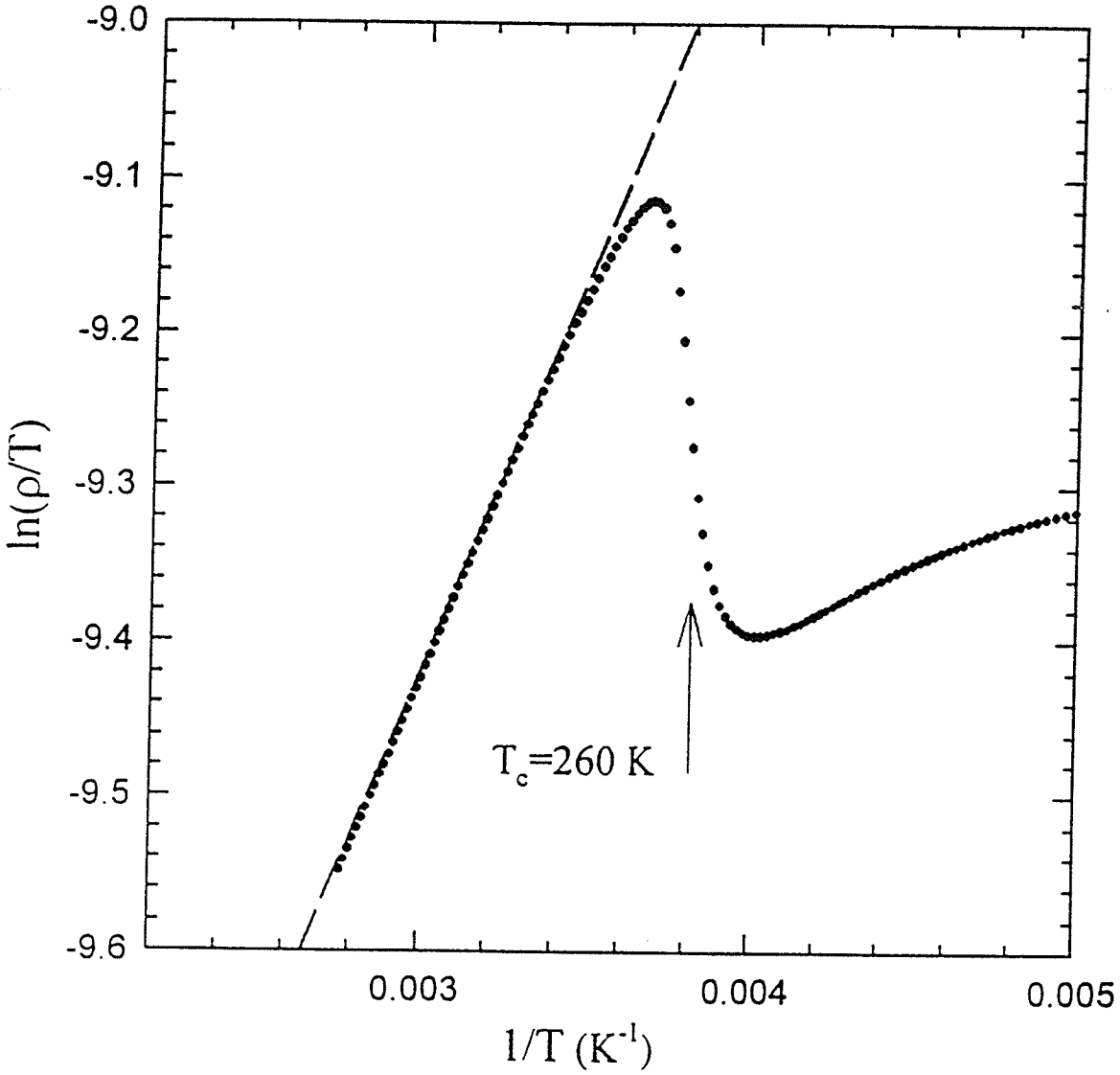

Figure 5.28: The plot of $\ln(\rho/T)$ versus 1/T in a form consistent with adiabatic small polaron transport for the untreated $La_{0.67}Ca_{0.33}MnO_3$ sample.

dictions for polaronic transport can be applied both above and below T_c. The data on this oxygen depleted specimen are also believed to be intrinsic despite the presence of grain boundaries, as evidenced by both the semiconducting character of these data over the entire temperature range examined and the same average grain size as in the untreated specimen. While it is impossible to separate grain boundary from intrinsic effects, indirect evidence is used to support the above contention. Referring to a comparable analysis [71] based on available oxygen self-diffusion coefficients for $La_{1-x}Sr_xMnO_3$ ($\sim 10^{-10}$ cm^2s^{-1} [91]), the diffusion length, resulting from the annealing procedure adopted here, is estimated to be over 100 μm. This is more than an order of magnitude larger than the average grain size, indicating the depletion of oxygen should occur throughout the entire grain, not preferentially from grain boundaries. This is reflected by the depression in T_c caused by the annealing procedure, a bulk effect, as well as by a decreased magnetoresistance discussed later, and it agrees with the results of deoxygenation effects in single-crystal $La_{0.85}Sr_{0.15}MnO_{3-\delta}$ [99]. In contrast, for the low temperature ferromagnetic metallic phase of untreated $La_{1-x}Ca_xMnO_3$, the low field magnetoresistance is strongly influenced by grain boundary scattering [69, 70].

Here the least-squares fits to equation (5.9), carried out in the paramagnetic regime, are again unable to distinguish conclusively between the adiabatic (n = 1) and non-adiabatic (n = 3/2) forms. The parameters deduced from such fits are also listed in Table (5.2). Despite the fact that these fitted data are comparable under both choices for the exponent n, further examination of the appropriateness of the fitting parameters, particularly ρ_0, enables the more appropriate model to

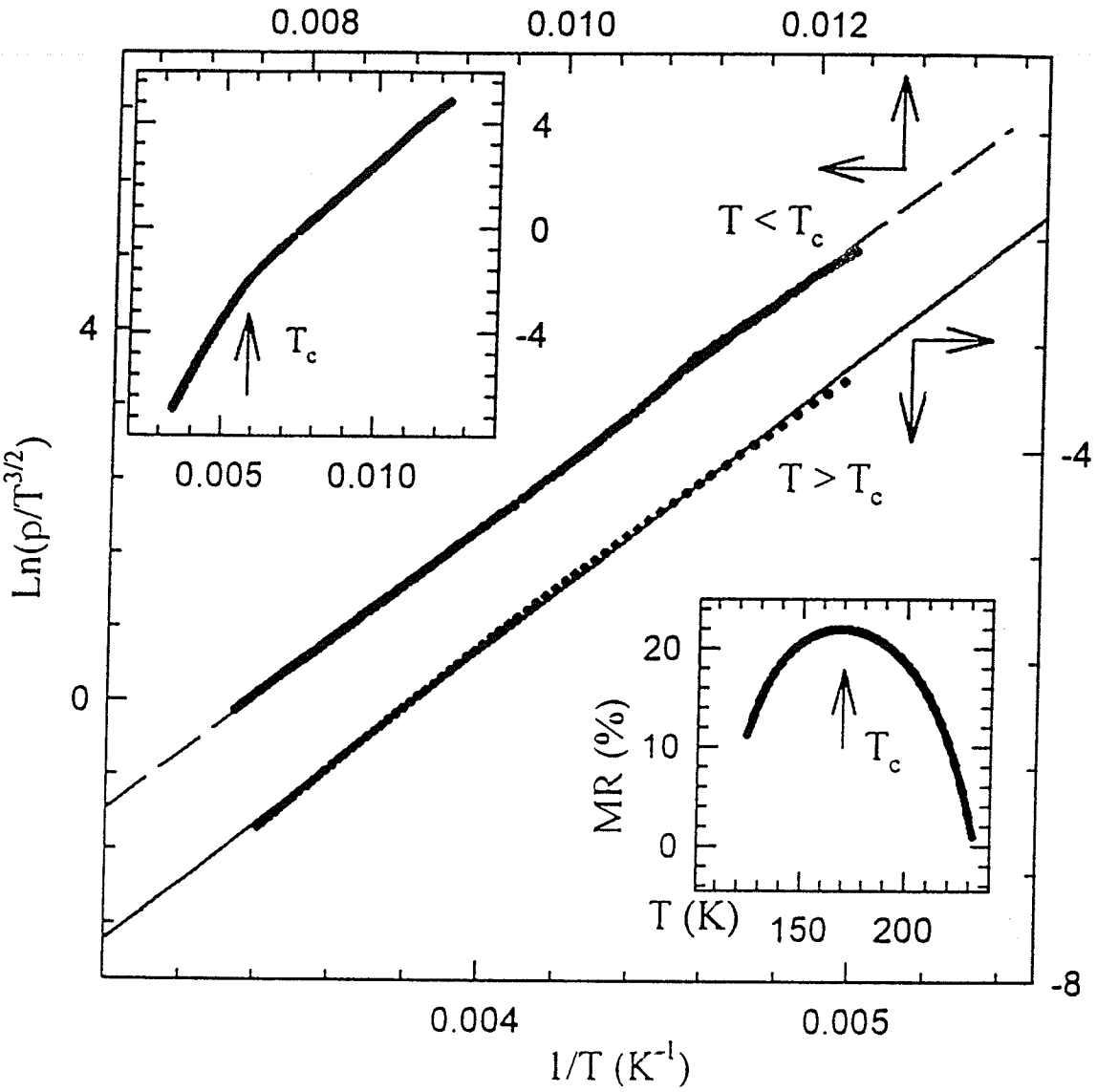

Figure 5.29: The plot of $ln(\rho/T^{3/2})$ versus 1/T in a form consistent with predictions for non-adiabatic small polaron transport. The upper inset shows these data over the entire temperature range, while the lower insert displays the variation of the magnetoresistance with temperature measured in a field of 1.5 Tesla.

be selected. This is demonstrated in the following analysis.

In the adiabatic limit, the prefactor ρ_0 has the form [22, 92]

$$\rho_0 = \frac{k_B}{g_d n a^2 e^2 \Omega_0} \tag{5.10}$$

In this equation the hopping distance, a, is taken as the separation between the nearest neighbour Mn ions; the carrier density, $n = 4x(1-x)/V$, includes the factor x(1-x) to account for the site occupation effects (with x being the hole/Mn^{4+} fraction and V the double-cell volume found from the listed lattice parameters); g_d is a numerical constant (≥ 1) reflecting the polaron hopping geometry, and Ω_0 is an attempt frequency, identified with a characteristic optical phonon frequency in the adiabatic limit. The corresponding expression for this prefactor in the non-adiabatic regime is [92]

$$\rho_0 = \frac{k_B}{n a^2 e^2} \cdot \frac{\hbar}{J^2} [\frac{4 E_a k_B}{\pi}]^{1/2} = \frac{k_B}{n a^2 e^2 \Omega_0 T^{1/2}} \tag{5.11}$$

this is valid when the electronic coupling factor J (the transfer matrix element) is much smaller than the polaron formation energy and also when the following inequality is satisfied

$$\Omega_0 = \frac{J^2}{\hbar} [\frac{\pi}{4 k_B E_a T}]^{1/2} << \omega_0 \tag{5.12}$$

where the characteristic optical phonon frequency ω_0 is generally in the range $10^{13} - 10^{14}$ Hz for such materials [92, 93].

In the picture of a phase-separation state [90], the parameter ρ_0 is found to

be

$$\rho_0 = \frac{k_B}{128\pi e^2 \nu_0 n^2 l^5} \tag{5.13}$$

where n is the polaron density (equal to the number of charge carriers introduced by doping), ν_0 is a characteristic magnon frequency and l a tunneling length. ν_0 is assumed to be of the order of the Fermi energy inside polarons, i.e. $h\nu_0 = k_B$T, with T estimated to be around 300 K, ν_0 is found to be 4×10^{13} Hz. Using the above equations and the calculated values for ρ_0, the parameters Ω_0 and l can be derived and compared with models assumptions. For the untreated sample equation (5.13) gives l values $\sim 1.8\mathring{A}$ and $1.36\mathring{A}$ for holes and electrons respectively. For the Ar-annealed sample, at T > T_c, l are $0.63\mathring{A}$ and $1.24\mathring{A}$; for T < T_c, $0.12\mathring{A}$ and $0.39\mathring{A}$ again for holes and electrons respectively. These values are obviously much smaller than that expected in the phase-separation model where the tunneling length is estimated to be $l \geq a_0 \sim 10\mathring{A}$ (a_0 is a polaron radius [100]), indicating the inapplicability of the model to current experimental results.

Next we examine the Ω_0. For the untreated sample, figure (5.28) shows the data plotted in a form consistent with adiabatic small polaron transport. Using the listed ρ_0 value for the adiabatic fits in Table (5.2) and taking $g_d = 1$, equation (5.10) produces $\Omega_0 = 4.5 \times 10^{13}$ Hz. Using the non-adiabatic approach, represented by equation (5.11), for a typical temperature T = 250 K, the value $\Omega_0 = 9 \times 10^{13}$ Hz is obtained. Both estimates fall within the range of 10^{13}-10^{14} Hz, typical values of optical-phonon frequencies for similar materials. This indicates that the adiabatic small polaron limit does provide an appropriate description

for this untreated sample. This is in agreement with the conclusion reached by previous measurements on this system at comparable doping levels, particularly data on thin films [22] [26] acquired in some cases over a wider temperature range extending up to 1200^0C [87].

By contrast, for the Ar treated specimen a similar analysis made by taking $\delta = 0.09$ (as discussed previously) produces values for Ω_0 of

$\Omega_0 = 10^{13}$ Hz for the adiabatic limit with $g_d \approx 1$.

$\Omega_0 = 1.6 \times 10^{13}$ Hz for the non-adiabatic regime with T = 250 K.

The above values of Ω_0 are close to the lower end of typical optical phonon frequencies, but they fall to lower values if higher values of g_d for polaronic hopping beyond nearest neighbors [87] are taken, or if the δ value estimated is indeed an upper limit. These reasons, complemented by the following discussion, suggest the applicability of the non-adiabatic form of equation (5.9) in this regime for this sample, and thus the form is used in figure (5.29).

Low temperature ferromagnetic ordered regime

While the above analysis on the small polaron mediated transport in the high temperature paramagnetic phase for the doped manganese perovskite systems agrees with the generally accepted picture, its applicability in the low temperature ferromagnetic regime, where no such consensus exists, is examined below. Prior to this discussion, other possible conduction mechanisms are examined in addition to equation (5.9). Two forms have often been used to discuss transport

data in related systems. The first of them uses

$$\rho(T) = \rho_0 e^{(T_0/T)^{1/4}} \tag{5.14}$$

which has been associated with both phonon-assisted hopping for temperatures at or below half the Debye temperature θ_D [92] (appropriate for this lower temperature region) and variable range hopping [93] in which T_0 measures the localization length. The second has the following form

$$\rho(T) = \rho_0 e^{E_a/k_B T} \tag{5.15}$$

a simple exponential behaviour which might result from a form of charge ordering, although the recent model of Rakhmanov et al. for non-metallic conduction in a phase separated enviroment suggests the form discussed in equation (5.9). Nevertheless, as far as the present system is concerned, the electronic phase separation picture of Dagotto et al [94] suggests that electron-rich antiferromagnetic insulating regions and hole-rich ferromagnetic conducting regimes might coexist below the ordering temperature. Whether or not this is physically applicable to the current ferromagnetic semiconducting behaviour is debatable. However it has been the subject of recent theoretical and experimental discussion [95].

The current data are analyzed below regarding the applicability of the above models. It is found that equation (5.14) is quite inappropriate for fitting these data, as shown in figure (5.30); this is similar to the conclusion reached for an untreated sample for temperature well above T_c [87]. Although equation (5.15)

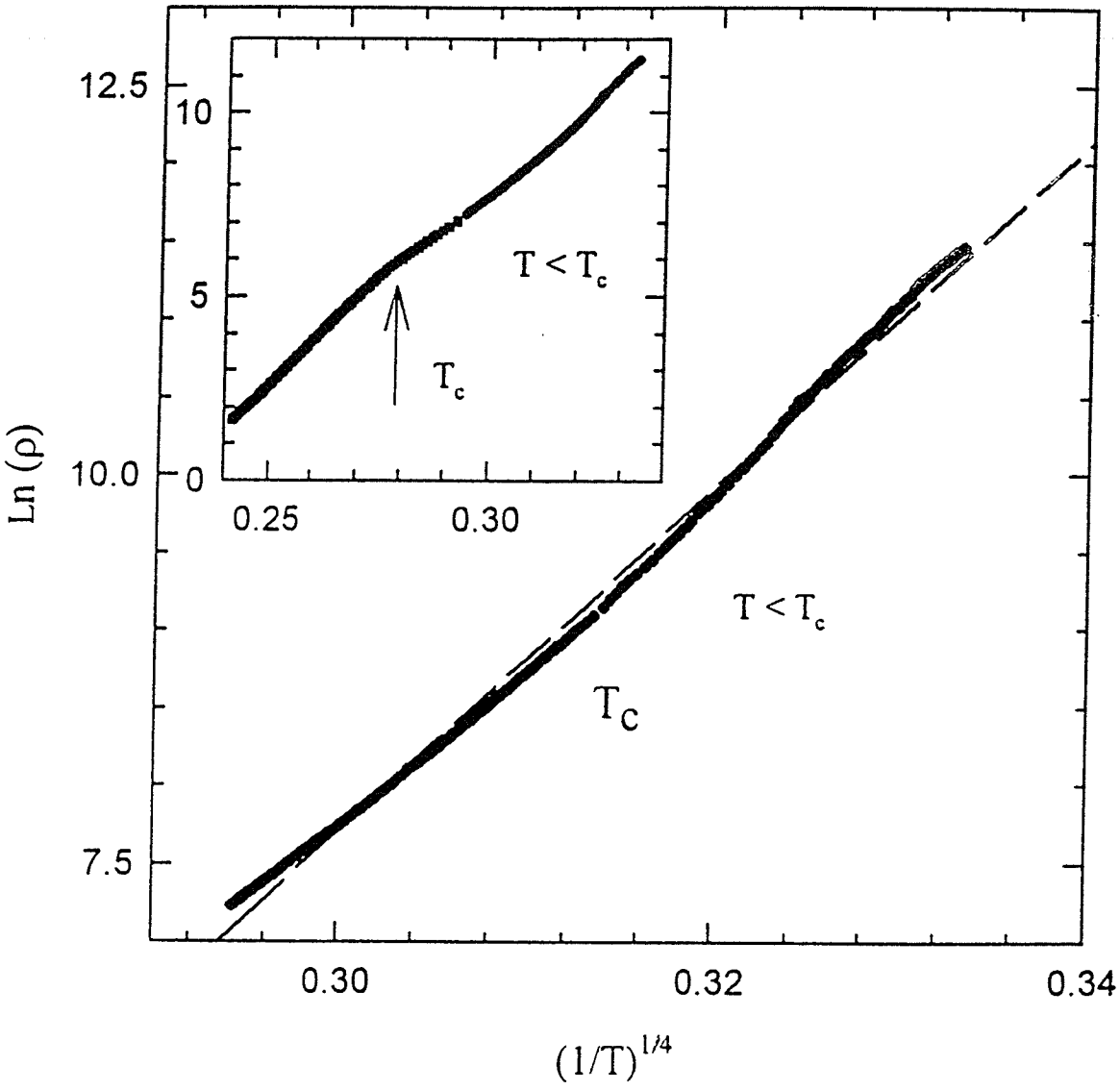

Figure 5.30: The plot of $\ln \rho$ versus $(1/T)^{1/4}$ at $T < T_c$. The straight line fitted by least-squares fit is obviously not appropriate.

Table 5.3: Fitting parameters extracted for the ferromagnetic phase.

$T < T_c$	Ar-treated sample		
	E_a (meV)	ρ_0 (Ω–cm)	Std Err
$\rho = \rho_0 T \exp(E_a/k_B T)$	86.49	5.53×10^{-3}	0.025
$\rho = \rho_0 T^{3/2} \exp(E_a/k_B T)$	90.95	3.28×10^{-4}	0.024
$\rho = \rho_0 \exp(E_a/k_B T)$	77.56	1.57	0.029
$\rho = \rho_0 \exp(T_0/T)^{1/4}$	1.29×10^{7}	8.51×10^{-12}	0.080

provides a significantly better fit, it is still statistically inferior to those provided by equation (5.9) with either choice for the exponent n. Table (5.3), for completeness, lists the characteristic parameters fitted for all models in the regime $T < T_c$. Our subsequent discussion focuses, however, on the small polaron approaches due to the superior quality of fits. Prior to this, however further discussion on the reasonable fit provided by equation (5.15) is needed. From the point of view of an inhomogeneous electron phase segregation picture, the occurrence of a ferromagnetic ground state would probably reflect the formation of an infinite, percolating ferromagnetic cluster, which was originally proposed for the AuFe system [96]. While some approaches suggest that such phase separation can occur with equal density clusters, the ferromagnetic regions still retain metallic characteristics; such features are predicted to appear near $x \approx 0.5$ [97]. At the lower doping levels of the present experiment the hole rich ferromagnetic metallic

regions would predominate. Since the ranges of the interactions responsible for magnetic coupling and charge transport appear comparable in these systems, the presence of an infinite, percolating cluster of this type would be inconsistent, in general, with the continuation of semiconducting behaviour (the occurrence of a ferromagnetic insulating phase in the specific case of $La_{1-x}Sr_xMnO_3$ for x $\approx$ 0.1 notwithstanding [98]).

Next, an examination of the parameters derived from the fits to equation (5.9) is carried out. It is clear that the activation energy E_a decreases on entering the ferromagnetic phase for both the adiabatic and non-adiabatic models. In both approaches $E_a^p \approx 2E_a^f$. This marked decrease in the characteristic energy E_a in the ferromagnetic regime likely reflects a significant magnetoelastic influence on polaron formation and its subsequent dynamics. The adiabatic fit to equation (5.9) produces the ρ_0 value listed in table (5.3), and using equation (5.10), the corresponding estimate for Ω_0 is 3×10^{10} Hz when $T < T_c$. For the non-adiabatic limit, using equation (5.11) and taking T $\approx$ 100 K, yields a comparatively low Ω_0 value of 5×10^{10} Hz when $T < T_c$. Both Ω_0 parameters are three orders of magnitude less than characteristic optical frequencies ω_0 under the assumption that the numerical values of other parameters in equation (5.10) and (5.11) remain unchanged. These Ω_0 values satisfy the inequality of equation (5.12). Thus, the non-adiabatic limit is applicable to this Ar annealed sample and the corresponding form of equation (5.9) is used to fit the data, shown in figure (5.29).

While the above results show the changes in the physical characteristics

represented by both E_a and the dynamics associated with polaronic motion in this ordered phase, the related characteristic parameter, the coupling constant J, also needs to be examined. When the non-adiabatic model expression (equation (5.11)) is appropriate, the ρ_0 and E_a values listed in Table (5.2) and Table (5.3) can be used to estimate this coupling factor from the equation (5.11). The value of J is about 28 meV for $T > T_c$, falling to about 1 meV while $T < T_c$. This low value for $\mid J \mid$ at $T < T_c$ directly reflects the above Ω_0 estimate. Both estimates satisfy the inequality $\mid J \mid << E_a$, providing support for the validity of equation (5.11) in the high temperature disordered and the low temperature ordered phase.

Our estimate for J at temperatures $T > T_c$ is comparable to those calculated from available high temperature data [92] on $LaMnO_3$ ($\mid J \mid = 26$ meV) and $LaCrO_3$ ($\mid J \mid = 8$ meV) by applying the non-adiabatic formalism. In this latter context it is interesting to note that the corresponding estimates for E_a (about 190 meV and 180 meV respectively) are also close to that found for the Ar treated specimen above T_c ($E_a \approx 189$ meV). The resistivity of $LaCrO_3$ is however close to three orders of magnitude larger than that for $LaMnO_3$ which, given the similarity in the activation energy E_a, is only partially accounted for by a reduced value for the electronic coupling factor $\mid J \mid$ in the former. Different polaron concentrations are believed to play an important role in these two systems [92]. It is suggested here that a substantial drop in the small polaron concentration occurs in the Ar treated sample below T_c. A decrease in E_a below the transition temperature naturally leads to the increases in ρ_0 in equation (5.9). However,

the associated marked decrease in Ω_0 (and hence | J |) occurs only if the polaron density remain unmodified in the ordered phase. This is unlikely according to the above discussion, and the point raised below.

One posssible physical picture of the processes occurring in the system is provided by the bipolaron model [8]. The bipolaron model has been developed to explain transport behaviour in doped perovskites and the associated colossal magnetoresistance (CMR). In this model, the metal-insulator transition is attributed to immobile bipolar formation in the paramagnetic region, the number density of immobile bipolar increases with decreasing temperature. When temperature becomes lower than T_c, the emergence of an exchange field results in polaron pair breaking, at least spin singlet pairing breaks up. This leads to a dramatic increase in the free polaron density, thus metallic conduction behaviour occurs although in the metallic phase of doped manganese perovskites this is characterized by polaronic tunneling rather than hopping. However, when semiconducting behaviour persists into the ordered ferromagnetic state, spin triplet rather than spin singlet bipolarons might be formed; these would survive below T_c. The number density of spin triplet would not decrease dramatically, in contrast to the case of spin-singlet bipolarons disassociating itself into single free polarons. This is schematically illustrated in figure (5.31). The observation of moderate (not colossal) magnetoresistance is in agreement with such a proposal. In the present context triplet pairing would increase the energy gap between the triplet bound pair and the free polaron below T_c shown in figure (5.31), so that the density of the single polaron would continue to fall below T_c as more polarons occupy the

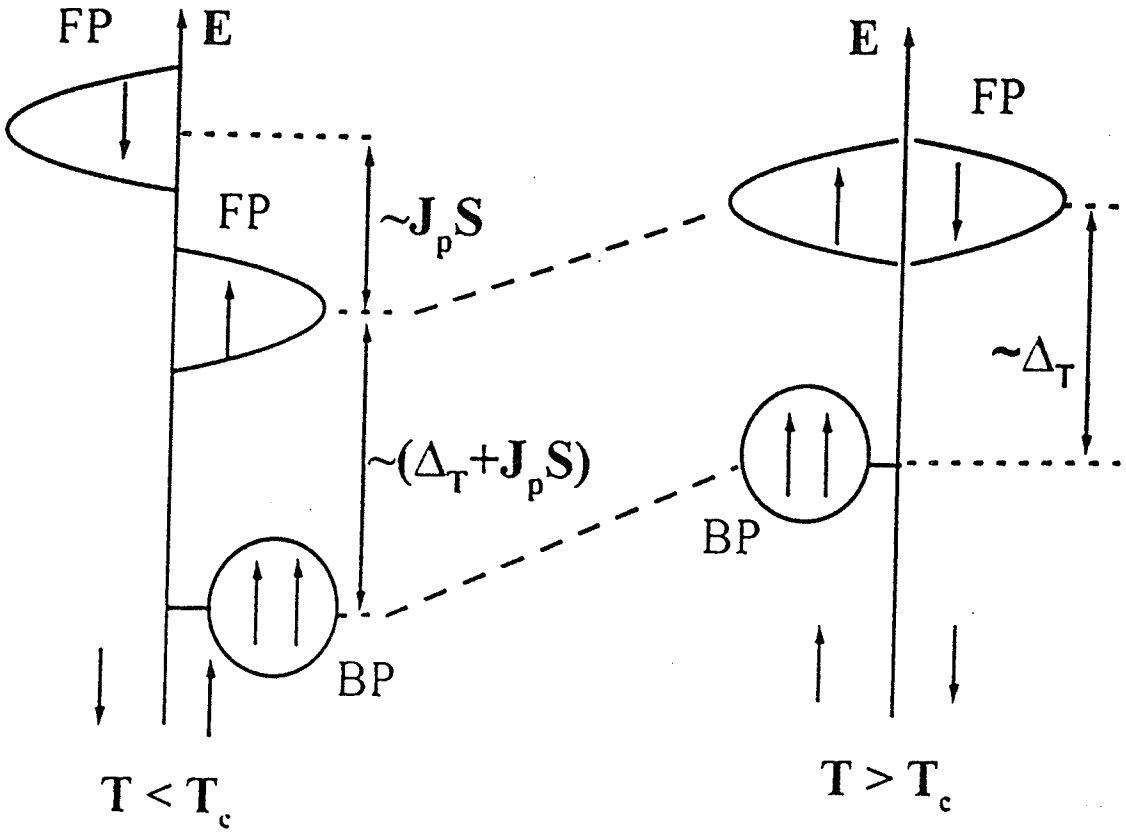

Figure 5.31: A schematic band structure illustrates the density of states for spin-up (↑) and spin-down (↓) free polaron (FP) and triplet polaron bound pairs (BP) in the ferromagnetic ($T < T_c$) and paramagnetic ($T > T_c$) regimes. Δ_T represents the binding energy of the triplet, while the exchange interaction (J_p) of polarons with Mn core spins (S) causes the energy difference between the triplet pair and the free polaron bands to increase below T_c, resulting in thermal depopulation of the latter.

lower triplet state. Such a decrease would mean that in the ferromagnetic state Ω_0 (and hence | J |) would takes values closer to those found in the paramagnetic region due to the decreased free polaron density. While changes in Ω_0 and | J | in the ordered phase are reasonable, changes in these parameters by several orders of magnitude appear less likely. Additionally, the underlying mechanism producing such changes is not clear currently, bipolaron formation therefore might provide more physical picture for this change.

Summary and conclusions

The transport and magnetic data on the Ar annealed $La_{0.67}Ca_{0.33}MnO_3$ are analyzed in detail in both the ordered ferromagnetic phase as well as the disorderd paramagnetic phase. The parameters extracted from the fit to a few models indicate that such transport data on the Ar annealed $La_{0.67}Ca_{0.33}MnO_3$ are generally consistent with the predictions of non-adiabatic small polaron hopping, as opposed to adiabatic hopping or tunneling with a phase-separated picture. The results also provide indirect support to the modeling of the metal-semiconducting transition and CMR in doped perovkites by polaronic behaviour.

5.5 The Magnetic and Electrical Transport Properties of the $La_{1-x}Mg_xMnO_3$ System

In this section experimental results for $La_{1-x}Mg_xMnO_3$ with doping levels, x, ranging from 0.05 to 0.6 will be presented. Mg^{2+} is a small ion in comparison with Ca^{2+} and Sr^{2+}, and it is interesting to investigate how the small average A-site radius, $< r_A >$, affects the magnetic and transport properties. Previous studies of this effect - particularly in the $La_{2/3-\delta}Y_\delta Ca_{1/3}MnO_3$ system through the progressive replacement of La by Y at constant (optimal) Ca doping [28] - revealed that this caused a progressive depression of the temperature of the metal-insulator transition, which is generally considered to be a direct consequence of a reduction in the Mn-O-Mn bond angle below its ideal value of 180^o. Correspondingly the $Mn(e_g)$ - O(2p) bandwidth decreases with the mean A-site radius $< r_A >$. Such effects are expected to be considerably more dramatic in the $La_{1-x}Mg_xMnO_3$ system due to the much smaller Mg^{2+} ion, as is reported below.

$La_{1-x}Mg_xMnO_3$ samples were prepared from stoichiometric quantities of ultra-pure La_2O_3, MgO (type FM) and MnO_2 (99%) using the standard ceramic techniques discussed previously in chapter 4. Here the samples were heated at 800^oC in air for 24 hours, then ground in a mortar and pestle and pressed into disks, which were then sintered for 48 hours in air at 1200^oC. Room temperature X-ray diffraction spectra using Cu K_α radiation were collected from 2θ values from 20 - 80^o in steps of 0.05^o using an automated Philips PW 1710 system incorporating a Bragg-Brentano goniometer equipped with incident and diffracted beam Soller slits. Figure (5.32) shows a typical example of the x-ray diffraction

pattern for $La_{0.95}Mg_{0.05}MnO_3$, confirming a single phased orthorhombic structure (Pbnm) with lattice constants summarized in Table (5.4) (together with all other samples), Also tabulated are the ferromagnetic ordering temperatures, T_c, paramagnetic Curie temperatures, θ, and the effective moments and maximum zero field susceptibilities, χ (0,T_H), the paramagnetic Curie temperatures and effective moments were obtained from a Curie-Weiss law fit to the measured susceptibility for temperatures between T_c and 400 K.

Ac susceptibility, dc magnetization and electrical transport data were collected on samples of approximate dimension $(1 \times 1 \times 7)$ mm^3. The magnetic data were acquired as a function of both temperature and field as discussed previously. Transport measurements were carried out using a standard 4-probe technique from liquid nitrogen temperature to room temperature; the semiconducting nature of samples prevented measurements at lower temperature.

Figures (5.33) and (5.34) show the zero field susceptibility variation with the temperature for all samples studied. The ac susceptibility in various static (dc) biasing fields, H_a, was measured as a function of temperature near the ferromagnetic ordering temperature, T_c, as shown in figures (5.35) and (5.36). The data for samples with x $\leq$ 0.4 show a similar critical behaviour which has the characteristics of a continuous (second order) phase transition, evident with the emergence of the critical peaks of the form discussed previously; this will be reviewed first. In contrast, the samples with x = 0.45, 0.5, 0.6 not only exhibit the paramagnetic/ferromagnetic transition features (critical peaks) at higher temperature, but also second and third peaks appearing in the low temperature region,

Table 5.4: Lattice parameters, distortion parameters $\epsilon_c = \mid 1 - \frac{c\sqrt{2}}{a+b} \mid \times 10^3$, ferromagnetic ordering (T_c), paramagnetic Curie temperature (θ), Hopkingson maximum susceptibility ($\chi(0, t_H)$) and the effective moments (P_{eff})

X	Lattice Parameters (Å)	ε_c	$\chi(0,T_H)$ (emu/g-Oe)	θ (K)	$P_{eff}(\mu_B)$	T_c(K)
X=0.05	a=5.4907	25	0.13	170	6.2(4)	147.2
	b=5.7097					
	c=7.7254					
X=0.1	a=5.5256	33	0.34	202	5.2(7)	154.5
	b=5.7491					
	c=7.7142					
X=0.2	a=5.5367	23	0.22	187	5.1(0)	139.5
	b=5.7524					
	c=7.8012					
X=0.33	a=5.5301	23	0.09	171	4.4(0)	118.0
	b=5.7566					
	c=7.8017					
X=0.4	a=5.5311	21	0.19	151	4.6(0)	114.8
	b=5.7206					
	c=7.7897					
X=0.45	a=5.5163	20	0.11	149	4.5(7)	98.5
	b=5.7190					
	c=7.7869					
X=0.5	a=5.5015	19	0.06	162	4.5(0)	79.0
	b=5.7174					
	c=7.7841					
X=0.6	a=5.5169	23	0.03	126	4.3(2)	46.0
	b=5.7437					
	c=7.7853					

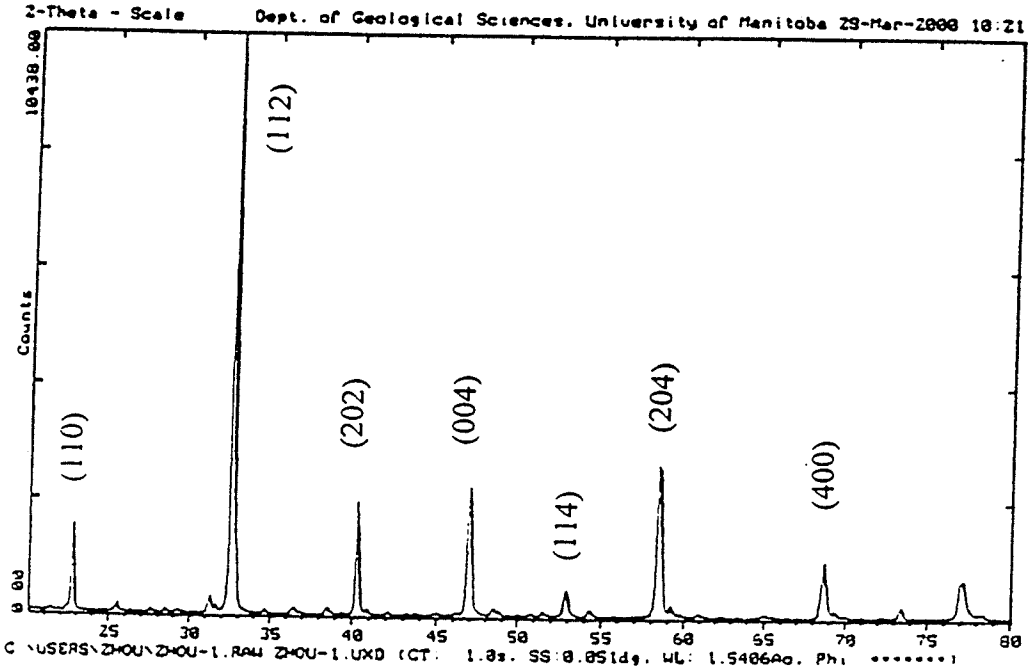

Figure 5.32: X-ray diffraction pattern for $La_{0.95}Mg_{0.05}MnO_3$.

reminiscent of reentrant behaviour from a ferromagnet to a spin-glass state. This will be discussed later in this section.

5.5.1 Hole-doped $La_{1-x}Mg_xMnO_3$ for x$\leq$ 0.4

Magnetic Properties for x = 0.05 sample

While all samples have been subject to detailed analysis, the x = 0.05 specimen - being the first in the series - was the most extensively examined. Its response is thus the first to be discussed. As is shown in Figure (5.33) (a), the susceptibility, measured in zero biasing field on warming with a driving field of amplitude of 30 mOe and frequency of 2.4 kHz, is plotted as a function of temperature. With decreasing temperature, the susceptibility increases rapidly through the ferromagnetic transition temperature, T_c, (~150 K) before peaking at the Hopkinson maximum and then decreases monotonically. Compared with $La_{0.67}Ca_{0.33}MnO_3$ and the pyrochlore discussed previously, this decrease in χ below T_c is much more rapid. The origin of the Hopkinson or principal maximum was discussed previously and will not be repeated here. Figure (5.35) (a) shows the ac susceptibility plotted against temperature in a range of superimposed static biasing fields between 400 and 3000 Oe (both the static and the ac driving field were applied along the largest sample dimension). The critical peak can be clearly seen and shows the same behaviour as discussed for the pyrochlore, from which magnetic critical exponents can be estimated. Figure (5.37) displays the peak temperature, T_m, against $H_i^{1/(\gamma+\beta)}$, where H_i ($H_i = H_a - NM$ in conventional notation) was determined from the measured magnetization M in the field, H_a,

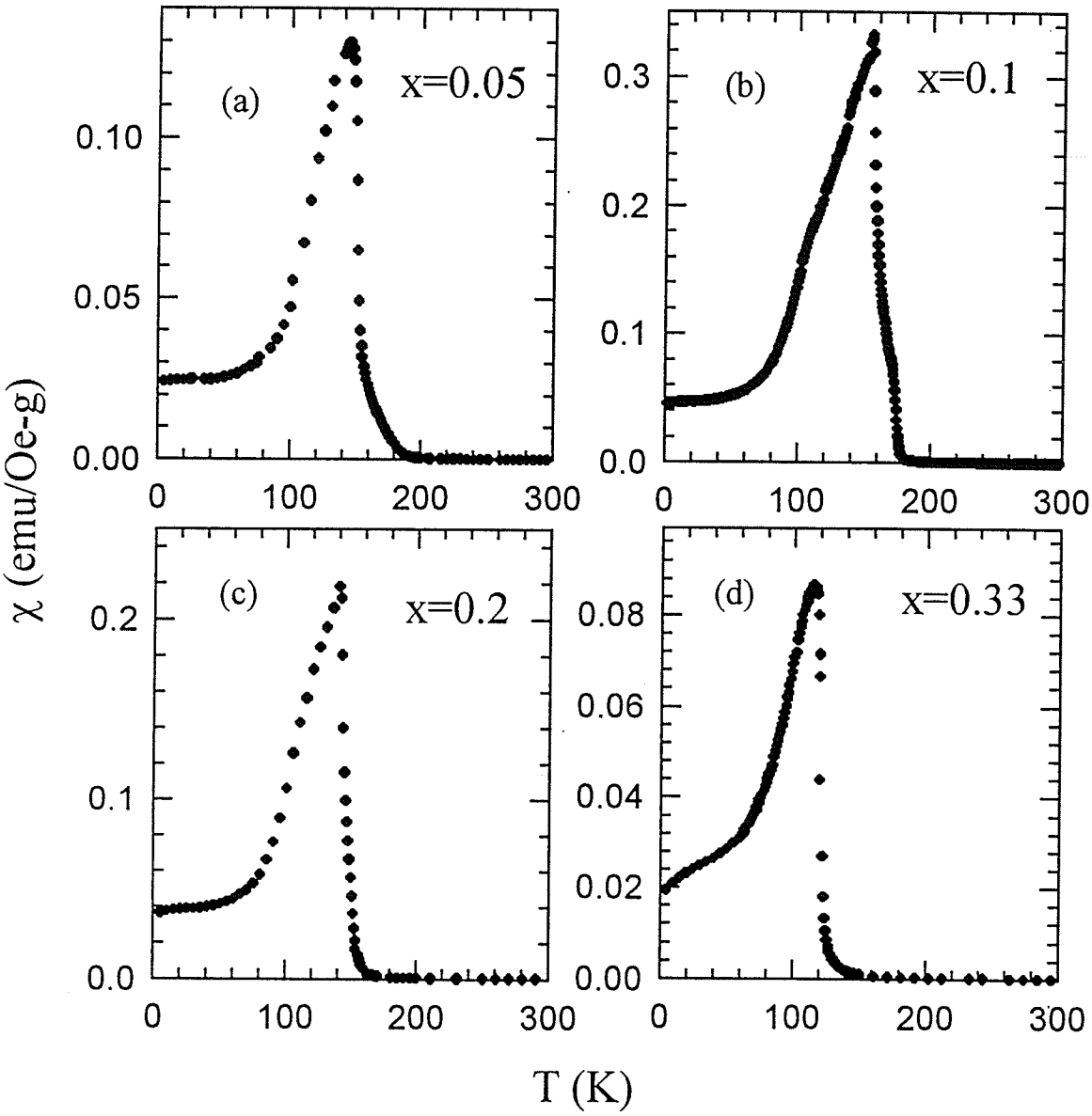

Figure 5.33: The temperature dependence of the zero-field susceptibility for the samples $La_{1-x}Mg_xMnO_3$ with x = 0.05, 0.1, 0.2, 0.33.

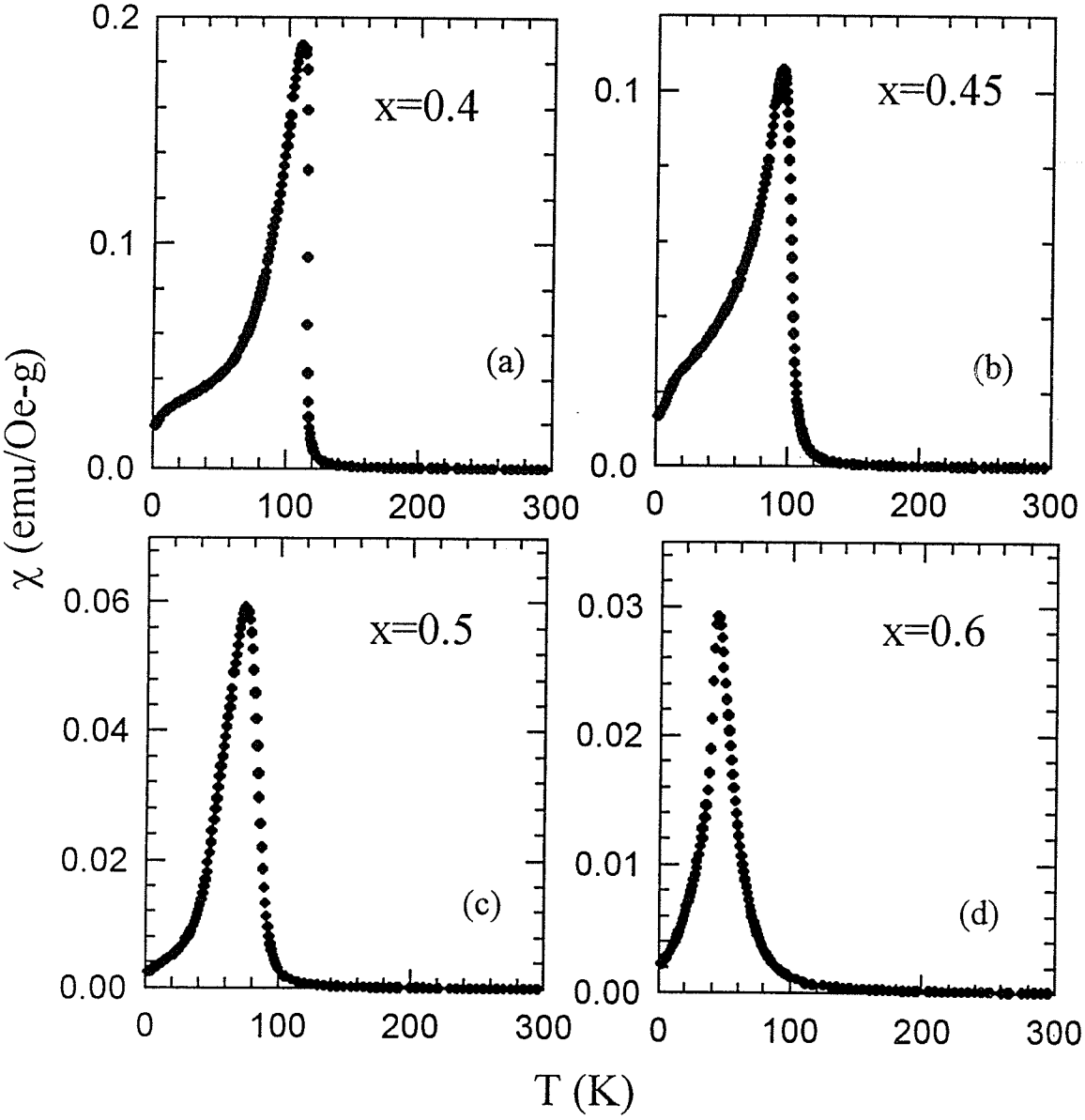

Figure 5.34: The temperature dependence of the zero-field susceptibility for the samples $La_{1-x}Mg_xMnO_3$ with x = 0.4, 0.45, 0.5, 0.6.

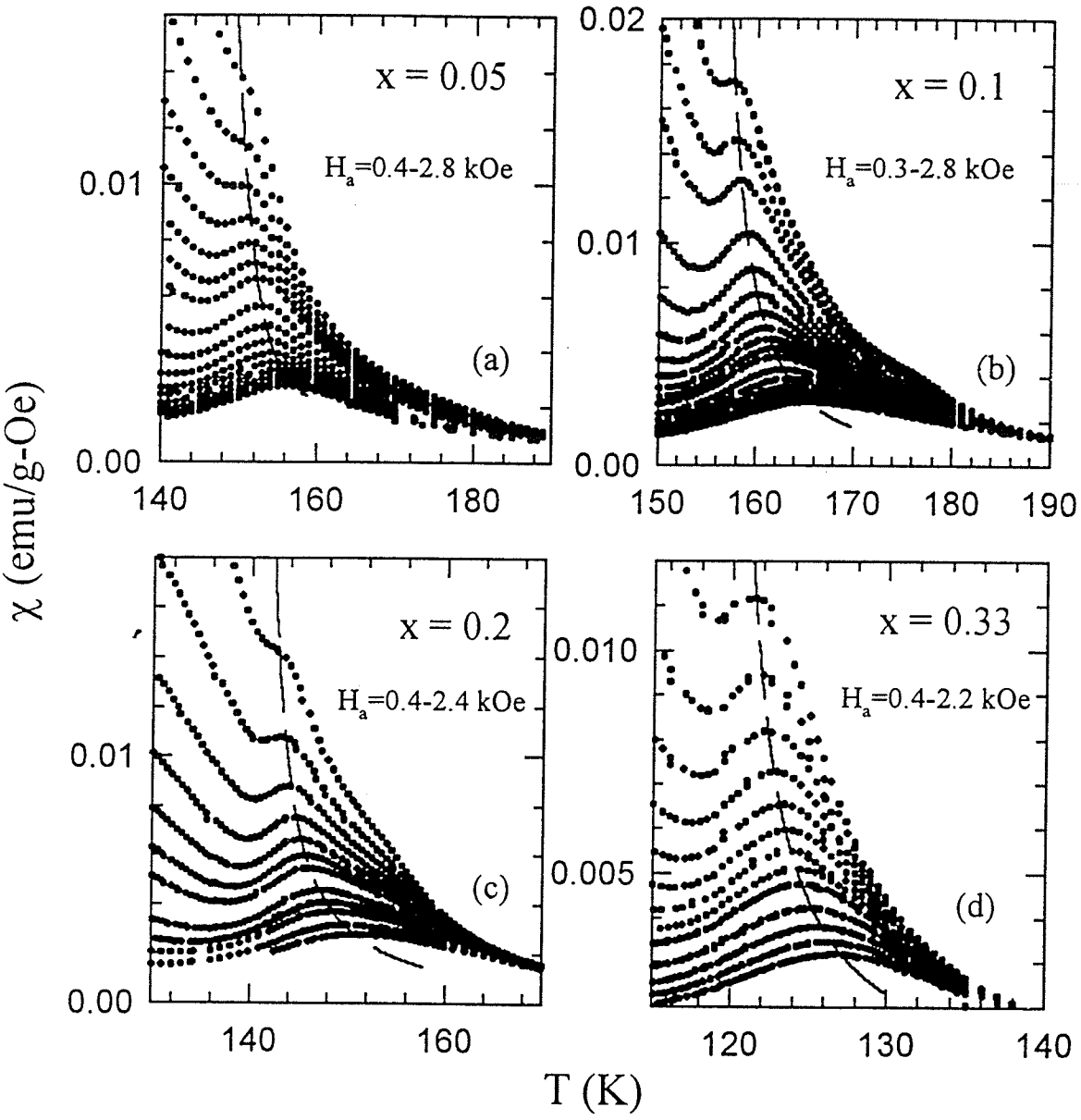

Figure 5.35: The temperature dependence of the field-dependent susceptibility for samples $La_{1-x}Mg_xMnO_3$. Fields increase from top to bottom over the range shown. The dashed line denotes the crossover line.

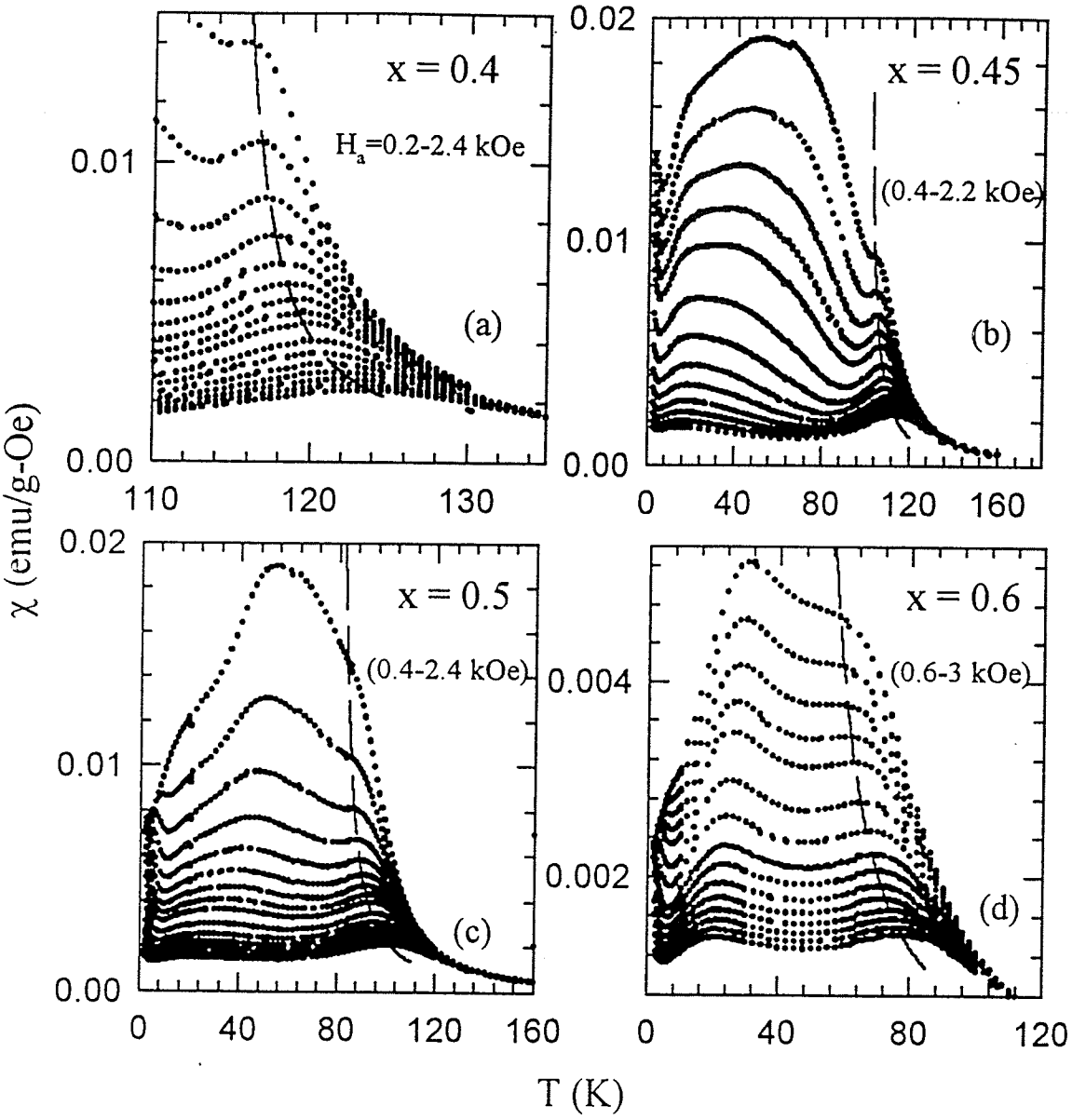

Figure 5.36: The temperature dependence of the field-dependent susceptibility for samples $La_{1-x}Mg_xMnO_3$. Fields increase from top to bottom over the range shown. The dashed line denotes the crossover line.

at temperature, T_m; N was found from the slope of the low field shearing curves near T_c, as shown in the inset. The critical temperature, T_c, was estimated to be 147.2 ($\pm$ 0.2) K. Figure (5.38) confirms the applicability of equation (3.27); the least squares fit to a straight line (power law) yields $\gamma + \beta = 1.75$ ($\pm$ 0.05) ($400 \leq H_a \leq 3$ kOe). This cross-over exponent is in excellent agreement with Heisenberg model predictions. Figure (5.39) shows a double logarithmic plot of the peak susceptibility, $\chi(h, t_m)$, (corrected for background and demagnetizing effects) against the reduced peak temperature, t_m. The straight line (least squares) fit shown corresponds to $\gamma = 1.39(\pm 0.03)$ ($t_m \geq 2 \times 10^{-2}$). The inset in figure (5.39) shows the temperature dependence of the effective Kouvel-Fisher susceptibility exponent deduced directly from the zero-field susceptibility, viz: $\gamma^*(t) = d(\ln \chi(0,t)/d\ln(t)$. For temperatures $t \geq 3 \times 10^{-2}$, this effective exponent falls monotonically with increasing temperature from a value of $\sim$1.34 towards the mean-field value of 1.0. Below $t \simeq 3 \times 10^{-2}$ the failure of the zero-field measured susceptibility to approach the demagnetization-factor-limited value precludes a reliable estimate of $\gamma^*(t)$ to be found from $\chi(0,t)$ in this region. The dashed line drawn in this inset for lower temperatures connects these $\gamma^*(t)$ data with the Heisenberg model value found from the field-dependent susceptibility peak data discussed above.

Figure (5.40) reproduces a double logarithmic plot of the critical peak amplitude, χ_m, against the internal field. The straight line drawn in this figure is a least squares fit to these data, the slope yields $\delta = 4.75(\pm 0.15)$ ($400 \leq H_a \leq 3$ kOe). This confirms the power-law prediction (equation (3.28)) and is in excellent

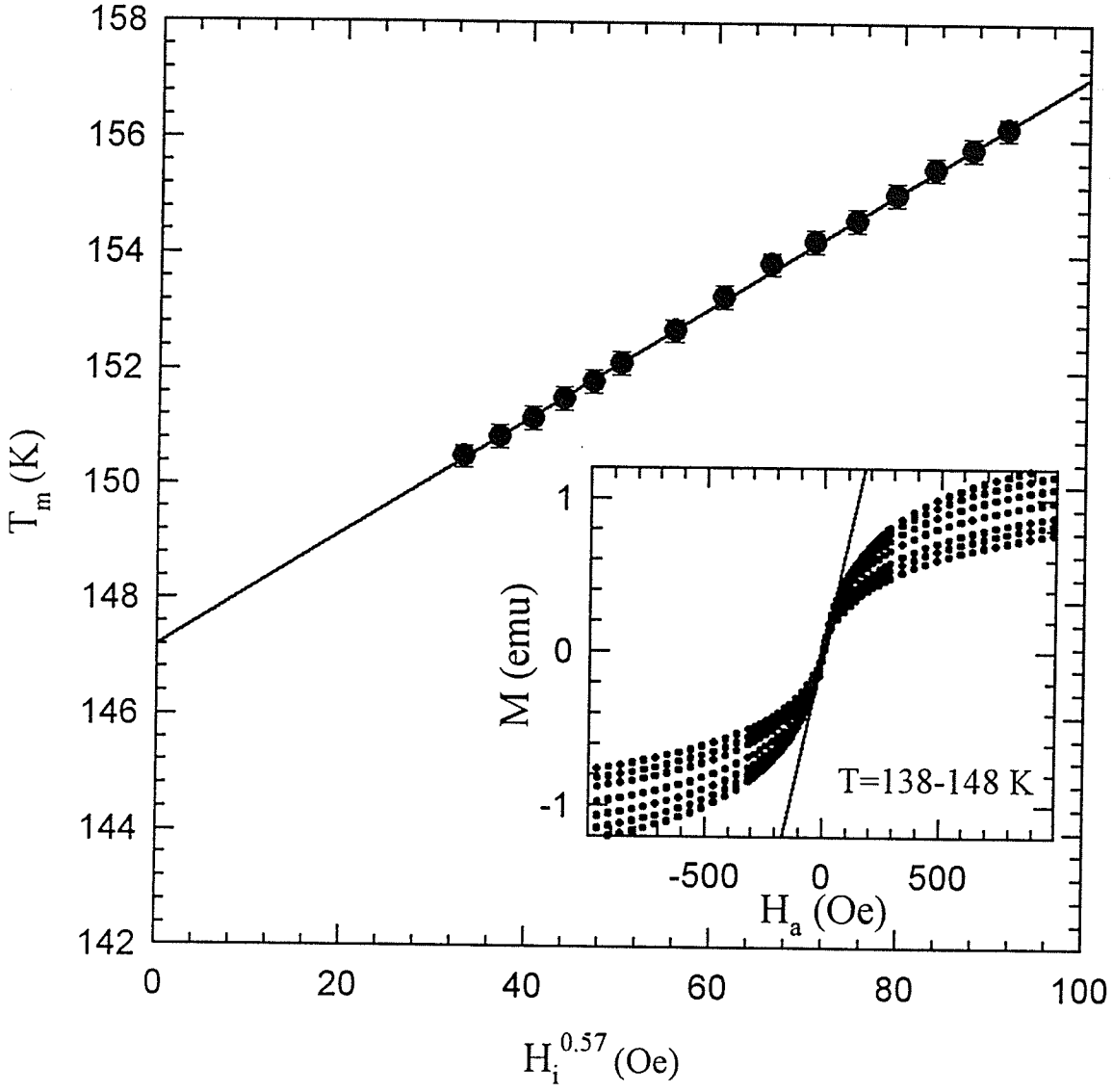

Figure 5.37: The peak temperature plotted against the internal field to the power 0.57 from which T_c is estimated as 147.2 ($\pm$0.2) K. The inset shows the so-called shearing curve measured in low fields near T_c over the temperature range shown. The line drawn is used to estimate the demagnetization factor.

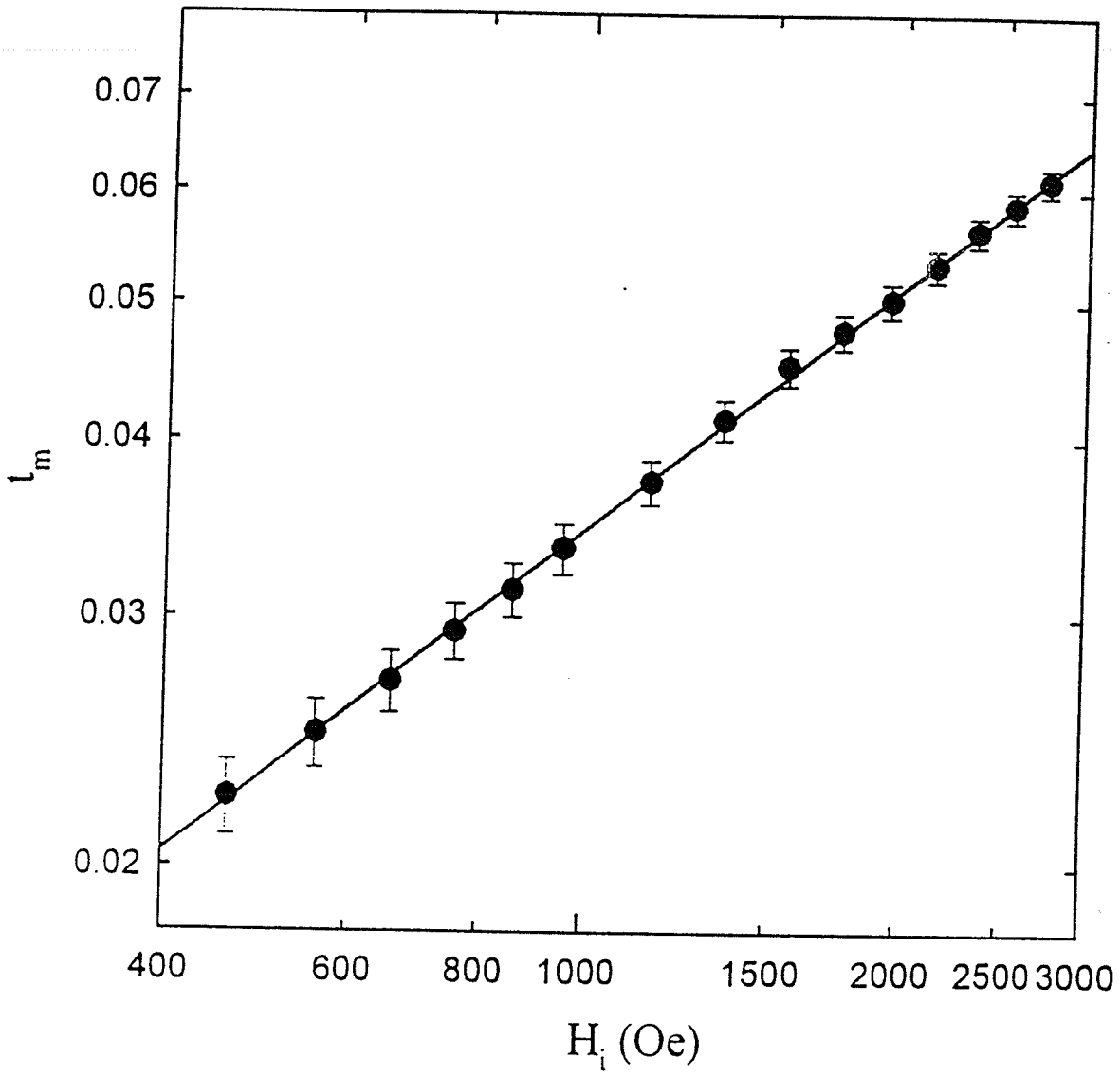

Figure 5.38: A plot of the susceptibility peak temperature, t_m, against the corresponding internal field, H_i (Oe), on a double logarithmic scale. The straight line confirms the power law prediction of equation (3.27) and yields $\gamma + \beta = 1.75$ (± 0.05).

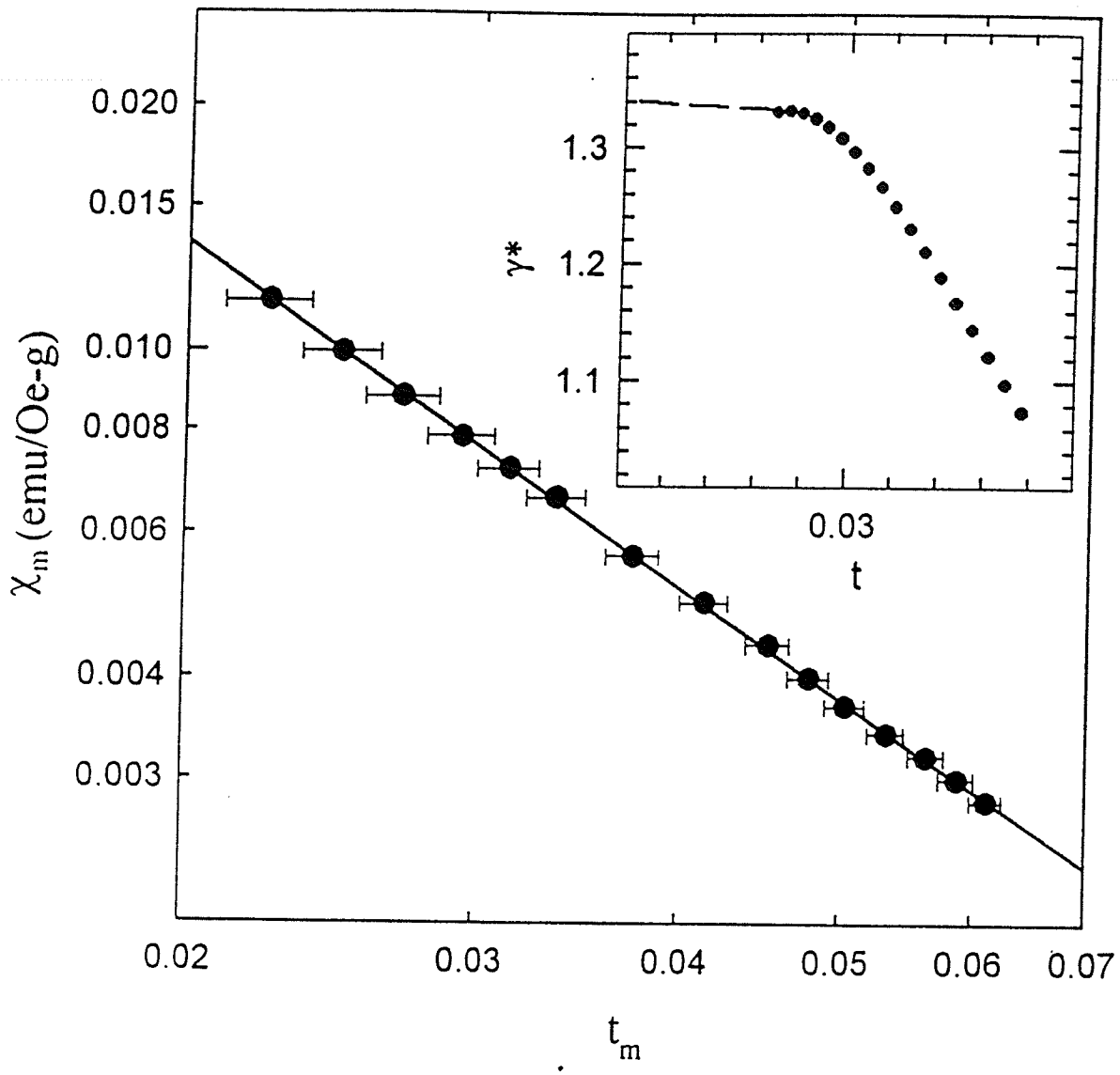

Figure 5.39: The peak susceptibility plotted against the reduced peak temperature on a double logarithmic scale, the slope of the line fitted yields $\gamma = 1.39$ (± 0.03). The inset gives the effective Kouvel-Fisher susceptibility exponent.

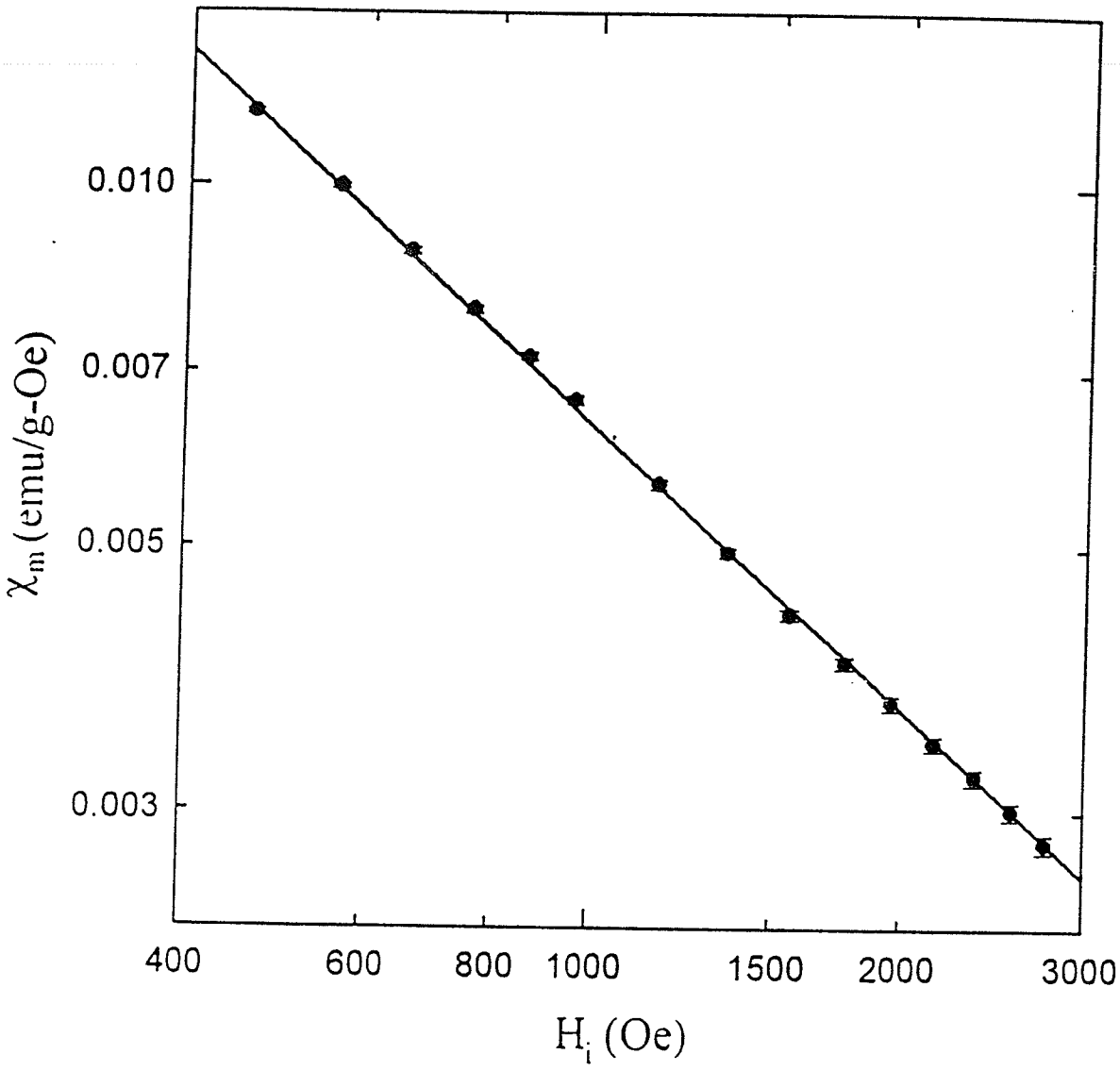

Figure 5.40: The peak susceptibility plotted against the internal field on a double logarithmic scale. The straight line fit gives a value of $\delta = 4.75(\pm 0.15)$.

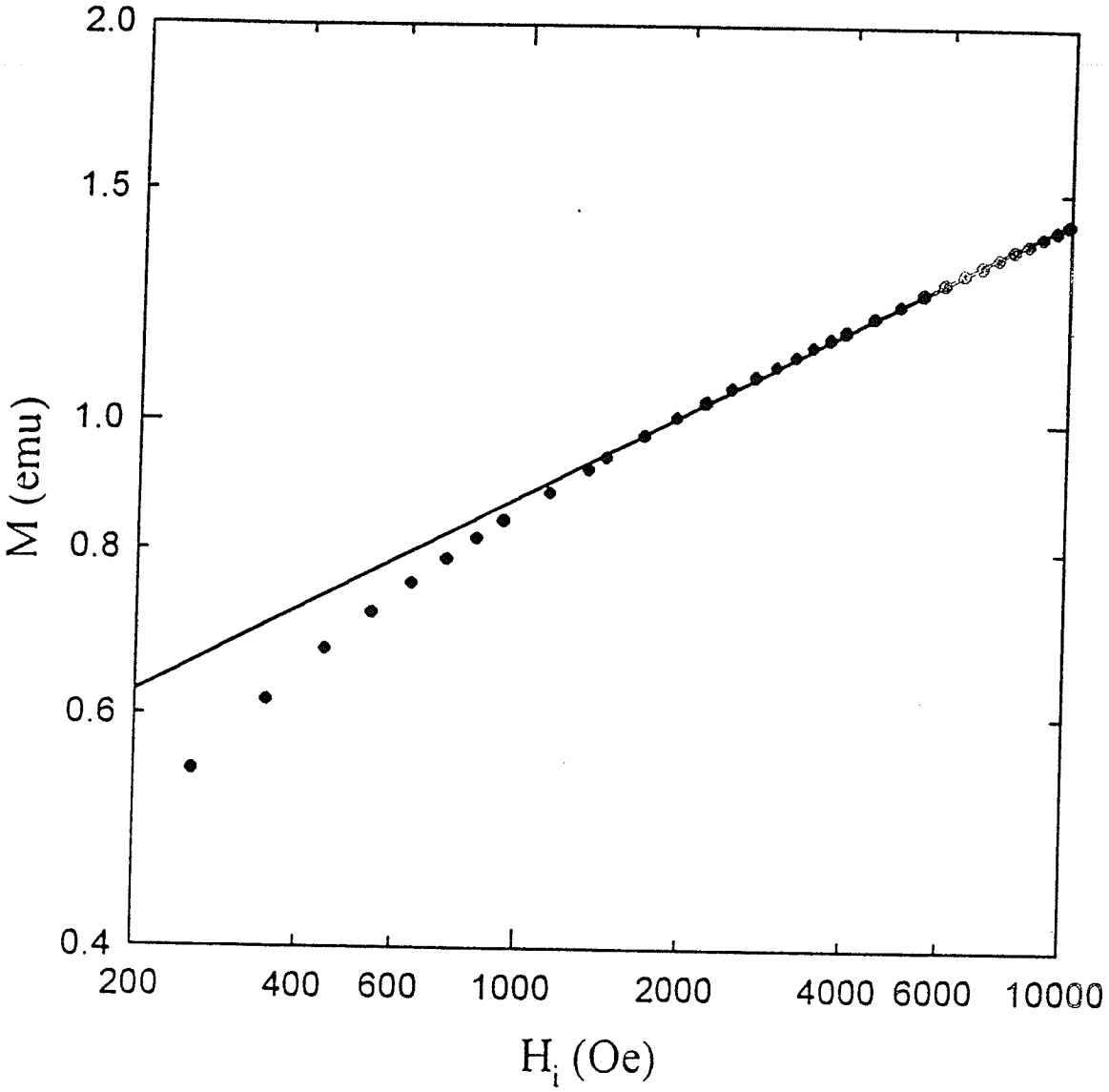

Figure 5.41: The magnetization measured along the critical isotherm plotted against the internal field. The line drawn corresponds to $\delta = 4.80(\pm 0.2)$.

agreement with the value predicted ($\delta = 4.80$) by renormalization group calculations for the nearest-neighbour, isotropic three dimensional Heisenberg model. The above approach yields these critical exponents values in a very direct manner. Additionally figure (5.41) presents a more conventional approach, namely the magnetization as a function of (internal) field along the critical isotherm ($M \propto H_i^{1/\delta}$ at $T = T_c$). From the line drawn on this double logarithmic plot, δ was estimated as $\delta = 4.80(\pm 0.2)$ (1 kOe $\leq H_a \leq$ 10 kOe), which agrees very well with the value deduced above in figure (5.40); the latter, however, has the advantage that the relationship between χ_m and H_i is independent of the choice for T_c.

In summary, the magnetic critical exponent values deduced above are consistent with Heisenberg model predictions. This result is different from those reported for some Sr doped perovskites [64, 66], but not for the pyrochlore system $Tl_2Mn_2O_7$ reported earlier in this thesis. The scaling plot in figure (5.42) further confirms the above analysis, i.e. showing that the susceptibility measured along each isokap or constant field curve, normalized to its peak value, scales onto a single curve when plotted against the argument ($h/t^{\gamma+\beta}$) of the scaling function, as for the pyrochlore.

In spite of the good agreement between the measured exponent values and model predictions, two points need more discussion. First is the effect of the demagnetization correction on $\chi_0(T)$; the second is whether the exponent estimates are of a true, asymptotic nature. The first point takes into account whether the demagnetization limit is attained, in which case the internal field ($H_i = H_a - NM$)

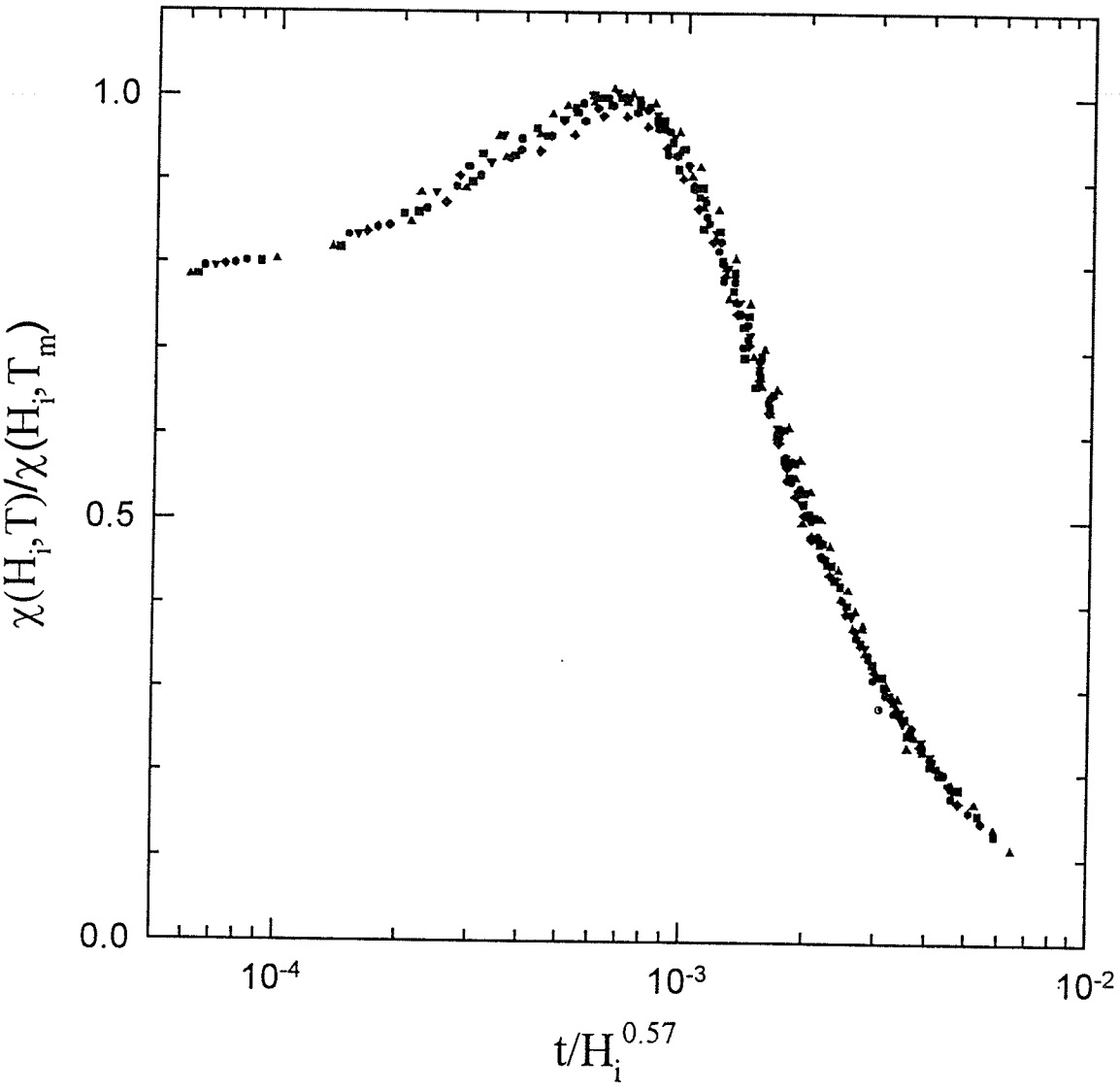

Figure 5.42: The scaling curve using Heisenberg model exponents shows the data collapse onto a single curve, confirming the scaling hypothesis.

is reduced to zero. In an ac measurement, the amplitude of the magnetization oscillations will have to increase as N decreases in order to attain this limit. It is obvious that this reversal is more readily realized by measurements on larger N specimens. In the present system magnetization reversal appears inhibited by single-ion anisotropy, likely arising from spin-orbit coupling at Mn^{3+} (Jahn -Teller) sites, so that the above condition is not realized. The second point concerns the approach of the present data to the critical point ($h \rightarrow 0, t \rightarrow 0$) and whether true asymptotic exponent values are estimated. The exponent value $\gamma = 1.39(\pm 0.06)$ was found in the reduced temperature range $t \geq 2 \times 10^{-2}$; this is at least an order of magnitude further from the critical point than some of the best estimates [67] although it is comparable to the range probed in many other studies. For the estimate of the exponent, δ, the data extends down to a magnetic field of 400 Oe, as indicated in figure (5.40), which is closer to the asymptotic limit ($h \rightarrow 0$) than that utilized in conventional estimates for δ from critical isotherm data (which seldom extends below 1 kOe). Nevertheless, exponent estimates here are based on the field and temperature variation of the susceptibility maxima extracted from fields some three orders of magnitude larger than those reported in the best metallic systems in which critical peak structure has been resolved in fields as low as $\sim$0.4 Oe [54]. The possible origin of such differences is discussed next.

The application of equation (3.27) is based on the assumption that the measured magnetic response is dominated by the singular/critical contribution. In many metallic systems, the orbital moment is essentially quenched and the

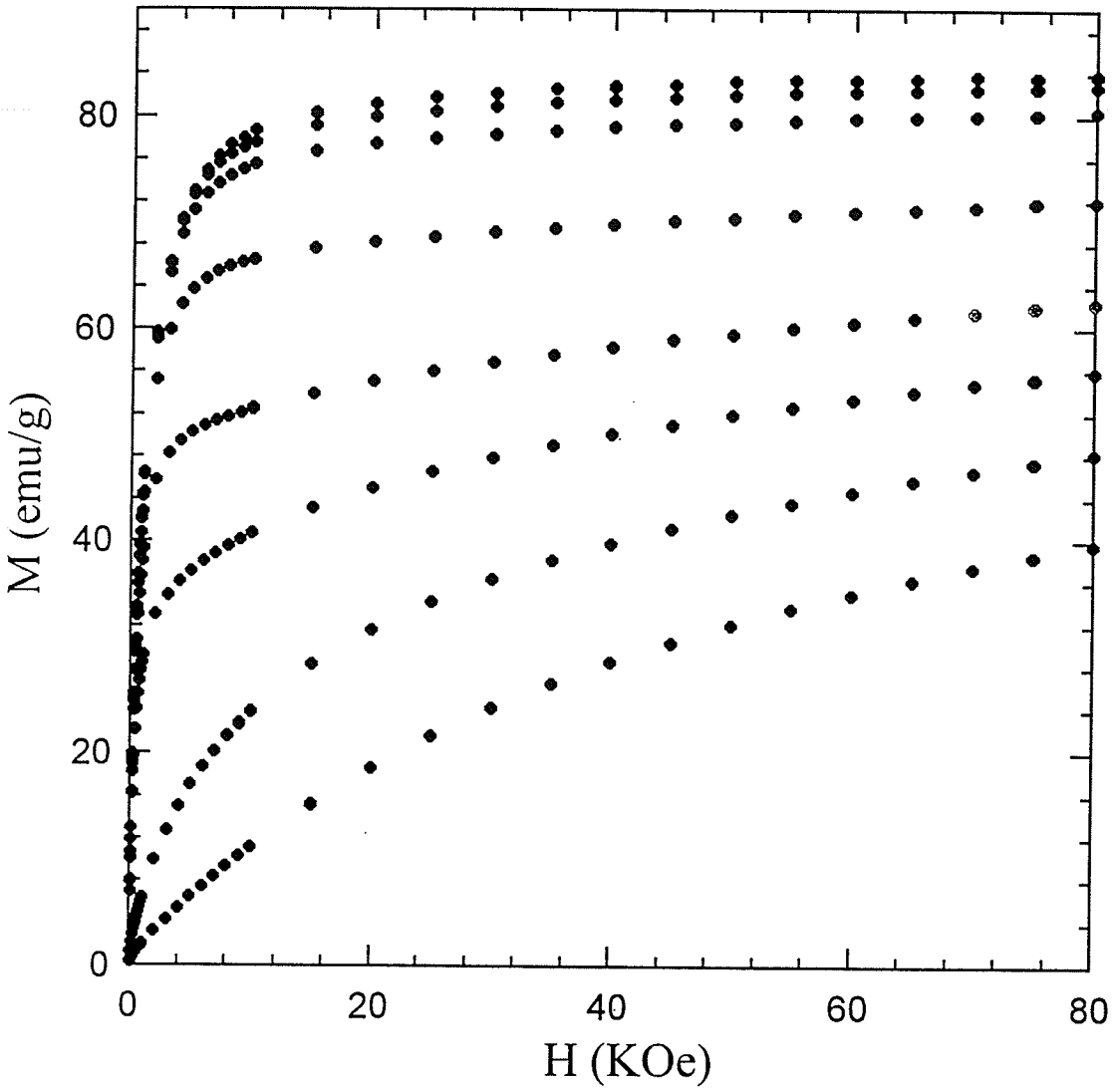

Figure 5.43: Magnetization curves are plotted against applied field at fixed temperatures of 4.2 K (top), 20 K, 40 K, 80 K, 120 K, 140 K, 160 K and 180 K (bottom).

associated single-ion anisotropy, through spin-orbital coupling, is thus zero, or at least small. As a consequence, technical saturation can be achieved in relatively low applied fields. Since the Hopkinson maximum originates from non-critical (regular) processes, such as domain wall motion and coherent rotation, it can be rapidly suppressed in amplitude and temperature by modest fields in such systems, and critical maxima are easily resolved. This does not happen here likely because of the presence of Mn^{3+} ions, a Jahn-Teller ion with spin-orbit mediated anisotropy, as the following illustrates.

The coercive field, H_c, directly measures the processes opposing magnetization reversal at any temperature. Figure (5.43) reproduces magnetization curves acquired for the present system at a variety of temperatures, and figure (5.45) gives the temperature dependence of the coercive field H_c(T) deduced from hysteresis loops, example of which are shown in figure (5.46). The measured H_c(T) falls from a value of about 65 Oe in the liquid helium range to zero at T_c; in particular at some 10 K below T_c measurements show $H_c(T) \leq 10$ Oe. In many systems studied previously, applied fields of typical magnitude 2-3 times H_c ($T \leq T_c$) have been found to saturate the (regular) component arising from technical contributions, thus enabling critical peak structure to be resolved. This does not occur here (nor indeed in several other doped perovskites or the pyrochlore system discussed previously). An examination of figure (5.46) reveals the source of this difference; it is not the relative magnitude of the applied field, H_a, and the coercive field, H_c(T), but rather the persistence of a significant higher field slope in these magnetization curves. The latter indicates a substantial reversible con-

tribution to the (technical) magnetization process at fields well beyond H_c(T). A possible origin for this reversible or non-saturating regular contribution was discussed for $La_{0.67}Ca_{0.33}MnO_3$ in terms of the existence of the intrinsically inhomogeneous mixed valent (Mn^{3+}-Mn^{4+}) state. Double exchange and the associated ferromagnetic fluctuations would predominate in those regions statistically rich in the substituted cation, whereas other regions statistically diminished in the divalent dopant species would be expected to display antiferromagnetic correlations that are characteristic of Mn^{3+}-Mn^{3+} (t_{2g}-O($2p_\pi$)-t_{2g}) superexchange in the undoped parent compound. While the ferromagnetic double-exchange dominates the overall critical behaviour, contributions from the antiferromagnetic superexchange still play a significant role. The incipient fluctuations associated with the antiferromagnetic order would be suppressed by an increasing field, H_a, and the associated magnetic response contributes to the measured regular response rather than the ferromagnetic, critical component, as argued previously.

To extend our understanding on this system, in general, but to investigate such effects in particular, additional experimental data were collected. Figure (5.44) displays the temperature dependence of the FC (field cooled) and ZFC (zero field cooled) magnetization measured in an applied field of 10 Oe. The ZFC data were obtained by first cooling the sample from 300 K to 4.2 K in zero applied field, and then measuring on warming in the field of $H_a = 10$ Oe. The FC data were obtained by first cooling in the applied field of $H_a = 10$ Oe and then warming from 4.2 K. It can be seen that the FC and ZFC curves show the same behaviour above $T_c \cong 150$ K, but they bifurcate just below T_c. This reveals the

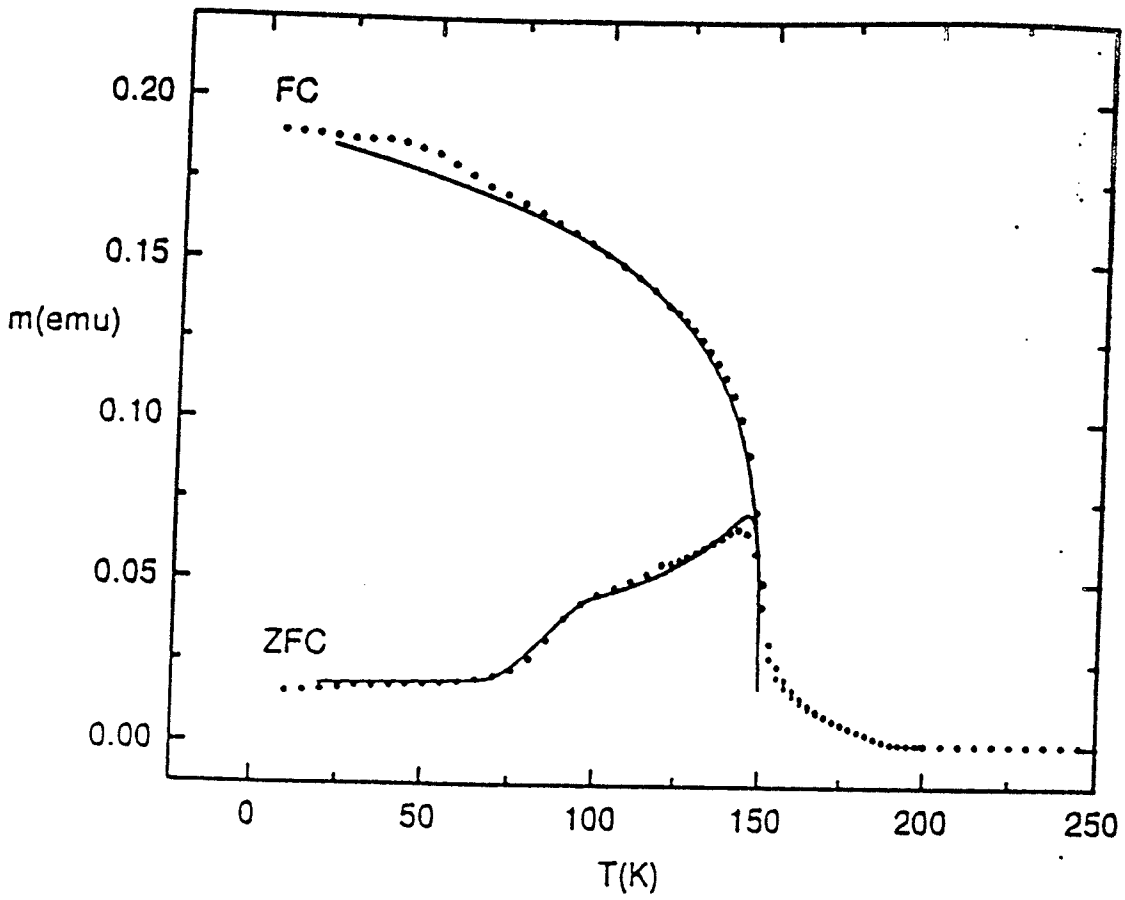

Figure 5.44: The temperature dependence of the field-cooled (FC) and zero-field-cooled (ZFC) magnetization measured in a nominal applied field $H_a = 10$ Oe. The solid curves are Preisach simulations.

presence of irreversibility and hysteresis. With increasing temperature, the ZFC data shows a rapid increase in magnetization near T = 85 K and then a slower increase to the maximum around T_c. The FC data displays normal ferromagnetic features below T_c.

The Preisach approach was used to analyze and interpret this irreversible component of the magnetic response as detailed in reference [101]. The model decomposes all magnetic systems into a collection of many bistable subsystems, all such entities in which are assumed to have the same moment, but are distinguished from each other by their characteristic coercive and interaction fields. Both fields are assumed to be described by Gaussian distributions, so that the combined probability density $P(H_c,H_i)$ consists of the product of two Gaussians:

$$P(H_c, H_i) = \frac{1}{\sigma_c\sqrt{2\pi}} \exp[-\frac{(H_c - \bar{H}_c)^2}{2\sigma_c^2}] \cdot \frac{1}{\sigma_i\sqrt{2\pi}} \exp[-\frac{H_i^2}{2\sigma_i^2}] \tag{5.16}$$

The data fitted using the Preisach model are shown as the solid lines in the figure (5.45) and (5.44). These fits reveal much about the technical magnetization processes characterizing the $La_{0.95}Mg_{0.05}MnO_3$ system. As is shown in figure (5.44), the step in the ZFC moment in the vicinity of T = 85 K is a manifestation of a crossover between regimes with distinctly different anisotropy characteristics. This crossover is clearly visible in the temperature dependence of the calculated coercivity shown in figure (5.45), and is coincident with a similar although somewhat weaker anomaly in the measured coercivity. Also the data for the hysteresis loop, the dotted line for experimental measurements and a solid line fitted using the Preisach model shown in figure (5.46), reveal a large reversible

contribution accounting for roughly 90% of the total system response. It is this large reversible component, superimposed on a smaller hysteretic contribution, that results in the system appearing technically softer than its intrinsic response. A possible physical origin for such hysteretic processes might associate them with moment reversal near the surface of grains, while large elastic (reversible) domain wall motion might occur in the main body of a grain. The reversible component in the magnetic response, no matter what the actual origin, is believed to be the essential element complicating the behaviour of these systems.

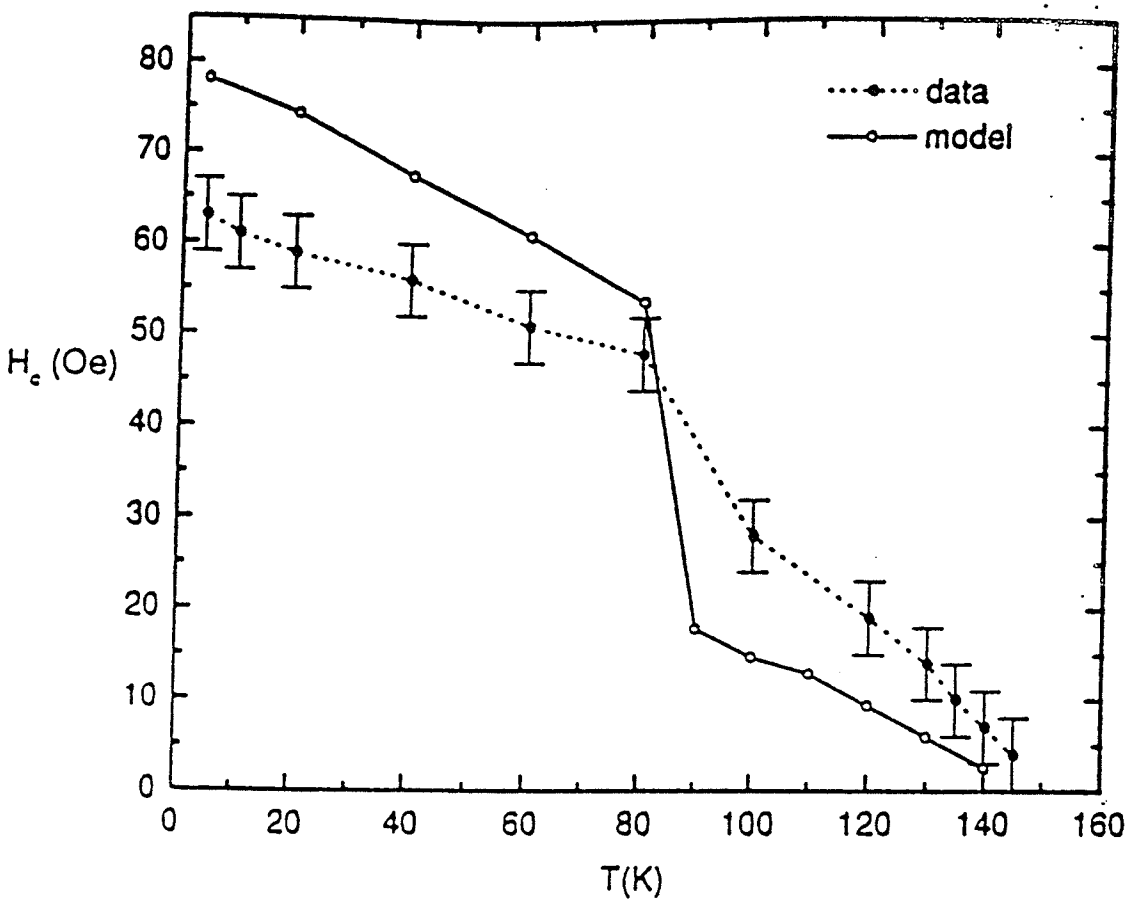

Figure 5.45: The temperature dependence of the measured coercivity H_c (T) of $La_{0.95}Mg_{0.05}MnO_3$ (dashed line) and of the coercivity calculated by the Preisach model (solid line).

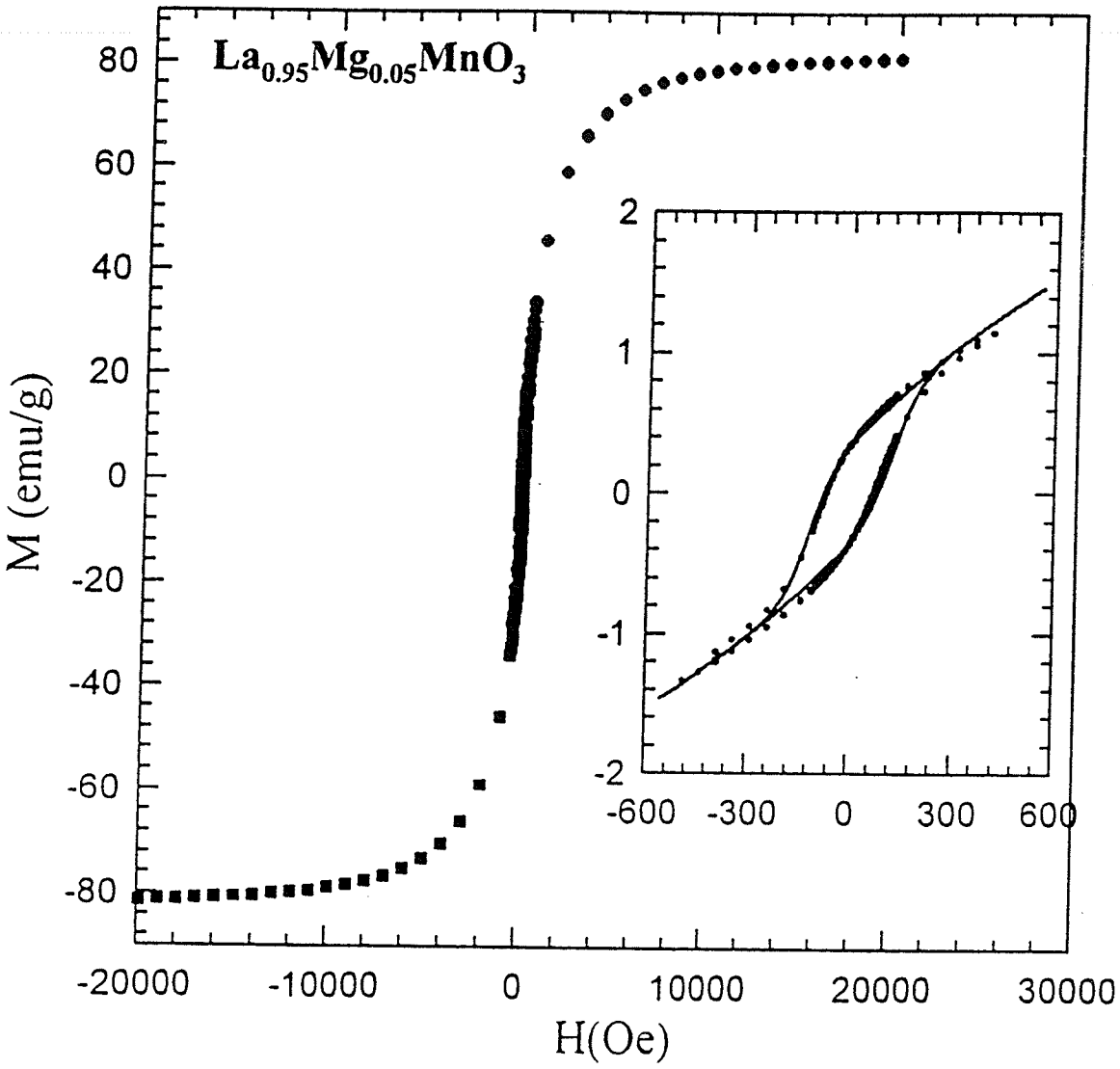

Figure 5.46: The major hysteresis loop of $La_{0.95}Mg_{0.05}MnO_3$ measured at T = 4.2 K. The low field portion is shown in the inset where the dotted line and solid line represent the measured and calculated Preisach loops respectively.

$0.1 \leq x \leq 0.4$

The samples in this doping range display similar critical behaviour, as revealed by measurements for the zero-field and the field-dependent susceptibility, and shown in Figures (5.33), (5.34), (5.35) and (5.36). Data analysis for the x = 0.1 sample are reproduced in figures (5.47) (a)-(d). The values for the critical exponents γ, β and δ have been found to be: $\delta = 4.75$ ($\pm$ 0.15), $\gamma + \beta = 1.75$ ($\pm$ 0.10), $\gamma = 1.39$ ($\pm$ 0.05), respectively. These exponent values are, within experimental uncertainty, again in agreement with those predicted by the nearest-neighbour, isotropic 3-dimensional Heisenberg model. They are also in excellent agreement with those reported above for the specimen with x = 0.05. Moreover, the near-ideal magnetic behaviour observed in the x = 0.1 sample indicates that these exponent values not only fall into the universality class of a well-established model system but they also remain unmodified in the entire range of field and temperature examined. The deduced exponent values satisfy the Widom relation, $\gamma = \beta(\delta - 1)$. The δ estimate is also confirmed by the measurements along the critical isotherm, i.e. they could be fitted to the form of $M \propto H_i^{1/\delta}$, $\delta = 4.66(\pm 0.15)$ in the regime of 500 Oe$\leq H_i \leq$ 20 kOe. This estimate is, however, dependent not only on the estimated values for T_c but also on the ability to remeasure at this temperature. The scaling law approach also predicts that the susceptibility, $\chi(h,t)$, measured in any fixed field and normalized to the peak value in the same field, should be a universal function of the argument of the scaling function, viz. the relationship $\chi(h,t)/\chi(h,t_m) \propto t/H_i^{1/(\gamma+\beta)}$; data for the x = 0.1 do indeed collapse onto a single scaling curve with Heisenberg model exponents,

$(\gamma + \beta)^{-1} = 0.57$. The results are similar to those presented previously for the x = 0.05 sample and hence are not reproduced here.

The critical exponent estimates for the x = 0.2 sample are presented in figure (5.48) (a)-(d). When compared with those for the x = 0.05 and 0.1 specimens, the effects of disorder associated with the increase in divalent ion substitution are observed, as the following discussion reveals.

Figure (5.48)d, a double logarithmic plot of the critical peak maxima, $\chi(h, t_m)$, against the internal field, H_i, shows that the power-law prediction of equation (3.28) is no longer valid over the entire field range. This plot now exhibits some curvature so that the effective exponent $\delta^*(H_i)$ (determined from the local slope $\partial\chi(H_i, T_m)/\partial H_i$ of this plot) decreases with increases in magnetic field. The solid line drawn in this figure, a least squares fit of the five points at lowest field, yields $\delta = 4.76(\pm 0.20)$, suggesting that the asymptotic (low-field) value for this exponent is still consistent with the 3-D Heisenberg model prediction. Fitting the entire data set shown in this figure yields a somewhat lower effective/average exponent value of $\delta^* = 4.43(\pm 0.23)$. Exponent values which vary with field and/or temperature have been reported previously for a variety of metallic and semiconducting systems [37, 86]. An extensive study of metallic systems has led to the conclusion that this variation is linked to a finite width in the distribution of exchange interactions coupling the spins (the Mn moments here). Further, while such disorder has been shown to be an irrelevant scaling field at the critical point, so that the asymptotic ($h \to 0$, $t \to 0$) exponent values remain unchanged, the effective exponent values (for $h \neq 0$, $t \neq 0$) are modified by its presence. This

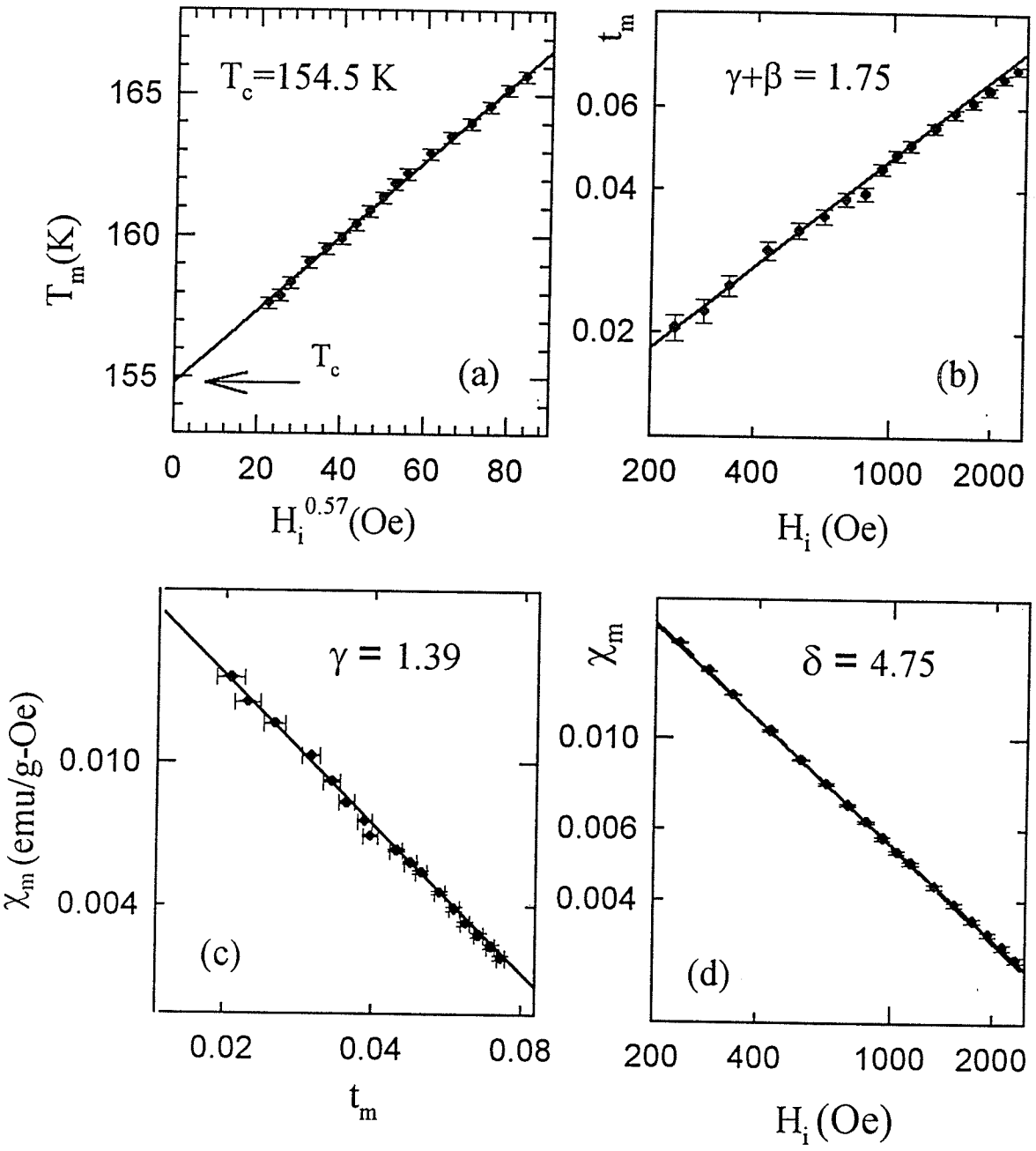

Figure 5.47: The plots show the data fit to find critical exponents values for the sample with x = 0.1.

modification becomes more pronounced as the ratio $\eta = J_0/J$ is reduced towards 1.0, which essentially is the limit of stability of a ferromagnetic ground state. Here J_0 is the mean value/first moment of the exchange distribution and controls the critical temperature, $k_BT = J_0$, while J measures the width/second moment as discussed in chapter 3.

Similar effects can be seen in Figures (5.48) (a)-(d) which also show effective exponent values that vary with field and/or temperature, but with low field/temperature (i.e.asymptotic) exponent values consistent with the same model predictions, viz. $\gamma + \beta = 1.75(\pm 0.15)$; $\gamma = 1.36(\pm 0.04)$. Results for the x = 0.33 sample are shown in figure (5.49), with critical exponents values $\delta^* = 4.38(\pm 0.20)$; $\gamma+\beta = 1.75(\pm 0.12)$; $\gamma = 1.34(\pm 0.07)$, very similar to the effective exponent values found above.

A possible physical picture describing the above results in the composition range $0.1 \leq x \leq 0.33$ is the following. A likely consequence of the increase in divalent cation substitution for La^{3+} is an increase in the width (J) of the distribution of exchange coupling strengths between Mn spins although the first moment J_0 remains relatively large (so that $\eta > 1$) because T_c is large. The double exchange theory gives a clear picture of the interactions which arises from the presence of an inhomogeneous mixed valent (Mn^{3+} - Mn^{4+}) state. In spite of the predominant coupling from ferromagnetic (Mn^{3+} - Mn^{4+}) double exchange, the presence of superexchange interactions of different magnitude (between Mn^{3+} - Mn^{3+} and Mn^{4+} - Mn^{4+}), and possibly different sign could lead to a progressively broadening of the exchange coupling distribution accompanying increases in doping level.

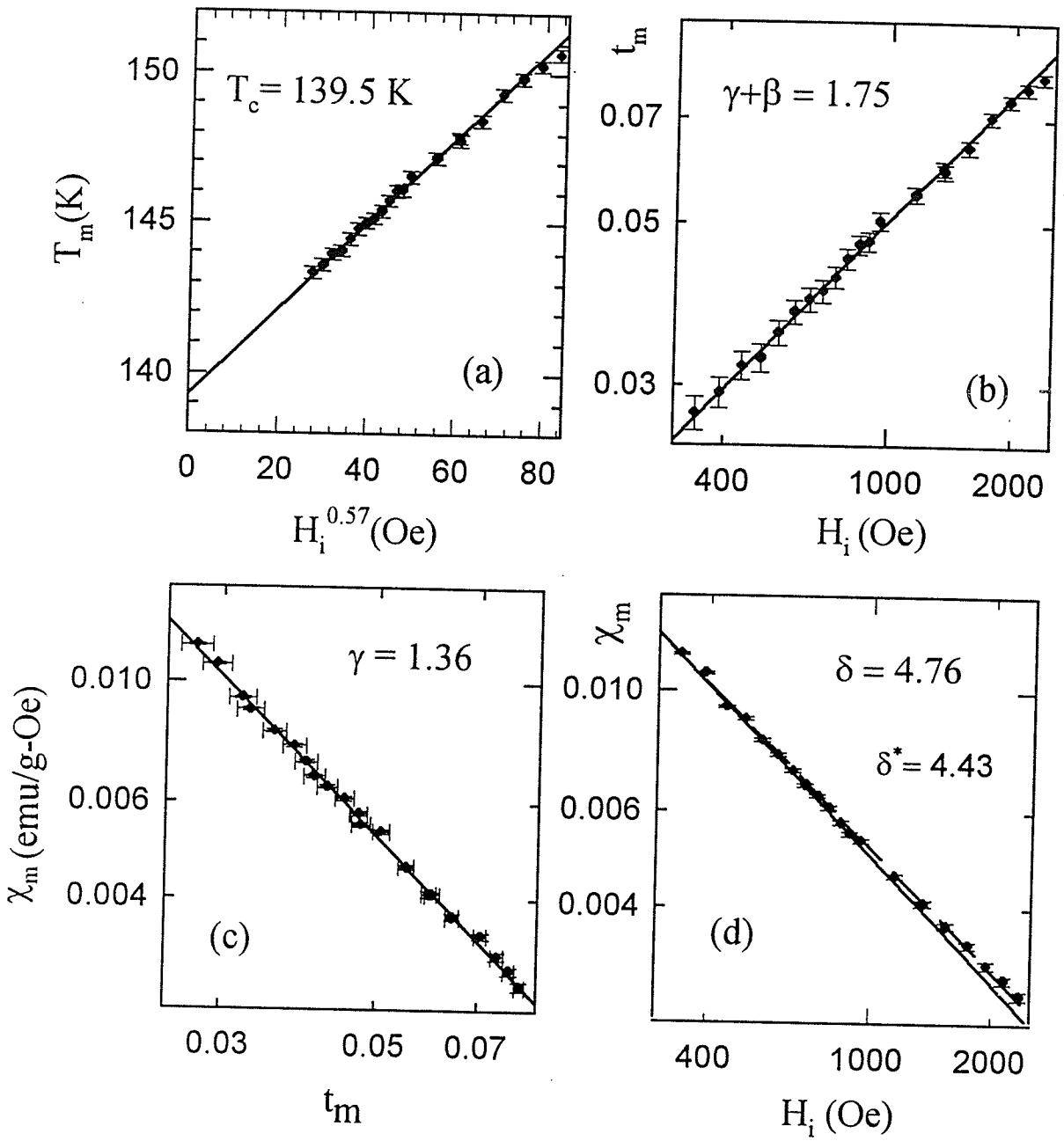

Figure 5.48: The plots show the data fit to find critical exponents values for the sample with x = 0.2.

Here $\eta > 1$ is still maintained, due to the strong ferromagnetism. Such effects are evident through close examination of the above results as a broadened exchange bond distribution is known to lead to the above form of effective exponent variation, and they are also likely to be even more prevalent at higher values for x, as discussed below.

Figure (5.50) reproduces the results of the critical exponent analysis for the sample with x = 0.4. The critical exponent values obtained here are quite different from those found at lower values of x, viz. figures (5.50) (a)-(d) give: $\delta^* = 3.0(\pm 0.1)$; $\gamma^* + \beta^* = 1.49(\pm 0.11)$; $\gamma^* = 1.01(\pm 0.06)$. These values are close to those predicted in mean field theory ($\gamma = 1$, $\gamma + \beta = 3/2$, $\delta = 3$), which, considering the basic (and short range) nature of double exchange and superexchange interaction, is not expected to apply to these systems. Two alternate reasons present themselves: the first is a fundamental change in the character of the basic interaction mechanisms as the divalent cation substitution increases from x = 0.33 to 0.4. For $x \leq 0.33$ the estimated exponents appear to be consistent with the prediction of the near-neighbour 3 D Heisenberg model. But, at x = 0.4 the range of the underlying interaction becomes infinite, a marked change indeed. Second, the trend presented for $0.2 \leq x \leq 0.33$ signals that the ratio $\eta = J_0/J$ continues to fall toward unity, so that the scope of the true asymptotic critical behaviour observed in the (h, t) plane contracts below the field and temperature range accessed by the present experiment for the x = 0.4 sample. In essence, the same limitations as conventional estimates of static critical exponents from magnetization measurements are encountered by the current experiment. Neither

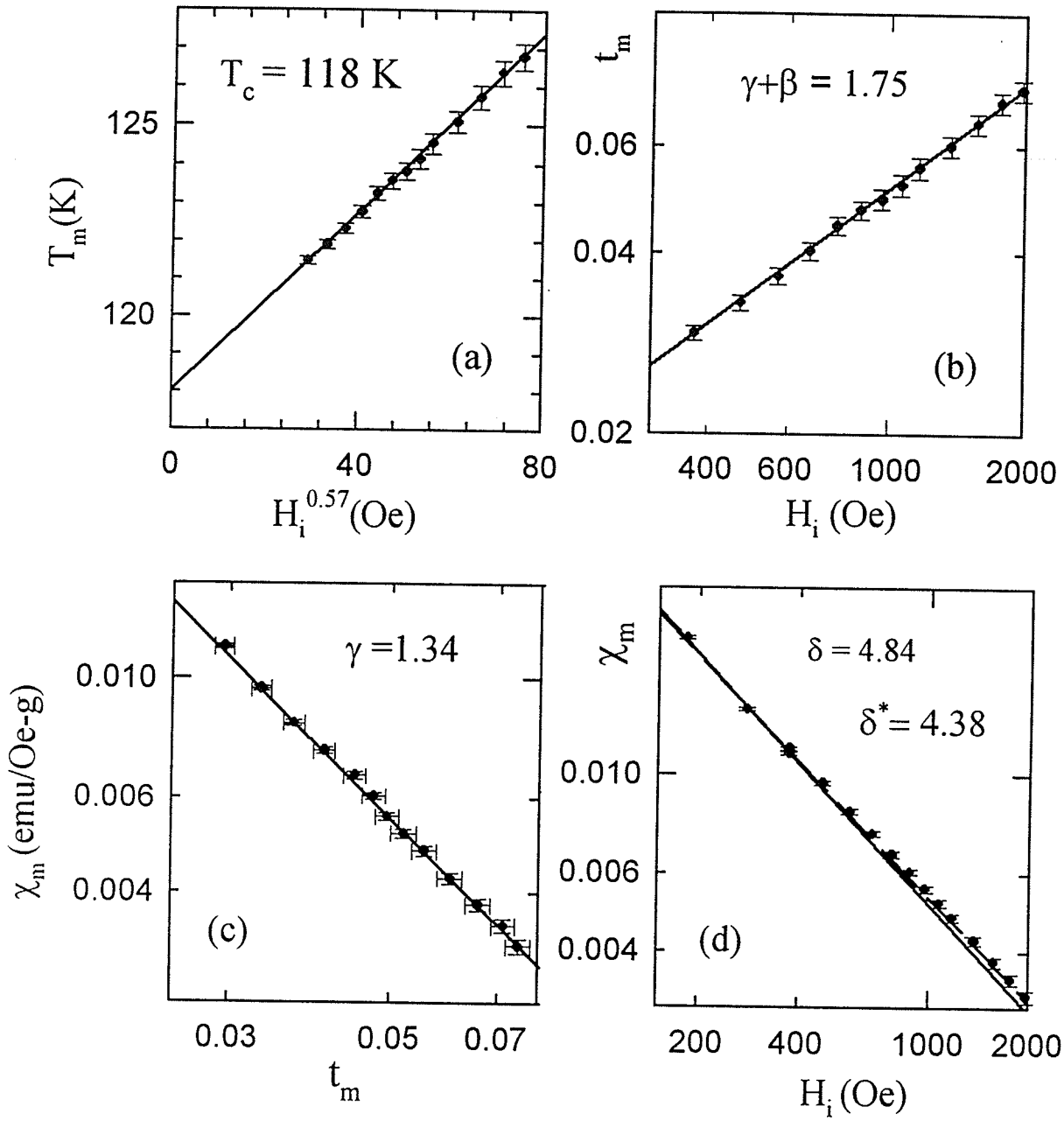

Figure 5.49: The plots show the data fit to find critical exponents values for the sample with x = 0.33.

can be extended to arbitrarily low field and reduced temperature, due to complications introduced by the presence of regular or non-critical contribution (i.e. domain wall motion and /or coherent rotation). These appear to limit the current measurements to internal fields down to 200 Oe. The true critical behaviour may thus prove very difficult to be accessed. Further, effective exponent values do approach mean-field predictions as the critical point becomes more distant. However, such a trend generally occurs in a more gradual way than that occurring for the x = 0.4 sample. Specifically, if the second point is correct, the true critical region contracts very rapidly for $x > 0.33$ in $La_{1-x}Mg_xMnO_3$, reflecting a rapid decline in the ratio $\eta = J_0/J$ towards unity as the dopant level is raised above this composition.

While these possibilities are difficult to differentiate on the basis of the present measurements, the second possibility is currently favored on the basis of preliminary measurement made at higher values of x. Furthermore, for $\eta \leq 1.0$ the ground state would be expected to evolve into a spin-glass. For $1.0 < \eta \leq 5/4$, so-called re-entrant behaviour, i.e. paramagnetic to (longitudinal) ferromagnetic to (transverse) spin-glass ordering, is predicted to occur by various model approaches, as discussed in Chapter 3. Preliminary measurements for $0.45 \leq x \leq 0.6$ display features superficially reminiscent of those associated with the so-called spin-glass phase, which will be further discussed in a later section.

Figure (5.51) displays the magnetization variation with temperature measured under FC and ZFC conditions in an applied field of 10 Oe. Similar to that discussed for the x = 0.05 sample, the ZFC magnetization measured on warming

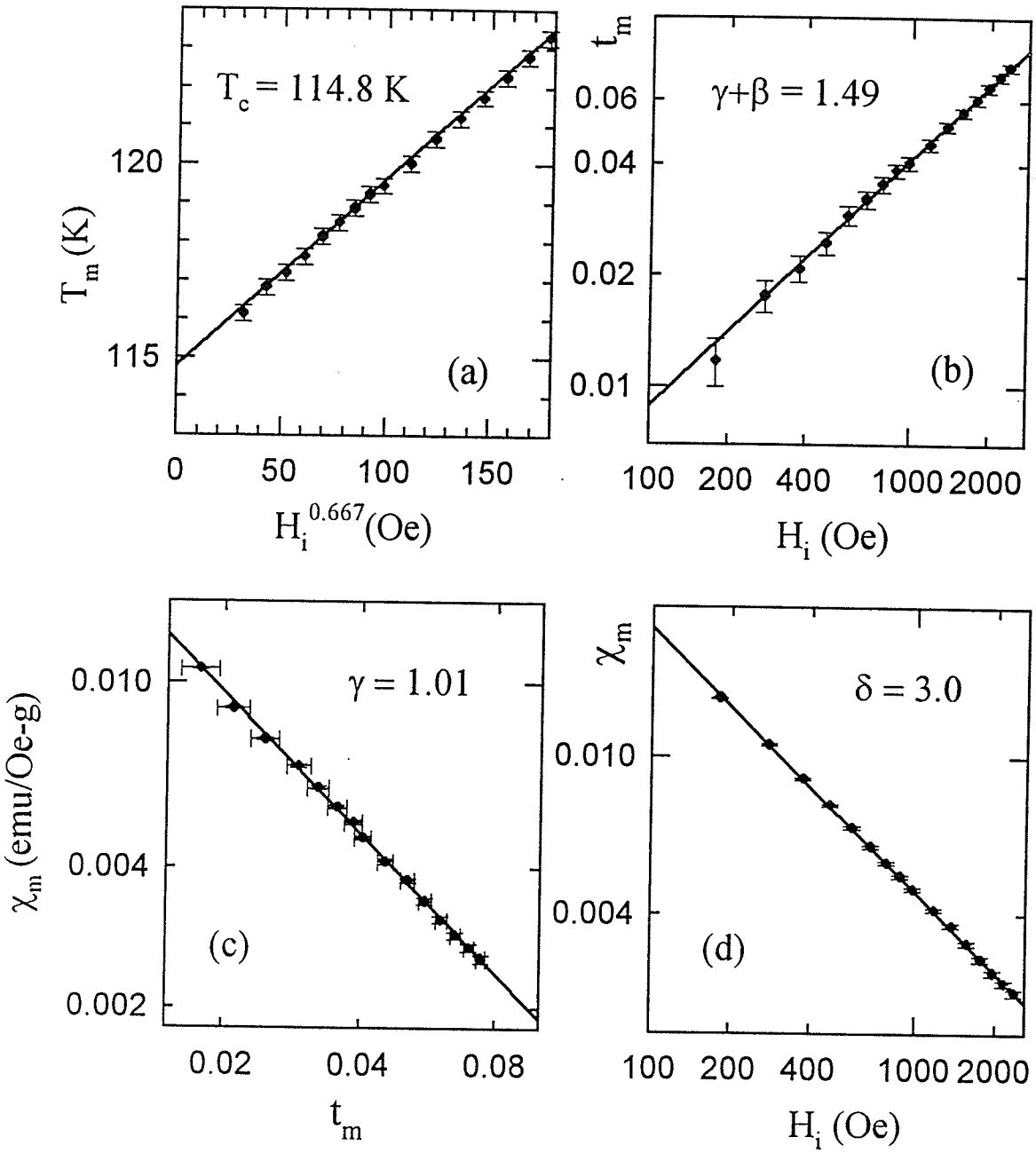

Figure 5.50: The plots show the data fit to find critical exponents values for the sample with x = 0.4.

rises slowly up to 70 K- 80 K, after which it climbs relatively rapidly to its highest level before dropping sharply. The relatively featureless FC magnetization measured on warming separates from the ZFC curve below T_c then merges at/above T_c. The change in dM/dT around 80 K, which is associated with the temperature dependence of the coercivity, has been discussed for the x = 0.05 sample in terms of the Preisach model. Figure (5.52) shows the temperature dependence of the coercivity for these samples (x = 0.1 - 0.4). They exhibit a relatively rapid increase around 70 K - 80 K, indicating the association of the ZFC and FC magnetizations with the temperature dependence of the coercivity. Because the Preisach model is phenomenological in nature, it is unable to identify the underlying mechanism leading to the rapid decrease in the ZFC data and, more fundamentally, to the H_c(T) distribution. Since this model has explicitly been applied to hysteretic processes, it might be argued that the features discussed above are intrinsically technical, i.e., they may not be linked with a true thermodynamic phase change.

After having discussed the magnetic data, especially the critical features, displayed by these samples with $x \leq 0.4$, some distinct characteristics exhibited by those samples with $x \geq 0.45$ lead to further investigation on them. These include the drop in the Hopkinson peak in the zero field susceptibility, the low temperature double-peak feature in the field-dependent susceptibility, a reduction in the magnetization at low temperature, as well as other features emerging from the ferromagnetic transition at T_c. Specifically, while there are some similarities in the critical behaviour seen above and below x = 0.4, these are some striking differences associated with the cross-over from hole to electron doping. Experi-

mental results of these electron-doped samples (actually $0.45 \leq x \leq 0.6$) are thus presented in the following section.

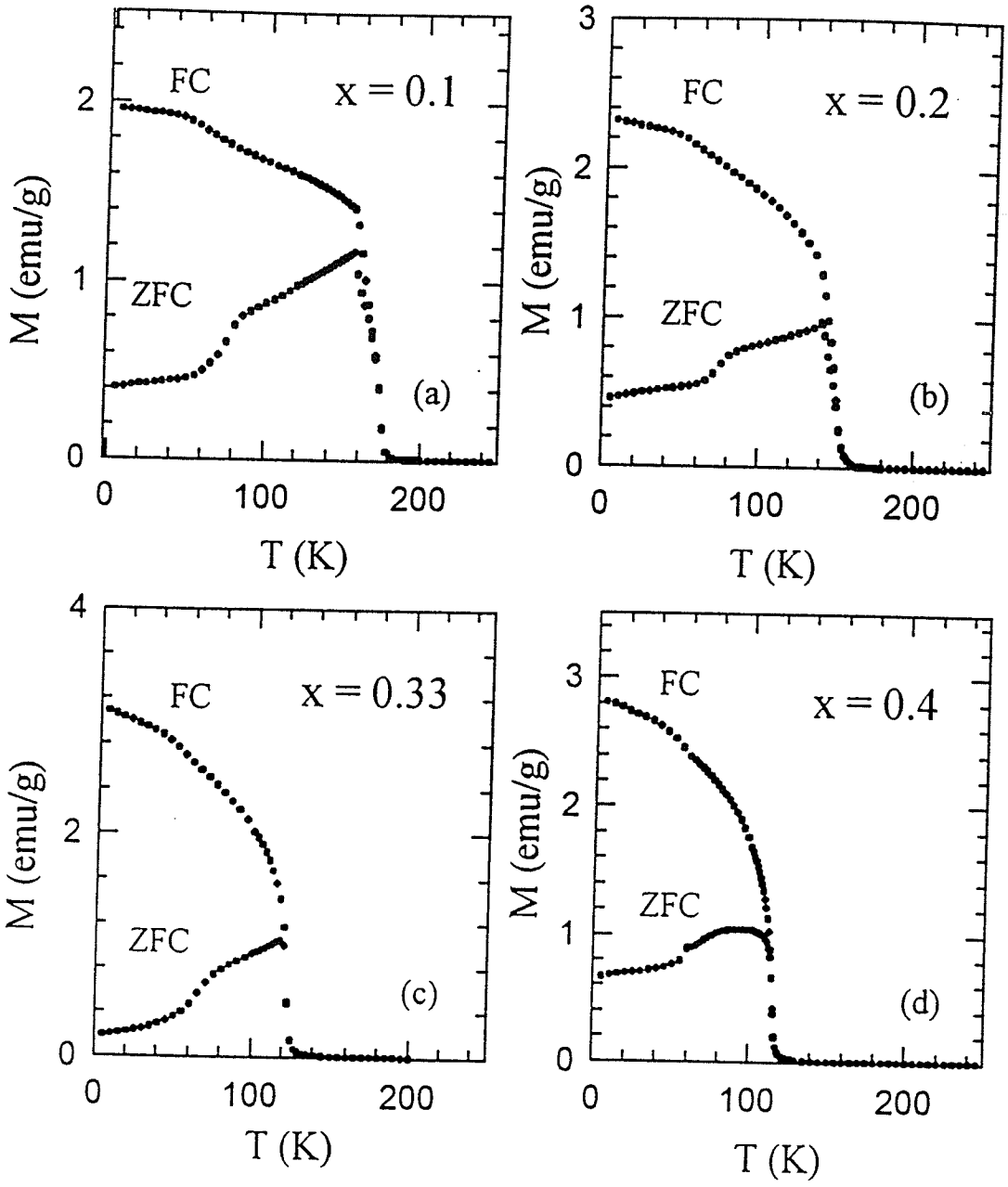

Figure 5.51: The temperature dependence of ZFC and FC magnetization curves measured in a field of 10 Oe for $La_{1-x}Mg_xMnO_3$ with $0.1 \leq x \leq 0.4$.

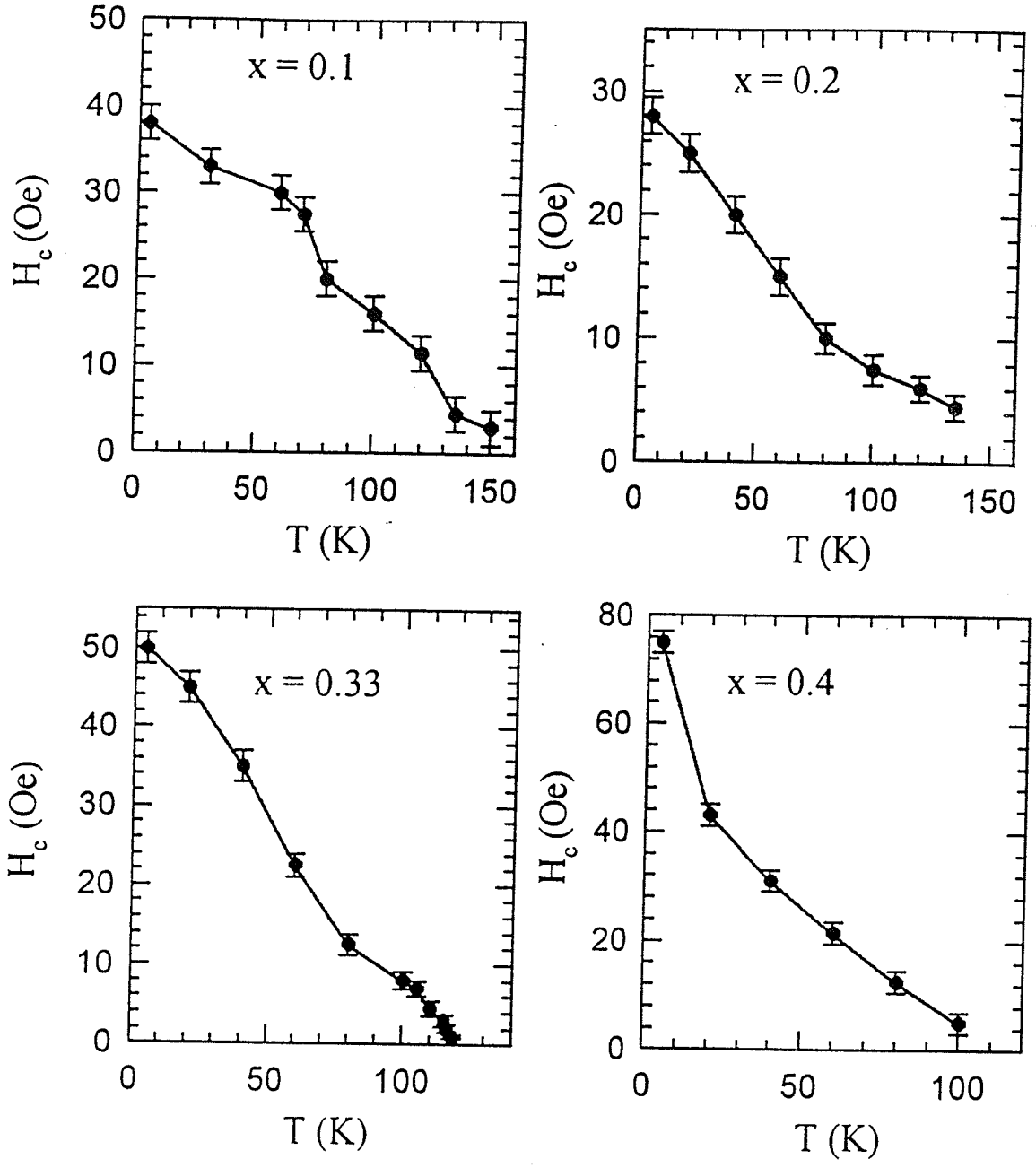

Figure 5.52: The temperature dependence of the coercivity for $La_{1-x}Mg_xMnO_3$ with $0.1 \leq x \leq 0.4$.

5.5.2 Electron-doped $La_{1-x}Mg_xMnO_3$ for $0.45 \leq x \leq 0.6$

For samples with x = 0.45, 0.5 and 0.6, the zero-field ac susceptibility, $\chi(0,T)$, was again measured with a driving field amplitude of 0.03 Oe and frequency of 2.4 kHz applied along the largest sample dimension. As shown in figure (5.34), $\chi(0,T)$ increases rapidly with decreasing temperature, then forms a peak (the principal (Hopkinson) maximum) at temperature T_H below the ferromagnetic ordering temperature (T_c). Below T_H χ(0,T) falls essentially monotonically as the temperature is further reduced. The data in the figures reveal some important features. First, $\chi(0,T)$ does not show any signal arising from either an Mn_3O_4 impurity phase (ordering near 40 K[102]), a mixed MnMgO phase[103] (with a lower ordering temperature), or self-doped $La_{1-y}MnO_3$ [102, 104] (which orders about 175 K for y $\geq$ 0.03). Second, the peak susceptibility χ(0,T_H), summarized in Table (5.4), decreases rapidly with increasing Mg composition x in this range, whereas at lower x it did not display such systematic changes. This behaviour appears to reflect the effects of increasing exchange bond disorder resulting in the suppression of ferromagnetism and thus the possible existence of a spin-glass-like phase.

The susceptibility data in various static biasing fields for these samples are shown in figure (5.36). It is clearly seen that the first (critical) peak at higher temperature has all the characteristic features previously associated with a continuous phase transition from a paramagnetic to a ferromagnetic state. Critical exponents values have been found for them using the methods discussed previously, and are shown in figures (5.53), (5.54) and (5.55). These are:

x = 0.45, T_c = 98.5(±0.5), δ = 4.50(±0.40) (400≤ H_i ≤700 Oe); $\gamma + \beta$ = 1.75(±0.09); γ = 1.33(±0.06); δ^* = 4.17(±0.2) (400≤ H_i ≤2.2 kOe).

x = 0.5, T_c = 79(±1), δ = 4.20(±0.60) (400≤ H_i ≤700 Oe); $\gamma + \beta$ = 1.78(±0.13); γ = 1.28(±0.07); δ^* = 3.65(±0.17) (400≤ H_i ≤2.4 kOe).

x = 0.6, T_c = 46(±1), δ = 4.15(±0.70) (600≤ H_i ≤900 Oe); $\gamma + \beta$ = 1.73(±0.09); γ = 1.25(±0.10); δ^* = 3.57(±0.30) (400≤ H_i ≤3 kOe).

The results show that the crossover exponent ($\gamma + \beta$) is very close to the value predicted by the Heisenberg model over the entire field and temperature range studied, while other exponents decrease with increasing field/reduced temperature, the latter effect becomes more pronounced with increasing composition x. The decrease in effective exponent values is often linked to exchange bond disorder, which is most likely related to the distribution of exchange interactions arising from the Mn^{3+}/Mn^{4+} ratio and the associated interactions such as double exchange and superexchange. Although such disorder does not modify the true asymptotic critical behaviour as h → 0 and t → 0, in agreement with the Harris criterion [105], effective exponent values are often observed to deviate from the true asymptotic values. The asymptotic exponents may be difficult to access as a result of the experimental limitations generally imposed by the presence of a technical /noncritical response. Here this effect appears to reflect the increase in coercivity as x increases. Nevertheless, the asymptotic/low-field exponent estimates are consistent with Heisenberg model predictions despite the exponent values, especially δ^*, showing an influence from the disorder. The ratio $\eta = J/J_0$, representing this disorder, appears to be close to unity in this composition range,

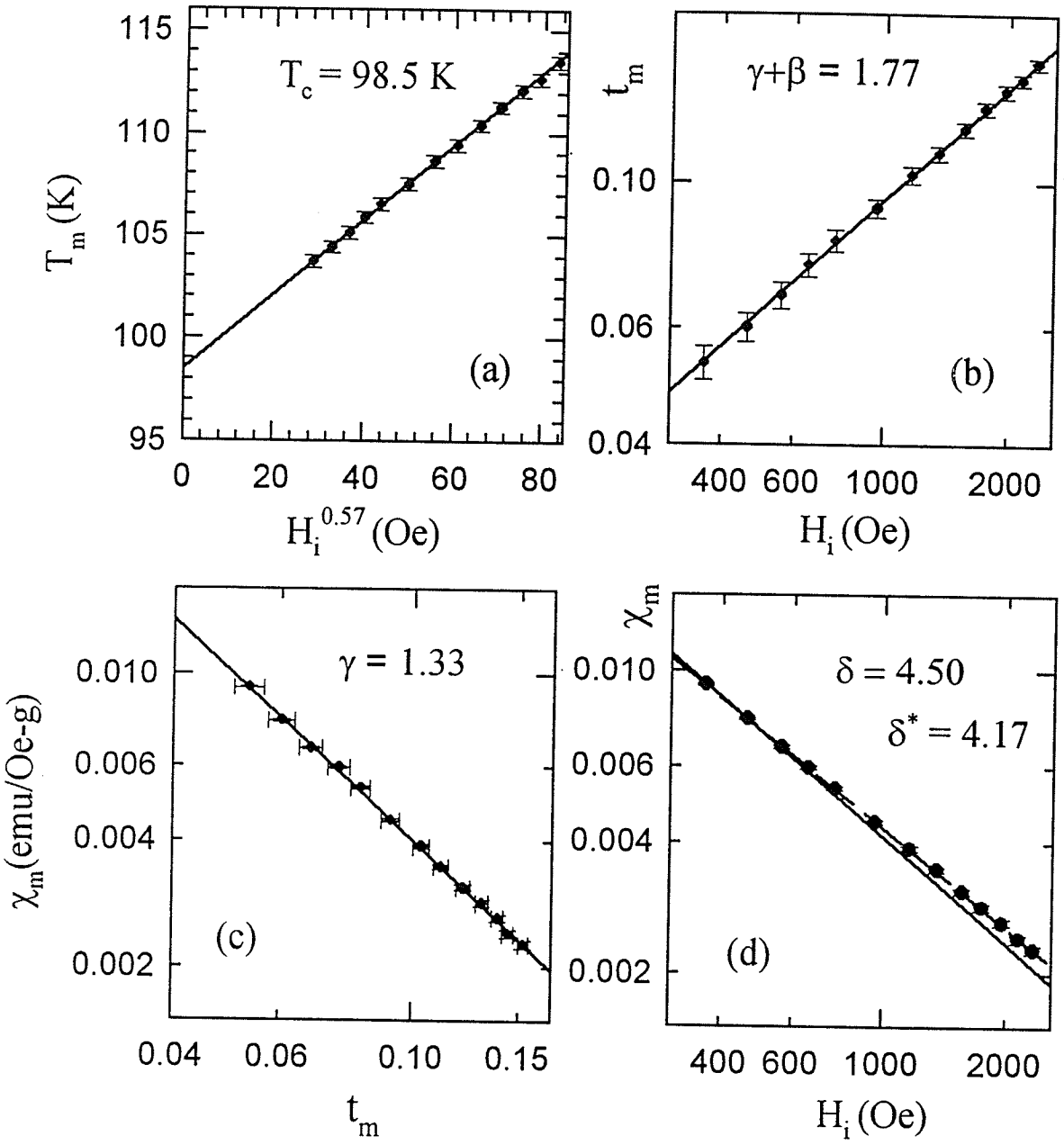

Figure 5.53: The plots show the data fit to find critical exponents values for the sample with x = 0.45.

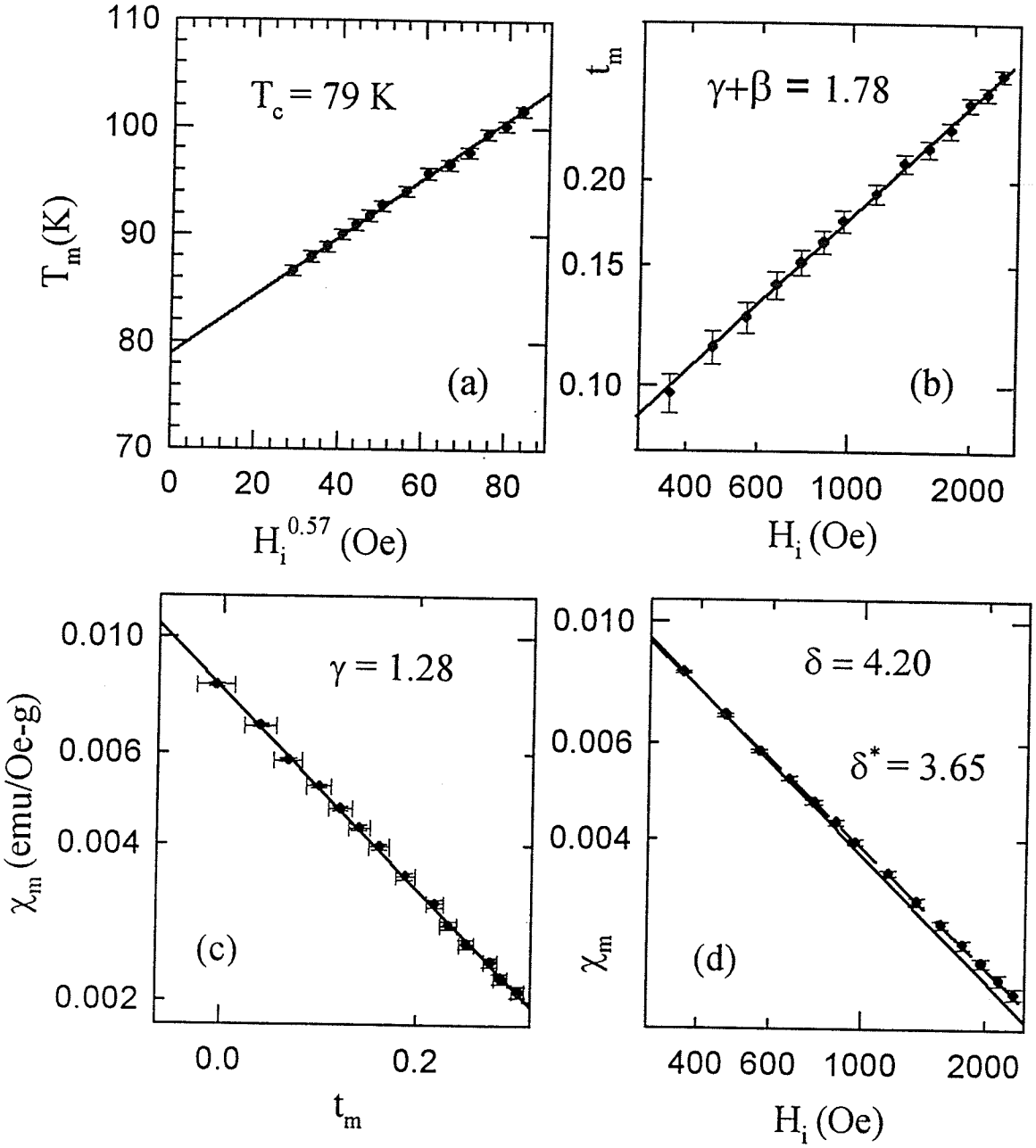

Figure 5.54: The plots show the data fit to find critical exponents values for the sample with x = 0.5.

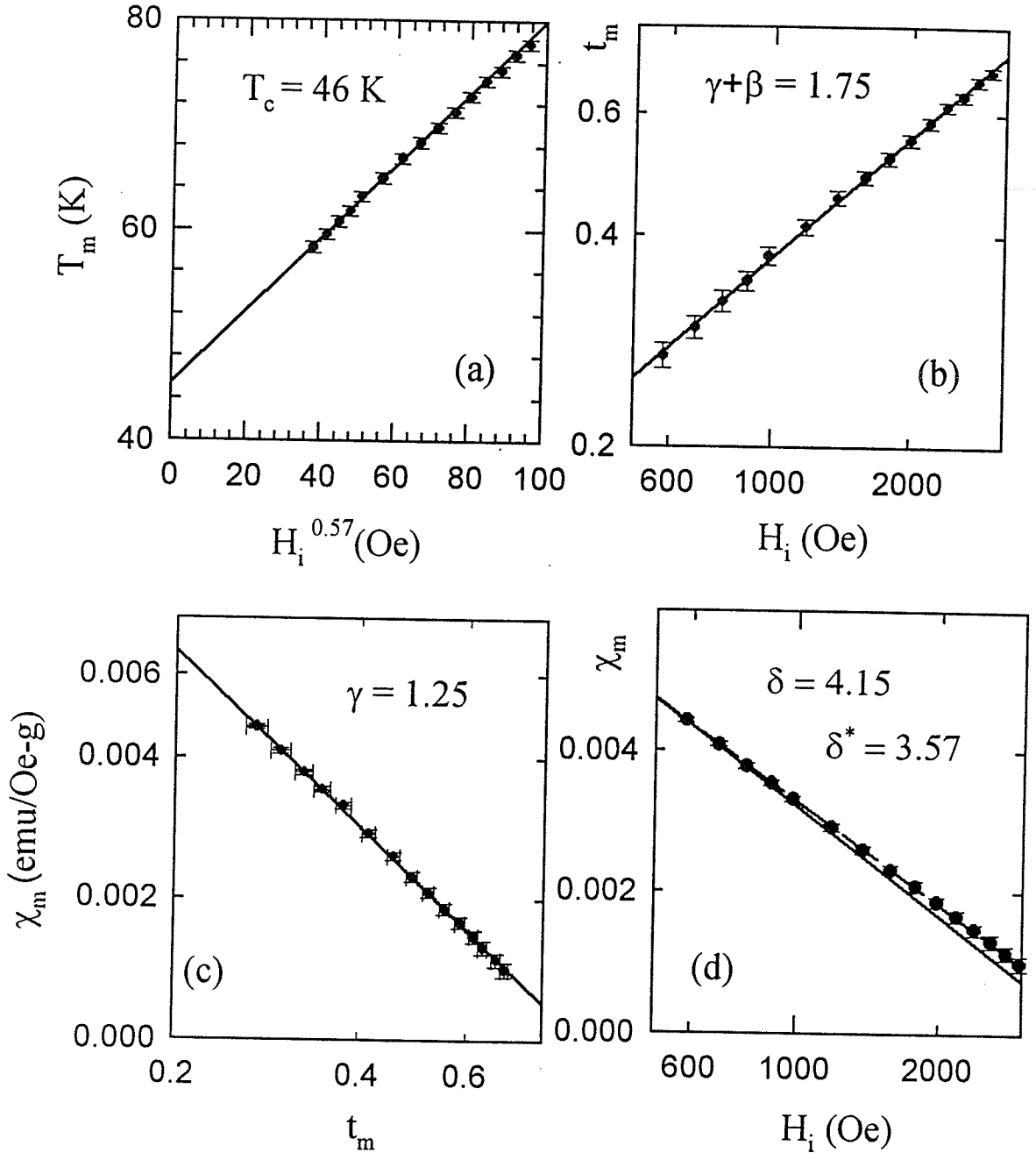

Figure 5.55: The plots show the data fit to find critical exponents for the sample with x = 0.6.

which is further supported by the following discussion on the low temperature structures evidenced in figure (5.36).

Low Temperature Structures

As can be seen in figure (5.36), for x = 0.45, 0.5 and 0.6, a multifeatured structure in the field and temperature dependent susceptibility appears below the ferromagnetic transition. The field-dependent susceptibilities first develop into a peak (upper peak at low temperature), then fall to very small values (trough) before displaying a weak increase again at low temperature. Some of these features may be taken as superficially signaling the existence of a reentrant transition from a ferromagnetic to a spin glass state which has been predicted by mean-field models (as stated in chapter 3). The corresponding characteristic parameter (in the SK model), η, falls below a value of 5/4. In addition, a vector spin approach [106, 107] was developed to deal with a ferromagnetic-spin glass transition at low temperature when $\eta < 5/4$. Gabay and Toulouse proposed a phase diagram for the infinite-range model for classical m-vector spins in the presence of a magnetic field and suggested the freezing of the transverse spin components (GT-line) in the presence of the longitudinal ferromagnetic order linked with the onset of weak irreversibility. At still lower temperatures, strong irreversibility occurred along the so-called de Alemeida-Thouless (AT) line. The AT and the GT-lines are given by the following forms:

$$\frac{(T_{AT}(0) - T_{AT}(H))}{T_{AT}(0)} = (\frac{3}{4})^{1/3}(\frac{g\mu_B H}{k_B T_{AT}(0)})^n \quad n < 1 \qquad (5.17)$$

$$T_{GT}(H) - T_{GT}(0) = \sqrt{2}(\frac{m^2+4m+2}{4(m+2)^2})(\frac{g\mu_B H}{k_B}) \qquad (5.18)$$

where m is the spin dimensionality. The models do not predict however that what specific experimental parameter represents the onset of weak or strong irreversibility, i.e. the GT-line and AT-line. Therefore all of the possible features appearing at low temperature in figure (5.36) have been compared with these predictions.

For the x = 0.45 sample, a trough at low temperature appears in applied fields $H_a > 400$ Oe, below which the susceptibility χ(H,T) increases but does not produce a well defined peak above 1.8 K. This trough temperature at 5 $\pm$ 0.5 K appears not to change with applied field, thus it does not show the features predicted by either the GT line or the AT line.

By contrast, the lower temperature features for the x = 0.5 and 0.6 samples are compared in more detail with the above models. Figure (5.56) plots the upper peak temperature designated T_{GT}(H) against the applied field H_a for the x = 0.5 sample. It is obvious in this figure that the data can be fitted by two straight lines in two different regions. In low fields (below about 1000 Oe), the straight line fit to the expression T_{GT}(H) - T_{GT}(0) = BH_a yields $T_{GT}(0) = 57.8$ ($\pm$ 1) K, and the slope was found as B = -2.6 $\times 10^{-2}$ K/Oe; the high field data are fitted to give $T_{GT}(0) = 37.0$ ($\pm$ 1) K, and B = -6.9 $\times 10^{-3}$ K/Oe. Apart from it not being clear why the data display the marked inflection at the field of about 1000 Oe, the important result is that the coefficient B obtained from these fits is three orders of magnitude larger than that predicted by the model calculation (about -4×10^{-5}

K/Oe). As for the AT line, equation (5.17) with n $<$ 1 would exhibit curvature generally consistent with features of the data in figure (5.56). However, the data exhibiting the two-straight-line form of figure (5.56) are very poorly fitted overall by the AT expression. The latter is thus rejected as a source of the features as is the GT line. This argues strongly against the upper peak really representing a phase transition associated with either the GT line or the AT line. Indeed this upper temperature peak most likely originates from technical sources, possibly associated with coercivity effects (discussed later) as it seems in fact to originate from the Hopkinson peak.

The remaining feature to be discussed for this sample is the trough structure appearing at still lower temperature (there is an increase in $\chi(H,T)$ below the trough, but no further peak emerges above 1.8 K as mentioned previously). Figure (5.57) reproduces the trough temperature, T_T(H), against field H_a, $T_{AT}(0)$ was found by fitting the data to be 15.9 K. Taking this value of $T_{AT}(0)$, the plot of t_{AT} (t_{AT} = (T_{AT}(H) - $T_{AT}(0)$)/$T_{AT}(0)$) against H_a on a double logarithmic scale is reproduced in figure (5.58). The straight line drawn in this figure gives the fitted value n of 0.51, lower than both the value n = 2/3 of mean field models [106] and n = 0.55 - 0.7 estimated from Monte Carlo simulations [108]. The prefactor A (in a form $t_{AT} = A(H_a)^n$) in equation (5.17) obtained by fitting is 1.3×10^{-2}; this is two orders of magnitude larger than the model-predicted value (about 10^{-4}). These data therefore do not convincingly conform with the AT model expectations.

Similar analysis was done at x = 0.6. Figure (5.59) displays the upper

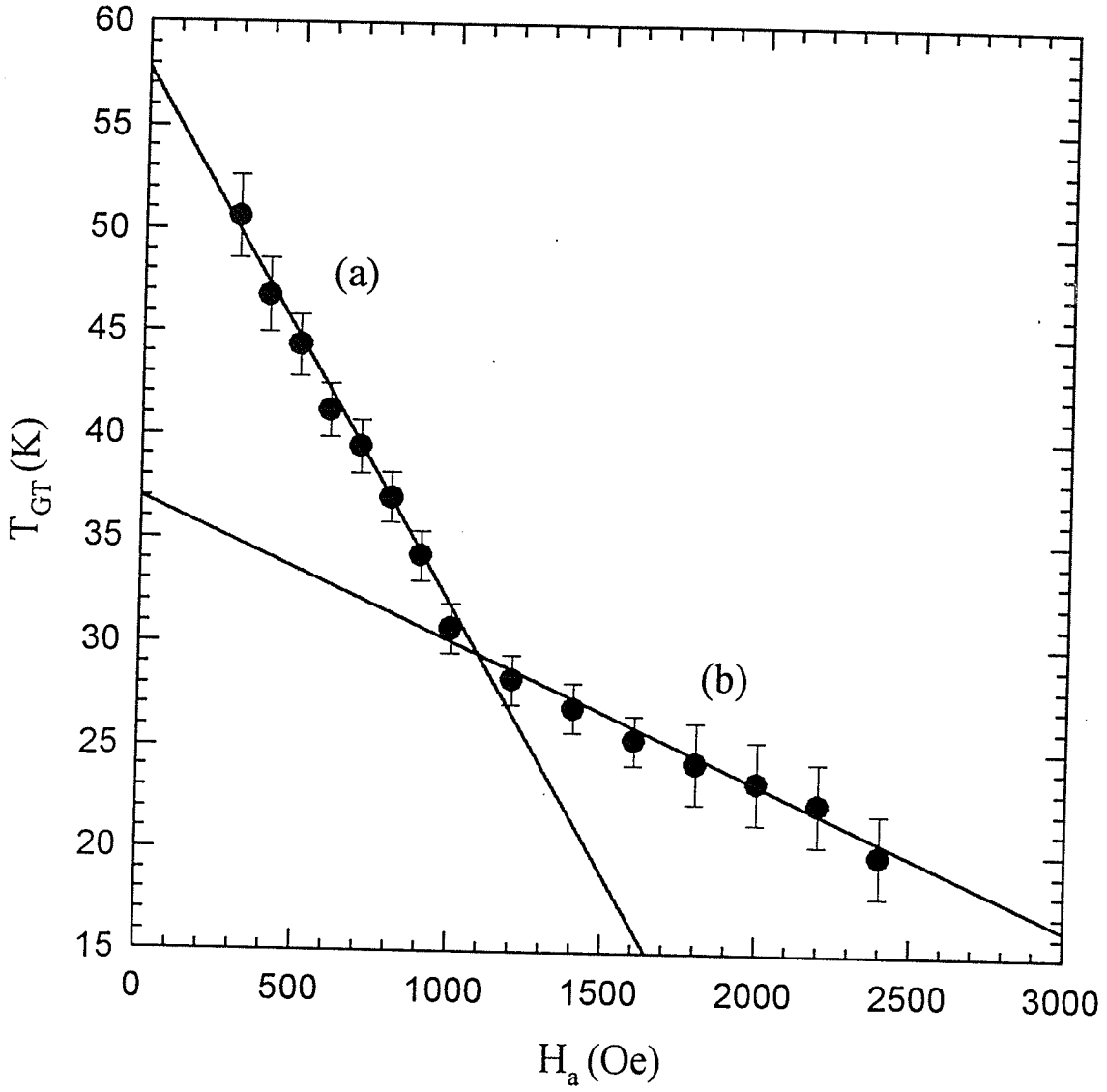

Figure 5.56: The upper peak temperature $T_{GT}(H)$ against the applied field H_a for the sample with x = 0.5

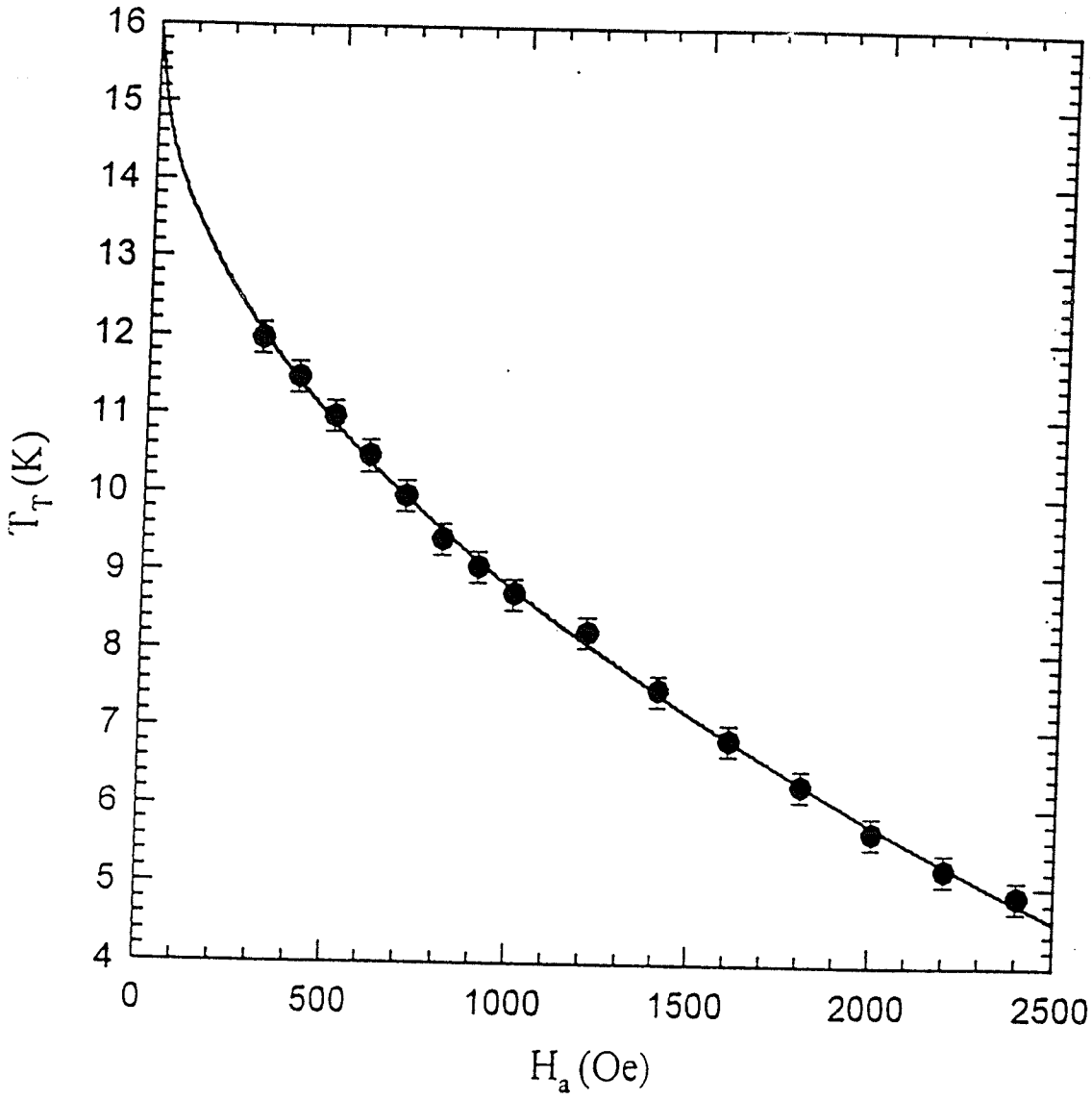

Figure 5.57: The trough temperature T_T(H) against the applied field H_a for the sample with x = 0.5

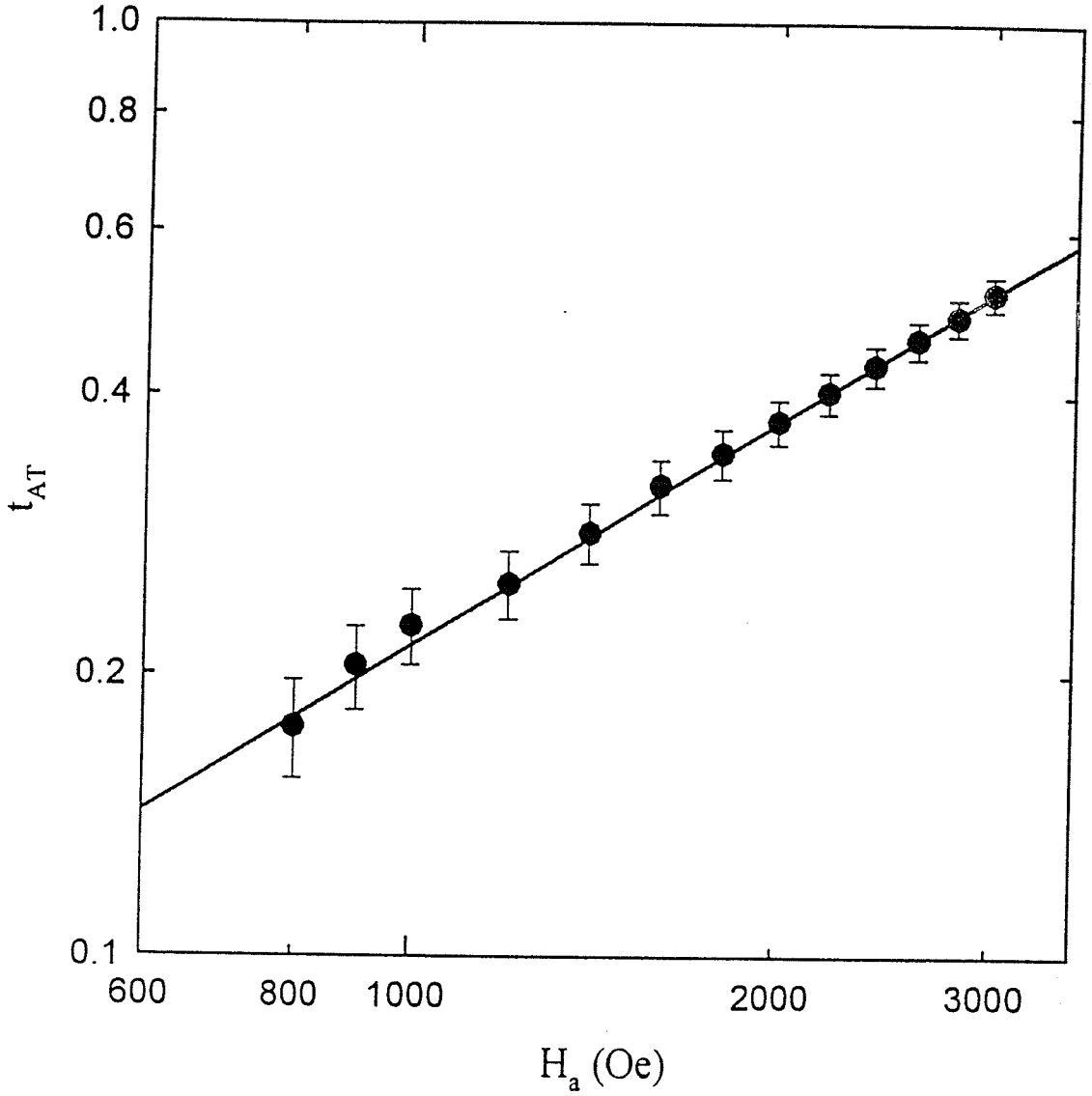

Figure 5.58: The reduced trough temperature t_{AT}(H) against the applied field H_a in a log-log plot for the sample with x = 0.5

peak temperatures $T_{GT}(H)$ against the applied fields H_a; the straight lines drawn through the data yield

$T_{GT}(0) = 37.5\ (\pm\ 1.5)$ K, B = -1.2 $\times$ 10^{-2} k/Oe (in low fields below 1000 Oe)

$T_{GT}(0) = 28.0\ (\pm\ 1.5)$ K, B = -2.4 $\times$ 10^{-3} k/Oe (in high fields above 1000 Oe)

Both prefactors are two or three orders of magnitude larger than the model prediction, according to the equation (5.18), indicating again the discrepancy between the experimental data and the model prediction. Also, the trough temperature vs applied field is plotted in figure (5.60); the line drawn gives $T_{AT}(0) = 9.5$ K. If this estimate for $T_{AT}(0)$ is used, the t_{AT} vs H_a (a double log-log plot) reproduced in figure (5.61) is obtained. The straight line fitted gives the n value of 0.78, which is larger than both value n = 2/3 from mean field models and n = 0.55-0.7 estimated from Monte Carlo simulations. The prefactor A is 1.03 $\times$ 10^{-3}, still an order magnitude larger than the model prediction.

These data analyses for both the x = 0.5 and 0.6 samples thus indicate that these low temperature features do not correspond to the vector model predictions for either the GT or the AT line, very similar to that reported earlier for amorphous $(Fe_{1-x}\ Mn_x)_{75}P_16B_6Al_3$ [109]. The above discussion is complemented with a further investigation of the non-linear magnetic behaviour and temperature-dependent low field magnetization, as presented below.

Non-linear susceptibility

The non-linear magnetic behaviour is examined in order to further investigate the above features. The magnetization M can generally be expressed as an

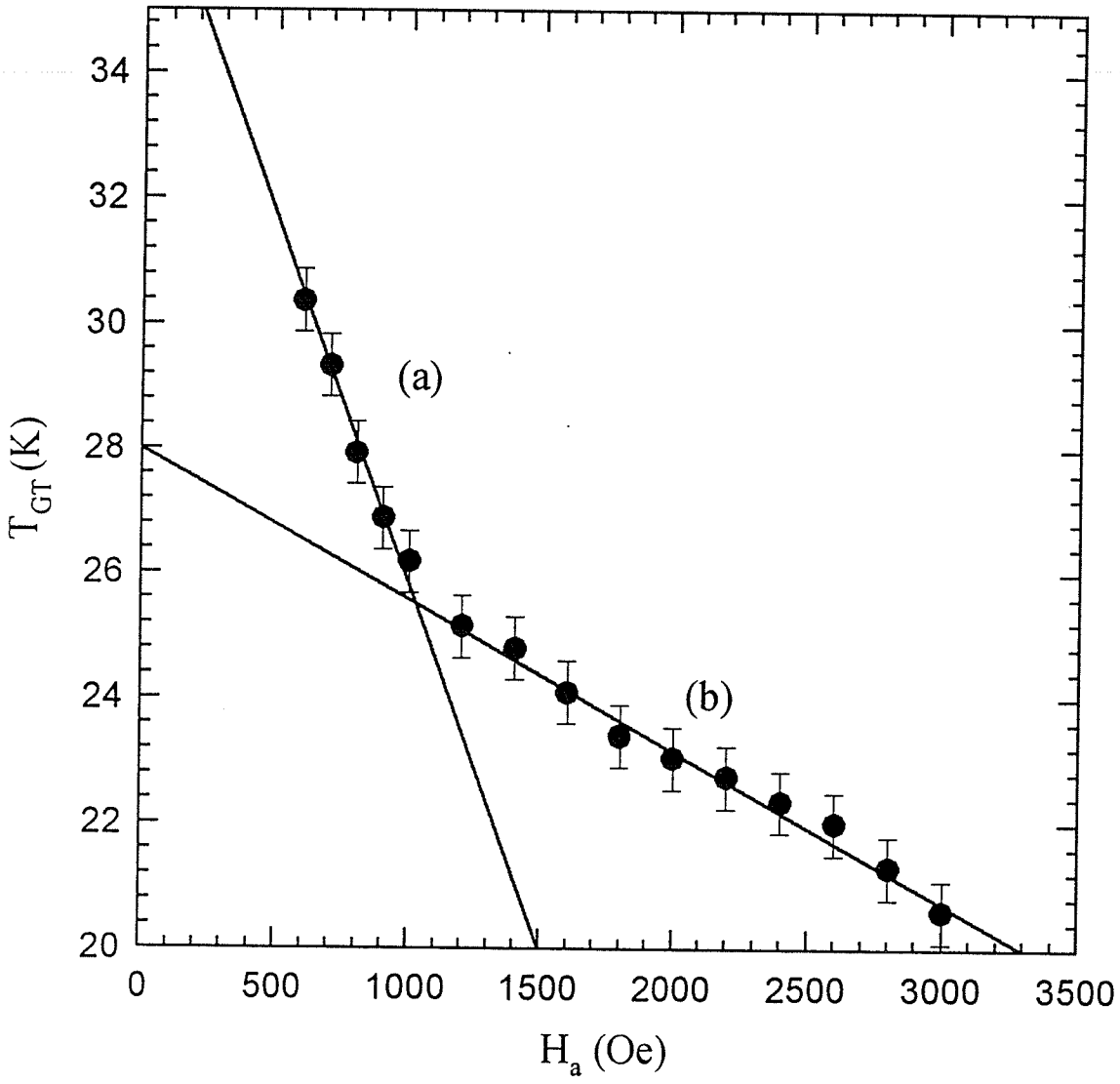

Figure 5.59: The upper peak temperature $T_{GT}(H)$ against the applied field H_a for the sample with x = 0.6

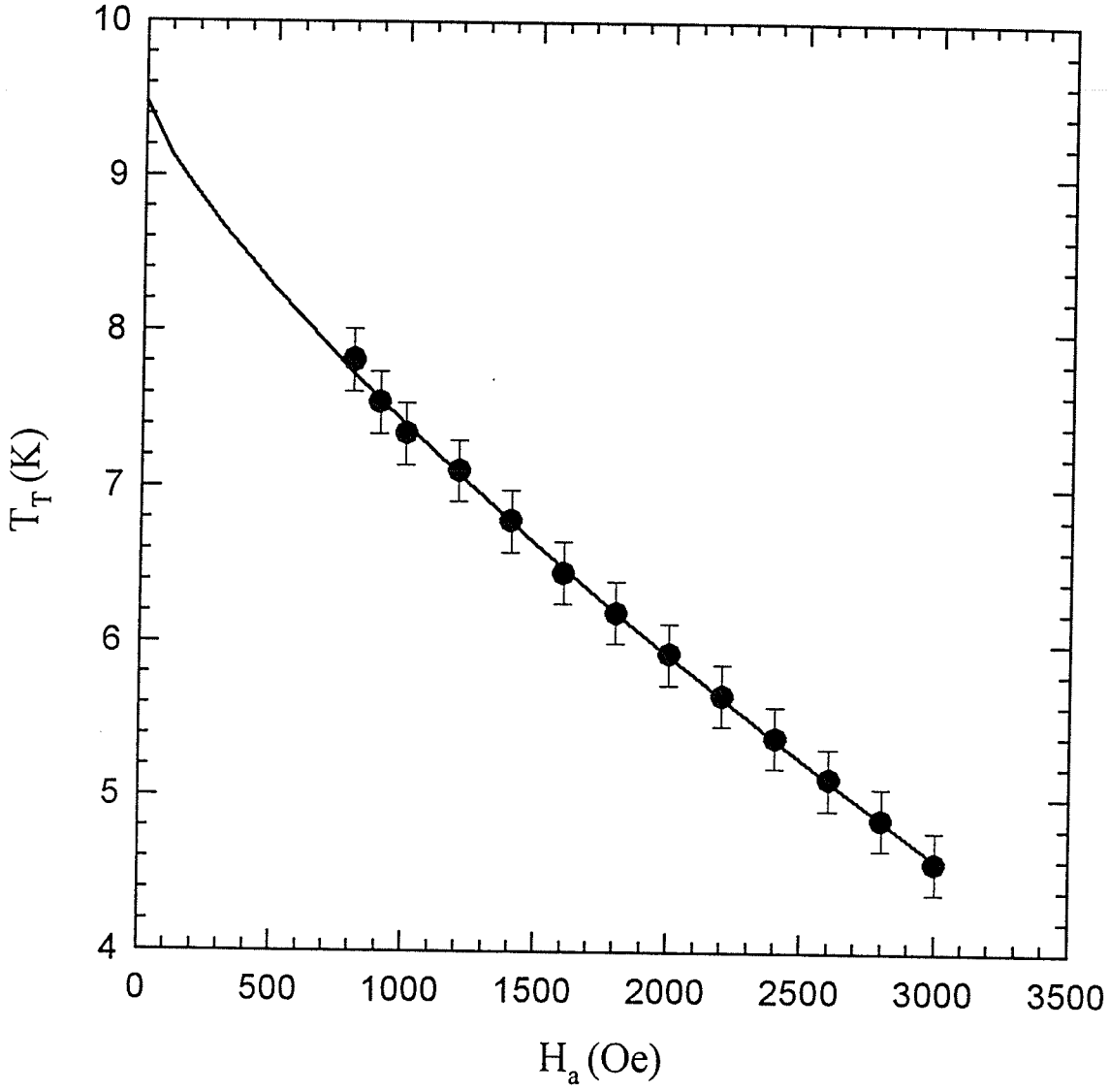

Figure 5.60: The trough temperature T_T(H) against the applied field H_a for the sample with x = 0.6

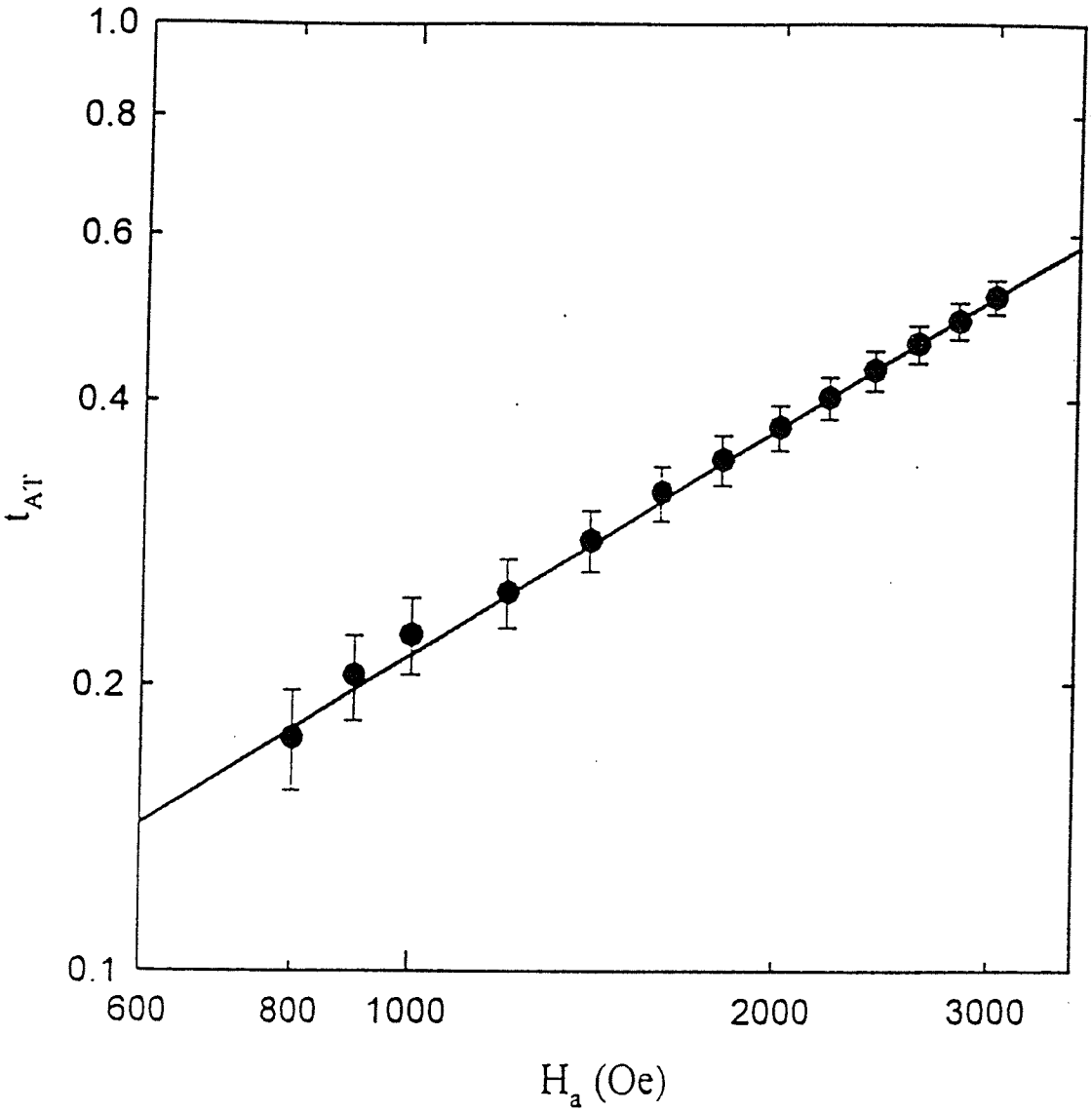

Figure 5.61: The reduced trough temperature t_{AT}(H) against the applied field H_a in a log-log plot for the sample with x = 0.6

odd power series with respect to the applied field H [111, 112]:

$$M = \chi_0 H + \chi_2 H^3 + \chi_4 H^5 + \cdots \tag{5.19}$$

where the coefficient χ_0 is linear response; χ_2 and χ_4 are various non-linear responses. When an ac exciting field $H = H_0 \sin \omega t$ is applied, the linear and non-linear susceptibilities χ_0', χ_2' etc are determined experimentally by detecting the fundamental (M_1), the third harmonic (M_3), etc, components of the ac magnetic response as follows:

$$\chi = dM/dH \propto \chi_0' \cos \omega t - 3/4\chi_2' H_0^2 \cos 3\omega t + 5/16\chi_4' H_0^4 \cos 5\omega t - \cdots \tag{5.20}$$

in which

$$\chi_0' = \frac{M_1}{H_0} = \chi_0 + 3/4\chi_2 H_0^2 + 5/8\chi_4 H_0^4 + \cdots \tag{5.21}$$

$$\chi_2' = \frac{-4M_3}{H_0^3} = \chi_2 + (5/4)\chi_4 H_0^2 + \cdots \tag{5.22}$$

so that as $H_0 \rightarrow 0$, M_1measures χ_0, M_3 measures χ_2, etc.

The non-linear ac susceptibility as a function of temperature was measured with an ac signal of amplitude 10 Oe and a frequency of 300 Hz using the PPMS system. Experimental data for all Mg doped samples are reproduced in figure (5.62) and (5.63). It is apparent that the non-linear susceptibility under the ZFC condition exhibits a two-peaked structure for $0.05 \leq x \leq 0.45$; a very small second peak at x = 0.5 and a single peak at x = 0.6. The first peak at high temperature, occurring close to T_c, corresponds to the rapid rise in the non-linear

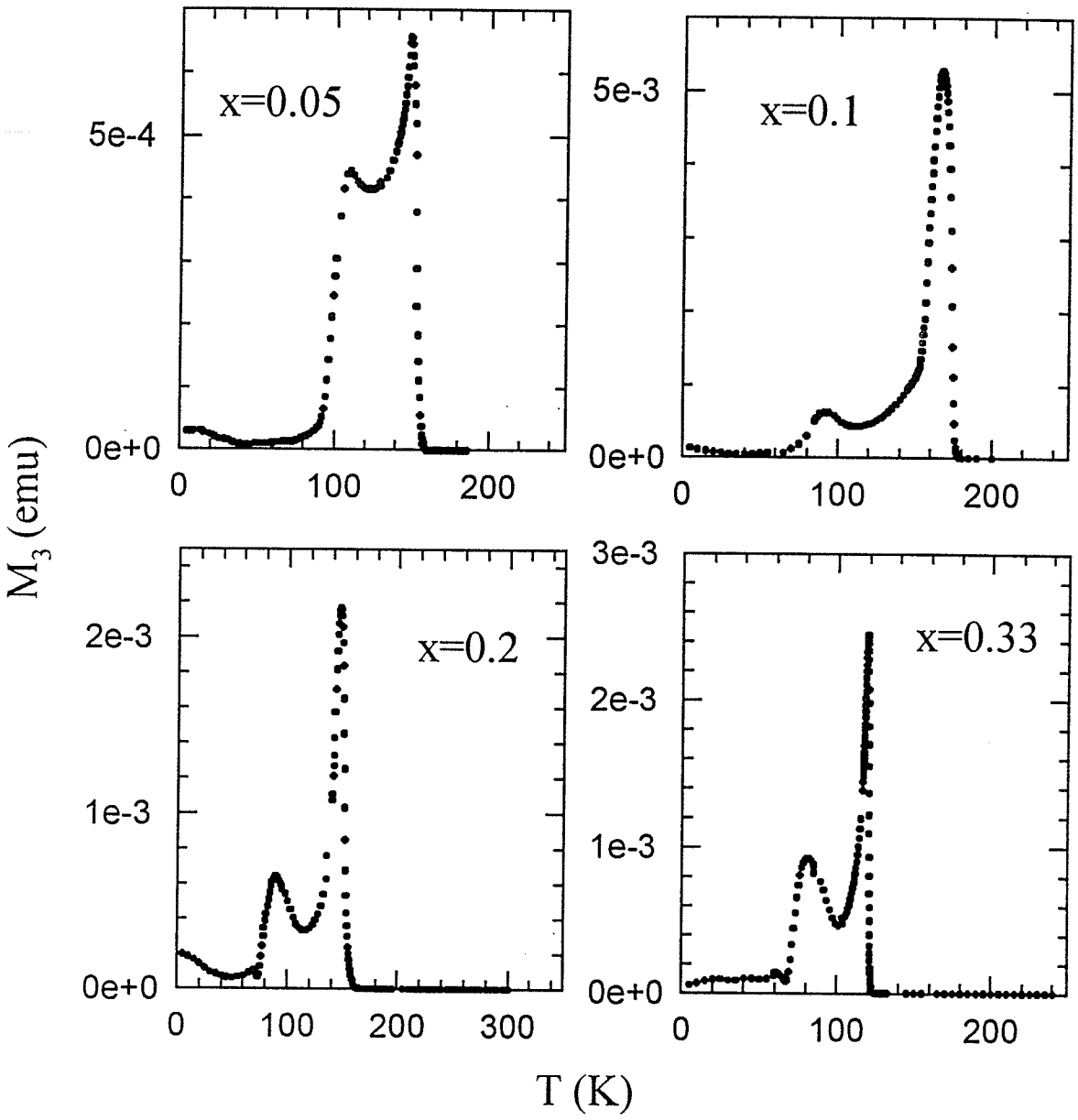

Figure 5.62: The non-linear susceptibility was measured in a driving field of 10 Oe with a frequency of 300 Hz for the samples with x = 0.05, 0.1, 0.2, 0.33.

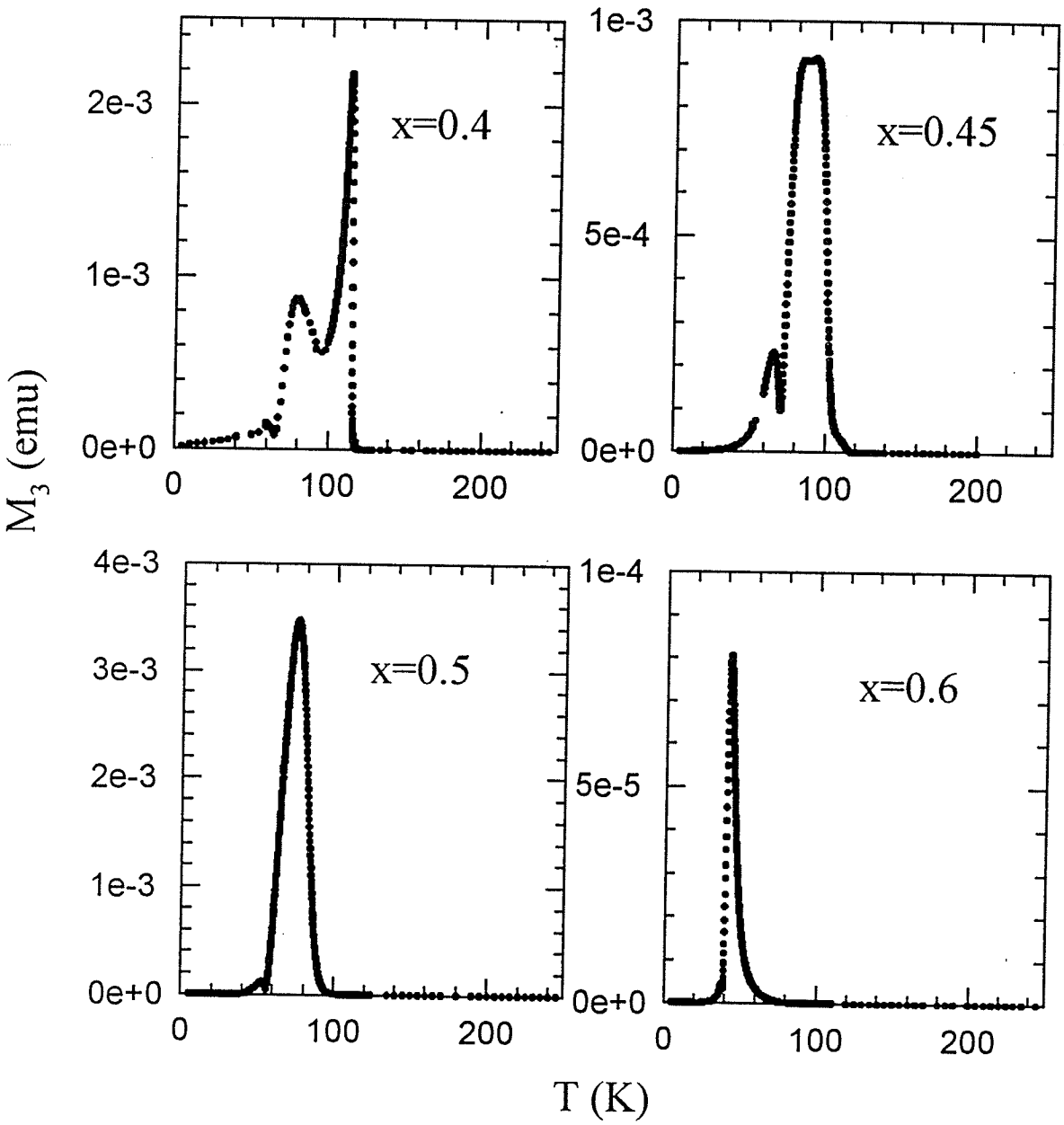

Figure 5.63: The non-linear susceptibility was measured in a driving field of 10 Oe with a frequency of 300 Hz for x = 0.4, 0.45, 0.5, 0.6.

susceptibilities, χ_2, which also diverge at the onset of ferromagnetic ordering. This can be understood using the conventional scaling theory introduced earlier in this thesis. As presented in chapter 3, the static scaling law equation of state gives the following relationship when $T>T_c$

$$m = t^{\beta} F[\frac{h}{t^{\gamma+\beta}}] = t^{\beta}[\frac{h}{t^{\gamma+\beta}} - \frac{h^3}{t^{3\gamma+3\beta}} + \cdots] \tag{5.23}$$

where the reduced magnetization m is expressed as an odd power series in the linear scaling field $h \propto H_i/T_c$ and $t = |T\text{-}T_c|/T_c$. The scaling function F is an odd function of its argument as is, for example, the Brillouin function.

From equation (5.23) it can be seen that the linear susceptibility $\chi_0 = m/h$ ($h \rightarrow 0$) diverges as $t^{-\gamma}$ when $T \rightarrow T_c$, an often used relationship in critical analysis; also the non-linear susceptibility χ_2 (M_3) diverges as $t^{-3\gamma-2\beta}$ as $T \rightarrow T_c$ from above T_c. This effect is evident in figure (5.62) and (5.63). Taking the $x = 0.33$ sample as an example, a log-log plot of M_3 vs t ($T_c = 118$ K) is reproduced in figure (5.64). The data were fitted quite well with the Heisenberg model exponents $(3\gamma + 2\beta) = 4.89$. As shown by the solid line, deviations above $t \sim 10^{-1}$ and below $t \sim 10^{-2}$ are evident; the former are due to passing out of the critical regime, while the latter reflect the effect of a large exciting field. The term χ_4, of opposite sign, is mixed into the χ_2 term when H_0 is finite, and this induces the decrease in these data which occurs most strikingly as $T \rightarrow T_c$. While this first peak at high temperature is well described using scaling theory, the second peak at low temperature is of more interest here since such a double-peaked structure is often associated with potentially reentrant behaviour, i.e. a possible transition

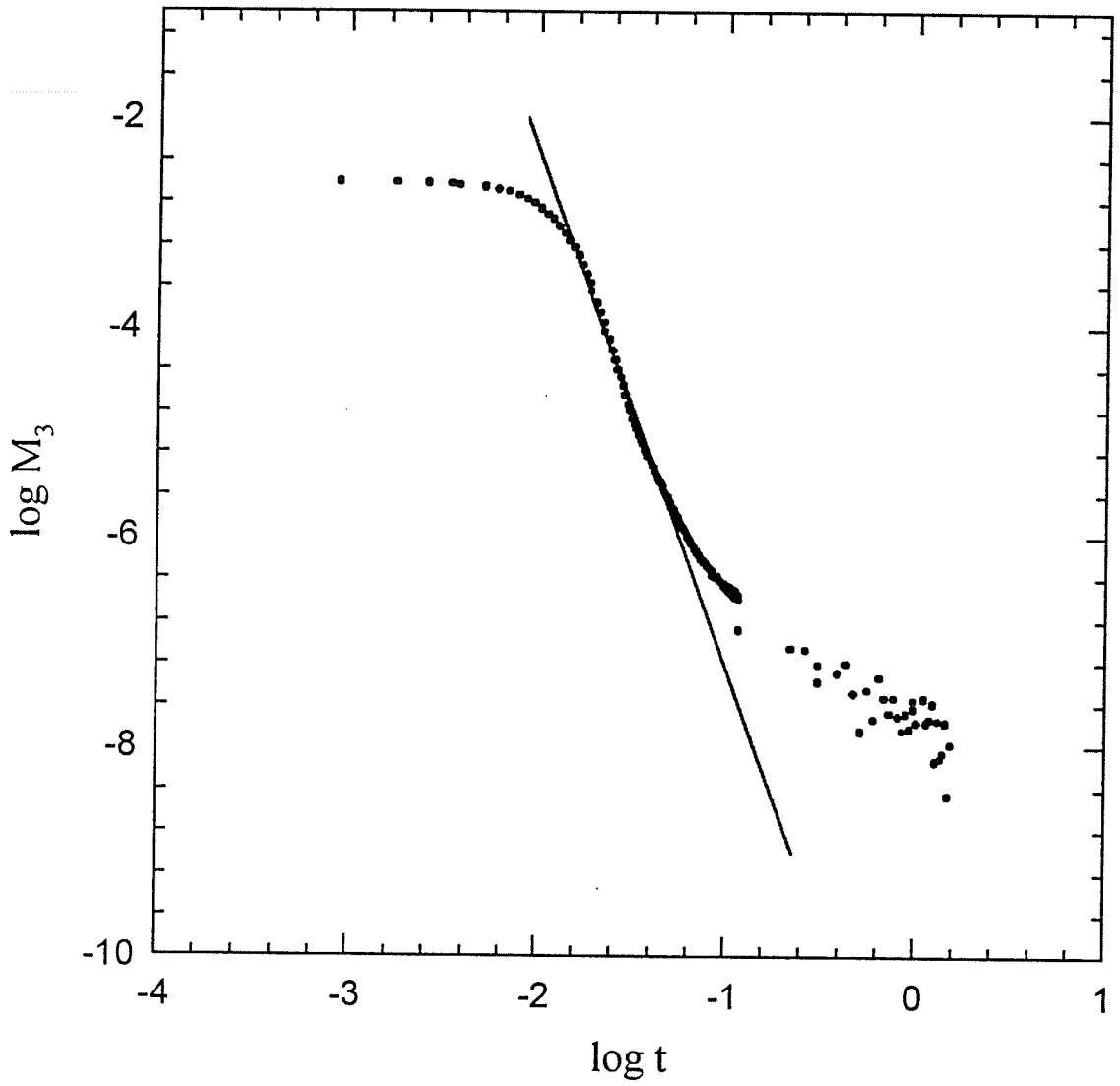

Figure 5.64: The plot of M_3 versus t on a double logarithmic scale. The solid line is fitted using Heisenberg model exponents ($3\gamma + 2\beta = 4.89$)

from the ferromagnetic to the spin glass state, [46, 47, 109], although this feature is not predicted by broken-symmetry models [110]. However mean-field Ising models produce such features which are indeed often observed experimentally; this second peak in the non-linear component χ_2 is thus often taken as signalling the reentrant transition. However, the above investigation raises questions about potential reentrant behaviour, which is examined in more detail by comparing model predictions with experiment. This comparison reveals discrepancies. First, the second (lower) peak is predicted by Ising models to be stronger than the first peak; the experimental data are not in agreement. Secondly, reentrant behaviour, associated with crossing the GT-line (or AT-line) as discussed above, should have a correspondence in the non-linear response, specifically the second peak temperature should agree with the estimated $T_{GT}(0)$ (or $T_{AT}(0)$); this does not occur here. Thirdly, the second peak in χ_2 is frequently associated with a rapid decrease observed in the linear component $\chi(0,T)$; no such feature appears in $\chi(0,T)$. Therefore, although the non-linear response $\chi_2(M_3)$ superficially exhibits reentrant features, the possibility of a true reentrant phase transition is basically precluded by the above comparisons. Such behaviour most likely originates from technical processes rather than critical ones, a contention that is supported by an examination of the ZFC and FC magnetization measured in low field.

ZFC and FC magnetization

Figure (5.65) reproduces the ZFC and FC magnetization curves measured in a field of 10 Oe for samples with $x = 0.45$, 0.5 and 0.6. The data show behaviour

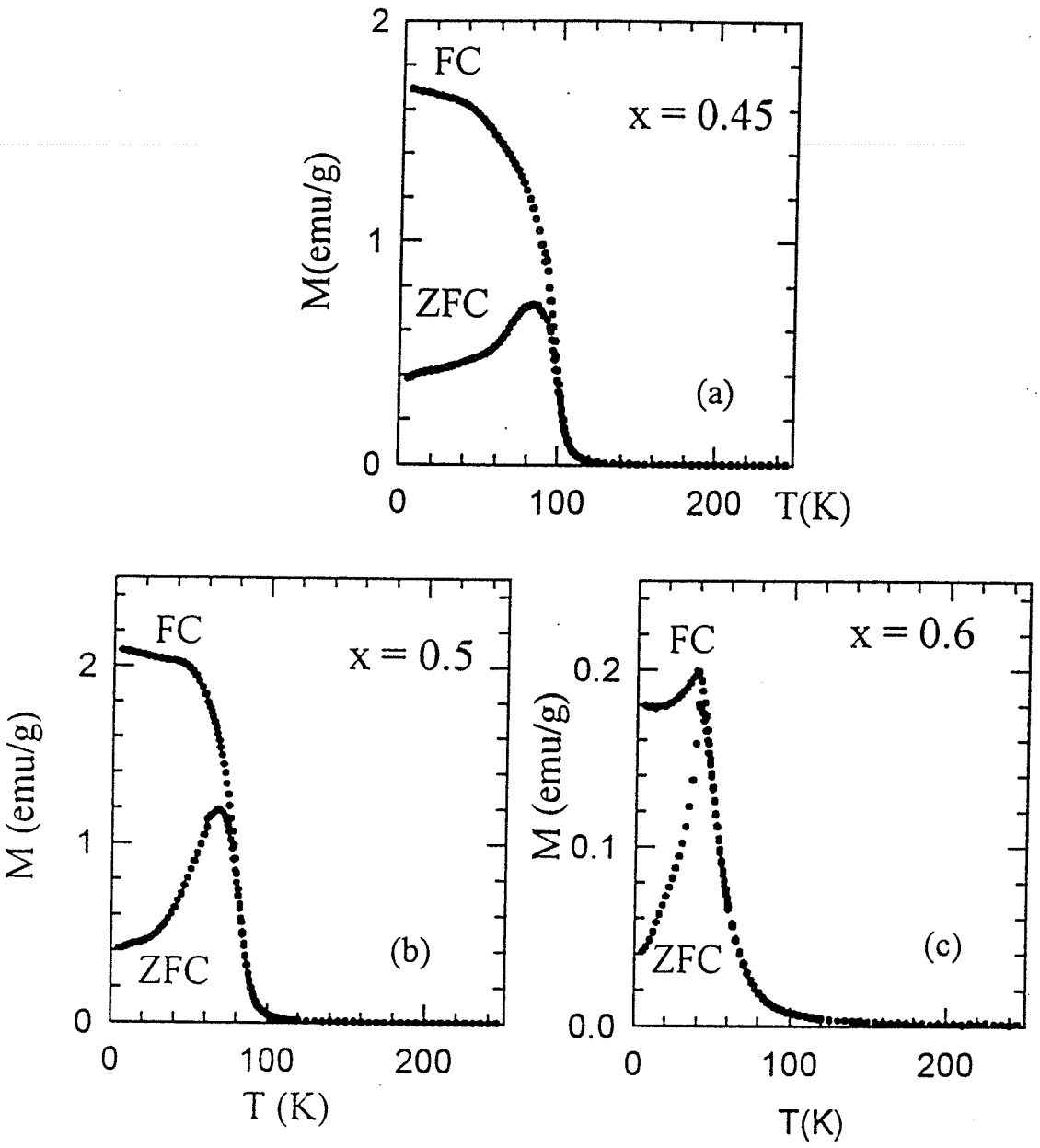

Figure 5.65: The temperature dependence of the ZFC and FC magnetization curves measured in a field of 10 Oe for the samples with x = 0.45, 0.5 and 0.6.

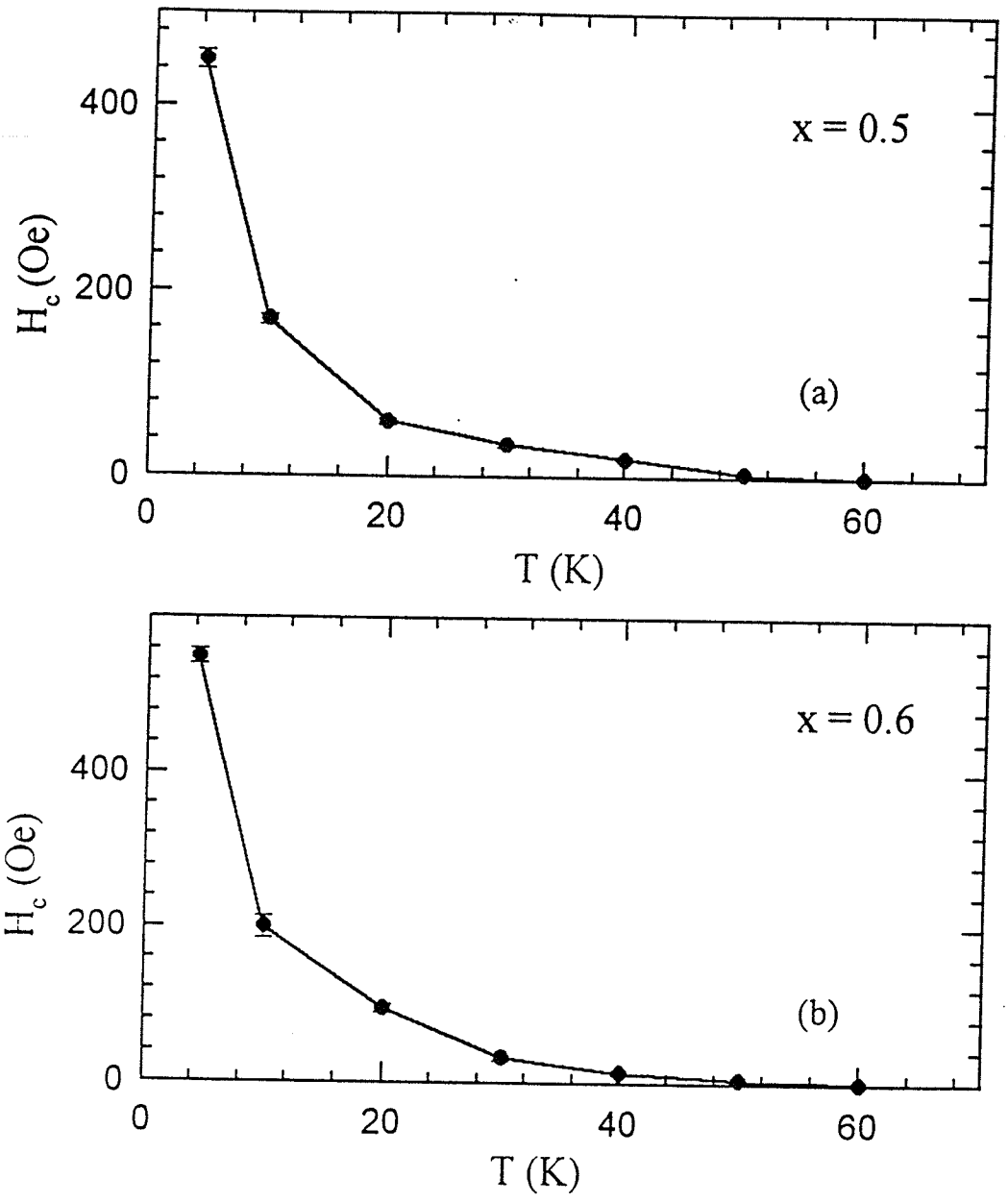

Figure 5.66: The temperature dependence of the coercivity for the samples with x = 0.5 and 0.6

similar to that for $0.05 \leq x \leq 0.4$. For these lower x samples the ZFC exhibit the rapid and clear decline at the temperature that can be seen to correspond with the appearance of the lower peak in non-linear response (M_3). This ZFC feature was already discussed and modeled in the x = 0.05 specimen in detail in association with the hysteresis and coercivity behaviour. This suggests it originates from technical processes for those samples with $0.05 \leq x \leq 0.45$. At higher x ($\geq$ 0.5), the correspondence is not so clear. Specifically, for the x = 0.5, the ZFC behaviour does not show any clear sign corresponding to the very small peak (just below the first peak corresponding to the onset of ferromagnetic ordering) in the non-linear susceptibility. For x = 0.6, the ZFC shows a rapid decline below its peak temperature very close to T_c. Only a single peak in non-linear response exists, which represents the ferromagnetic ordering. This rapid decrease in the ZFC branch can be related to the rapid increase in coercivity with decreasing temperature as shown in Figure (5.66).

In addition to this temperature-dependent feature, the significant enhancement in coercivity with increasing doping level x, as indicated in figure (5.67), plays an important role for the evolution of the above behaviour displayed by both the ZFC/FC and non-linear susceptibility. Other relevant experimental data are the temperature-dependent ZFC magnetizations measured in fields between 200 and 2.4 kOe as shown in figure (5.68). It is seen that the magnetization falls at low temperature well below T_c. Although this drop in the magnetization data appears to have a correlation with the various features discussed above, close examination fails to establish a convincing relationship between them. The coercivity-related

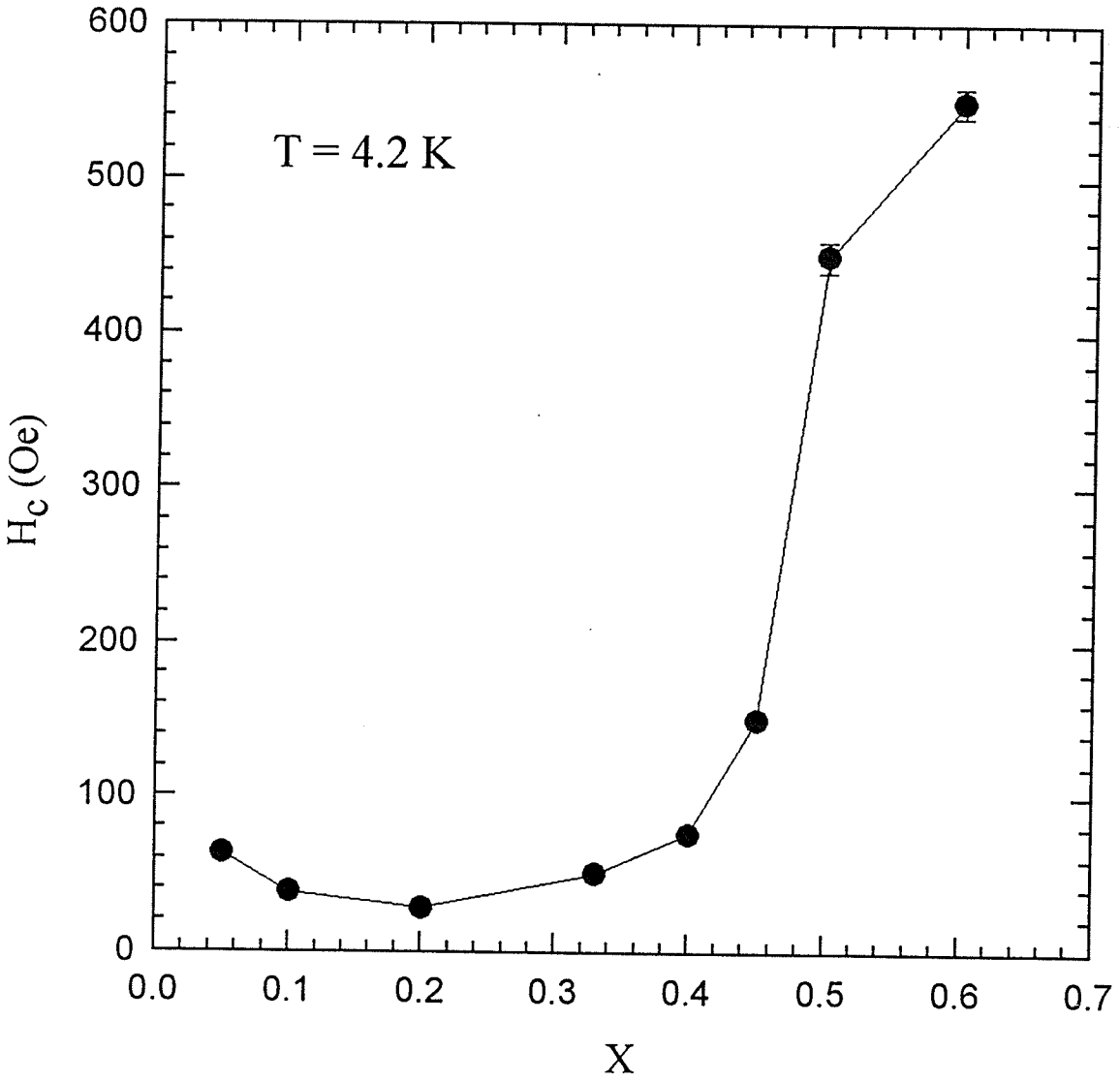

Figure 5.67: The coercivity H_c at temperature 4.2 K versus the composition x.

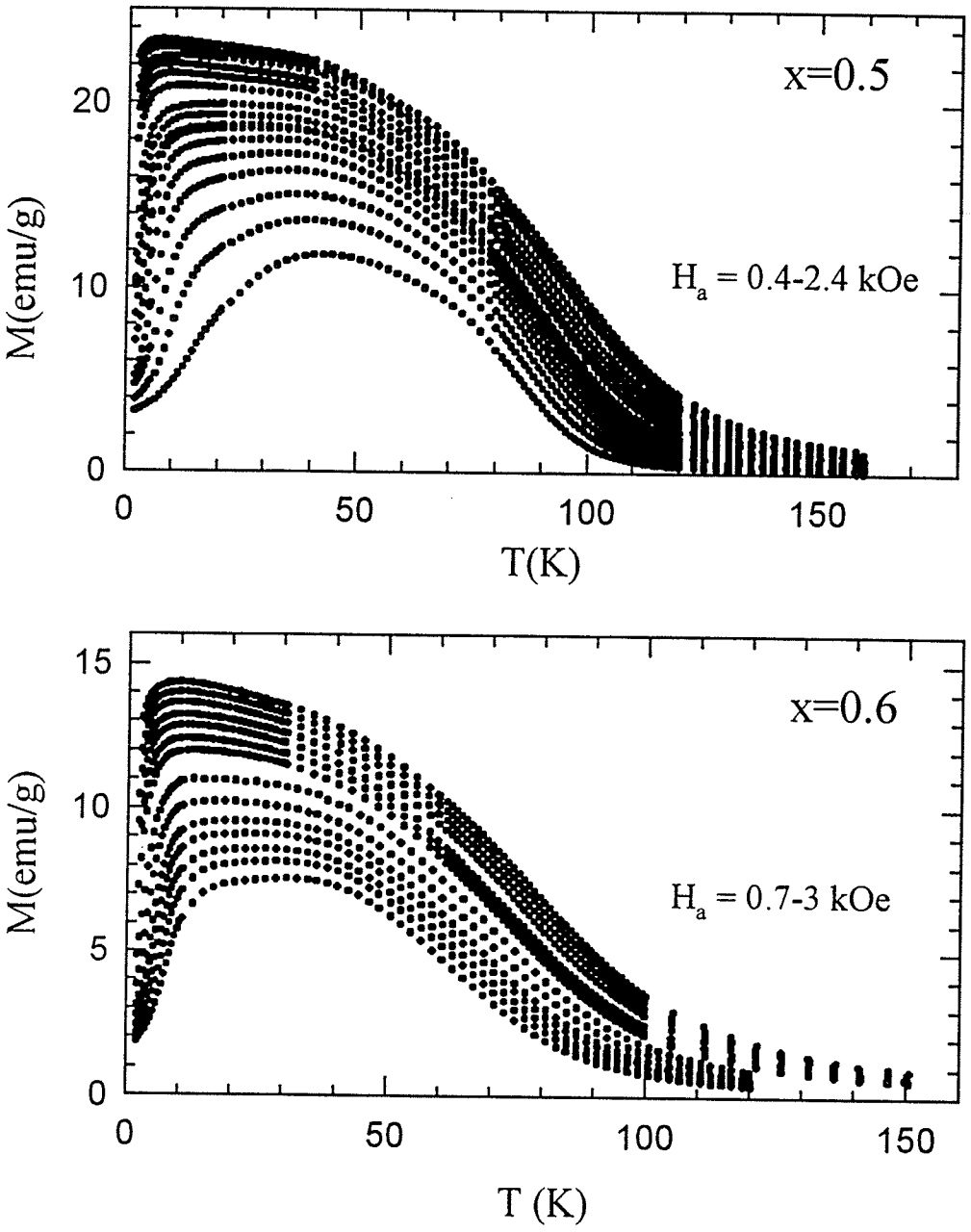

Figure 5.68: The temperature dependence of the magnetization measured in the fields over the indicated range for the $La_{1-x}Mg_xMnO_3$ with x = 0.5 and 0.6.

sources are believed to result in these complications in the magnetic data.

Figure (5.69) displays the saturation moment deduced from magnetization curves taken at 4.2 K by extrapolating M vs H^{-1} plots. This moment actually decreases with increasing x, showing the opposite trend to that predicted in a double exchange picture as shown in the inset. This result confirms that a double exchange picture alone cannot account comprehensively for the properties of doped manganese perovskites, as first reported by a detailed analysis of transport data. The transport behaviour of the present samples is investigated and presented below.

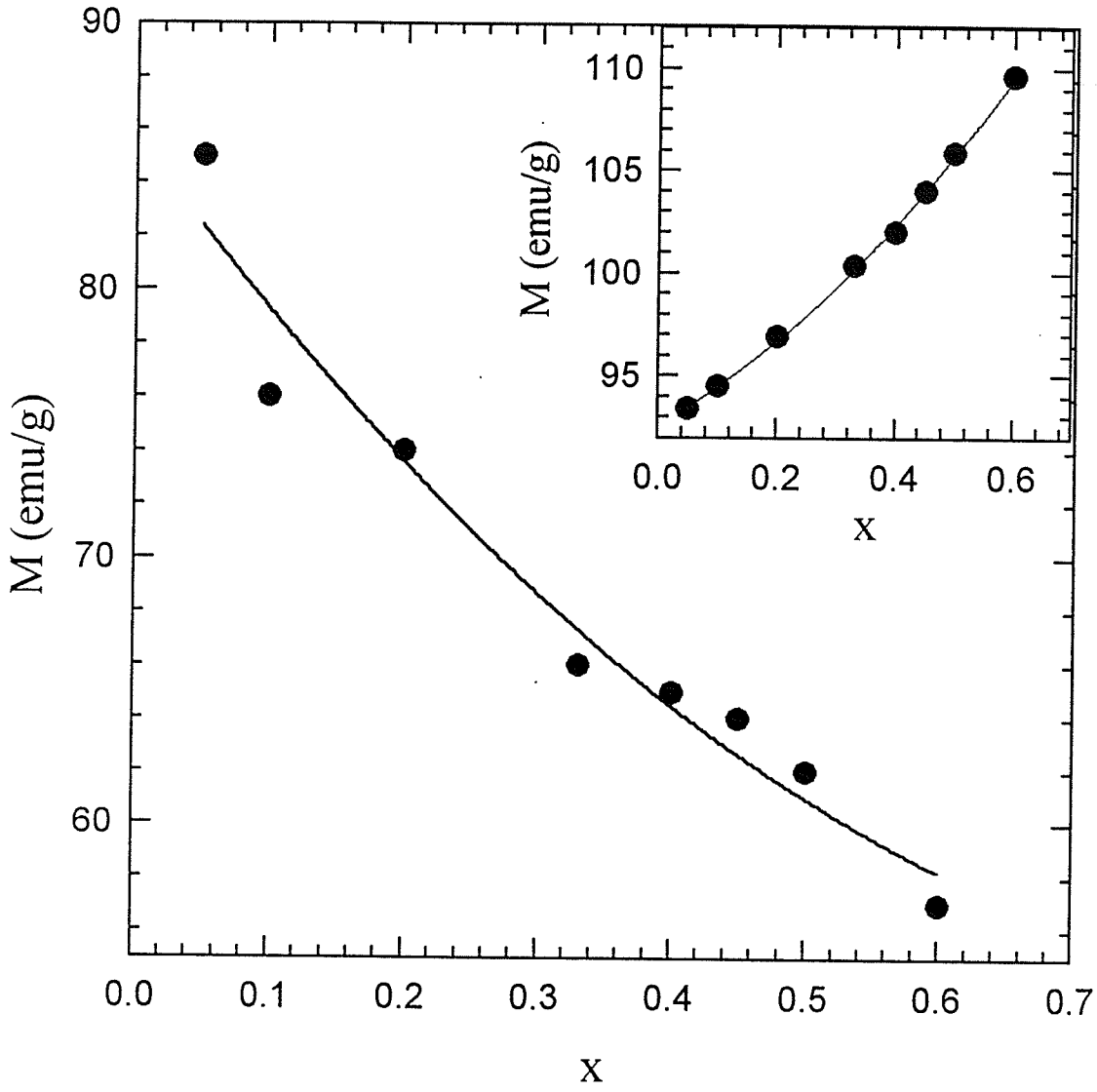

Figure 5.69: The composition dependence of the saturation moment measured by extrapolating M vs H^{-1} at 4.2 K. The inset gives the values predicted by the double exchange model.

5.5.3 Transport Properties

The single common feature in the magnetic properties of $La_{1-x}Mg_xMnO_3$ is that this system always undergoes a paramagnetic to ferromagnetic transition at an ordering temperature, T_c, the magnetic phase transition belonging to the continuous/secondary order type. The magnetic state below T_c, however, displays some unusual features, but these appear at high doping level x. Here the transport behaviour, both above and below T_c, is investigated and discussed.

The resistivity data for all samples in zero field and an applied field of 1.5 T were collected from about 80 K to room temperature. Figure (5.70) and (5.71) show the temperature dependence of the resistivity in the form $\ln \rho$ versus temperature; Since all the specimens examined remain insulating, their continuing increase in resistivity $\rho(T)$ with decreasing temperature generally precluded measurements being carried out below about 80 K. Most important, no metal-insulator transition was observed in the vicinity of the paramagnetic/ferromagnetic transition temperature in any of the samples studied ($0.05 \leq x \leq 0.6$). For the samples with x = 0.05, 0.33, 0.4, 0.45, 0.5 and 0.6, $\rho(T)$ increases monotonically with decreasing temperature with no obvious anomaly in $\rho(T)$ or its derivative at T_c. For x = 0.1 and 0.2 $d\rho(T)/dT$ displays a maximum in the vincinity of T_c but remains negative. At a true metal-insulator transition this derivative displays a maximum but also changes sign from the negative to positive. A similar behaviour was reported in earlier measurements on the $La_{1-x}Sr_xMnO_3$ system [98], in which, however, further increase in x (≥ 0.175) raises T_c and results in a true metal-insulator transition. By contrast, in the $La_{1-x}Mg_xMnO_3$, increasing

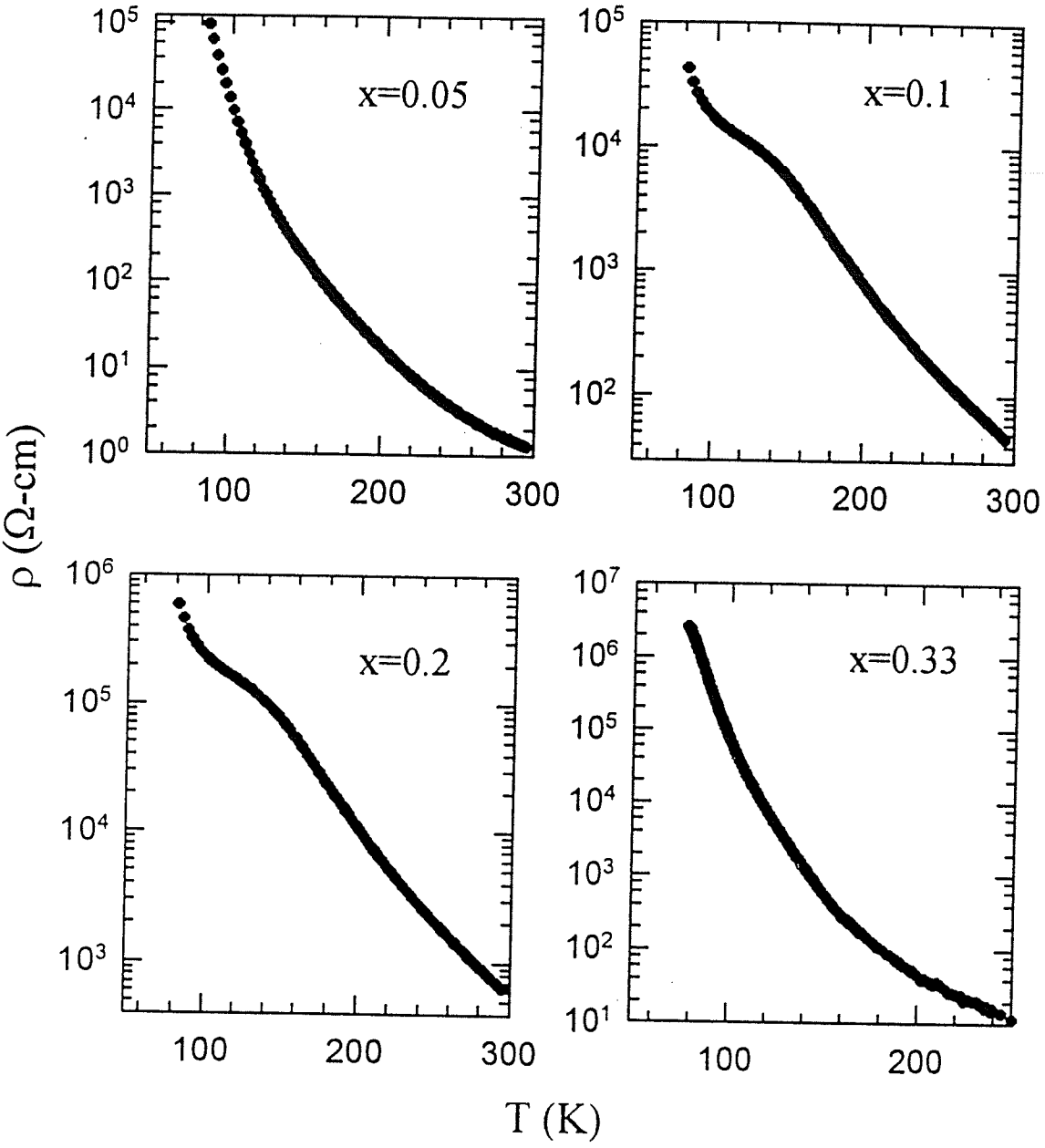

Figure 5.70: The temperature dependence of the zero-field resistivity is plotted in a form of $\ln \rho$ vs T for the x = 0.05, 0.1, 0.2 and 0.33 samples.

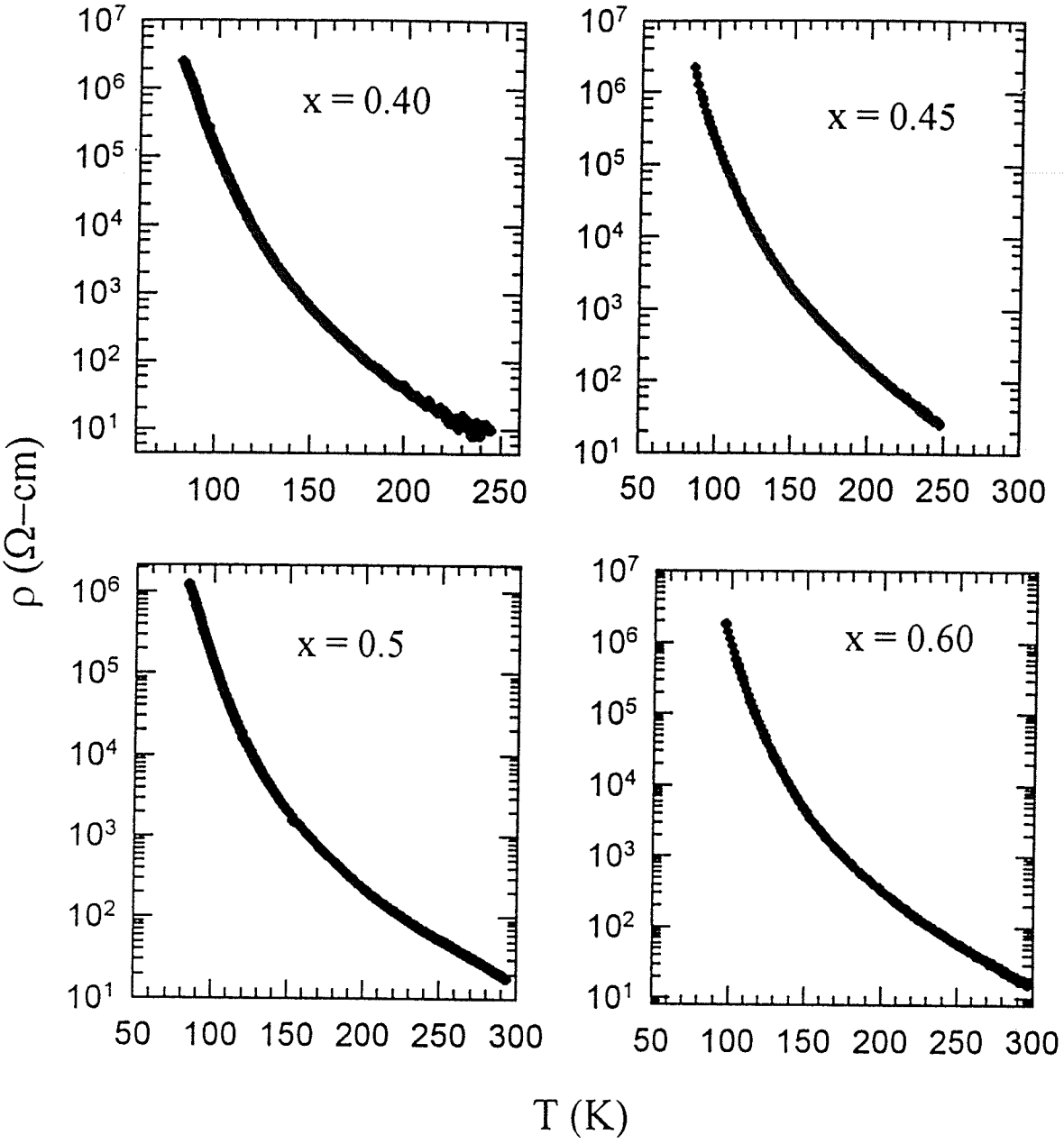

Figure 5.71: The temperature dependence of the zero-field resistivity is plotted in a form of the $\ln(\rho)$ vs T for the x = 0.4, 0.45, 0.5, and 0.6 samples

x beyond 0.1 - 0.2 causes a reduction in T_c and leads to the continuing monotonic semiconducting response. These results indicate a strong tendency at x $\sim 0.1 - 0.2$ to undergo such a transition, but this is suppressed likely by the influence of the average A-site size on the Mn(e_g) - O($2p_\sigma$) bandwidth and the associated Mn-O-Mn bond angle.

When these experimental data are replotted in a double logarithmic plot in a form suggested by the theory of small polaron hopping, viz. $\rho(T) = \rho_0 T^n e^{E_a/k_B T}$, as done for the Ar-annealed $La_{0.67}Ca_{0.33}MnO_3$ sample, it can be clearly seen that the slope shows a marked difference below and above the critical point T_c defined by the susceptibility data. These resistivity data for $La_{1-x}Mg_xMnO_3$ are thus analyzed and discussed in a manner similar to that used for the Ar-annealed $La_{0.67}Ca_{0.33}MnO_3$ sample.

Again, the small polaron model appears to be more applicable than others, such as a band-gap or variable range hopping models, as judged by the standard errors. Both adiabatic and non-adiabatic limits are utilized to deal with the experimental data. The fitted parameters are summarized in the Table (5.5) and (5.6). Taking $La_{0.95}Mg_{0.05}MnO_3$ as an example, a typical plot of $\ln(\rho/T^{3/2})$ versus 1/T in zero field is reproduced in figure (5.72). The data for this sample in Table (5.5) show a relatively comparable fitting for both adiabatic and non-adiabatic models. The activation energy E_a drops upon entering the ferromagnetic phase for both models, but not as much as in Ar-annealed $La_{0.67}Ca_{0.33}MnO_3$. The attempt frequency, Ω_0, and the electric coupling factor J for both $T < T_c$ and $T > T_c$ are deduced in terms of the equation (5.11) in those cases where the non-adiabatic

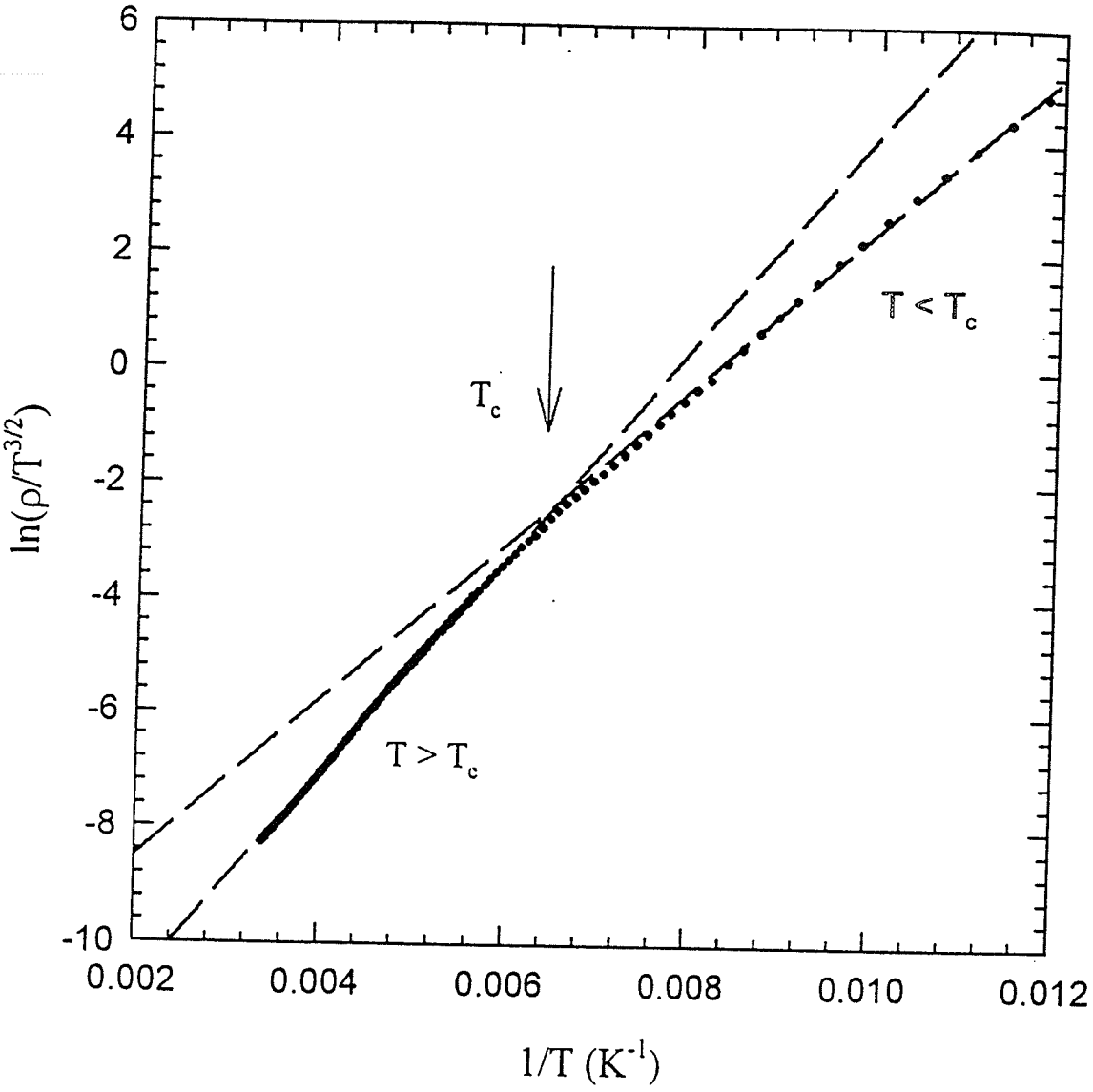

Figure 5.72: The non-adiabatic fit to the zero field resistivity is plotted in a form of $\ln(\rho\ /T^{3/2})$ versus 1/T for the x = 0.05.

Table 5.5: The fitting parameters calculated from the small polaron models

x	T	Adiabatic (n = 1)			Non-Adiabatic (n = 3/2)		
		E_a (meV)	ρ_0 (Ω-cm/K)	Std Err	E_a (meV)	ρ_0 (Ω-cm/$K^{3/2}$)	Std Err
0.05	$T > T_c$	139	7.8×10^{-6}	0.014	171	3.1×10^{-7}	0.012
	$T < T_c$	116	1.6×10^{-4}	0.049	121	9.2×10^{-6}	0.054
0.1	$T > T_c$	176	1.7×10^{-4}	0.033	186	6.5×10^{-6}	0.036
	$T < T_c$	-	-	-	-	-	-
0.2	$T > T_c$	176	2.3×10^{-3}	0.034	192	6.8×10^{-5}	0.025
	$T < T_c$	-	-	-	-	-	-
0.33	$T > T_c$	192	6.5×10^{-6}	0.004	202	2.8×10^{-7}	0.004
	$T < T_c$	135	3.6×10^{-4}	0.017	140	2.1×10^{-5}	0.021
0.4	$T > T_c$	160	1.8×10^{-5}	0.093	165	9.7×10^{-7}	0.091
	$T < T_c$	116	1.2×10^{-3}	0.047	123	8.4×10^{-5}	0.054
0.45	$T > T_c$	129	5.5×10^{-4}	0.11	139	2.2×10^{-5}	0.09
	$T < T_c$	-	-	-	-	-	-
0.5	$T > T_c$	125.8	6.8×10^{-4}	0.17	132.4	3.1×10^{-5}	0.19
	$T < T_c$	-	-	-	-	-	-
0.6	$T > T_c$	154.6	6.2×10^{-4}	0.14	162.0	9.1×10^{-6}	0.16
	$T < T_c$	-	-	-	-	-	-

Table 5.6: The deduced parameters from the transport data

x	$T > T_c$				$T < T_c$			
	Adiabatic/phase separation		Non-adiabatic		Adiabatic/phase separation		Non-adiabatic	
	Ω_0	l(Å)	Ω_0	$\|J\|$ (meV)	Ω_0	l(Å)	Ω_0	$\|J\|$ (meV)
0.05	6×10^{13}	0.7	9×10^{13}	—	3×10^{12}	0.4	4×10^{12}	11
0.10	1.5×10^{12}	0.4	2.5×10^{12}	10	—	—	—	—
0.20	6×10^{10}	0.2	1×10^{11}	2.5	—	—	—	—
0.33	1.5×10^{13}	0.9	2.5×10^{13}	—	3×10^{11}	0.2	5×10^{11}	3.5
0.40	5×10^{12}	0.7	6×10^{12}	16	4×10^{10}	0.3	1×10^{11}	1.5
0.45	1.6×10^{11}	0.4	2.2×10^{11}	3.1	—	—	—	—
0.50	1.3×10^{11}	0.4	1.9×10^{11}	2.5	—	—	—	—
0.60	1.4×10^{11}	0.4	6.9×10^{11}	5.2	—	—	—	—

model is deemed appropriate; in addition, the tunneling length l is derived on the basis of the phase-separation model. As shown in Table (5.6), for the x = 0.05 sample, Ω_0, estimated from the prefactor ρ_0, falls in the range of the characteristic optical phonon frequency ω_0 $(10^{13} - 10^{14})$ when $T > T_c$, whereas it has a lower value when $T < T_c$. These indicate that the adiabatic limit is valid when $T > T_c$ and the non-adiabatic limit is operative when $T < T_c$. The estimate of J was done only for $T < T_c$; its value falls between those calculated from available high temperature data on $LaMnO_3$ (26 meV) and $LaCrO_3$ (8 meV) where the non-adiabatic formula was also employed. As to the tunneling length l, the values of 0.7 $\AA$ and 0.4 $\AA$ for both $T > T_c$ and $T < T_c$ are much smaller than that predicted by the phase-separation model, where the value of l is expected as being larger than 10 $\AA$ (polaron radius). This indicates the model is not applicable to the present experimental data, as was also found for the Ar-annealed $La_{0.67}Ca_{0.33}MnO_3$ studied previously. In addition, the temperature-dependent resistivity in a fixed field of 1.5 T was also measured for x = 0.05, the associated magnetoresistance, $\Delta\rho = (\rho(0,T) - \rho(h,T))/\rho(0,T)$, as a function of temperature, was found to be moderate, not colossal, displaying a broad maximum of some 17 percent near T_c as shown in figure (5.73), the inset illustrates data in a field plotted in a form of $\ln(\rho/T^{3/2})$ versus 1/T. It is evident that these data show a difference in slope above and below T_c despite it not being as distinct as in the zero field data. Further, a reduction in hopping energy below T_c is observed, with the data fits yielding the following parameters values:

$E_a = 156$ meV, $\quad \rho_0 = 7.5 \times 10^{-7}\ \Omega$ cm/K$^{3/2}$ $\quad (T > T_c)$

$E_a' = 118$ meV, $\rho_0 = 1.12 \times 10^{-5}$ Ω cm/K$^{3/2}$ (T < T$_c$)

This analysis suggests that the quasi-itinerant Mn(e_g) electrons have a polaronic character in the paramagnetic phase, reflecting a combination of strong electron-phonon coupling and/or Jahn-Teller distortions, and these Mn(e_g) electrons achieve limited mobility on entering the ferromagnetic state. Obviously polaronic transport persists into the ferromagnetic regime below T_c, too, providing more supportive evidence for polaronic characteristics in the magnetically ordered state but with insulating features, not metallic ones as reported for undepleted $La_{0.67}Ca_{0.33}MnO_3$. The discussion for the Ar-annealed $La_{0.67}Ca_{0.33}MnO_3$, in principle, applies to the current study, specifically to this sample with x = 0.05.

The transport data for all the other samples ($0.1 \leq x \leq 0.6$) are analyzed and discussed in the same way as for the x = 0.05 sample. Below T_c, the fits by polaronic models are possible for the x = 0.33 and 0.4; no fits for the x = 0.1 and 0.2 are possible due to their behaviour of dρ/dT around T$_c$ discussed above; for x = 0.45 - 0.6 fits were precluded owing to the low T$_c$ values there. The estimates for Ω_0 indicate the general applicability of the non-adiabatic limit in the ordered state. In the paramagnetic regime above T_c, the adiabatic model appears to apply to the x = 0.33 (and x = 0.05, noted above), whereas the results for all others are better fitted using the non-adiabatic formalism. Thus no systematic change in model applicability with x is observed. For all samples ($0.05 \leq x \leq 0.6$), further data analysis in the phase separation model yield the tunneling length as being lower than 1 $\AA$, much smaller than model prediction (about 10 $\AA$), indicating significant discrepancy between the experimental data

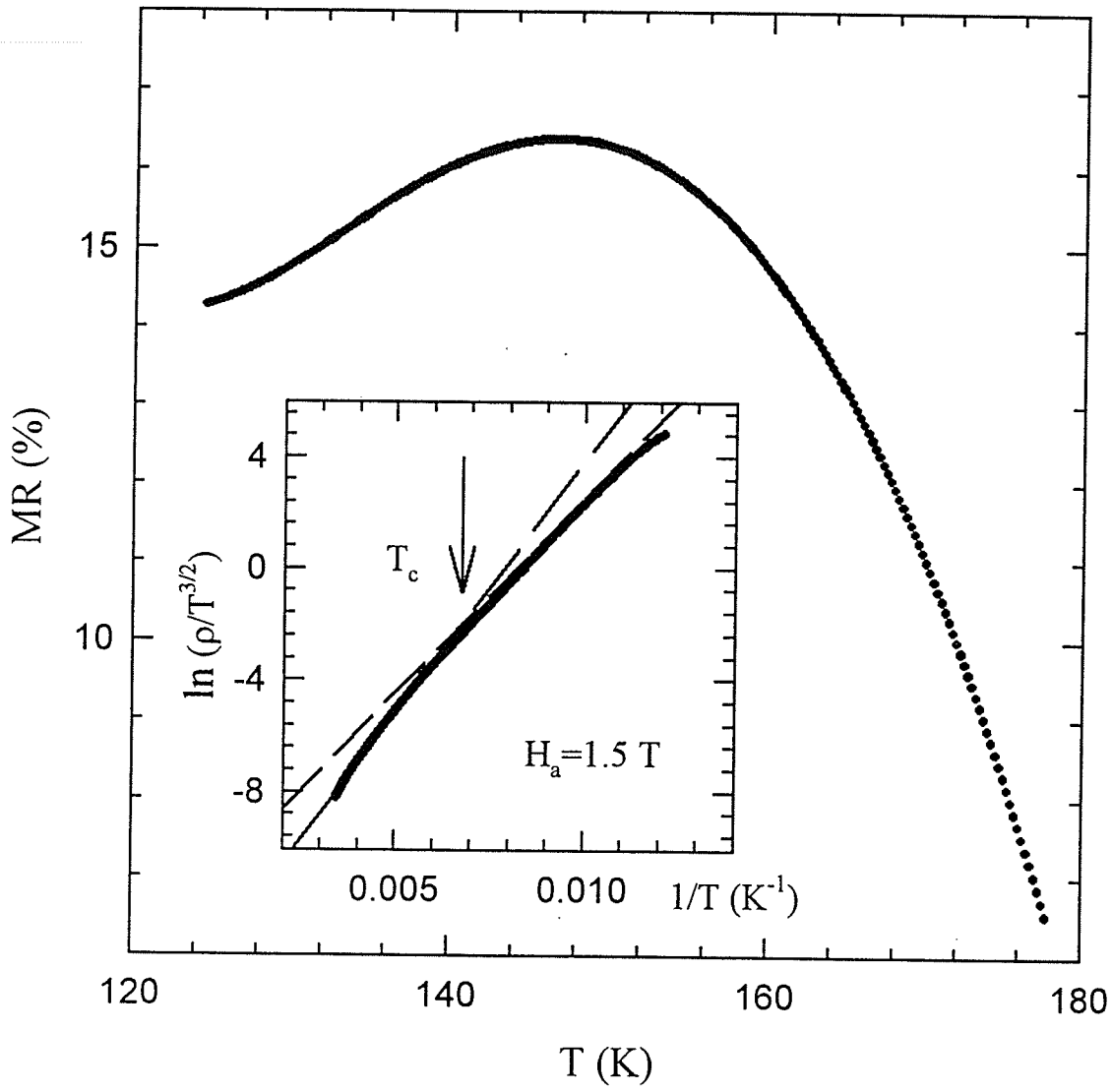

Figure 5.73: The percentage magnetoresistance measured in an applied field of 1.5 T is plotted against temperature. The inset displays the resistivity in a field of 1.5 T plotted in a form of $\ln(\rho\ /T^{3/2})$ versus $1/T$ for the $x = 0.05$ sample.

and model expectation. In the non-adiabatic limit, the coupling constant J can be estimated using equation (5.12) and the tabulated ρ_0 and E_a values in Table (5.5). Such estimates are summarized in Table (5.6), their values fall in the range | J | $\sim 1.5 - 16$ meV, comparable to those for $LaMnO_3$, $LaCrO_3$ [92] and Ar-annealed $La_{0.67}Ca_{0.33}MnO_{3-\delta}$ where the non-adiabatic limit is also operative.

Figure (5.74) shows representative fits of equation $\rho(T) = \rho_0 T^n e^{E_a/k_B T}$ to the experimental data in a double logarithmic scale, in which (a) reproduces a fit of the adiabatic form (n = 1) to the x = 0.33 specimen for $T > T_c$, and (b) the non-adiabatic form (n = 3/2) to the x = 0.4 sample for $T < T_c$. Figure (5.75) shows the magnetoresistance near the Curie temperature, which was deduced from resistivity measurements in zero field and in a field of 1.5 Tesla. They clearly demonstrate that around the critical temperature the magnetoresistance shows a maximum.

Despite the differences displayed by these various samples in the high temperature paramagnetic regime, the experimental results indicate that polaronic models are appropriate to describe the behaviour of $La_{1-x}Mg_xMnO_3$ both above and below T_c, although either adiabatic or non-adiabatic models seem applicable for the paramagnetic phase. The current measurements further show that the activation energy E_a falls on entering the order phase, and that the inequality | J | $<< E_a$ meets the requirement necessary for the formation of small polarons. The prefactor ρ_0 increases sharply in the ferromagnetic phase, leading to a marked decrease in Ω_0. This behaviour conflicts with the predictions of Emin and Liu [113] that ferromagnetic ordering should have a minor effect on the magnitude and

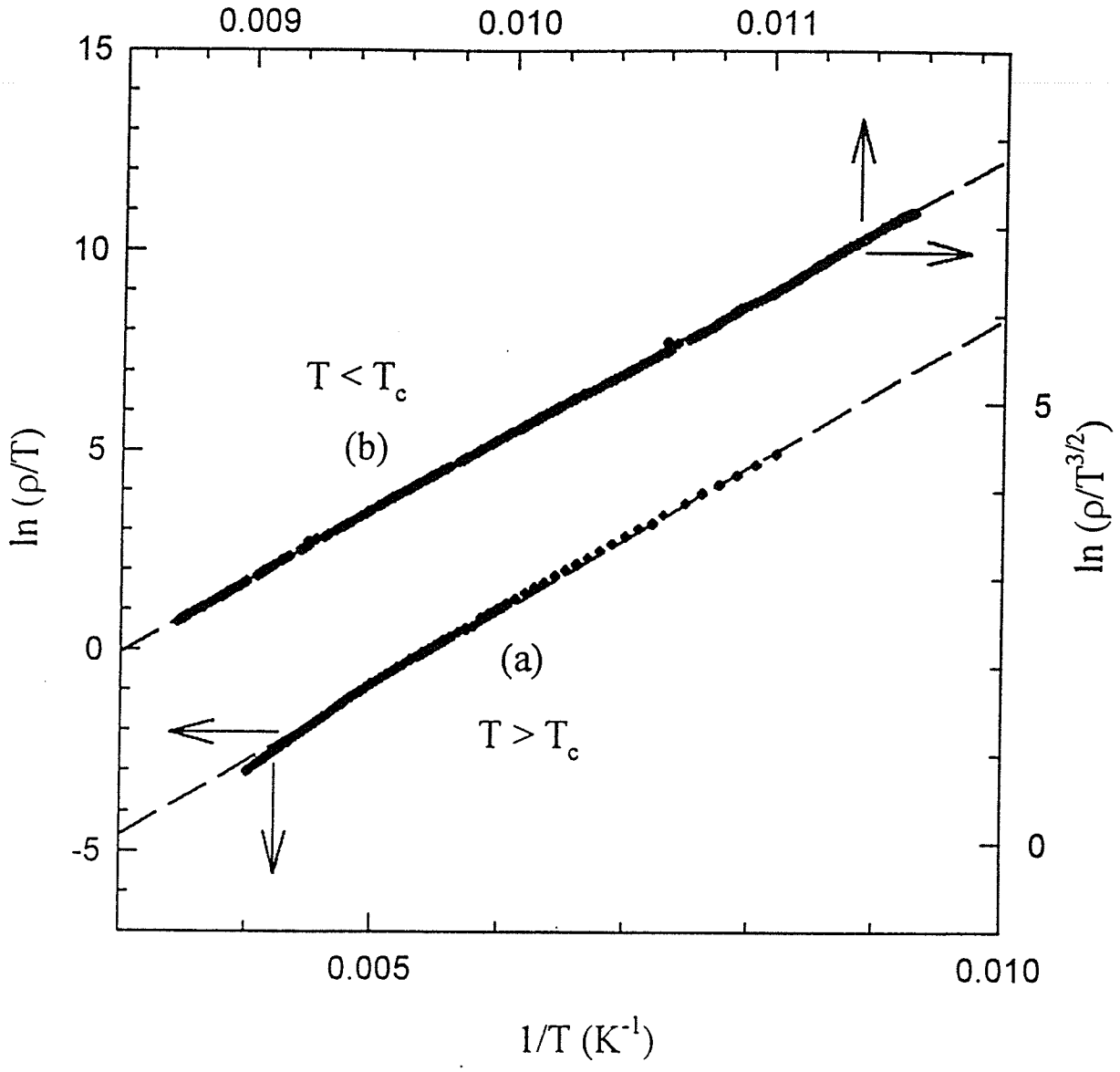

Figure 5.74: (a) A fit of the data above T_c for x = 0.33 to the adiabatic formalism with n = 1; (b) a fit of the data below T_c for x = 0.4 to the non-adiabatic form with n = 3/2.

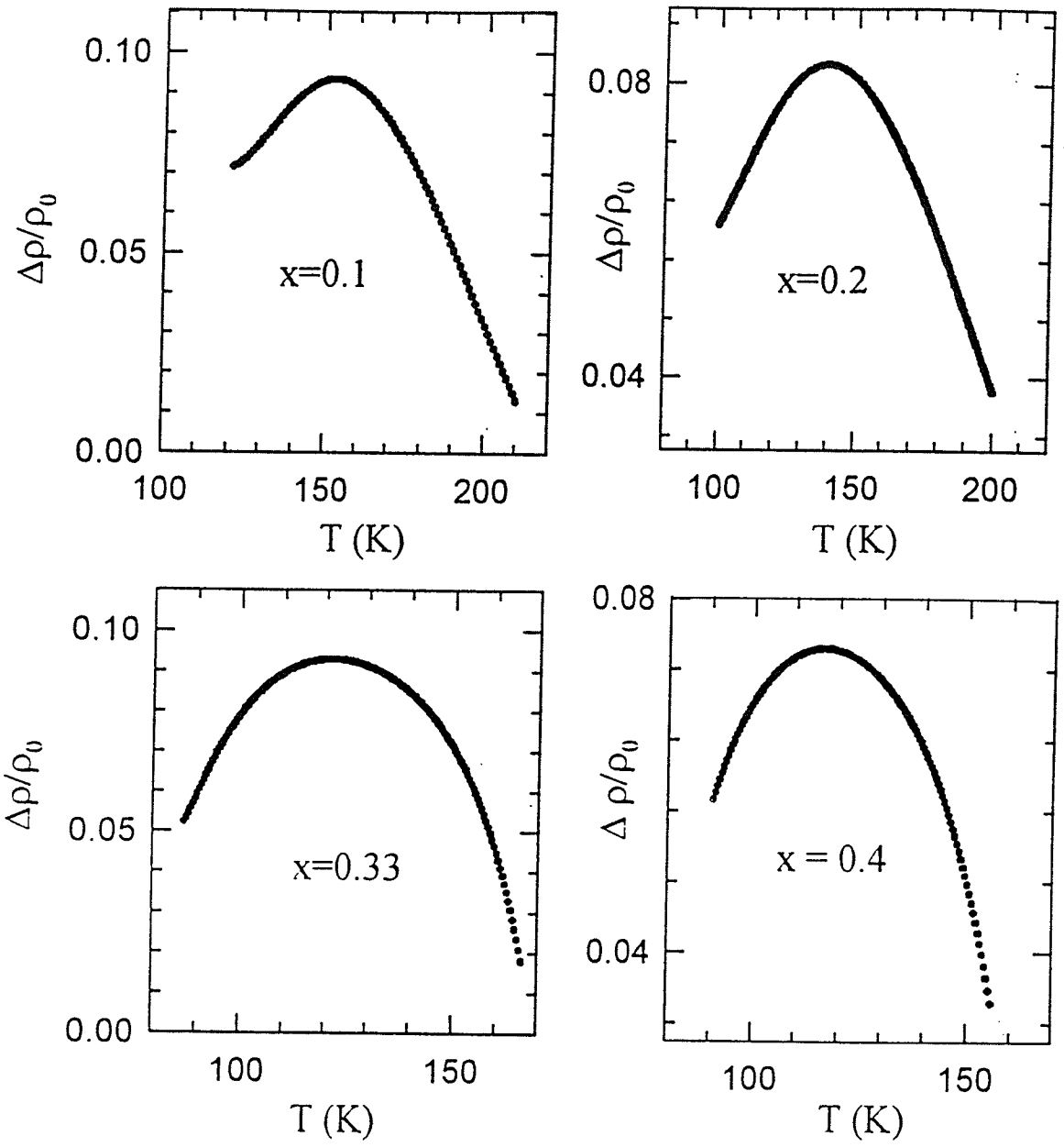

Figure 5.75: The magnetoresistance plotted as a function of temperature shows the maximum near critical temperature for $0.1 \leq x \leq 0.4$.

temperature dependence of the small polaron jump rate. In the previous studies on the Ar-annealed $La_{0.67}Ca_{0.33}MnO_3$, the bipolaron model has been tentatively utilized to explain such observation for the polaronic transport. The discussion provided there is considered generally applicable to the current system. Of course, the specific role played by (bi)polaron formation is still not well established in this system, and thus more experimental observations are necessary to provide further evidence for this theoretical approach.

In summary, the experimental data on the magnetic and electrical properties indicate that the Mg^{2+} ion doped perovskites do not exhibit a transition from a semiconductor to a metal on entering the ferromagnetic state from the paramagnetic state, in both of which the polaronic hopping process prevails.

By summarizing the above analysis, incorporating all magnetic and transport data over the entire doping range $0.05 \leq x \leq 0.6$, a phase diagram is constructed as shown in the figure (5.76). Here the solid line represents a true thermodynamic transition (a second order nature) from a paramagnetic insulating to a ferromagnetic insulating phase; the dashed line, taken from the lower temperature features exhibited by M_3 and the ZFC data described above, does not represent a thermodynamic transition as argued; it simply indicates the onset of a marked technical hardness. The overlap of the two boundaries at x = 0.5 thus reflects the marked increase in H_c with x, and the consequent coincidence of T_c and the peak in the ZFC branch.

The phase diagram looks very simple when compared with other systems, particularly that for $La_{1-x}Ca_xMnO_3$ as shown in chapter two. This difference is

partly because of the complete insulating behaviour for all compositions studied, i.e. the metal-insulator transition being completely suppressed due to the small A-site radius, (r_A), resulting from Mg substitution. Any comprehensive theories of these systems must account for such effects, and in that sense current theoretical approaches are inadequate.

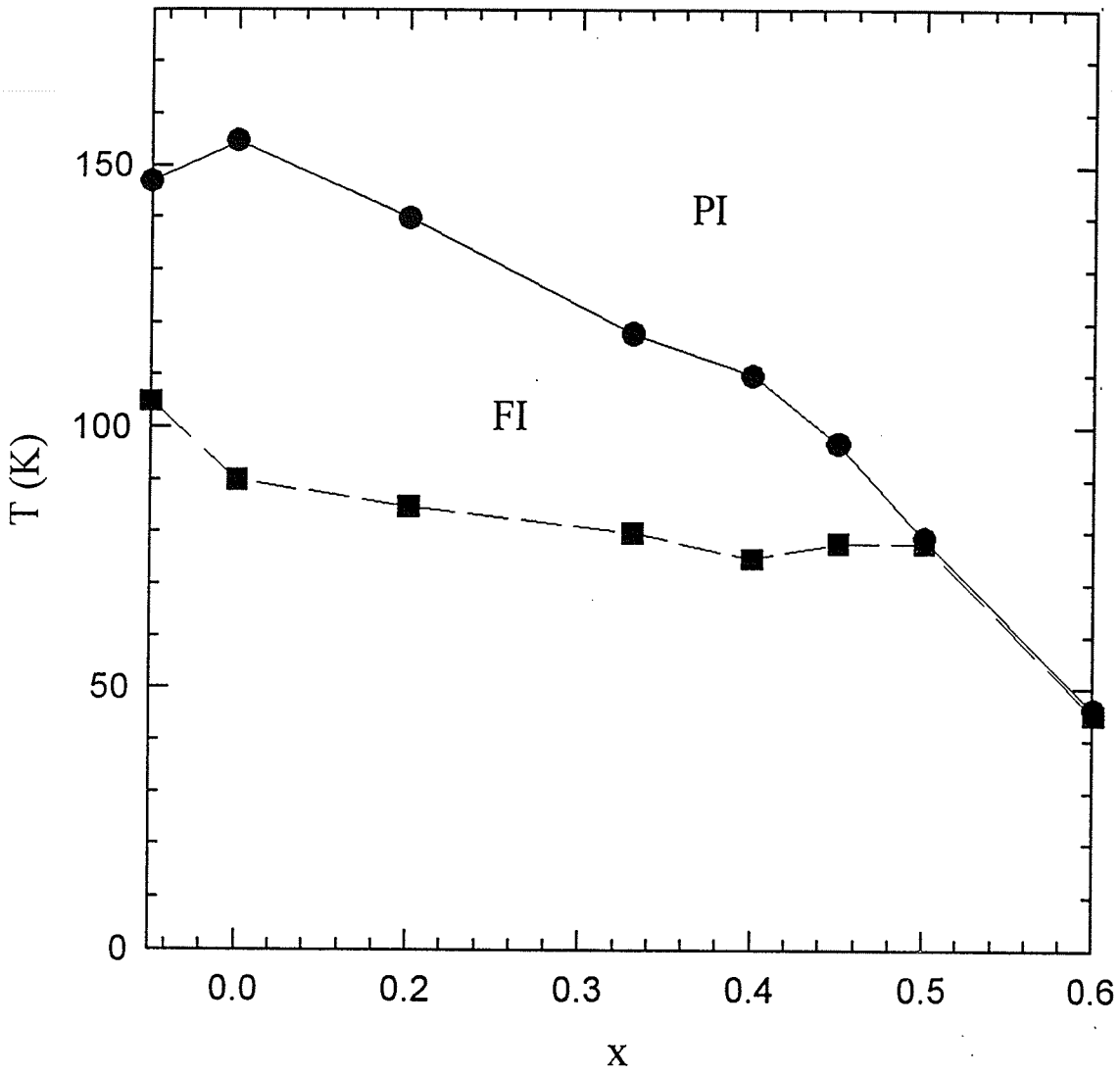

Figure 5.76: The schematic phase diagram are deduced from the experimental data for $La_{1-x}Mg_xMnO_3$.

5.6 Preliminary Study of $(La_{1-x}Nd_x)_{0.67}Pb_{0.33}MnO_3$

In the previous section the $La_{1-x}Mg_xMnO_3$ system with a variation of hole doping level, x, was investigated. The substitution of the small Mg^{2+} ions at the A sites produces a marked change in the magnetic and transport properties, contrasting with the effect of relatively large ions, such as Ca or Sr. Here a somewhat different line of investigation is followed. An earlier study of polycrystalline ceramic $La_{0.67}Pb_{0.33}MnO_3$ [80] in this laboratory confirmed its relatively high ordering temperature - $T_c \approx 340$ K - an important consideration in possible device applications and also demonstrated by quantitative means the coincidence of the ferromagnetic ordering temperature T_c and the metal-insulator transition temperature (identified with the maximum in $d\rho/dT$). By contrast with the study of divalent cation substitution at the A sites which - in a double exchange picture - modulates the Mn^{3+}/Mn^{4+} ratio, it was decided to carry out a study of the effects of substitution at the rare-earth (La) sites at fixed divalent cation doping i.e. at a fixed Mn^{3+}/Mn^{4+} ratio. While an earlier study of such effects in $(La_{1-x}Y_x)_{0.67}Ca_{0.33}MnO_3$ was amongst the first [28] to illustrate the influence of average A-site radius $< r_A >$ on the transport and magnetic properties, it was planned to further investigate such effects using a moment bearing rare-earth, Nd. It is known that the average size of A-site cation represents the disorder arising from ionic size mismatch between the various ions at the same crystallographic site, which affects the lattice structure and thus the electronic bandwidth. Transport is strongly correlated with magnetism due to the double exchange interaction in the doped perovskites, therefore, both of them can be modulated by the ap-

propriate selection of $< r_A >$. It has been found experimentally that a decrease in $< r_A >$ can make T_c decline [26].

The single crystal $La_{1-x}Pb_xMnO_3$ compounds were thoroughly investigated [114] in the 1960's, and the polycrystalline ceramic $La_{0.67}Pb_{0.33}MnO_3$, was studied in detail with the emphasis on the nature of critical phase transition and spontaneous resistive anisotropy. Here the experiments data on $(La_{1-x}Nd_x)_{0.67}Pb_{0.33}MnO_3$ are reported concerning the effect of the substitution of the relative smaller Nd^{3+} ion at the A-site on the magnetic and transport properties under the condition of a fixed number of charge carriers. The results for the sample $Nd_{0.67}Pb_{0.33}MnO_3$ (i.e. x = 1) are first discussed and then $(La_{1-x}Nd_x)_{0.67}Pb_{0.33}MnO_3$ with x varying from 1 to 0 in steps of 0.2.

The samples were prepared using standard solid state reaction techniques with the following specific heat-treatment procedure: the samples were first preheated at $850°C$ for 24 hours in air, then the products were ground, granulated and pressed into disks, subsequently sintered at $1100°C$ for 48 hours in flowing air, finally annealed at $950°C$ for 48 hours and at $650°C$ for 24 hours in flowing air respectively. The x-ray diffraction patterns of all samples were examined and confirm that the samples are single phase with rhombohedral structure. The lattice constants are summarized in Table (5.7). The magnetic measurements were carried out using the PPMS measuring system and the magnetoresistance was measured by the four-probe method.

Table 5.7: The lattice parameters of the $(La_{1-x}Nd_x)_{0.67}Pb_{0.33}MnO_3$ samples

x	structure	2a (Å)	θ (°)
0	rhombohedral	7.7953 (0.0012)	90.28
0.2	rhombohedral	7.7807 (0.0011)	90.31
0.4	rhombohedral	7.7780(0.0014)	90.34
0.6	rhombohedral	7.7905 (0.0009)	90.16
0.8	rhombohedral	7.7719 (0.0008)	90.19
1.0	rhombohedral	7.7672 (0.0005)	90.12

5.6.1 $Nd_{0.67}Pb_{0.33}MnO_3$

Figure (5.77) reproduces the temperature dependence of the susceptibility measured using an ac driving field with amplitude of 0.03 Oe and frequency of 2400 Hz in various superimposed static biasing fields. The zero field susceptibility is shown in the inset of this figure. The critical behaviour here is very similar to that described earlier for the $La_{0.67}Ca_{0.33}MnO_3$, $La_{0.95}Mg_{0.05}MnO_3$, and the pyrochlore $Tl_2Mn_2O_7$ although here a static field of some 900 Oe is required to first resolve the critical peak; the latter confirming a continuous phase transition. The critical exponent values can be extracted from peak susceptibilities, peak temperatures and applied fields based on the static scaling law. Figure (5.78)(a-d) show the fitted data from which:

T_c= 163.8 K, $1/(\gamma+\beta) = 0.57(\pm 0.03)$, $\gamma = 1.27(\pm 0.07)$, $\delta* = 3.70(\pm 0.41)$, $\delta = 4.01(\pm 0.05)$.

The crossover exponent $(\gamma+\beta)$ value agrees with that predicted by the 3D Heisenberg model, γ is a little bit less and δ is much lower but greater than the mean-field value. The results are similar to those reported for $La_{0.67}Pb_{0.33}MnO_3$ [80] and reflect the presence of disorder in this compound as discussed previously.

Figure (5.79) shows the temperature dependence of the zero-field cooled (ZFC) and field cooled (FC) magnetization measured in a field of 50 Oe on warming. The ZFC and FC curves separate just below T_c; this confirms the existence of irreversibility and hysteresis in the ferromagnetic state resulting in a coercivity of about 80 Oe at 4.2 K (estimated from the susceptibility versus field, a butterfly plot shown in figure (5.80)). The coercivity likely arises from the magnetocrystalline anisotropy associated with the presence of Nd, thus the relatively small difference between the ZFC and FC curves reflects a small contribution from such anisotropy. The inset in Figure (5.79) shows magnetization curves measured up to 8 Tesla at temperatures of 4.2 K, 40 K, 80 K, 100 K, 120 K, 160 K, 180 K, and 200 K respectively. It can be clearly seen that the high field slope of the magnetization at temperatures below 40 K is significantly greater than that above 40 K. The low field slope shows a little decline below 40 K, also evidenced in the ZFC and FC and zero susceptibility data. This behaviour indicates that the Nd rare earth ions play an important role, in particular at low temperature.

The temperature dependence of resistivity is reproduced in the figure (5.81). The zero field resistivity displays a maximum at 169.5 K. In the higher tempera-

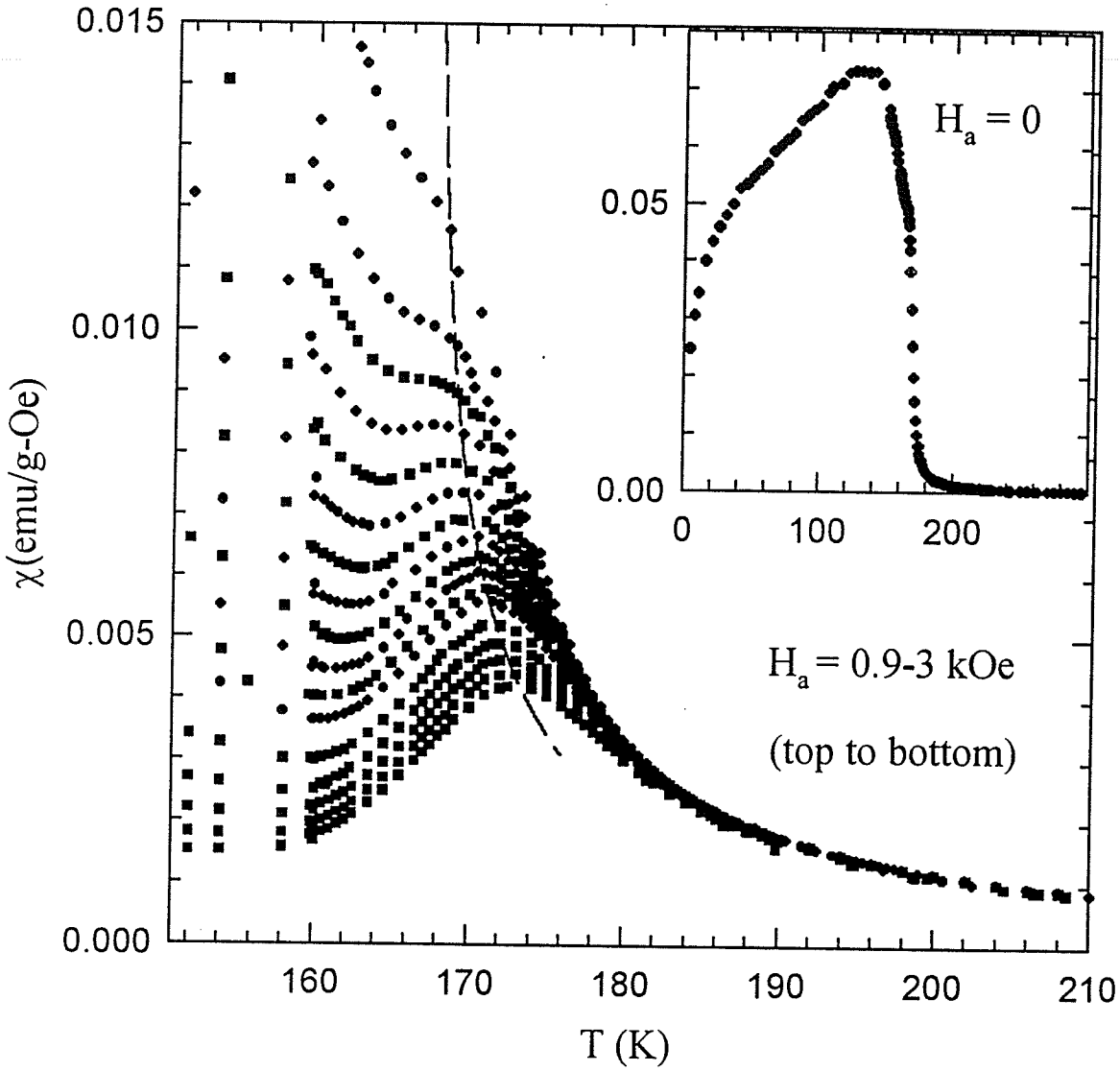

Figure 5.77: The field-dependent ac susceptibility versus temperature in applied fields increasing from 900 Oe (top) to 3000 Oe (bottom) showing the critical peaks. The dashed line represents the crossover line. The inset shows the temperature dependence of the zero field susceptibility.

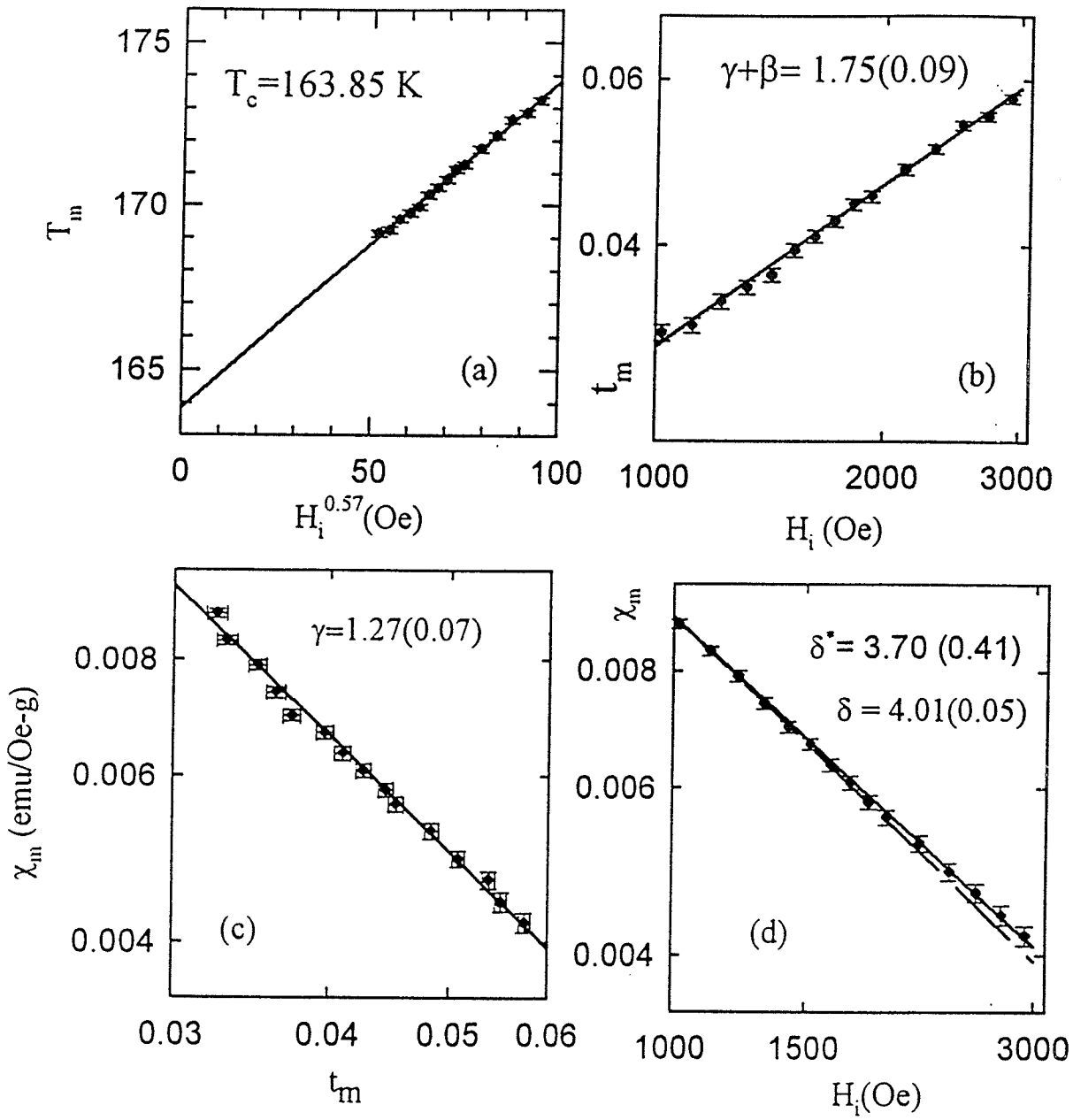

Figure 5.78: The critical exponent values are obtained according to the static scaling law.

ture range above the peak the transport displays semiconducting-like behaviour which can be generally attributed to the small polaron hopping as is discussed in the Ar-annealed $La_{0.67}Ca_{0.33}MnO_3$. At low temperature, well below transition temperature, the resistivity is difficult to fit to any specific mechanism such as electron-electron scattering, electron-magnon scattering etc. because of grain boundary effects commonly existing in polycrystalline compounds. Near the transition temperature, the polarons are dissolved into band electrons due to rapid growth of the double-exchange coupling interaction, and the transport behaviour changes from a semiconducting-like to a metallic-like state. The inset in this figure shows the field dependence of the resistivity measured in fields up to 3 tesla at 4.2 K. With increasing field the resistivity initially drops rapidly and then decreases at a relatively slower rate in above 1 tesla. This behaviour is likely to be related to the magnetic state attained by the Nd ions at low temperature mentioned above, in contrast to the Ca doped sample where the resistivity drops very quickly in much lower fields and then decreases very slowly. Figure (5.82) shows the temperature dependence of the resistivity in applied fields of 0, 0.8 T and 1.6 T respectively; they clearly show a decrease in resistivity with increasing applied field, reflecting the reduction of spin dependent scattering with application of a magnetic field. The inset of this figure reproduces the magnetoresistance (MR) measured in the applied fields indicated. The amplitude of the MR in a field of 1.6 T reaches a maximum of 80% at a temperature of 166.5 K which is very close to the transition temperature, T_c, of the paramagnetic to ferromagnetic state. This is in agreement with the double-exchange picture. The MR of up to 30-40% at

low temperature is generally attributed to the spin polarization tunneling across grain boundaries. [69, 70].

The $Nd_{0.67}Pb_{0.33}MnO_3$ parent compound thus exhibits a magnetic transition from the paramagnetic to ferromagnetic state which is accompanied by a semiconductor to metal transition; around the transition temperature a colossal magnetoresistance is observed when a magnetic field is applied. The susceptibility data demonstrates that the magnetic transition is continuous/second order. The magnetic state at low temperature is obviously affected by the presence of and the magnetic ordering established by Nd^{3+} moments.

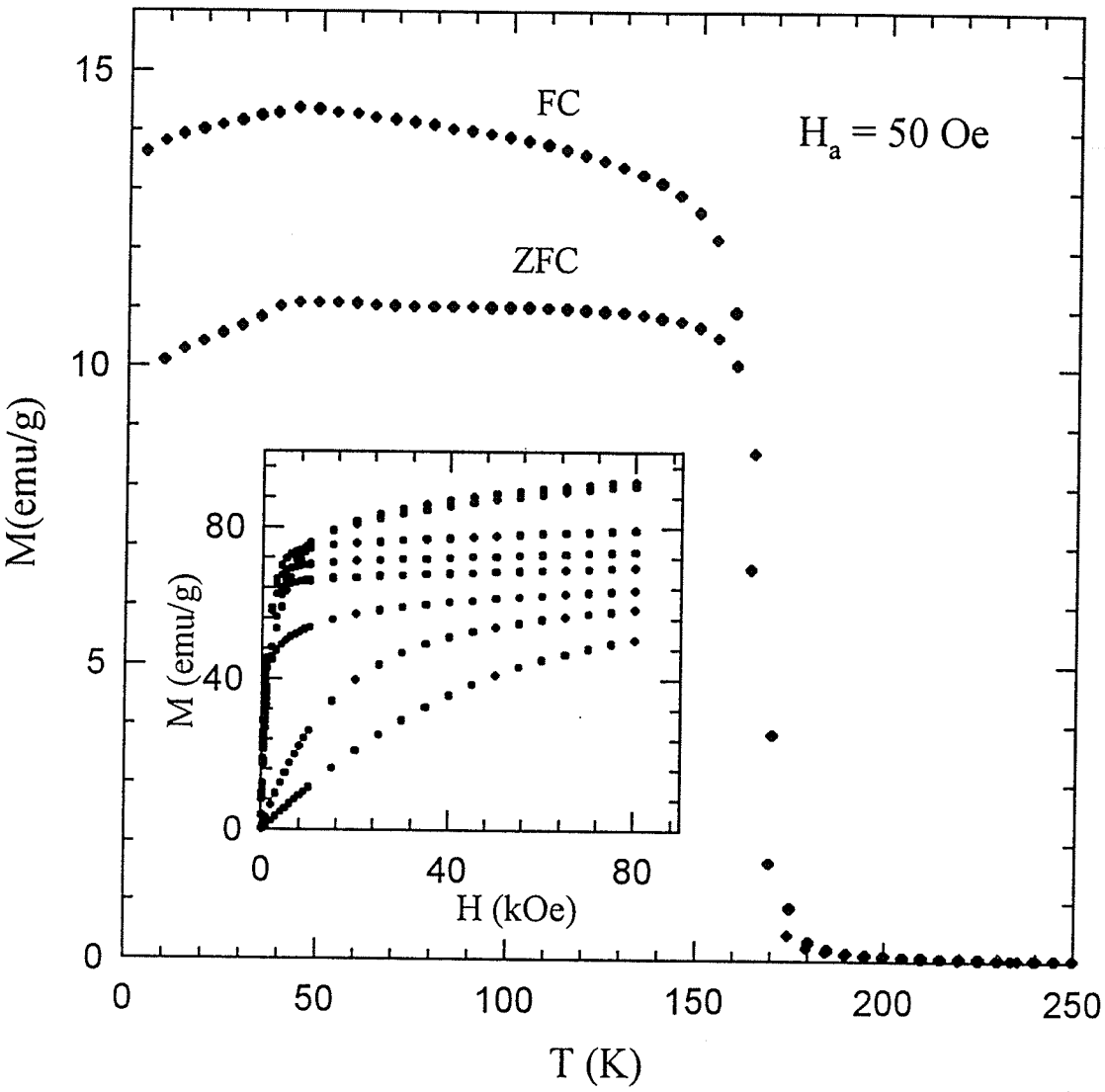

Figure 5.79: The ZFC and FC curves measured in a field 50 Oe. The inset shows magnetization curves measured at the temperatures of 4.2 K, 40 K, 80 K, 100 K, 120 K, 160 K, 180 K, 200 K, top to bottom.

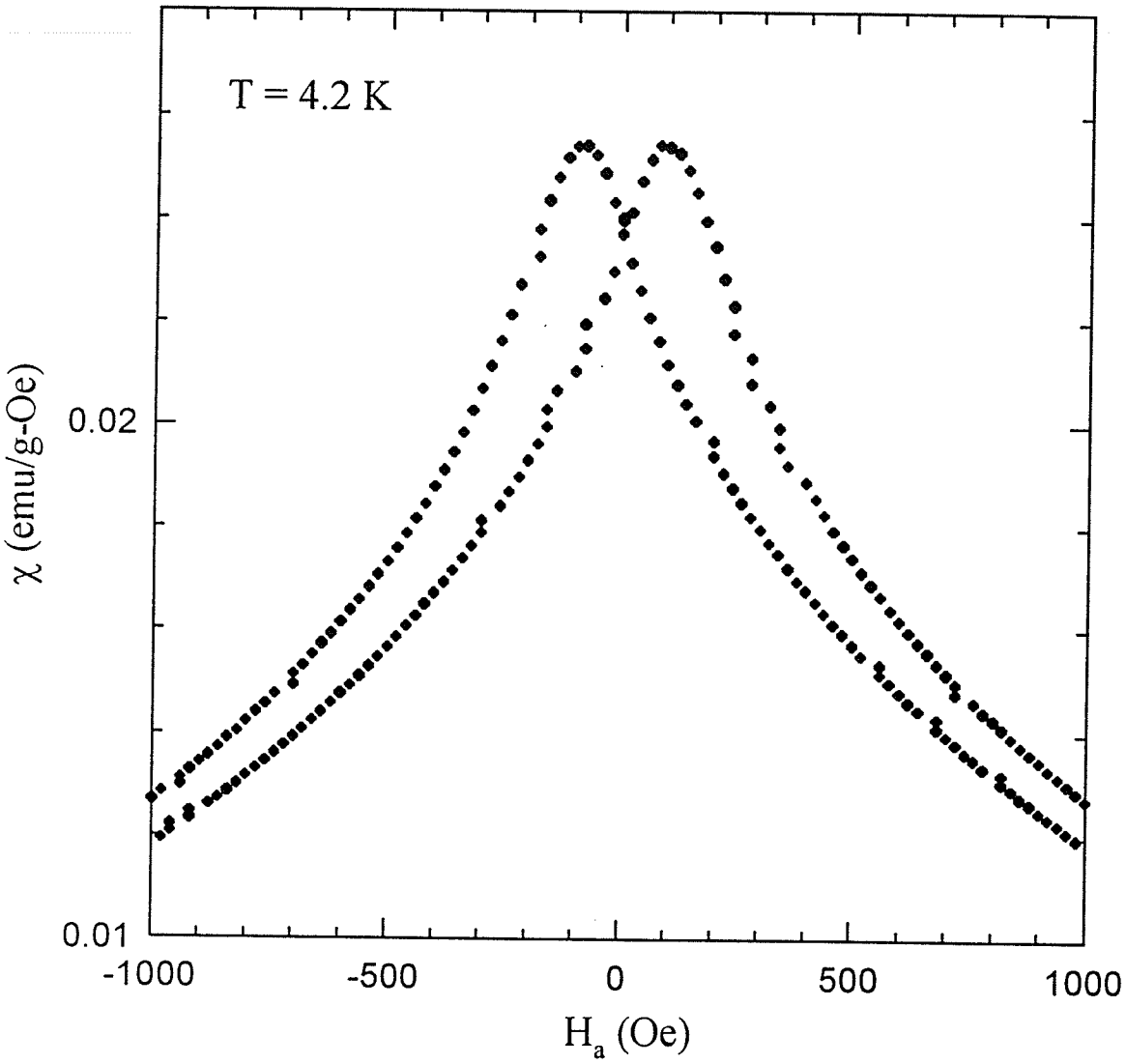

Figure 5.80: The susceptibility is plotted against applied field, coercivity can be estimated from the separation of two peaks of this butterfly loop.

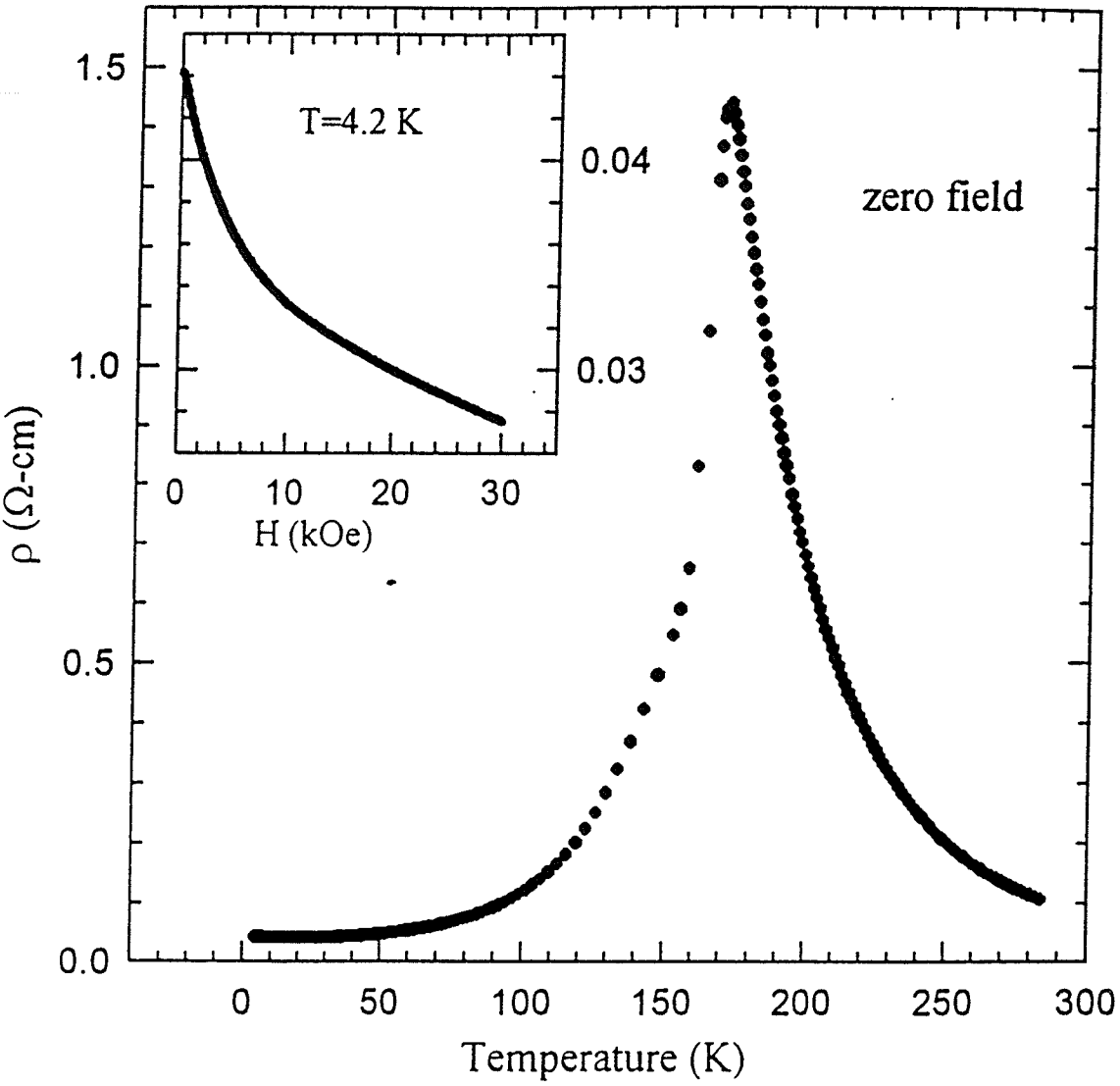

Figure 5.81: The variation of the resistivity with temperature. The inset shows the field dependence of the resistivity measured at 4.2 K.

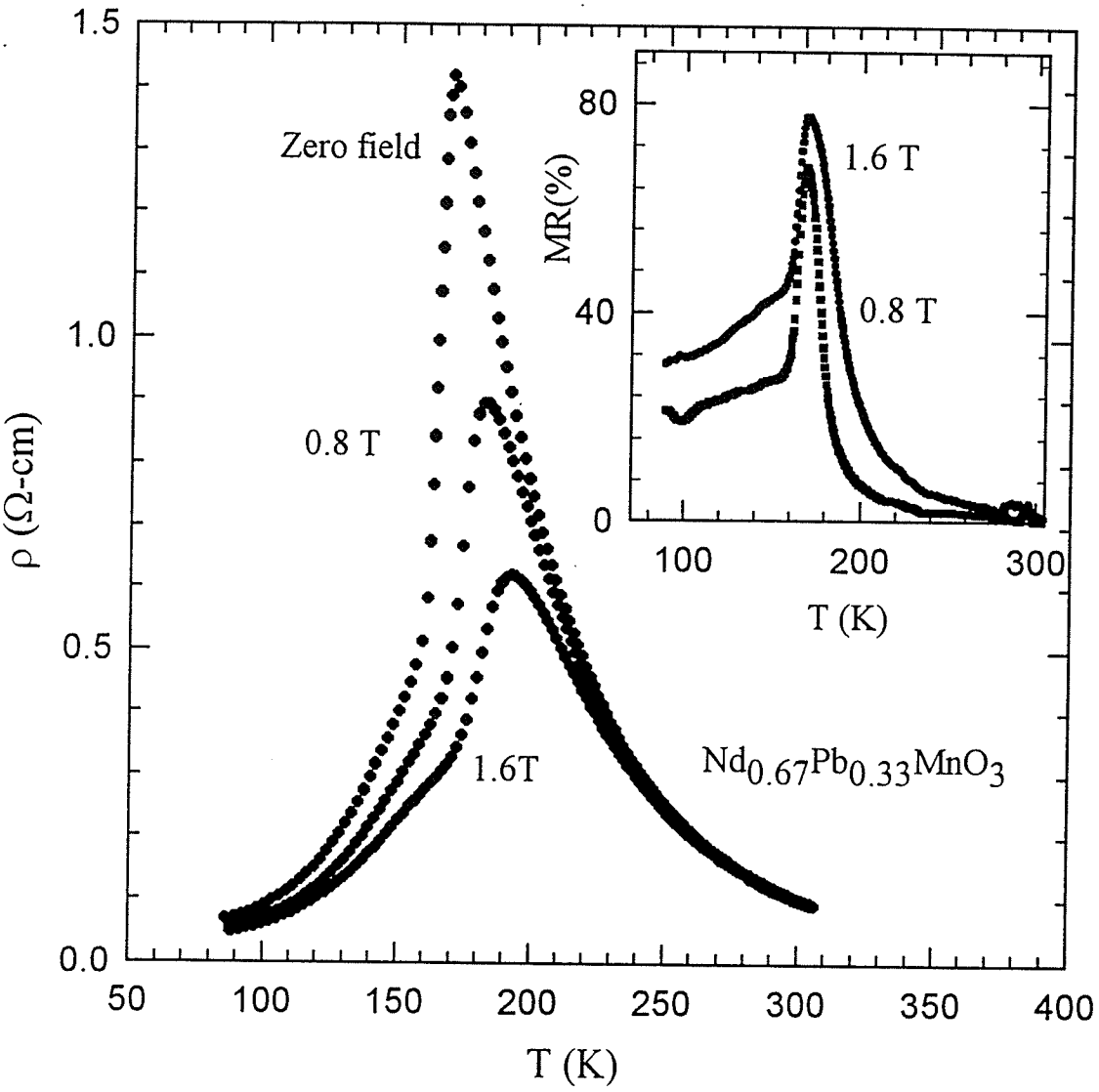

Figure 5.82: The temperature dependence of the resistivity measured in different applied magnetic fields. The inset shows the temperature dependence of the magnetoresistance.

5.6.2 $(La_{1-x}Nd_x)_{0.67}Pb_{0.33}MnO_3$

Figure (5.83) displays the temperature dependence of the zero field ac susceptibility for all samples prepared with doping levels, x, varying from 1 to 0 by every 0.2. All samples exhibit susceptibility behaviour similar to that for $Nd_{0.67}Pb_{0.33}MnO_3$. The magnetic state changes from paramagnetic at high temperature to ferromagnetic at lower temperature, and correspondingly the transport properties change from insulator to metal in figure (5.84). The effect of Nd^{3+} doping level on the magnetic and transport properties is presented below.

With increasing doping level, x, the critical temperature T_c decreases and the magnetic response in the ferromagnetic regime below the critical point becomes weaker, reflecting a gradual reduction in the ferromagnetic coupling. The substitution of Nd^{3+} ions at the A sites, however, should not modify the density of charge carriers, indicating that the ferromagnetic coupling mediated by the double-exchange interaction must be influenced by other factors. The first and direct consideration is the average ion size at the A-site. The tolerance factor is often used to assess this ion size effect. The average values, $< r_A >$, for the A site ions La^{3+}, Nd^{3+} and Pb^{2+} and $< r_B >$ for the B site ions Mn^{3+} and Mn^{4+} were calculated using the ionic radii provided by Shanon [115] for 12-fold coordination for the A sites and 6-fold coordination for the B sites (i.e. taking r $(La^{3+}) = 1.36$ $\AA$, r $(Nd^{3+}) = 1.27$ $\AA$, r $(Pb^{2+}) = 1.49$ $\AA$, r $(Mn^{3+}) = 0.645$ $\AA$, r $(Mn^{4+}) = 0.53$ $\AA$ and r $(O^{2-}) = 1.40$ $\AA$). The tolerance factor t is plotted against x as shown in figure (5.85). The substitution of smaller Nd^{3+} ions for relatively larger La^{3+} ions induces modifications to the lattice structure, such as a smaller Mn-O-Mn bond

angle. This subsititution reduces the overlap between the orbitals and results in a narrower energy bandwidth which weakens the ferromagnetic coupling and leads to a lower Curie temperature. Another structure parameter, σ^2, the variance of the ionic radius distribution of cations at the A sites, was introduced to describe the static structural effects that influence the electronic and magnetic properties [116]. For two or more A-site species with fractional occupancies y_i ($\Sigma y_i = 1$), the variance of the ionic radii r_i about the mean $< r_A >$ is $\sigma^2 = \Sigma y_i r_i^2 - < r_A >^2$. Figure (5.86) shows the resistivity peak temperature, T_m, versus the variance of the ionic radius distribution at the A sites and the inset displays the average radius dependence of the resistivity peak temperature for this Nd doped system.

Figure (5.84) shows the temperature dependence of the resistivity plotted in a form of $\log \rho$ versus T. All of the samples exhibit a transition from a semiconducting-like to a metallic-like state, and the transition temperature decreases with increasing x. It should be noted that the magnitude of the resistivity becomes larger with increase of x, this could indicate that the magnetic Nd^{3+} ions provide an additional contribution to resistivity due to the enhanced magnetic scattering although the additional moment at the Nd site does not enhance T_c, as might be expected from simple arguments. Figure (5.87) displays the magnetoresistivity versus temperature for all samples; the increase of MR with increasing Nd^{3+} concentration, generally consistent with a suppression of T_c, provides evidence of spin ordering by the external magnetic field, leading to a significant reduction in resistivity. The dependence of peak resistivity and peak temperature on the $< r_A >$ is shown in figure (5.88); the variation of peak MR

and peak MR temperature with $< r_A >$ is reproduced in figure (5.89). In figure (5.90) (a) shows the magnetization extrapolated from the data measured at 4.2 K in fields up to 9 Tesla; (b) is the calculated result as the moment of Nd ion is included. Both of them increase with increasing Nd doping level while (a) gradually deviates from (b), reflecting the effect of an additional moment at Nd sites. In figure (5.91) the coercivity measured at 4.2 K shows a non-monotonic variation with x.

All samples (x from 0 to 1) thus display a transition from a paramagnetic insulator to a ferromagnetic metal; the critical behaviour indicates that the magnetic transition belongs to the secondary order type (continuous), as demonstrated by the two end points (i.e. x = 1 in this thesis and x = 0 in reference [80]), although a relatively high field is necessary to resolve the critical peaks and the critical exponent values are not in complete agreement with those predicted by the Heisenberg model. A semiconductor-metal transition accompanies the magnetic transition, indicating a strong correlation between the magnetism and electrical transport. The substitution of the rare earth element, Nd, at the A sites results in a decrease of the transition temperature, showing that the Nd ions cause a weakening of the exchange coupling and a narrowing of the bandwidth, consequently leading to a lower Curie temperature and an increase in resistivity.

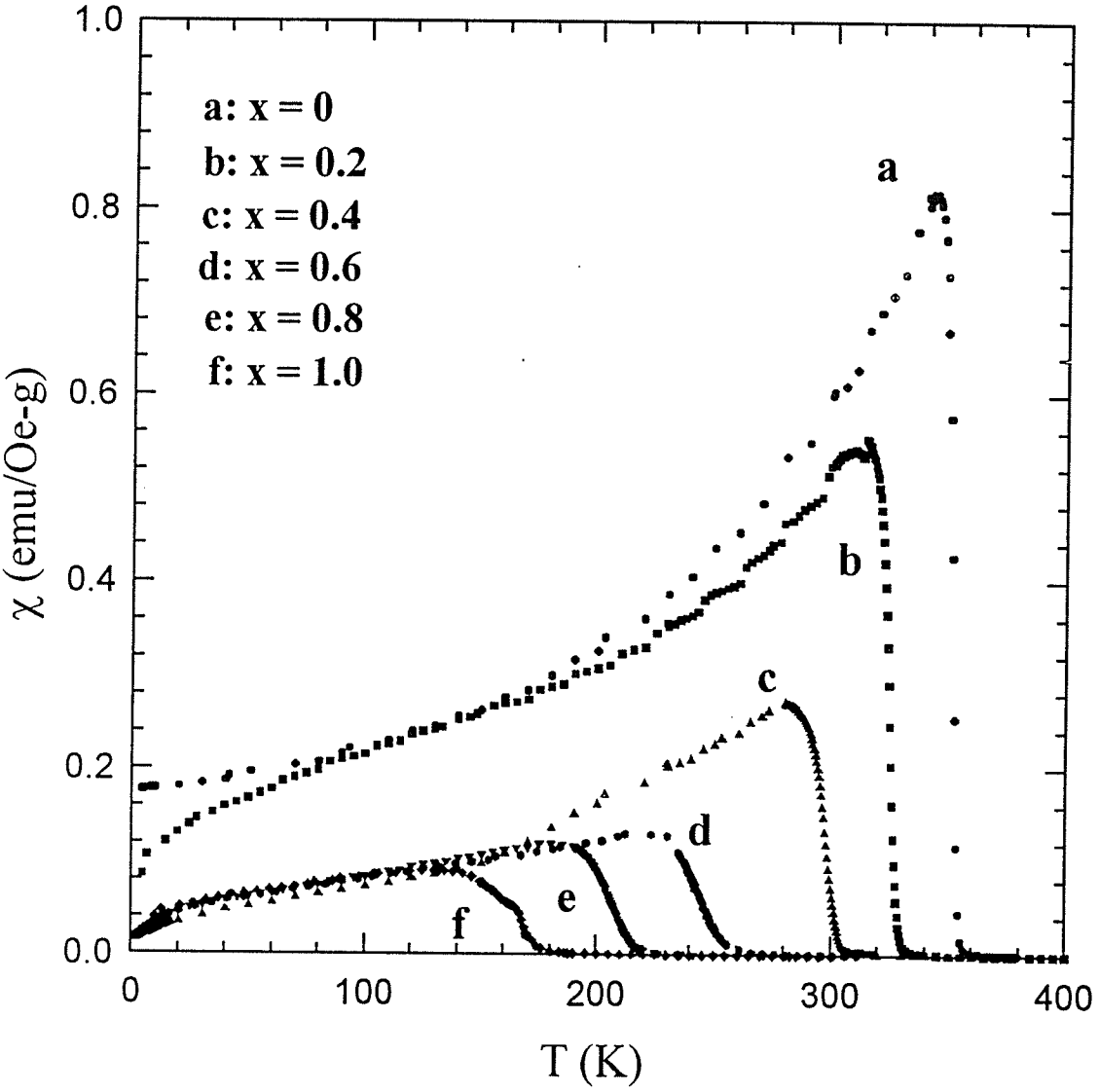

Figure 5.83: The temperature-dependent susceptibility measured in a zero field for $(La_{1-x}Nd_x)_{0.67}Pb_{0.33}MnO_3$ with doping level, x, varying from 0 to 1 in steps of 0.2.

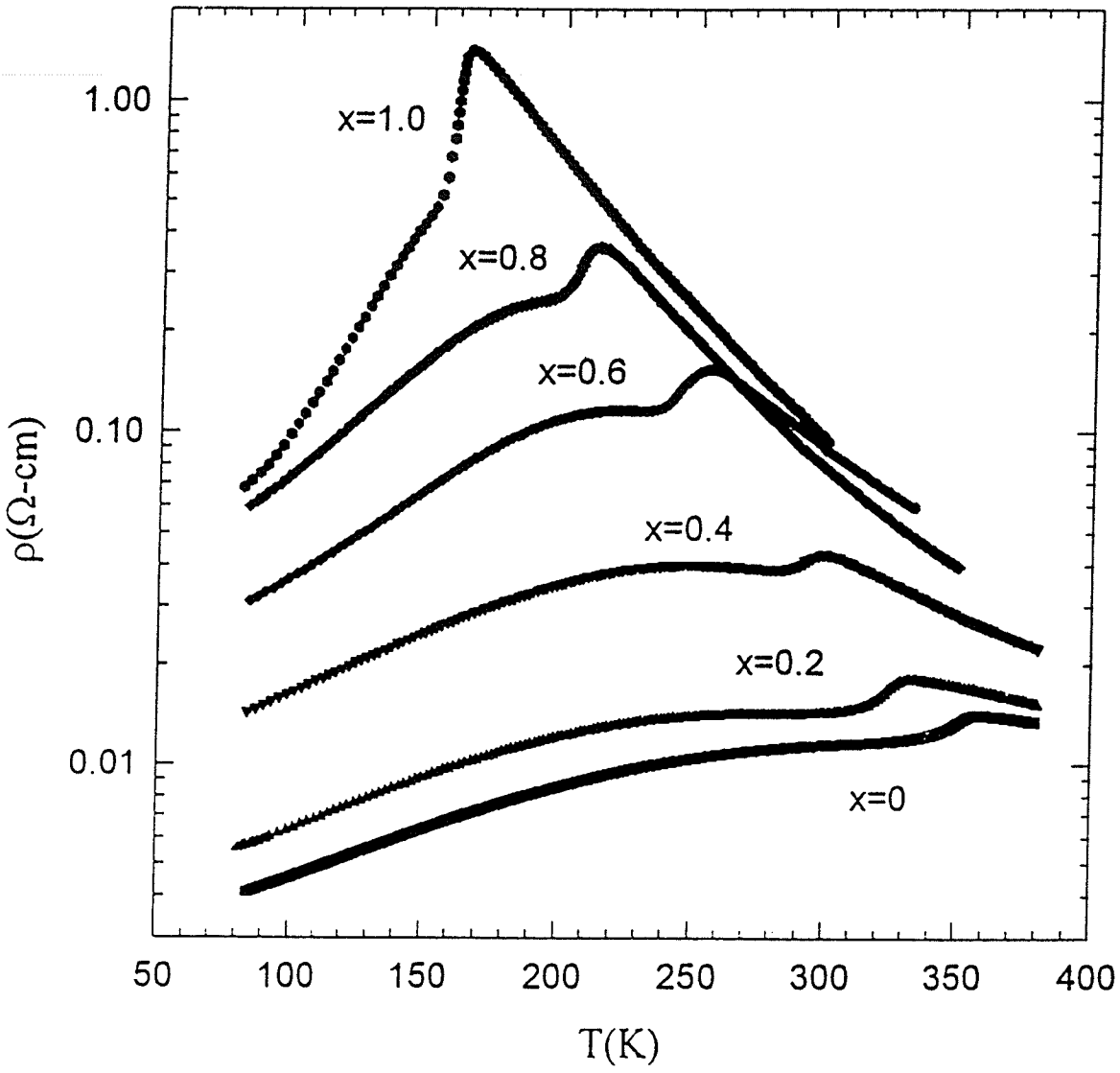

Figure 5.84: The temperature dependence of resistivity in the form of $\log \rho$ vs T for the samples $(La_{1-x}Nd_x)_{0.67}Pb_{0.33}MnO_3$.

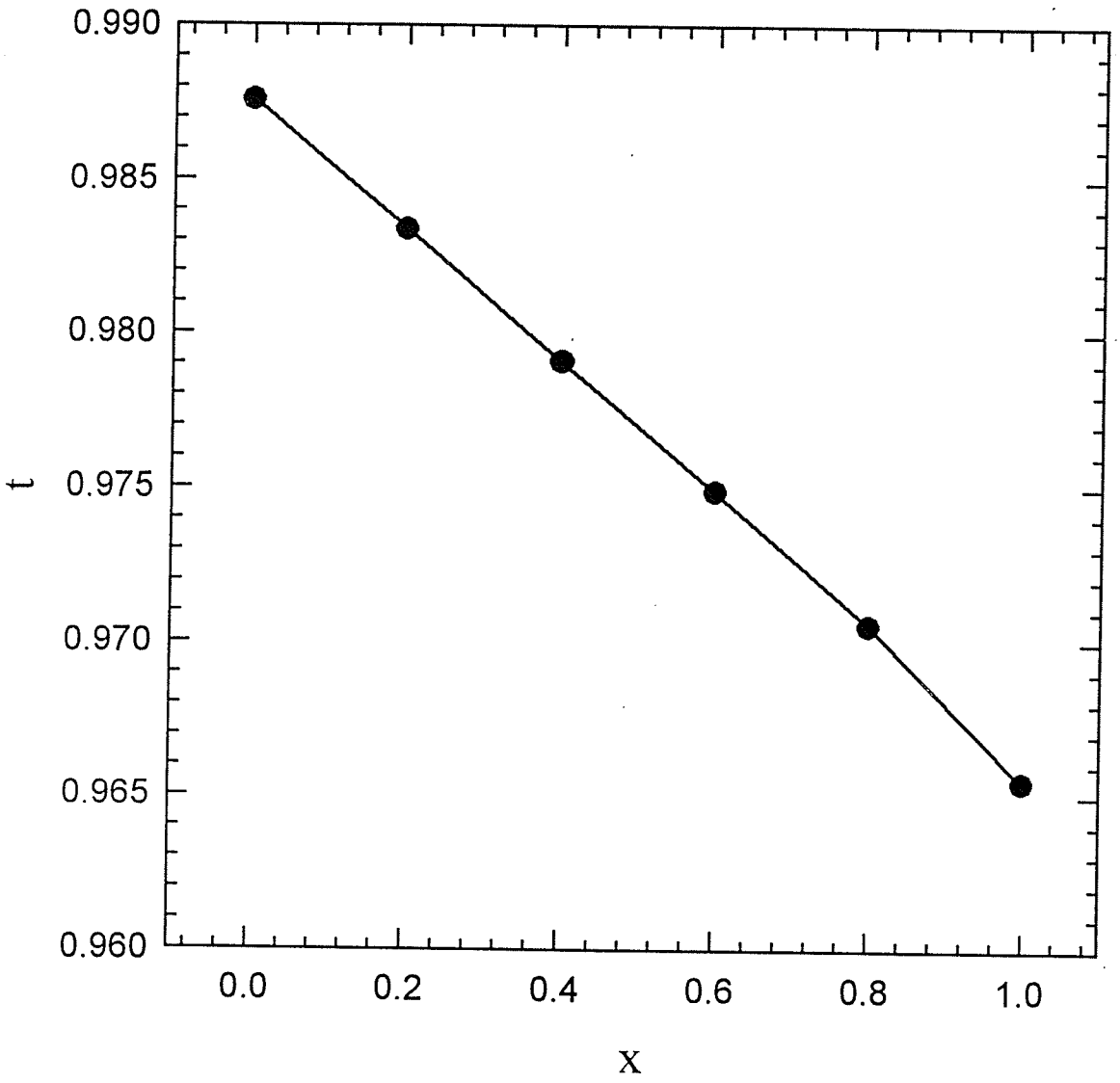

Figure 5.85: The tolerance factor t versus concentration x for $(La_{1-x}Nd_x)_{0.67}Pb_{0.33}MnO_3$.

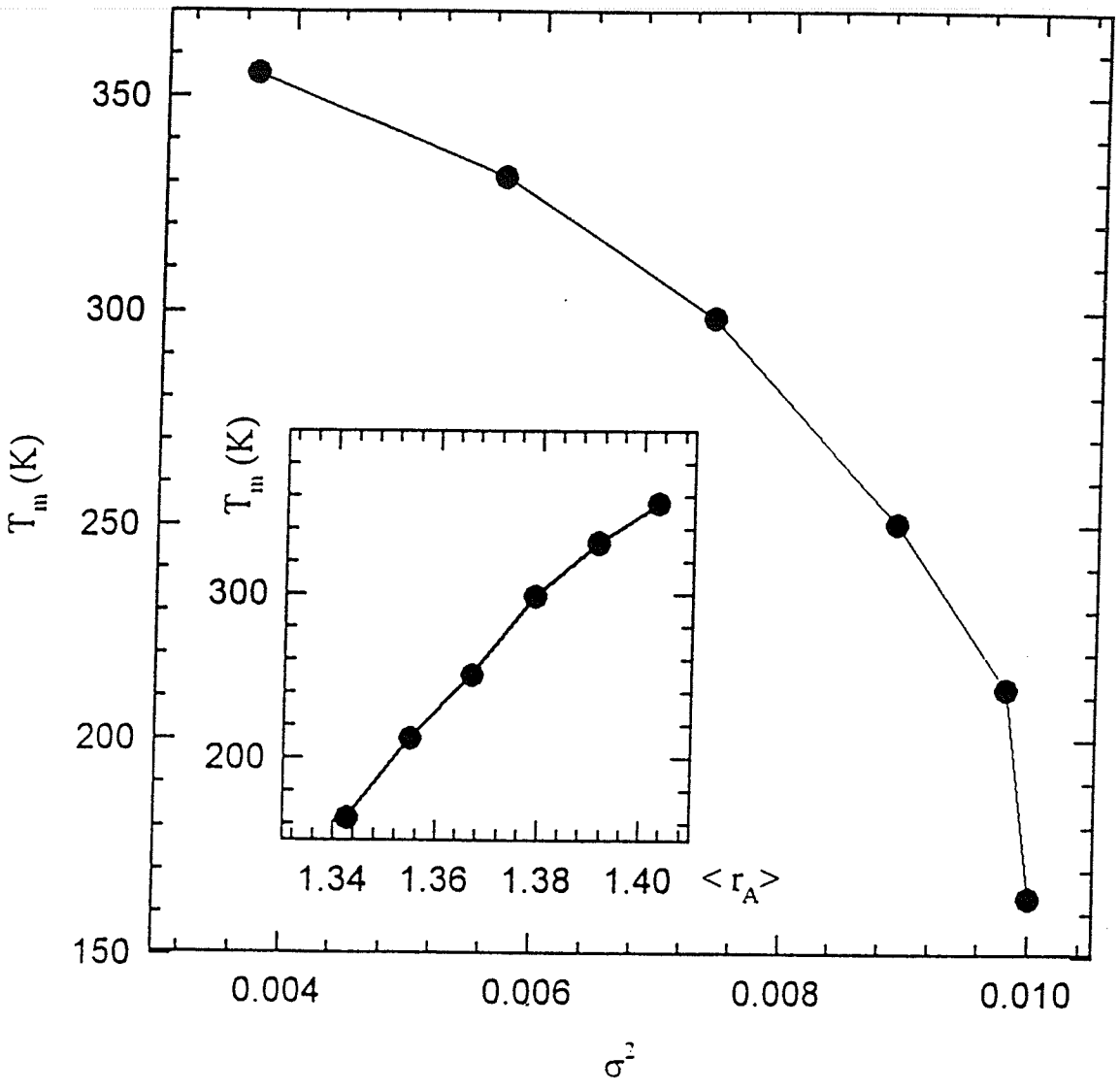

Figure 5.86: The resistivity peak temperature T_m versus the variance of A cation radius distribution σ^2. The inset shows the $< r_A >$ dependence of the T_m.

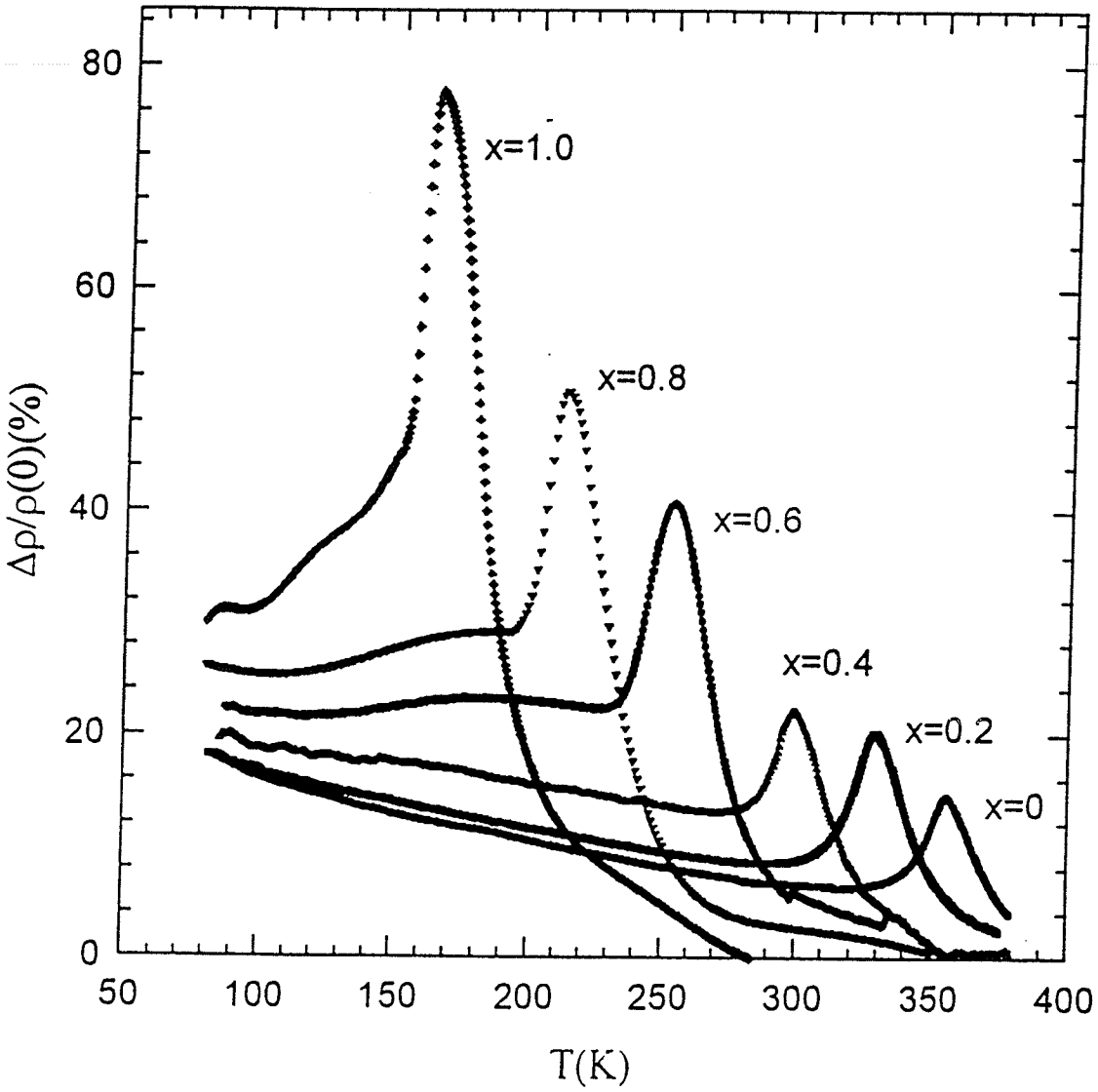

Figure 5.87: The temperature dependence of magnetoresistance measured in a field of 1.6 T for $(La_{1-x}Nd_x)_{0.67}Pb_{0.33}MnO_3$.

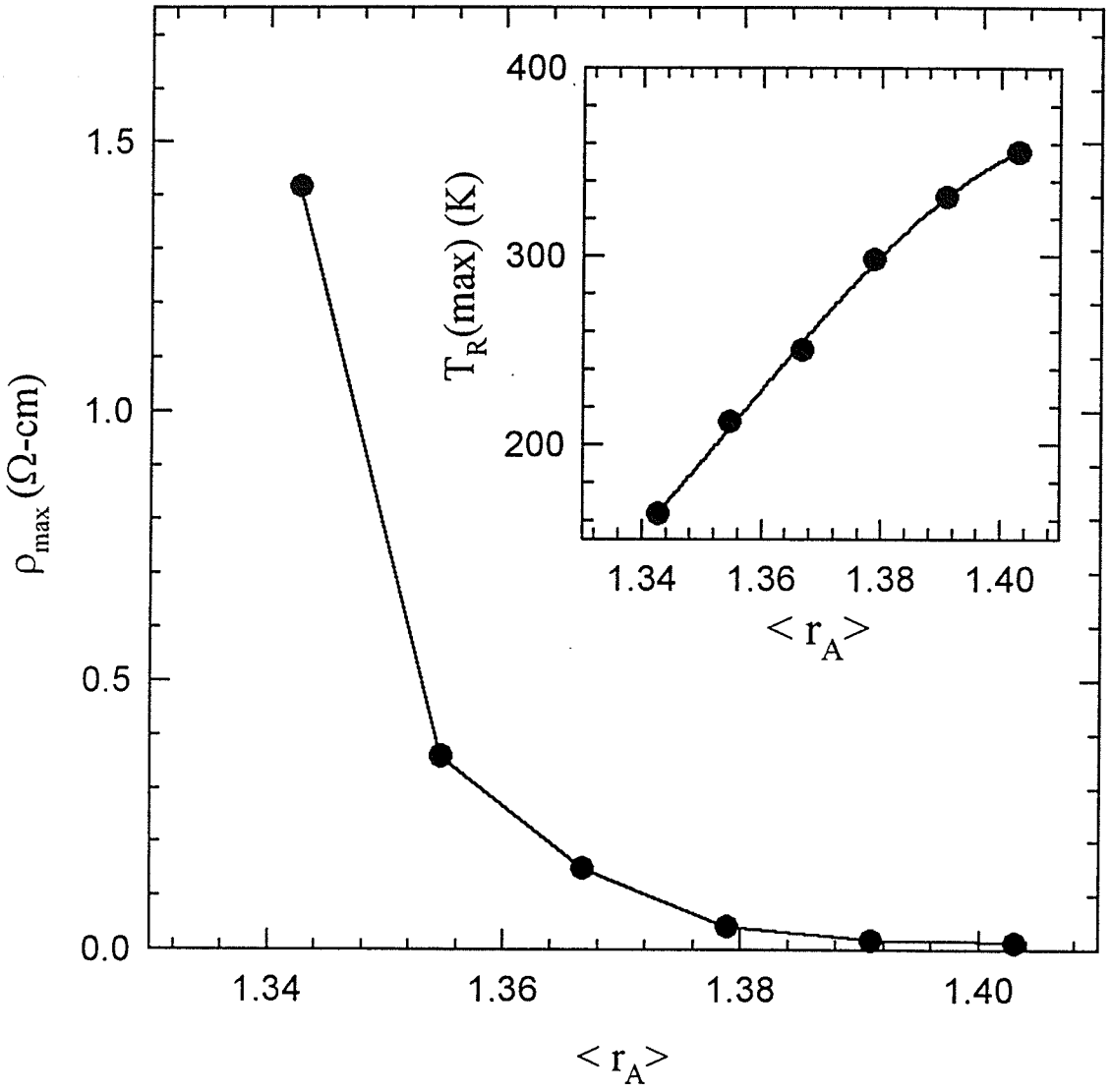

Figure 5.88: The value of peak resistivity, ρ_{max}, and its corresponding temperature, $T_{R(max)}$, versus $< r_A >$ for $(La_{1-x}Nd_x)_{0.67}Pb_{0.33}MnO_3$.

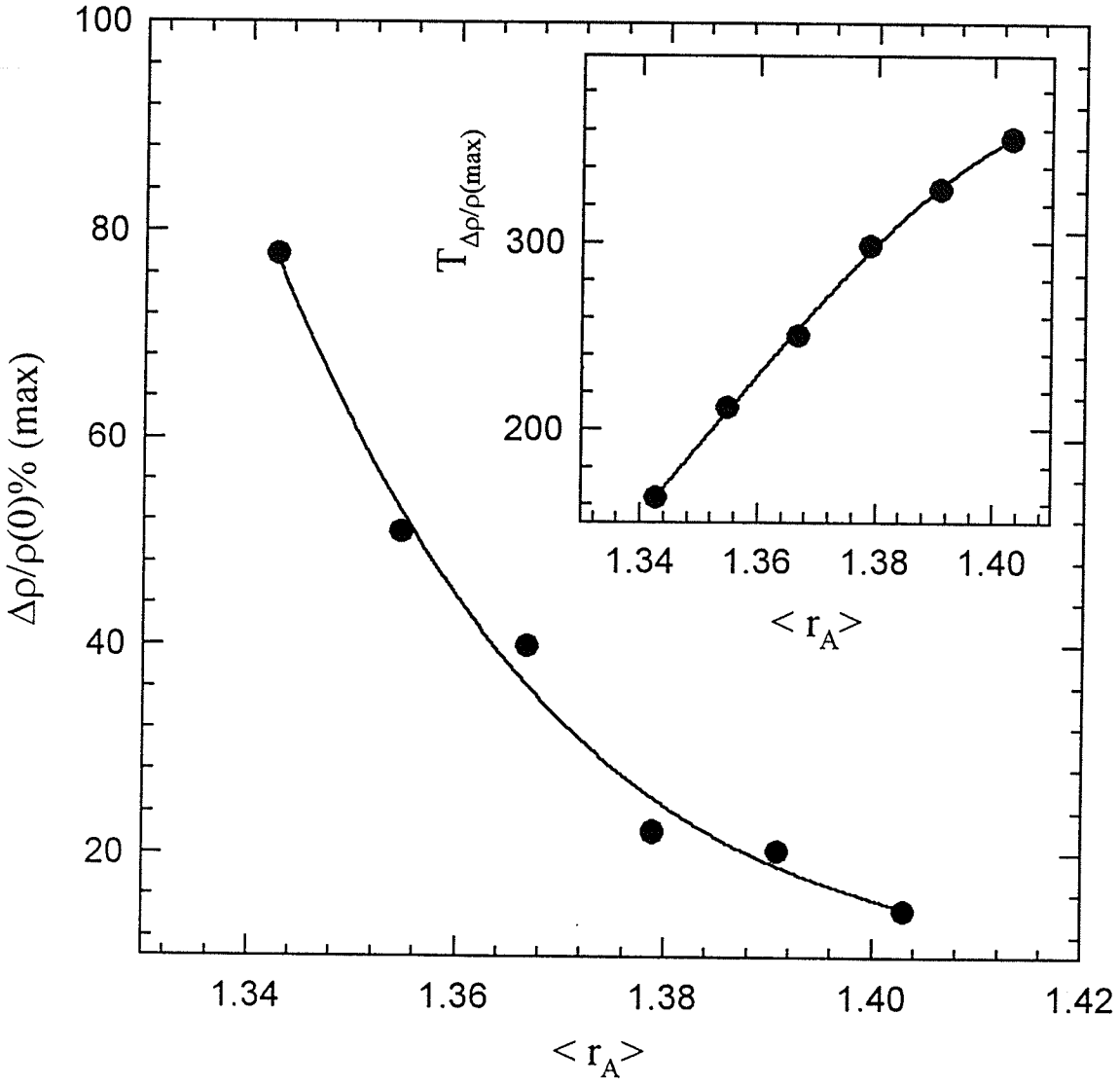

Figure 5.89: The value of peak magnetoresistivity and its corresponding temperature versus $< r_A >$ for $(La_{1-x}Nd_x)_{0.67}Pb_{0.33}MnO_3$.

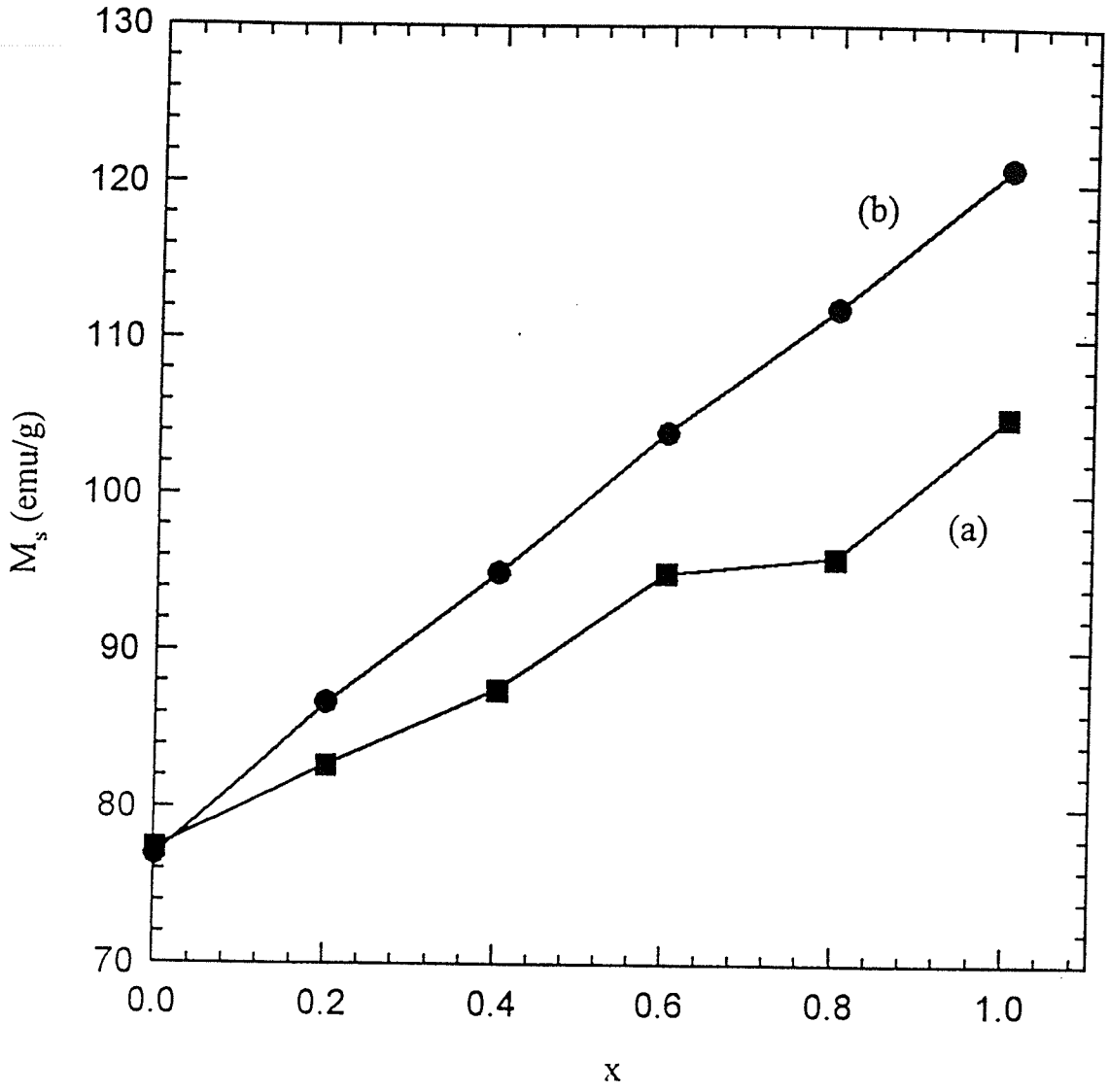

Figure 5.90: (a) The magnetization is extrapolated from the data measured in applied field up to 9 Tesla at 4.2 K; (b) the data is calculated when the moment of Nd ion is considered.

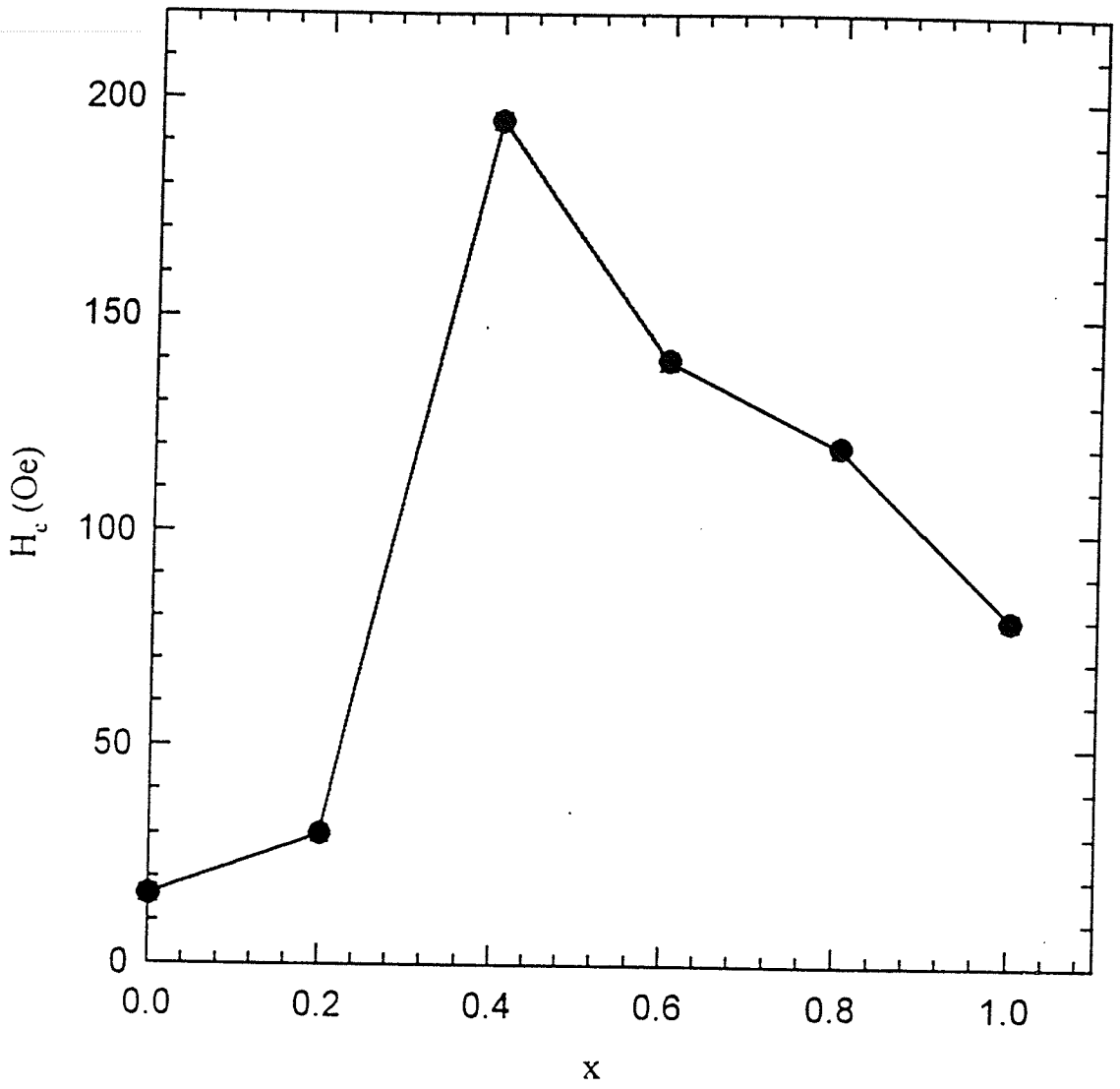

Figure 5.91: The coercivity measured at 4.2 K versus x.

Chapter 6

Conclusions

Recent extensive experimental studies on perovskite compounds with the general chemical formula $A_{1-x}B_xMnO_3$ have demonstrated that they exhibit a variety of magnetic and electrical properties depending upon the doping conditions (mainly the specific doping ion at the A site and its substitution level, x). The main interests in these systems arise from their colossal magnetoresistive effects which occur when a field is applied near a critical point. The MR is generally associated with a insulator/metal transition accompanying a paramagnetic/feromagnetic transition. The underlying physics of this effect has attracted a large amount of research both experimentally and theoretically; the principal models proposed were based initially on the double-exchange mechanism and, more recently, (bi)polaronic ones.

This thesis has concentrated on two issues; firstly on investigations of the critical magnetic phase transition and the precise role played by it in CMR, viz. the correlation between the paramagnetic/ferromagnetic phase transition and the insulator/metal one; secondly the transport behaviours have been examined and

discussed in terms of various model predictions.

The experimental studies on the $La_{0.67}Ca_{0.33}MnO_3$ system have shown that the magnetic phase transition is of a second order/continuous nature. The critical exponents values analyzed according to the static scaling law shows qualitative agreement with the predictions of the Hesienberg model despite some uncertainty in the low field response. Further complications are evident away from the critical point, and it has been suggested that they are caused by the existence of an inhomogeneous mixed valent (Mn^{3+}/Mn^{4+}) state which might result in both antiferromagnetic and ferromagnetic interactions. In addition, technical hardness, originating from single ion spin-orbit coupling (induced by Jahn-Teller Mn^{3+} ions) has an important effect on the ability to evaluate the critical response. The presence of spin-orbit coupling has been confirmed by measurements of the spontaneous resistive anisotropy (SRA). The SRA is present in the ordered state below the critical temperature, and declines to zero when the critical point is approached from below, qualititatively consistent with the theoretical expectations.

In contrast with the critical characteristics associated with double exchange, another important system, the pyrochlore type compound, $Tl_2Mn_2O_7$, has been investigated. In this pyrochlore, the mechanisms controling the exchange interaction and electrical transport are different from the manganese perovskits, the former being conventional superexchange exchange. Data analysis for this system has shown that the magnetic phase transition is again second order and the static magnetic critical exponents values are consistent with those predicted by the isotropic, near neighbour three dimensional Heisenberg model. The comparison

between the pyrochlore and the Ca-doped manganese perovskites shows that two systems belong to the same universality class despite differences in the underlying interactions.

The resistivity behaviour of untreated Ca doped manganese perovskite displays an insulating/metallic transition around the magnetic phase transition temperature, T_c, where CMR occurs. In the high temperature paramagnetic state, the resistivity behaviour can be well fitted by the small polaron model. This conclusion is further demonstrated by the experimental data of the Ar-annealed $La_{0.67}Ca_{0.33}MnO_3$. The results suggest that polaronic transport not only exists in the paramagnetic state but also persists into the ferromagnetic phase, providing supportive evidence for the validity of (bi)polaron models. The fitting parameters show that the adiabatic limit in the small polaron model is applicable to the high temperature paramagnetic region for the untreated sample, and that for the Ar-annealed specimen the non-adiabatic limit applies to both the high temperature paramagnetic and the low temperature ferromagnetic regimes. The charge carries reduce their activation energy in the ordered state rather than dissolve into free band electrons when entering the ordered state, unlike the situation in the untreated sample. The phase separation picture is also examined by comparing fitting parameters, particularly the tunneling length l, from experimental data with model predictions, the results show the model is not suitable for this system.

The $La_{1-x}Mg_xMnO_3$ system with doping level, x, from 0.05 to 0.6 has also been investigated, particular for the effect of subsititution of smaller Mg^{2+} ions

at the A sites. The data indicate that all samples studied undergo a magnetic phase transition from a paramagnetic to a ferromagnetic state as temperature decreases while the transport behaviour remains insulating without the occurrence of an insulator/metal transition. Critical exponent analysis indicates that for 0.05 $\leq x \leq$ 0.4 the effective exponent values reduce with increasing doping level x. This reflects a decrease in the ratio η= J_0/J, the latter declining towards unity as the doping level increases. For 0.45 $\leq x \leq$0.6 features at temperatures below T_c superficially resemble those associated with reentrent behaviour, which would correspond, in the SK model, to the ratio η falling below a value of 5/4. However careful analysis demonstrates that no such transition occurs, and these effects are likely caused by technical processes. The semiconducting transport behaviour, which has been demonstrated to be consistent with the predictions for charge transport by small polaron hopping in both the paramagnetic and ferromagnetic phases, arising from the complete suppression of a metal insulator transition in this system. In turn, this behaviour reflects a reduction in the $Mn(e_g)$-$O(2p_\pi)$ bandwidth due to decrease in the mean A site radius, $< r_A >$, with increasing doping level x. Based on the magnetic and transport data, a phase diagram for this system has been constructed, showing just a paramagnetic insulating to ferromagnetic insulating transition. This is relatively simpler than that exhibited by the Ca-doped system.

The $(La_{1-x}Nd_x)_{0.67}Pb_{0.33}MnO_3$ system ($0 \leq x \leq 1$) with Nd^{3+} ion substitution at the A sites has been shown to display both a paramagnetic/ferromagnetic phase transition and a metal-insulator phase change. With increases in x, the

tolerance factor t decreases, leading to a reduction in the overlap between orbitals and a narrowing bandwidth. As a result, the transition temperature T_c decreases from about 350 K to 170 K while resistivity and magnetoresistance increase with a decline in the insulator/metal transition temperature. These results reflect the effects of both smaller Nd ion substitution on the magnetic and transport properties as well as the influence of the Nd magnetic moments on these characteristics.

Bibliography

[1] G. A. Prinz, Physics Today 48, No. 4, (1995) 58.

[2] A. P. Ramirez, J. Phys.: Condens. Matter 9 (1997) 8171-8199.

[3] Josep Fontcuberta, Physics World, February (1999) 33

[4] G. H. Jonker and J. H. Van Santen, Physica, 16 (1950) 337; ibid 599

[5] C. Zener, Phys.Rev. 82,(1951) 403.

[6] P. W. Anderson and H. Hasegawa, Phys.Rev. 100 (1995) 675; P.G. De Gennes, Phys. Rev. 118 (1960) 141. N. Furukawa, J. Phys. Soc. Jpn. 63, 3214 (1994); ibid. 64,3164 (1995); ibid. 64, 4321 (1995)

[7] A. J. Millis, P. B. Littlewood and B. I. Shraiman, Phys. Rev. Lett. 74 (1995) 5144; A. J. Millis, B .I . Shraiman and R, Mueller, Phys. Rev. lett. 77, 175 (1996); Q. Li, J. Zhang, A. R. Bishop and C. M. Soukalis, Phys. Rev. B56, 4541 (1997); A. J. Millis, Nature 392 (1998) 147

[8] A. S. Alexandrov and A. M. Bratkovsky, J. Phys.: Condens. Matter 11 (1999) L531

[9] A. S. Alexandrov and A. M. Bratkovsky, J. Phys.: Condens. Matter 11 (1999) L531

[10] A. H. Morrish, The Physical Principles of Magnetism. John Wiley Sons. New York 1965

[11] H. A. Kramers, Physica, 182 (1934)

[12] P. W. Anderson, Phys. Rev. 79 (1950) 450

[13] A. Matthiessen and G. Vogt, Pogg. Ann. 122 (1864) 19

[14] F. Bloch, Z. Phys. 52(1929)555; ibid 539 (1929) 216; ibid 59 (1930) 208

[15] P. G. De Gennes and J. Friedel, J. Phys. Chem. Solids 4 (1958) 71

[16] I. A. Campbell and A. Fert, Ch 9, "Ferromagnetic materials" Vol 3, ed E.P. Wohlfarth, North Holland. Amsterdam (1982)

[17] A. Abragran and B. Bleaney, Electron Paramagnetic Resonance of Transitions. Clarendon Press, Oxford (1970)

[18] C. Kittel, Introduction to Solid State Physics. John Wiley Sons Inc. New York

[19] S. Satpathy, et al, Phys. Rev.Lett. 76 (1996) 960

[20] J-H Park, et al., Phys. Rev.Lett. 76 (1996) 4215

[21] H.Y. Hwang, et al., Phys. Rev.Lett. 77 (1996) 2041

[22] M. Jaime et al., Phys. Rev.Lett. 78 (1997) 951.

[23] H. L. Ju, et al., Phys. Rev.Lett. 79 (1996) 3230

[24] T. Saitoh, et al., Phys. Rev. Lett. 76 (1996) 4215

[25] P. Schiffer, et al., Phys. Rev. Lett. 75 (1995) 3336

[26] H. Y. Hwang, et al., Phys. Rev. Lett. 75 (1995) 914

[27] R. Mahesh, et al., J. Solid State Chem. 120 (1995) 204

[28] J. Foncuberta, et al., Phys. Rev. Lett. 76 (1996) 1122

[29] H. Y. Hwang, et al., Phys. Rev. B 52 (1995) 15046

[30] Y. Moritomo, et al., Phys. Rev. B 51 (1995) 16491

[31] J. J. Neumerier, et al., Phys. Rev. B 52 (1995) R7006

[32] H. Eugene Stanley, Introduction to Phase Transition and Critical Phenomena. Oxford University Press, Oxford, 1971

[33] M. Collins, Magnetic Critical Scattering, OXFORD UNIVERSITY PRESS, 1989

[34] J. J. Binney, N. J. Dowrick, A. J. Fisher,and M. E. J. Newman, The Theory of Critical Phenomena. Oxford Science Publication. 1992

[35] L. P. Kadanoff, Physics 2 (1966) 263

[36] M. J. Cooper, Phy.Rev. 168 (1968)183

[37] G. Williams, Magnetic Susceptibility of Superconductors and Other Spin Systems. Ed R.A.Hein et al. (New York: Plenum) (1991) P475

[38] S. C. Ho, I. Maartense and Gwyn Williams, J. Phys. F.: Metal Phys. 11 (1981) 699; ibid 1107; M. Saran and Gwyn Williams, J. Phys. F.: Metals 17 (1987) 731

[39] R. M. Roshko and G. Williams, J. Phys. F: Metal Phys. 14 (1984) 703

[40] H. Yoshizawa, et al, J. Phys. Soc. JPN. 65, (1996)1043

[41] J. M. De Teresa et al., Phys. Rev. Lett. 76, (1996) 3392

[42] A, Sundaresan et al., Phys. Rev. B 55 (1997) 5596

[43] D. Sherriton and S. Kirkpatrick, Phys. Rev. Lett. B 35 (1975) 1792.

[44] R. M. Roshko and G. Williams, J. Mag. Mag. Mat. 50 (1985) 311.

[45] J. A. Mydosh, Spin Glass, Taylor Francis London. Washington, DC, 1993.

[46] H. P. Kunkel and G. Williams, J. Magn. Magn. Mater. 75 (1988) 98.

[47] H. Ma, H. P. Kunkel and G. Williams, J. Phys.: Condens. Matter. 3 (1991) 5563.

[48] Z. Wang, Ph.D. Thesis, University of Manitoba, 1991

[49] P. A. Stampe, Ph.D. Thesis, University of Manitoba, 1997

[50] C. J. Schinkel and W. D. Van Amstel, Phys.Lett., 44A, 7 (1973) 467

[51] S. Jin, et al., Science 264 (1994) 413

[52] J. S. Kouvel and M. E. Fisher, Phys. Rev. A 136 (1964) 1626

[53] P. A. Stampe and Gwyn Williams, J. Phys. Condens. Matter, 10 (1998) 6771

[54] Z. Wang, H. P. Kunkel and Gwyn Williams, J. Phys.: Condens. Matter, 4 (1992)10385

[55] J. W. Lynn et al., Phys. Rev.Lett. 76 (1996) 4046

[56] T. G. Perring et al., Phys. Rev.Lett. 78 (1997) 3197

[57] A. J. Millis, Phys. Rev.Lett. 80 (1998) 4358 T. G. Perring et al., Phys. Rev.Lett. 80 (1998) 4359

[58] J. W. Lynn , L. vasilin-Doloc and M. A. Subramanian, Phys. Rev. Lett. 80 (1998) 4582

[59] Y. Shimakwa, Y. Kubo and T. Manako, Nature, 379 (1996) 53

[60] S-W Cheng, etal., Solid State Commun. 98 (1996) 163

[61] A. P. Ramirez and M. A. Subramanian, Science 277 (1997) 546

[62] M. A. Subramanian, et al., Science, 273 (1996) 81

[63] D-K Seo, et al., Solid State Commun., 101 (1997) 417

[64] K. Gosh, et al., Phy. Rev. Lett. 81 (1998) 4740

[65] Z .Wang, H. P. Kunkel and Gwyn Williams, J. Phys.: Condens. Matter, 2 (1990) 4173

[66] Ch. Mohan, et al., J. Magn. Magn. Mater. 183 (1998) 348

[67] S. N. Kaul, J. Phys. F. Met. Phys. 18 (1988) 2089 S. N. Kaul and C. V. Mohan, Phys. Rev. B50 (1994) 6157

[68] Ning Zhang et al., Phys. Rev. B 56 (1997) 8138; X. L. Wang et al., Applied Physics Letters, 73 (1998) 396

[69] A. Gupta, et al., Phys. Rev. B54 (1996) R15629

[70] H. Y. Hwang, Phys. Rev. Lett. 77 (1996) 2041

[71] A. K. M. Akther Hossain et al., J. M. M. M., 195 (1999) 31-36; L. E. Hueso et al., J.M.M.M., 189 (1998) 321-328; H. J. Ju, et al., Phys. Rev. B 51 (1995) 6143

[72] G. M. Zhao et al., Phys. Rev. Lett. 84 (2000) 6086

[73] A. Freiderich and A. Fert, Phys. Rev. Lett. 33 (1972) 1214

[74] J. W. F. Dorleijn, Philips. Res. Rep. 31 (1976) 287

[75] A. Fert, et al, Phys. Rev. B16 (1977) 5040

[76] A. P. Malezemoff, Phys. Rev. B 32 (1985) 6080; ibid B34 (1986) 1853

[77] P. A. Stampe, X. Chen, Z. Wang, H. P. Kunkel and G. Williams, J. Phys.: Condensed Mater, 6 (1994) 3045

[78] X. W. Li, A. Gupta, X. Gang, and G. Q. Gong, Appl. Phys. Lett., 71 (1997) 1124

[79] M. Ziese and S. P. Sena J. Phys.: Condens. Matter 10 (1998) 2727

[80] A. Peles, Thesis, University of Manitoba, 1999

[81] G. M. Zhao, K.Conder, H. Keller and K .A. Müller, Nature (London) 381 (1996) 676; J. P. Franck, I. Isacc, W. Chen, J, Chrzanowski and J. C. Irwin, Phys. Rev. B58, (1998) 5189.

[82] G. Zhao, H. Keller and W. Prellier, J. Phys.: Condens. Matter, 12 (2000) L361;

[83] R.V. Krishnan and A. Banerjee, J. Phys.: Condens. Matter 12,7887 (2000)

[84] K. Dörr et al., J. Phys.: Condens. Matter 12 (2000) 7099.

[85] S. Chikazumi in Physics of Ferromagnetism, (2nd edition; Clarendon: Oxford 1997), P. 486

[86] S. Kaul and C. V. Mohan, Phys. Rev. B50 (1994) 6157; S .Kaul, J. Magn. Magn. Mater. 53 (1985) 5

[87] M. Jaime and M. B. Salamon in Physics of Manganites, edited by T. A. Kaplan and S. D. Mahanti (Plenum, New York 1999), p 243 et. Seq; D. C. Worledge, L. Mieville and T. Geballe, Phys. Rev. B57, 15267 (1998); L. C. LeGuillon and J. Zinn-Justin, Phys. Rev. B21, 3976 (1980).

[88] I. O. Troyanchuk, et al., J. Phys.: Condens. Matter, 12 (2000) L155

[89] D. Emin and T. Holstein, Ann. Phys. (NY) 53 (1969) 439.

[90] A. L. Rakhmanov et al. Phys. Rev. B63 (2001) 174424.

[91] A. Belzner, et al., Solid state Ion. 57 (1992)327.

[92] R. Raffaelle, H. U. Anderson, D. M. Sparlin and P. E. Parris, Phys. Rev. B43, 799 (1991); M. Jaime, et al Phys. Rev. B54, 11914 (1996); N. F. Mott and E.A. Davis, in Electronic Processes in Non-crystalline Material (Clarendon press, Oxford, 1971; 1979); G. J. Snyder, et al, Phys. Rev. B53, 14, 434 (1996).

[93] J. C. Philips in Physics of High-Tc Superconductors (Academic Press, San Diego, 1989).

[94] D. Bhattacharya et al. J. Phys.: Condens. Matter 13 (2001) L431.

[95] G. Papvassiliou et al., Phys. Rev. Lett. 84, 761 (2000); A. Lanzara et al., Phys. Rev. Lett. 81, 878 (1998); M. Hennion et al., Phys.Rev. B56, R497 (1997); S. Billinge, in Physics of Manganites, edited by T. A. Kaplan and S. D. Mahanti (Plenum, New York, 1999), p 201 et seq.

[96] B. R. Coles, B. V. B. Sarkissian and R. H. Taylor, Phil. Mag. B37, 489 (1978)

[97] A. Moreo, M. Mayr, A. Feiguin, S. Yunoki and E. Dagotte, Phys. Rev. lett. 84, 5568 (2000)

[98] A. Urushibara, et al., Phys. Rev. B51, 14103 (1995); B. Dabrowski et al., Phys. Rev. B60, 7006 (1999)

[99] A. M. De Leon-Guevara, et al. Phys. Rev. B 56 (1997) 6031

[100] M. Yu. Kagan, et al. Eur. Phys. J. B12 (1999) 217

[101] J. H. Zhao, T. Song, H. P. Kunkle, X. Z. Roshko, and G. Williams, J. Phys.: Condens, Matter 12 (2000) 1-16

[102] S. de Brion et al. Phys. Rev. B59 (1999)1470; K. Dwight and N. Menyuk, Phys. Rev. 119 (1960) 1470

[103] I. S. Jacobs and J. S. Kouvel, Phys. Rev. 122 (1961) 412

[104] J. S. Kang et al. J. Phys.: Condens.Matter 13 (2001) 3779

[105] A. B. Harris. J. Phys. C: Solid state physics 7 (1974) 1671

[106] M. Gabay, G. Toulouse, Phys. Rev. Lett. 47(1981) 201

[107] S. M. Dubiel, Phys. Rev. B36 (1987) 360

[108] R. N. Bhatt and A. P. Young, Phys. Rev. Lett. 54 (1985) 924

[109] A. G. Berndt et al., Phys. Rev. B52 (1995) 10160; B59 (1999) 8391

[110] K. Binder and A. p. Young Rev. Mod. Phys. 58 (1986) 801

[111] Toshifumi Taniguchi et al, Journal of the Physical Society of Japan, 54 (1985) 220

[112] A. Tobo, A. Ito, J. M. M. M. 177-181(1998) 105-106

[113] D. Emin and L. H. Liu, Phys Rev. B27 (1983) 4788

[114] C. W. Searle and S. T. Wang, Can. J. Phys. 47 (1969) 2703; 48 (1970) 2023

[115] R. D. Shannon, Acta Crystallogr. Sec. A 32, 751 (1976)

[116] Lide M. Rodriguez-Martinez and J. Paul Attfield, Phys. Rev. B 54 (1996) R15622